ISSN 1983-4195

IBRACON

# IBRACON Structures and Materials Journal

## Revista IBRACON de Estruturas e Materiais

**Volume 16, Number 1**
February 2023

ISSN 1983-4195
Volume 16, Number 1
February 2023

# IBRACON Structures and Materials Journal
## Revista IBRACON de Estruturas e Materiais

## Contents



**Courtesy:** Marcela Noronha P. de O. e Sousa

IBRACON

**Ibracon Structures and Materials Journal** is published bimonthly (February, April, June, August, October, and December) by IBRACON.

**IBRACON**
Instituto Brasileiro do Concreto Founded in 1972

Av. Queiroz Filho, nº 1700 — sala 407/408
Torre D — Villa Lobos Office Park
CEP 05319-000 — São Paulo, SP — Brazil
Phone: +55 11 3735-0202
Fax: +55 11 3733-2190
**E-mail:** riem@ibracon.org.br
**Website:** http://www.ibracon.org.br

**Cover design & Layout:** Editora Cubo www.editoracubo.com.br

**Support:** Wallison Angelim Medeiros

# Aims and Scope

## Aims and Scope

The IBRACON Structures and Materials Journal (in Portuguese: Revista IBRACON de Estruturas e Materiais) is a technical and scientific divulgation vehicle of IBRACON (Brazilian Concrete Institute), published every two months. Each issue has 12 to 15 articles and, possibly, a technical note and/or a technical discussion regarding a previously published paper. All contributions are reviewed and approved by professionals with recognized scientific competence in the area. The IBRACON Structures and Materials Journal is an open access Journal, free of charges for authors and readers.

## Objectives

The IBRACON Structures and Materials Journal´s main objectives are:

- Present current developments and advances in concrete structures and materials.
- Make possible the better understanding of structural concrete behavior, supplying subsidies for a continuous interaction among researchers, producers, and users.
- Stimulate the development of scientific and technological research in the areas of concrete structures and materials, through papers peer-reviewed by a qualified Editorial Board.
- Promote the interaction among researchers, constructors and users of concrete structures and materials and the development of Civil Construction.
- Provide a vehicle of communication of high technical level for researchers and designers in the areas of concrete structures and materials.

## Submission Procedure

The procedure to submit and revise the contributions, as well as the formats, are detailed in the Journal Website (ismj.org).

The papers and the technical notes are revised by at least two reviewers indicated by the editors. Discussions and replies are accepted for publication after a review by the editors and at least one member of the Editorial Board. In case of disagreement between the reviewer and the authors, the contribution will be sent to a specialist in the area, not necessarily linked to the Editorial Board. Conflict of interests is carefully handled by the Editors.

## Contribution Types

The Journal will publish original papers, short technical notes, and paper discussions. Original papers will be accepted if they are in accordance with the objectives of the Journal and present quality of information and presentation. A technical note is a brief manuscript. It may present a new feature of research, development, or technological application in the areas of Concrete Structures and Materials, and Civil Construction. This is an opportunity to be used by industries, companies, universities, institutions of research, researchers, and professionals willing to promote their works and products under development.

A discussion is received no later than 3 months after the publication of the paper or technical note. The discussion must be limited to the topic addressed in the published paper and must not be offensive. The right of reply is granted to the Authors. The discussions and the replies are published in the subsequent issues of the Journal.

The submission file should be in accordance with the paper template available at the Journal Website. It is recommended that the length of the papers does not exceed 25 pages. Where available, URLs for the references should be provided.

The IBRACON Structures and Materials Journal will conduct the review process for manuscripts submitted in English. Titles, abstracts, and keywords are presented in English, and in Portuguese or Spanish. Articles and technical notes are peer-reviewed and only published after approval of the reviewers and the Editorial Board.

Once accepted, an article is typeset according to the journal layout. The author will be required to review and approve the galleys before publishing. At this stage only typesetting errors will be considered.

## Internet Access

The IBRACON Structures and Materials Journal Webpage is available at http://ismj.org.

## Sponsors

The funds for the maintenance of the Journal are currently obtained from the IBRACON. The Journal is not supposed to be maintained with funds from private sponsorship, which could diminish the credit of the publications.

## Photocopying

Photocopying in Brazil. Brazilian Copyright Law is applicable to users in Brazil. IBRACON holds the copyright of contributions in the journal unless stated otherwise at the bottom of the first page of any contribution. Where IBRACON holds the copyright, authorization to photocopy items for internal or personal use, or the internal or personal use of specific clients, is granted for libraries and other users registered at IBRACON.

## Copyright



## IBRACON

Av. Queiroz Filho, 1700 – sala 407/408 – Torre D
Villa Lobos Office Park
05319-000 – Vila Hamburguesa
São Paulo – SP
Phone: +55 (11) 3735-0202
E-mail: riem@ibracon.org.br

## Disclaimer

Papers and other contributions and the statements made or opinions expressed therein are published on the understanding that the authors of the contribution are the only responsible for the opinions expressed in them and that their publication does not necessarily reflect the views of IBRACON or of the Journal Editorial Board.

# Editorial Board

# Editorial Board

# Direction

## Board of Direction 2021/2023 Biennium

**President**
Paulo Helene

**1st Vice-President Director**
Júlio Timerman

**2nd Vice-President Director**
Enio José Pazini Figueiredo

**Presidency Advisors**
Arnaldo Forti Battagin
Eduardo Antonio Serrano
Gilberto Antonio Giuzio
Iria Lícia Oliva Doniak
Jaques Pinto
João Luis Casagrande
Jorge Batlouni Neto
José Marques Filho
Mario William Esper
Ronaldo Tartuce
Rubens Machado Bittencourt
Selmo Chapira Kuperman
Simão Priszkulnik
Túlio Nogueira Bittencourt
Wagner Roberto Lopes

**1st Director-Secretary**
Cláudio Sbrighi Neto

**2nd Director-Secretary**
Carlos José Massucato

**1st Treasurer Director**
Júlio Timerman

**2nd Treasurer Director**
Hugo S. Armelin

**Marketing Director**
Alexandre Britez

**Marketing Director Advisor**
Guilherme Covas

**Publications Director**
Guilherme Parsekian

**Publications Director Advisor**
Túlio Nogueira Bittencourt

**Event Director**
Rafael Timerman

**Event Director Advisor**
Luis César De Luca

**Technical Director**
Carlos Britez

**Technical Director Advisor**
Emílio Takagi

**Institutional Relations Director**
César Henrique Daher

**Institutional Relations Director Advisor**
José Vanderley de Abreu

**Course Director**
Jéssica Pacheco

**Course Director Advisor**
André Mendes

**Student Activities Director**
Jéssica Andrade Dantas

**Student Activities Director Advisor**
Patrícia Bauer

**Personnel Certification Director**
Adriano Damásio Soterio

**Personnel Certification Director Advisor**
Paula Baillot

**Research and Development Director**
Bernardo Tutikian

**Research and Development Director Advisor**
Roberto Christ

## Council 2021/2023 Biennium

**Individual Members**
Alio Ernesto Kimura
Antônio Carlos dos Santos
Antônio Domingues de Figueiredo
Arnaldo Forti Battagin
Bernardo Fonseca Tutikian
Carlos José Massucato
César Henrique Sato Daher
Claudio Sbrighi Neto
Enio José Pazini Figueiredo
Geraldo Cechella Isaia
Iberê Martins da Silva
Inês Laranjeira da Silva Battagin
Iria Lícia Oliva Doniak
Jéssika Mariana Pacheco Misko
José Tadeu Balbo
Leandro Mouta Trautwein
Luiz Prado Vieira Júnior (*in memoriam*)
Mário William Esper
Rafael Timerman
Rubens Curti
Vladimir Antonio Paulon

**Past President Members**
Eduardo Antônio Serrano
José Marques Filho
Júlio Timerman
Paulo Roberto do Lago Helene
Ronaldo Tartuce
Rubens Machado Bittencourt
Selmo Chapira Kuperman
Simão Priszkulnik
Túlio Nogueira Bittencourt

**Corporate Members**

ABCIC - Associação Brasileira da Construção Industrializada de Concreto – Iria Lícia Oliva Doniak

ABCP - Associação Brasileira de Cimento Portland – Paulo Camilo Penna

ABECE - Associação Brasileira de Engenharia e Consultoria Estrutural – João Alberto de Abreu Vendramini

ABESC - Associação Brasileira das Empresas de Serviços de Concretagem – Wagner Roberto Lopes

EPUSP - Escola Politécnica da Universidade de São Paulo – Túlio Nogueira Bittencourt

IPT - Instituto de Pesquisas Tecnológicas do Estado de São Paulo – José Maria de Camargo Barros

MC-BAUCHEMIE BRASIL INDÚSTRIA E COMÉRCIO LTDA – Jaques Pinto

PhD Engenharia Ltda – Douglas de Andreza Couto

TQS Informática Ltda – Nelson Covas

VOTORANTIM Cimentos S/A – Mauricio Bianchi

IBRACON Structures and Materials Journal
Revista IBRACON de Estruturas e Materiais
ISSN 1983-4195 ismj.org

ORIGINAL ARTICLE

# A new methodology to assess the structural capacity of bridge portfolios: application in Northeastern Brazilian bridges

## *Uma nova metodologia para avaliação da capacidade estrutural de portfólios de pontes: aplicação nas pontes situadas no Nordeste do Brasil*

Gustavo Henrique Ferreira Cavalcante[a]
Eduardo Marques Vieira Pereira[a]
Isabela Durci Rodrigues[b]
Luiz Carlos Marcos Vieira Júnior[a]
Gustavo Henrique Siqueira[a]

[a]Universidade Estadual de Campinas – Unicamp, Faculdade de Engenharia Civil, Arquitetura e Urbanismo, Departamento de Estruturas, Campinas, SP, Brasil

[b]Universidade de São Paulo – USP, Escola de Engenharia de São Carlos, Departamento de Estruturas, São Carlos, SP, Brasil

**Received** 12 November 2021
**Accepted** 03 March 2022

**Abstract:** This article presents a new proposal to estimate structural capacity models for bridge portfolios. A common approach is the use of ductility-based capacity models. Herein, a ductility replacement for curvature or drift as engineering demand parameters is conducted, as variability within the bridge's classes is considered in the results and multidirectional pushover analyses are performed to assess a bi-directional load scenario. Application of the methodology is exemplified for an inventory of Northeastern Brazilian bridges. Parametric analyses are performed by varying the reinforcement ratios to estimate the capacity limit states within the range of values used. These results from probabilistic models define the capacity limit state that can be used to perform vulnerability assessment of bridges to different hazard sources, such as earthquakes.

**Keywords:** structural capacity, parametric analysis, multidirectional pushover analysis.

**Resumo:** Este artigo apresenta uma proposta para determinação da capacidade estrutural de portfólios de pontes. Uma prática comum é o uso de modelos de capacidade baseados na ductilidade. Neste trabalho, a ductilidade é substituída por curvatura ou *drift* como parâmetros de demanda, uma vez que a variabilidade dos parâmetros que definem classes de pontes é considerada nos resultados e análises multidirecionais do tipo *Pushover* são realizadas para avaliar cenários de forças bidirecionais. Uma aplicação da metodologia é exemplificada para um inventário de pontes típicas situadas no Nordeste do Brasil. Análises paramétricas são realizadas por meio da variação das taxas de armaduras para determinação dos estados-limites dentro dos valores estudados. Os resultados dos estados limites de capacidade são informações valiosas para realização de estudos de vulnerabilidade de portfólios de pontes para diferentes fontes de ameaça, como sismos.

**Palavras-chave:** capacidade estrutural, análise paramétrica, pushover multidirecional.

**How to cite:** G. H. F. Cavalcante, E. M. V. Pereira, I. D. Rodrigues, L. C. M. Vieira Júnior, and G. H. Siqueira, "A new methodology to assess the structural capacity of bridge portfolios: application in Northeastern Brazilian bridges," *Rev. IBRACON Estrut. Mater.*, vol. 16, no. 1, e16101, 2023, https://doi.org/10.1590/S1983-41952023000100001

**Corresponding author:** Gustavo Henrique Ferreira Cavalcante. E-mail: ghenriquefc@hotmail.com
**Financial support:** This study was financed in part by the Coordenação de Aperfeiçoamento de Pessoal de Nível Superior - Brasil (CAPES) - Finance Code 001; and by the São Paulo Research Foundation (FAPESP) - Finance Code 2018/23304-9. The opinions, findings, and conclusions or recommendations expressed in this paper are those of the authors only and do not necessarily reflect the views of the sponsors or affiliates.
**Conflict of interest:** Nothing to declare.
**Data Availability:** The data that support the findings of this study are available from the corresponding author, GHFC, upon reasonable request.

## 1 INTRODUCTION

Bridges have fundamental importance in the economic and social development of cities. Such structures, based on past earthquake events, can be considered the most vulnerable components in a highway transportation system, as highlighted by well-known cases of earthquakes [1]-[3], and other natural hazards [4]-[8]. In order to assess the seismic vulnerability of bridges, Performance-based earthquake engineering (PBEE) can be used, since it is a comprehensive framework of vulnerability in terms of the expected performance [9].

As an essential part of the PBEE framework, there are the fragility functions, which are defined as the conditional probability of damage over a range of potential hazard intensities. Therefore, these functions are important tools in several analyses, such as in regional seismic risk assessments to estimate the potential for damage or losses due to seismic events, or in evaluating the efficiency of seismic design provisions. Fragility assessment requires the probabilistic distributions of the demand and the capacity of each component of the system. The demand is the peak structural response for a given intensity measure, whereas the capacity depicts the response at the limit states' thresholds. Therefore, in order to generate reliable fragility functions, one needs reliable capacity models for all bridge components (e.g., bearing, abutments, columns, deck). Traditionally, these models have been defined in terms of qualitative damage states such as slight, moderate, extensive and complete [10] associated with a timeline for the restoration of the bridge functionality [11].

The columns of a bridge are commonly adopted as a system's component, since severe damage to them may lead to bridge closure or collapse [12]; hence, an adequate determination of the bents' structural capacity probabilistic model is of utmost importance. Most studies on fragility analysis of bridges measure damage based on the column's ductility demand ratio [13], i.e., the ratio of the peak structural response and the structural response that causes the first yield on a reinforcement bar (yield parameter hereafter). Several researchers [9], [11]-[16] adopt the curvature ductility ($\mu_\phi$) as an engineering demand parameter (EDP) to define column capacity models. This methodology provides probabilistic distributions to properly account for uncertainties about the association between quantitative (e.g., curvature ductility values) and qualitative damage states. For that, it is necessary to associate expert opinion regarding post-event failures [17] and numerical or experimental results [13], [18], [19].

A fragility assessment based on the column's ductility demand ratio requires an adequate definition of the yield parameter (e.g., yield curvature, yield drift, yield displacement). Therefore, analytical equations based on experimental results [20]-[23] or numerical approaches through sectional analysis [24] and Pushover analysis (PA) [25] are commonly adopted. PA is also used to define the limit state models of several types of structural systems, such as buildings [26], bridges [27], and free-form shells [28].

PA consists of the application of incremental forces to evaluate the inelastic behavior of a structure in each step until collapse, or whether any desired displacement, is reached. This procedure allows the definition of the exact step corresponding to the first yield of reinforcing steel, which provides the yield parameter considering the three-dimensional behavior of the structural system and the section properties in the numerical modeling.

Bridges' bents situated in one plane only (e.g., two-column bents) combined with a flexible superstructure using elastomeric bearings can be sensitive to torsion [27]. In addition, ground motions comprise three translational components, which means that simultaneous seismic demand imposes itself in more than one direction (consequently a large resultant demand). Bi-directional loading also increases the strength and stiffness degradation of columns [29]-[30]; therefore, the structural capacity model should be consistently able to reflect this behavior. This means that the traditional methods [20]-[24] may not be adequate to estimate the capacity of bridge bents; however, a multidirectional Pushover procedure can adequately estimate the yield parameter for bi-directional horizontal loads.

In view of the above, this article aims to propose a new probabilistic framework to determine the structural capacity model of bridge's bents coupled with Multidirectional Pushover Analyses (MPA). Nonlinear numerical simulations are conducted using finite element models with features of bridges in Northeastern Brazil, obtained from a robust background statistical study. The MPA are performed to investigate the effect of bi-directional loads on the yield parameter of bridge's bents in Northeastern Brazil. Given that information on the detailing of the existing bridges' bents is hardly available, parametric analyses are also performed to investigate the impact of the column's reinforcement ratios on the yield parameter. The contribution of this study is, therefore, multifold, in the sense that it provides not only insights on the effect of MPA and other parameters in the structural capacity probabilistic models, but also contributes to the development of capacity models for bridges through a new methodology.

## 2 BRIDGE CHARACTERISTICS AND NUMERICAL MODELING

### 2.1 Characteristics and variability of bridges

There are approximately 5000 bridges located on federal highways in Brazil, under the supervision of the National Department of Infrastructure and Transportation (DNIT). About 50% of these bridges are located in Northeastern Brazil, which presents one of the highest seismic activities compared to other parts of Brazil [31]-[33]. Furthermore, bridges have the worst structural condition countrywide; 6.6% of them require immediate or mid-term interventions, as seen in [34]. Recurrent floods in the region also aggravate bridges' condition [7]. These specific effects, however, are not explored herein.

A recent study conducted by [35] evaluated 250 reports of bridges located in Northeastern Brazil and grouped them into classes with similar structural characteristics. Table 1 presents the description and representativeness of the bridges' classes, according to the number and spans' continuity, deck section, number of columns per bents, and type of abutments. Cast-in-place and straight concrete bridges supported on elastomeric bearings represent these classes, since they represent the vast majority of the reports.

**Table 1.** Representativeness and description of the bridges' classes.

| Bridge's class | Bridge description | % |
|---|---|---|
| SS-SD-Abut | Single-span, slab deck and non-integral abutments | 16.4% |
| SS-TB-Abut | Single-span, T-beam deck and non-integral abutments | 27.6% |
| MSC-TB | Multi-span continuous, T-beam deck, two column bents and no abutments | 17.2% |
| MSC-TB-Abut | Multi-span continuous, T-beam deck, two column bents and non-integral abutments | 6.4% |
| Others | | 32.4% |

Two bridges' classes with bents (MSC-TB and MSC-TB-Abut) are analyzed herein and represent 23.6% of the total of the selected bridges (250). Figure 1 illustrates the geometric properties of the typical bridges' classes described in Table 1. Gravity or U seat-type abutments support MSC-TB-Abut bridge's classes. All decks of the bridges' classes (MSC-TB and MSC-TB-Abut) are considered supported on elastomeric bearings.

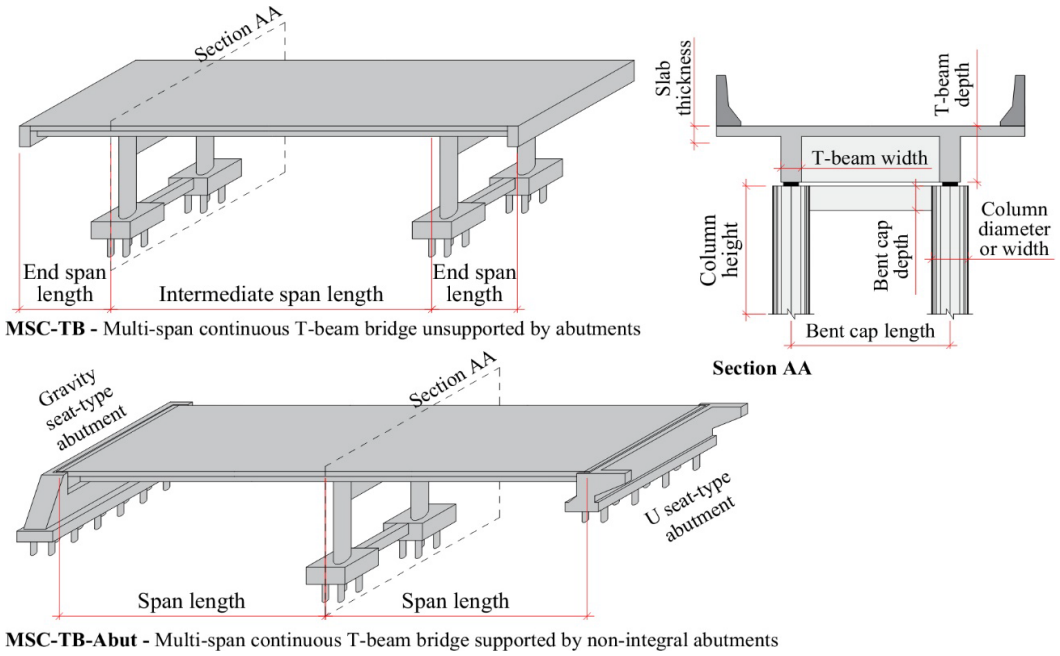


**Figure 1.** Geometric properties of the bridges' classes.

Several geometric features are adopted as variable to define each bridge's class, such as: number of spans; span length; slab deck width and thickness; T-beam deck width; depth, width and slab thickness; column height and cross section dimensions; bent cap length, depth and width; abutment type and dimensions. Discrete and continuous distributions describe independent geometric variabilities (i.e., span length and column height). However, some parameter variabilities (i.e., T-beam depth and span length) are defined as a function of these independent variables, since strong correlations are observed in [35]. Pearson's linear correlation coefficients ($\rho_{xy}$) are calculated and $\rho_{xy} > 0.7$ is assumed to indicate a strong correlation. The foundations, material properties and design details are not informed in the reports.

### 2.1.1 MSC-TB bridge's class variability

Table 2 summarizes the characterization of the portfolio variabilities for the MSC-TB bridge's classes. In addition, the widths of the T-beams and bent caps are assumed to be 0.4 m, as few reports present this information. Further details on distribution and function fits are available in [35]. Geometric parameters (e.g., intermediate span length) fitted by normal distributions are truncated using a 5% percentile cutoff point to avoid negative values, which are not physically representative.

**Table 2.** Characterization of the portfolio variabilities for the MSC-TB bridge's class [35].

| Variable | Distribution or function | Subclass | Parameters (m) |
|---|---|---|---|
| Number of spans (Ns) | Discrete | - | Ns = 3 (51.4%) |
| | | | Ns = 4 (11.4%) |
| | | | Ns = 5 (37.1%) |
| Intermediate span length (Lis) | Normal | - | $\mu = 18.24$, $\sigma = 4.79$ |
| | | | and Lis ≥ 10.4 |
| End span length (Les) | Linear regression | - | Les(Lis) = 0.18 Lis + 1.03 |
| T-beam depth (Db) | Linear regression | - | Db(Lis) = 0.05 Lis + 0.78 |
| Deck width (Dw) | Lognormal | - | $\lambda = 2.35$ and $\zeta = 0.14$ |
| Bent cap length (Lbc) | Linear regression | - | Lbc(Dw) = 0.56 Dw + 0.64 |
| Bent cap depth (Dbc) | Linear regression | - | Dbc(Lbc) = 0.12 Lbc + 0.33 |
| Slab thickness (Sd) | Linear regression | - | Sd(Lbc) = 0.04 Lbc |
| Column height (Hc) | Lognormal | - | $\lambda = 1.25$ and $\zeta = 0.47$ |
| Column diameter (Dc) or width (Wc) | Linear regression | 1[1] | Dc(Lis) = 0.02 Lis + 0.37 |
| | | 2[1] | Wc(Lis) = 0.03 Lis + 0.25 |

[1] Subclass 1 indicates bridges composed of circular columns with 73.7% occurrence
[2] Subclass 2 indicates bridges composed of rectangular columns with 26.3% occurrence

### 2.1.2 MSC-TB-Abut bridge's class variability

The summary of the portfolio variabilities of the MSC-TB-Abut bridge's class are illustrated in Table 3. According to the reports, some parameters are assumed to have constant values, such as the slab thickness of 0.3 m, deck width of 10 m, and the width and depth of the bent caps of 0.4 m and 1.0 m, respectively.

**Table 3.** Characterization of the portfolio variabilities for the MSC-TB-Abut bridge's class [35].

| Variable | Distribution or function | Subclass | Parameters (m) |
|---|---|---|---|
| Number of spans (Ns) | Discrete | - | Ns = 2 (66.7%) |
| | | | Ns = 3 (26.7%) |
| | | | Ns = 4 (6.6%) |
| Span length (Ls) | Lognormal | - | $\lambda = 2.7$ and $\zeta = 0.37$ |
| T-beam depth (Db) | Linear regression | - | Db(Ls) = 0.09 Ls + 0.07 |
| Bent cap length (Lbc) | Lognormal | - | $\lambda = 1.57$ and $\zeta = 0.04$ |
| Column diameter (Dc) | Linear regression | - | Dc(Ls) = 0.03 Ls + 0.36 |
| Column height (Hc) | Normal | - | $\mu = 4.82$, $\sigma = 1.58$ and Hc ≥ 1.66 |
| Abutment height (Ha) | Lognormal | 1[1] | $\lambda = 1.65$ and $\zeta = 0.41$ |
| | | 2[1] | $\lambda = 1.96$ and $\zeta = 0.13$ |

[1] Subclass 1 indicates gravity seat-type abutments with 42.9% occurrence
[2] Subclass 2 indicates U seat-type abutments with 57.1% occurrence

### 2.1.3 Material variability

Some parameters are not available in the DNIT database, such as compressive strength of concrete (fc), steel yield stress (fy) and steel Young's modulus (Es). Their mean values (μ) and standard deviation (σ) are considered based on the literature, as shown in Table 4. Therefore, they are used as material variabilities to create different bridge samples. A conservative approach is used in the characterization of the fc values, which is based on the C20 concrete class, since 77.7% of the age bridges recorded in DNIT reports were built up to 1975 [34]. Furthermore, the steel Young's Modulus is used as 210 GPa [36] for all analyses, as it has a small coefficient of variation value (i.e., about 3% in [37]).

**Table 4.** Material variability considered herein.

| Variable | Distribution | Parameters | Reference |
|---|---|---|---|
| fc (MPa) | Normal | μ = 26.2 and σ = 4.3 | Santiago and Beck [38] |
| fy (MPa) | Normal | μ = 576 and σ = 46.1 | Nogueira [39] |

Longitudinal and transverse reinforcement ratios for bent caps are calculated based on the minimum requirements of [36], since the T-beams are supported directly on the columns. A longitudinal reinforcement ratio of 1% is adopted for the columns according to [40] since Brazilian's bridges are usually not designed considering seismic detailing. Any other seismic details (e.g., shear keys, restrainer cables, elastomeric isolation bearing, steel jacket) were not seen in the reports, indicating that these seismic resistance features are not significantly used. In addition, transverse ties with diameters of 8 mm and a spacing of 20 cm (ϕ8 each 20) are used in the columns according to [36]. Note that column's reinforcement ratios are studied through parametric analyses in Subsection 4.4.

## 2.2 Numerical modeling

A generic finite-element (FE) model is created using OpenSees [41], which includes variation in geometric features and component modeling. The generic FE model is presented in Figure 2, where the dead loads from the superstructure are considered to be vertically concentrated at the top of the columns (force P).

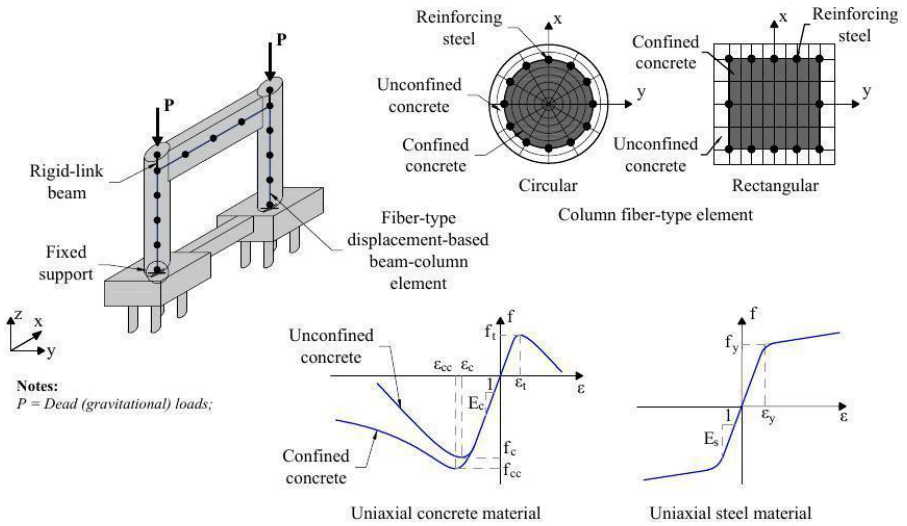


**Figure 2.** Generic FE model and nonlinear beam-column elements model behavior.

Rigid-link beams are used in vertical direction over the bridge piers to transfer lateral and gravitational loads from the deck to the bents. Bent beams and columns are modeled using fiber-type displacement-based beam-column elements with spread plasticity. The cross section of the element is divided into several fibers that delineate the regions of confined and unconfined concrete and the longitudinal reinforcement steel. The behavior of the uniaxial concrete material is based on the model proposed by [42], while the behavior of the reinforcement steel material is described by [43] with an isotropic strain-hardening ratio of 1%. Each column is divided into several elements along their height

with an approximate length of 50 centimeters and each bent beam and grade beam is divided into 4 elements along their length. The soil-structure interaction is not considered in the analysis and fixed support conditions are applied.

The numerical model is calibrated with the results of two cyclic experiments, as presented in Figure 3. The first is Experiment 5 by [44] in which a single column can simulate a lateral force acting in the longitudinal direction of the bridge. Meanwhile, the second experiment represents a frame composed of two columns [45] similar to the structural behavior of the bents in the transverse direction.

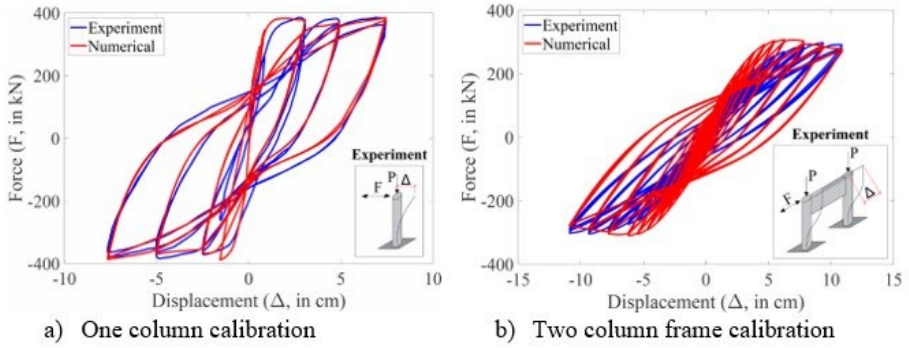


**Figure 3.** Numerical model calibration of the columns.

Note that hysteretic curves depicted in Figure 3 are in fair agreement. More information on the calibration can be found elsewhere [46], [47].

## 3 METHODOLOGY

In this section, the new methodology to estimate the structural capacity of the bridges' bents is described. It is proposed to replace the column's ductility ratio ($\mu$) by a new parameter (e.g., curvature, drift) as an EDP. The methodology is divided into the following steps:

- Definition of the structural response to be adopted as the EDP, for example, section curvature ($\phi$) or drift ($\theta$). Note that this new EDP needs to be able to be written in function of the ductility ratio, as $EDP = \mu_{EDP} \times EDP_y$ , where subscript $y$ refers to the EDP values (e.g., $\phi$ or $\theta$) in which the first longitudinal reinforcement yields. This approach allows the EDP to be obtained directly from the demand analysis, since it is not straightforward to obtain the column's yield parameter value in a portfolio analysis, because in some simulations yielding may not occur;
- Obtain from the literature, or develop, capacity models based on the column's ductility ratio that provide a clear relation between damage states. These capacity models are defined as median ($S_C[\mu_{EDP}|LS]$) and logarithmic dispersion ($\beta_C[\mu_{EDP}|LS]$) for each limit state (LS). These probabilistic distributions consider the uncertainties about the association between quantitative and qualitative damage states, as mentioned before. In addition, several authors adopt the capacity models based on lognormal distributions [11]-[16];
- Generate structural samples considering the variation of physical and geometric parameters to account for their variability within the bridges' classes;
- Perform PAs (or MPA if a bi-directional load scenario is required) in each structural sample to determine the $EDP_y$ values;
- Fit the $EDP_y$ values to a lognormal distribution, described by the median ($S_C[EDP_y]$) and the logarithmic dispersion ($\beta_C[EDP_y]$). One can also verify if the $EDP_y$ values follow a lognormal distribution using a two-sample Kolmogorov-Smirnov (K-S) test. The dispersion obtained in these analyses would be based on the variability within the bridge's class, and this distribution is not yet associated to a LS;
- Assuming that there is no correlation between $\mu_{EDP}$ and $EDP_y$, the distribution of the structural capacity for each LS, given by a median $S_C$ and a dispersion $\beta_C$, can be determined from the product between the distributions of $\mu_{EDP}$ and $EDP_y$, given by the following Equations 1 and 2 [48]:

$$S_C[EDP] = S_C[EDP_y] \times S_C[\mu_{EDP}|LS] \quad (1)$$

$$\beta_C[EDP] = \sqrt{\beta_C[EDP_y]^2 + \beta_C[\mu_{EDP}|LS]^2} \quad (2)$$

Figure 4 illustrates a summary of the proposed framework to determine the capacity model of bridge's bents. As seen in Figure 4, the characterization of the $EDP_y$ value is based on simultaneous monitoring of the EDP (i.e., section curvature, drift) values (pushover curve) and the steel stress (f) values of each longitudinal rebar (stress-strain curve) in the critical section at each PA step. In the step in which the first longitudinal rebar yields (f=fy), the EDP value is equal to $EDP_y$.

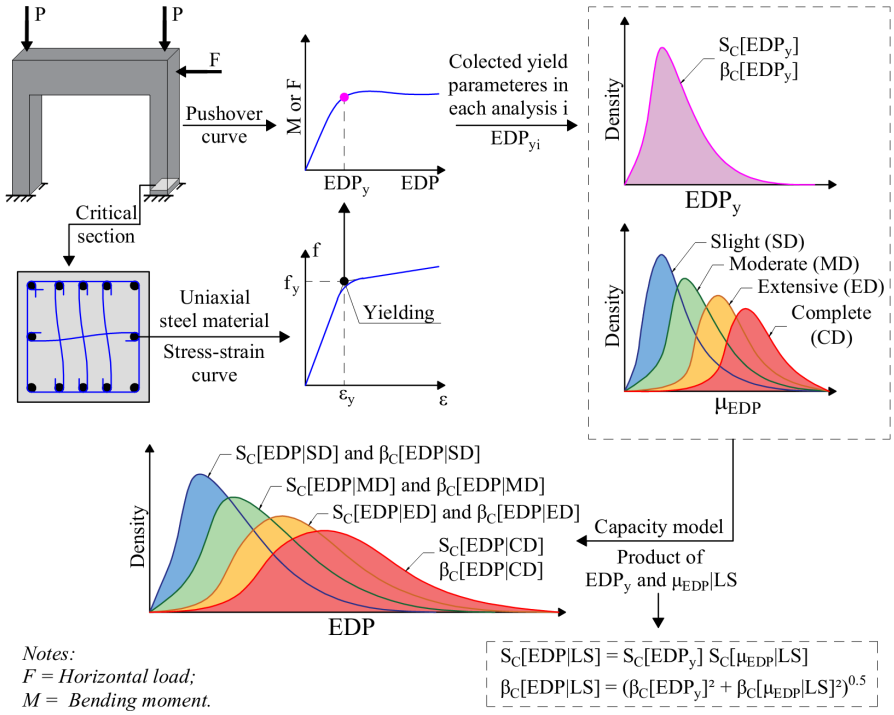


**Figure 4.** Methodology for defining a capacity model for bridge's bents.

This framework allows a most adequate definition of the yield parameter through nonlinear analyses, and the consideration of the variability within a group of structures in the capacity model. In addition, Multidirectional Pushover Analyses (MPA) are performed to provide a better estimate of the yield parameter based on a bi-directional load scenario, as seen in Figure 5.

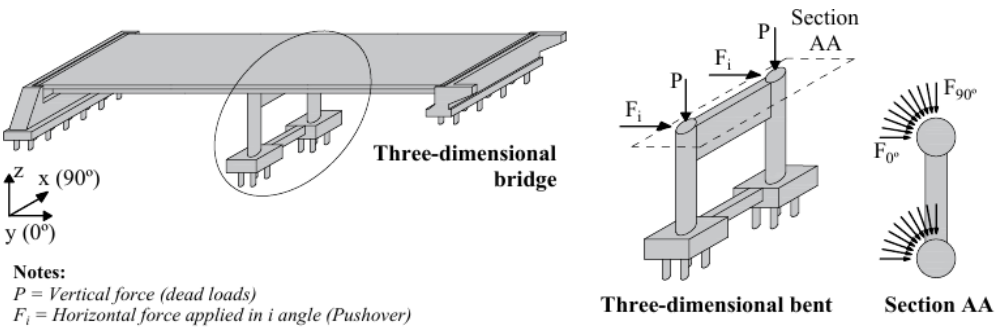


**Figure 5.** Direction of the horizontal force at the top of the bents.

The definition of qualitative damage states adopted herein follows [10] prescriptions (Table 5), which are divided into slight, moderate, extensive and complete damage.

**Table 5.** Description of damaged states.

| Damage state | Description |
|---|---|
| Slight | Minor spalling at the column (damage requires no more than cosmetic repair) |
| Moderate | Any column experiencing moderate (shear cracks) cracking and spalling (column structurally still sound) |
| Extensive | Any column degrading without collapse – shear failure – (column structurally unsafe) |
| Complete | Any column collapsing |

In order to obtain results from this methodology, 50 structural samples of bridges using the Latin-hypercube sampling (LHS) technique [49] are generated with variation of physical and geometric parameters to account for their variability within the bridges' classes. The LHS is used to create a set of nominally identical but statistically different bridge samples, which considers a constrained sampling approach instead of randomly selected samples. The application of the LHS on the sampling of continuous distributions (independent parameters, e.g., span length, column height) is well known, and more information can be found elsewhere [50]. After sampling the independent parameters (e.g., span length), the dependent parameters described as linear functions (e.g., T-beam depth) are calculated. The sampling of the subclasses is performed based on the probability of occurrence, i.e., 73.7% (37 samples) of the columns of the MSC-TB class have a circular section and 26.3% (13 samples) have a rectangular section.

MPA are performed in each structural sample. In each analysis, the angle of application of the horizontal force is varied every 15° from 0° (bridge's longitudinal direction) to 90° (transverse direction, i.e., bent's plane). The yield curvature ($\phi_y$) and the yield drift ($\theta_y$) are selected as the yield parameters and are determined in each analysis.

The results of this research are presented in the next section, and divided into subsections, as described below:

- Comparison of the yield parameters ($\phi_y$ and $\theta_y$) obtained in the MPA with the results of analytical equations proposed by [20]- [23]. This subsection intends to assess whether the use of analytical models properly estimates the yield parameters;
- Analysis of the influence of the bi-directional load scenario on the yield parameters ($\phi_y$ and $\theta_y$). The main objective is to evaluate which parameter is less impacted by the variation of the angle of application of horizontal forces. These results help to select the most suitable yield parameter to generate the capacity models;
- Generation of limit state models for each bridge's class based on the most suitable yield parameter using the proposed methodology in this article.;
- Parametric analysis considering different columns' reinforcement ratio using MPA to determine the influence on the yield parameter (used in the above-mentioned analysis). The longitudinal reinforcement ratio is varied with values of 0.5%, 1.0%, 1.5% and 2%, and the transverse ties with diameters of 8, 10 and 12.5 mm and spacing of 20, 15 and 10 cm, respectively. From these results for each bridge's class, analytical equations are proposed to extrapolate the yield parameter within a range of analyzed values for reinforcement ratios. Therefore, when this data (reinforcement ratios) is available, it will be possible to properly estimate the capacity of these columns.

## 4 RESULTS

### 4.1 Comparison of analytical and numerical models to obtain yield parameters

In this subsection, the adequacy of the adoption of analytical models to calculate yield parameters ($\phi_y$ and $\theta_y$) is discussed. Priestley et al. [22] proposed Equations 3 and 4 to estimate $\phi_y$ and $\theta_y$, respectively.

$$\phi_y = 2{,}25 \times \frac{\varepsilon_y}{D_c} \tag{3}$$

$$\theta_y = \phi_y \times \frac{(H_c + L_{sp})^2}{3 \times H_c} \tag{4}$$

In Equation 3, $\varepsilon_y$ is the yield strain of the longitudinal reinforcement and $D_c$ is the column diameter. In Equation 4, $H_c$ is the column height and $L_{sp}$ is the strain penetration length, as defined in Equation 5.

$$L_{sp} = 0{,}022 \times f_y \times \Phi_{bl} \tag{5}$$

Where $f_y$ is the longitudinal reinforcement yield strength and $\Phi_{bl}$ is the longitudinal reinforcement bar diameter. Note that these expressions are proposed for circular columns; therefore, the authors adapted them for rectangular columns by replacing $D_c$ with $W_c$ (column width).

The values of $EDP_y$ ($\phi_y$ and $\theta_y$) are calculated using the Equations 3 to 5 for each structural sample per bridge's class, which are independent of the direction of analysis (e.g., longitudinal or transverse directions). Note that each sample provides unique parameter values (e.g., column height, column diameter, steel yield strength) to properly estimate one $EDP_y$. Each analytical result is related to each $EDP_y$ obtained by the MPA for the seven angles of application of the horizontal force varying from 0º to 90º, as seen in Figure 6. In Figure 6, the vertical axes indicate the yield parameters obtained by the MPA divided by those calculated by the analytical models proposed by Priestley et al. [22], and the horizontal axes illustrate the results for each degree analyzed in the MPA.

The yield curvature results, shown in Figure 6, indicate that there is not a significant effect of the angle of application of forces on them, since the mean values range from 0.83 to 0.77 (about 8%) and from 0.86 to 0.84 (about 2%) for the MSC-TB and MSC-TB-Abut bridge's classes, respectively. This influence on yield drift values is clearly stronger, as the same variations are around 857% (from 0.67 to 0.07) and 644% (from 0.67 to 0.09), respectively. The standard deviation of the MSC-TB results is higher due to the division of the class into circular and rectangular sections, and the greater number of variable geometric parameters (e.g., slab thickness, bent cap height), as detailed in Section 2.

All results in Figure 6 show that the yield parameters obtained with the analytical model are overestimated, except one sample that generated higher values of $\theta_y$ through the MPA (Figure 6d). This sample features a bridge with columns 1.7 m high and 1.4 m in diameter, which is unusual. Note that the LHS technique must be performed with uncorrelated parameters to adequately represent a large group of samples with small size data; therefore, it is common to provide a small number of samples with unusual characteristics.

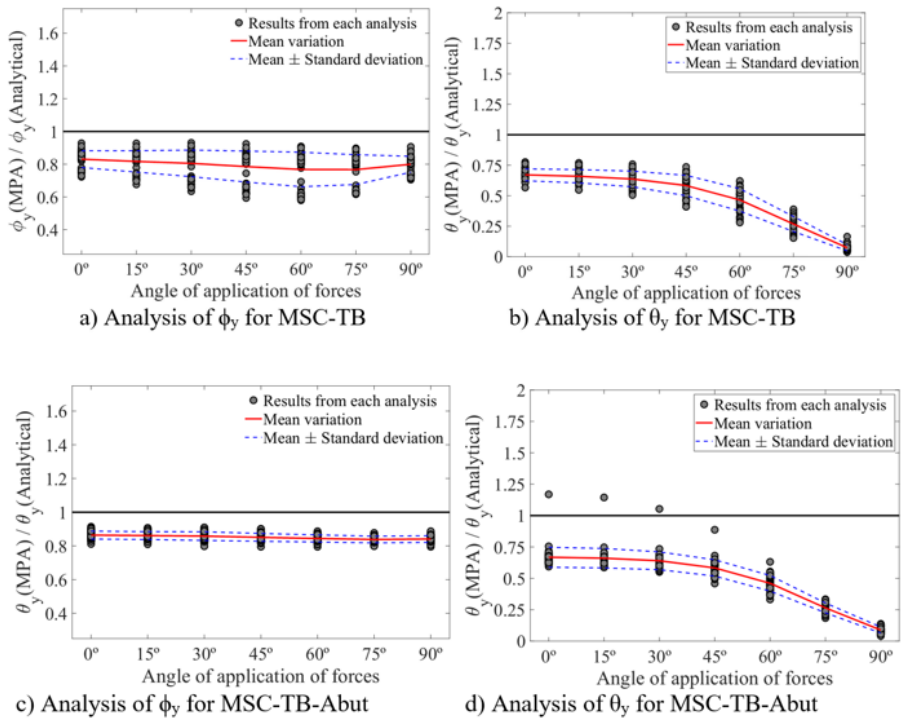


**Figure 6.** Relation between yield parameters obtained by MPA and by an analytical model proposed by Priestley et al. [22] for each angle of the MPA.

Other studies have also proposed analytical equations to estimate the yield curvature based on experimental results, such as Hernández-Montes and Aschleim [20] and Sheikh et al. [23]. [20] studied circular and rectangular columns and evaluated the influence of the axial load ratio on the yield curvature; while [23] evaluated circular columns to estimate equations based on the axial load ratio, longitudinal reinforcement ratio and compressive strength of concrete. Both models also consider the yield strain of the longitudinal reinforcement and the dimensions of the column's cross section, as proposed by Priestley et al. [22]. In addition, Brachmann et al. [21] estimated the yield drift values as a function of the axial load ratio only.

A similar approach is also conducted to assess the suitability of using the analytical models [20]-[23] to estimate the yield parameters, which also utilizes the previous results from Figure 6. This intends to verify whether the $EDP_y$ overestimation (i.e., using Priestley et al. [22] model) is also obtained using the aforementioned analytical models [20]-[21] and [23]. Therefore, longitudinal (0º) and transverse (90º) directions are evaluated based on the results obtained with the MPA. Figure 7 shows through box-and-whisker plots the comparison of yield parameters calculated from the equations proposed by [20]-[23] and determined with the MPA.

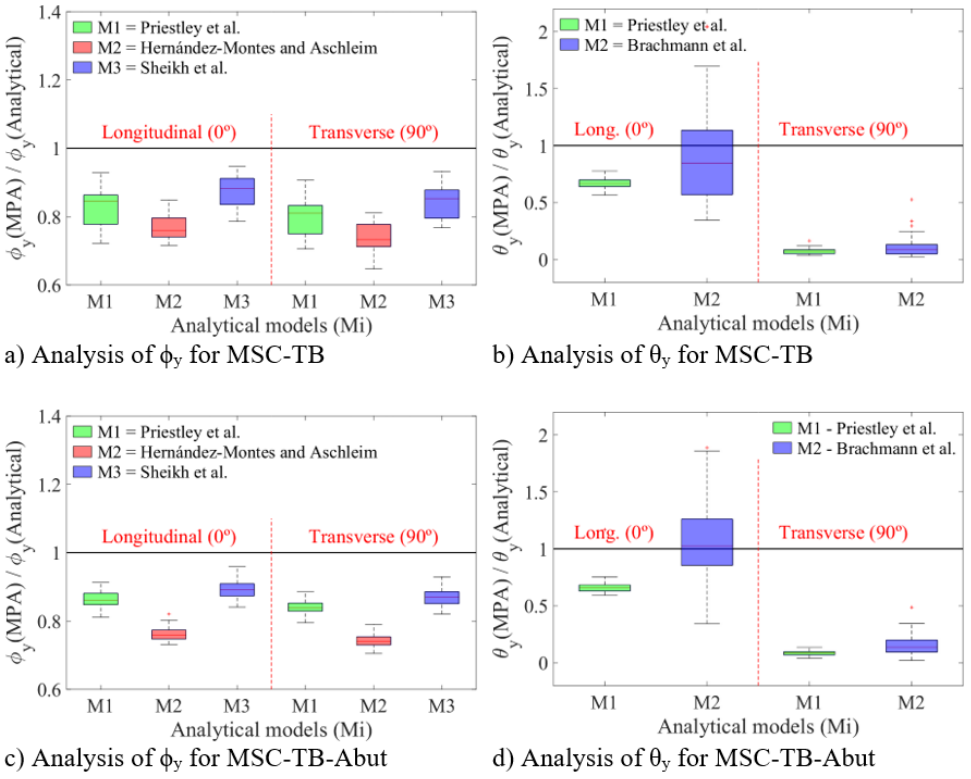


**Figure 7.** Relation between yield parameters obtained by MPA and by analytical models proposed by [20]-[23].

The results illustrated in Figure 7 indicate that the evaluated analytical equations overestimated the yield curvature. The model proposed by Sheik et al. [23] presented more accurate results, as more parameters are used to define $\phi_y$. The results obtained using Hernández-Montes and Aschleim [20] are the least accurate, but with the smallest dispersion, which is consistent with the equations considering circular and rectangular columns. The yield drift results using Brachmann et al. [21] have a significantly greater dispersion, which is attributed to the single consideration of the axial load ratio in the equations; however, the results are more accurate with a lower tendency of overestimation.

Finally, the estimation of the yield parameters using analytical models may underestimate the fragility assessment of these bridge's classes. Therefore, the employment of MPA is certainly a more accurate approach to estimating the capacity of bridge's classes for a fragility assessment.

### 4.2 Comparison and selection of a most suitable EDP

This subsection presents an analysis of the appropriate EDP (i.e., $\phi_y$ or $\theta_y$) to be adopted in the capacity models of the bridge's bents considering a bi-directional load scenario. The MPA results of $\phi_y$ and $\theta_y$ for each degree of force application are described in Table 6, which includes the p-values of the two-sample K-S test. A significance level ($\alpha$) of 0.05 is used [28], which means that the data follow a lognormal distribution if the p-value≥$\alpha$.

**Table 6.** Comparison of $\phi_y$ and $\theta_y$ using the MPA for the bridge's classes.

| Yield parameter | Degree | MSC-TB | | | MSC-TB-Abut | | |
|---|---|---|---|---|---|---|---|
| | | $S_C$ | $\beta_C$ | p-value[1] | $S_C$ | $\beta_C$ | p-value[1] |
| $\phi_y$ (rad/m) | 0º | 0.0072 | 0.218 | 0.838 | 0.0068 | 0.228 | 0.498 |
| | 15º | 0.0070 | 0.224 | 0.723 | 0.0068 | 0.228 | 0.573 |
| | 30º | 0.0069 | 0.233 | 0.726 | 0.0068 | 0.231 | 0.597 |
| | 45º | 0.0068 | 0.241 | 0.550 | 0.0067 | 0.228 | 0.632 |
| | 60º | 0.0066 | 0.246 | 0.587 | 0.0066 | 0.226 | 0.625 |
| | 75º | 0.0066 | 0.231 | 0.641 | 0.0066 | 0.223 | 0.716 |
| | 90º | 0.0069 | 0.210 | 0.689 | 0.0066 | 0.220 | 0.615 |
| $\theta_y$ (%) | 0º | 0.784 | 0.437 | 0.841 | 0.903 | 0.368 | 0.953 |
| | 15º | 0.769 | 0.444 | 0.891 | 0.893 | 0.371 | 0.937 |
| | 30º | 0.743 | 0.454 | 0.976 | 0.866 | 0.378 | 0.918 |
| | 45º | 0.678 | 0.470 | 0.976 | 0.789 | 0.399 | 0.886 |
| | 60º | 0.538 | 0.495 | 0.979 | 0.623 | 0.430 | 0.935 |
| | 75º | 0.307 | 0.521 | 0.952 | 0.358 | 0.450 | 0.937 |
| | 90º | 0.082 | 0.729 | 0.985 | 0.118 | 0.536 | 0.949 |

[1] These results indicate p-values from the two-sample K-S test.

The results indicate that the median values ($S_C$) of column yield curvatures are greater in longitudinal direction (0º) pushover analyses than in the transverse direction (90º). This is caused by the reduction of axial forces in the critical column when a transverse force or displacement is applied in the top of the bent, since the yielding of the longitudinal rebar occurs by excessive elongation. This reduction is directly related to the column height, since the bending moments generated by horizontal transverse forces (as a function of column height, bent cap length and number of columns) increase axial forces in an end column and decrease at the other extremity. The largest variations in median values and logarithmic dispersion are observed in the yield curvature of the MSC-TB bridge's class, when the angle of the pushover analysis increases. Median values are up to 9.1% (from 0.0072 to 0.0066), and logarithmic dispersion up to 17.1% (from 0.246 to 0.210). For the MSC-TB-Abut bridge's class, these variations are up to 3.0% and 5.0% for median values and logarithmic dispersions, respectively.

According to Table 6, the yield drift values are dependent on the angle of application of the forces, since variations of 856% in the median values (from 0.784% to 0.082%) and 66.8% in the dispersion values (from 0.437 to 0.729) are obtained for the longitudinal and transverse directions considering MSC-TB bridge's class, respectively. This variation is related to the greater structural stiffness in the transverse direction. Finally, it is assumed that the data follow lognormal distributions, since all p-values are higher than the adopted significance level.

The conventional limit state models define lognormal distributions to describe a column's capacity, without distinguishing between longitudinal and transverse structural behavior [11]-[16]. Therefore, the results for these bridges' classes indicate the curvature is a better EDP when the forces acting in both directions are significant, since the yield drift is more dependent on the angle's direction. An alternative approach to use a drift-based EDP is to develop independent capacity models for longitudinal and transverse directions, as seen in other bridge components (e.g., bearings, abutments) [11]-[16]. Based on this discussion, the yield curvature is used in further analyses presented herein.

### 4.3 Column limit state capacities

This subsection presents new limit state capacity models for the bridge's classes based on the assumption that there is no seismic detailing. The first step is to estimate the yield curvature parameter through lognormal distributions (i.e., $S_C$ and $\beta_C$). Table 6 shows the probabilistic distributions for each degree of force application; however, only one distribution per bridge's class must be used. Therefore, an attempt to gather all data (i.e., 7 degrees times 50 structural samples per bridge's class) to be fitted by lognormal distributions is conducted. Figure 8 illustrates the results of fitting the data by lognormal distributions, graphically shown by empirical and lognormal cumulative distribution functions (CDF).

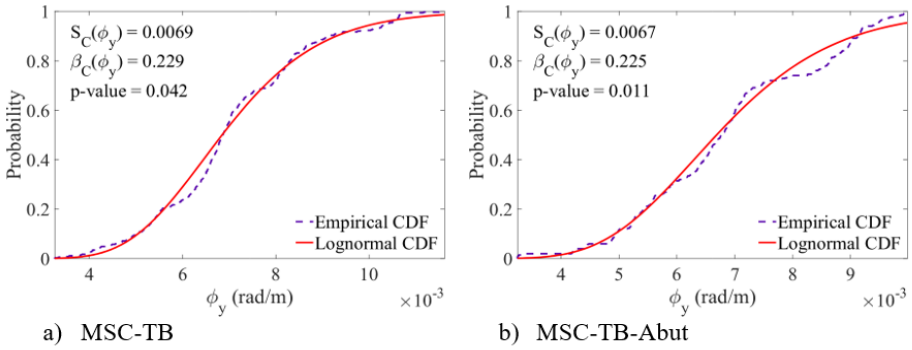


**Figure 8.** Two-sample K-S test results for the bridge's classes, considering all data (350 analyses per class).

The results indicate that these data do not follow lognormal distributions (p-value < α). Therefore, the mean values of $\phi_y$ are calculated for each structural sample, totaling 50 values of $\phi_y$ per bridge's class, i.e., the mean results of the angle variations are used hereafter. The p-values results of the two-sample K-S test using mean values of $\phi_y$ are 0.857 and 0.537 for the MSC-TB and MSC-TB-Abut bridge's classes, respectively. Table 7 presents the results of the parameters that describe the lognormal distributions of $\phi_y$.

The next step on developing limit state capacity models is to define the probabilistic distributions of curvature ductility ratios. Therefore, the models proposed by [11] are used, since poorly confined concrete columns are adopted in the study. Using Equations 1 and 2, the column's capacity models for each bridge's class are proposed, as seen in Table 7.

**Table 7.** Column's capacity models for typical bridges in Northeastern Brazil.

| Bridge's class | Damage state | $\mu_{\phi\|LS}$ | | $\phi_y$ | | EDP: $\phi_{LS}$[1] | |
|---|---|---|---|---|---|---|---|
| | | $S_C[\mu_\phi]$ | $\beta_C[\mu_\phi]$ | $S_C[\phi_y]$ | $\beta_C[\phi_y]$ | $S_C[\phi]$ | $\beta_C[\phi]$ |
| MSC-TB | Slight | 1.29 | 0.59 | 0.0069 | 0.227 | 0.0089 | 0.632 |
| | Moderate | 2.10 | 0.51 | | | 0.0145 | 0.558 |
| | Extensive | 3.52 | 0.64 | | | 0.0243 | 0.679 |
| | Complete | 5.24 | 0.65 | | | 0.0362 | 0.688 |
| MSC-TB-Abut | Slight | 1.29 | 0.59 | 0.0067 | 0.226 | 0.0086 | 0.632 |
| | Moderate | 2.10 | 0.51 | | | 0.0141 | 0.558 |
| | Extensive | 3.52 | 0.64 | | | 0.0236 | 0.679 |
| | Complete | 5.24 | 0.65 | | | 0.0351 | 0.688 |

[1] Indicates the proposed column's capacity model

Figure 9 illustrates the probability density functions (PDF) for column's limit state models of each bridge's class. These capacity models may be used for further fragility assessments of this bridge inventory.

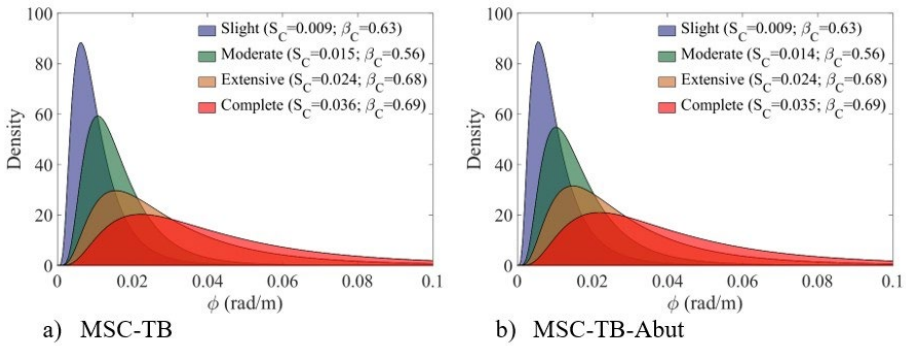


**Figure 9.** PDF for column's capacity models.

### 4.4 Parametric analyses

This subsection presents a parametric analysis of column reinforcement ratios (i.e., longitudinal and transverse) to study their impact on the yield curvature ($\phi_y$). Note that these ratios are unknown on a regional scale, and these results intend to extrapolate limit state capacities of columns. All results presented herein consider the variation of the angle of application of the forces (i.e., mean values of $\phi_y$) and its influence is not evaluated separately.

An approach similar to the one presented in Section 4.3 is used, where the same 50 structural samples per bridge's class are analyzed varying the angle of application by 15º to perform the PA with each reinforcement configuration. Table 8 presents the results of the yielding curvature for each configuration of longitudinal reinforcement ratio and transverse ties.

**Table 8.** Yielding curvature results for different reinforcement ratios.

| Longitudinal reinforcement ratio (ρ) | Distribution of transverse ties | Yielding curvature (rad/m) | | | |
|---|---|---|---|---|---|
| | | MSC-TB | | MSC-TB-Abut | |
| | | $S_c$ | $\beta_C$ | $S_c$ | $\beta_C$ |
| 0,50% | ϕ8 s/20 | 0.00659 | 0.223 | 0.00642 | 0.223 |
| | ϕ 10 s/15 | 0.00664 | | 0.00646 | |
| | ϕ 12.5 s/10 | 0.00668 | | 0.00649 | |
| 1,00% | ϕ8 s/20 | 0.00683 | 0.225 | 0.00665 | 0.226 |
| | ϕ 10 s/15 | 0.00687 | | 0.00669 | |
| | ϕ 12.5 s/10 | 0.00691 | | 0.00672 | |
| 1,50% | ϕ8 s/20 | 0.00706 | 0.228 | 0.00686 | 0.229 |
| | ϕ 10 s/15 | 0.00711 | | 0.00691 | |
| | ϕ 12.5 s/10 | 0.00714 | | 0.00693 | |
| 2,00% | ϕ8 s/20 | 0.00726 | 0.230 | 0.00706 | 0.229 |
| | ϕ 10 s/15 | 0.00730 | | 0.0071 | |
| | ϕ 12.5 s/10 | 0.00733 | | 0.00713 | |

The variation in dispersion due to the increase of the transverse reinforcement ratio is less than 0.4%, which is neglected in the results. The average variation in the median of the yield curvature due to the increase of the lower to the upper values of the transverse reinforcement ratio is 1.09%, which is about ten times less than the average variation due to the increase in the longitudinal reinforcement ratio (9.93%). By increasing the longitudinal reinforcement four times, the dispersion varies up to 3.14%. Therefore, the increase in the transverse reinforcement ratio does not significantly influence the yield curvature results, which agrees with the results observed in [51]; however, the confinement effect may increase the ductility demand ratios (or capacity ratios) associated with each limit state (Table 7), which is not considered herein. Experimental results indicate that increasing the transverse reinforcement ratio causes an increase in ductility levels, dissipated energy and equivalent viscous damping [51], since the role of stirrups is to enhance confinement effect, to restrain the lateral expansion of concrete, thus modifying the concrete stress-strain constitutive law and enabling higher compression strains and higher ductility [52].

Using all the analysis results, a linear regression is performed in the logarithmic space to determine median values of the yield curvature ($S_c$) as a function of the longitudinal reinforcement ratio (ρ), as presented in Figure 10, since the impact of the transverse reinforcement ratio is neglected. Furthermore, the logarithmic standard deviation is assumed to have a constant value (Equation 7), which is consistent with the low variation obtained, as shown in Table 7. The linear relation is established (Equation 6), where *a* and *b* are the regression coefficients.

$$ln\,(S_C) = ln\,(a) + b \times ln\,(\rho) \tag{6}$$

The logarithmic standard deviation of the capacity ($\beta_c$) is calculated through the same linear regression, as shown in Equation 4.

$$\beta_c \cong \sqrt{\frac{\sum[ln\,(\phi_{yi}) - ln\,(a \times \rho^b)\,]}{N-2}} \tag{7}$$

where N is the number of simulations and $\phi_{yi}$ are the mean yield curvature values of each simulation i. The dispersion values determined are constant (0.23) and compatible with those found in Table 7.

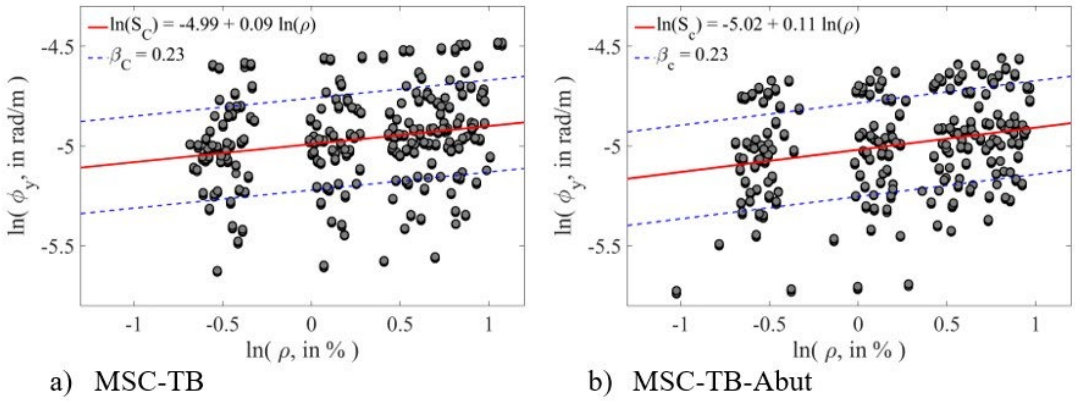


**Figure 10.** Linear regression of the median values of $\phi_y$ as a function of ρ.

Equations 8 and 9 define the relationship between the median values of $\phi_y$ and ρ for the MSC-TB and MSC-TB-Abut bridges' classes, respectively. Therefore, it allows defining the distribution of capacity for different values of the longitudinal reinforcement ratios.

$$ln\,(S_C) = -4.99 + 0.09 \times ln\,(\rho) \quad (8)$$

$$ln\,(S_C) = -5.02 + 0.11 \times ln\,(\rho) \quad (9)$$

## 5 CONCLUSIONS

This article presents a new proposal to estimate the structural capacity analysis for typical bridge bents in Northeastern Brazil. Multidirectional pushover analyses are performed to assess the influence of the angle of application of the force in the bridge bents. Drift and curvature are evaluated as yield parameters for excitation loads that occur at two horizontal component forces (i.e., earthquakes). The results of analytical models used herein overestimate the yield parameters when compared to the MPA results. In addition, the yield drift is more sensitive to the angle of application of the forces, which presents a variation up to 856% in the median drift values obtained in the longitudinal and transverse directions to the first reinforcement yielding of the critical section. Therefore, the curvature is adopted as EDP for the new methodology proposed here, as it presents a better performance in a multidirectional pushover analysis with less variation in the results (up to 19%). Finally, capacity limit states are provided, considering uncertainties about the association between quantitative and qualitative damage states and variability within the bridge's classes.

Parametric analyses are performed to assess the impact of longitudinal and transverse reinforcement ratios on the structural capacity of the bents. The results show that the variation in the longitudinal reinforcement ratio has a greater influence on the yield curvature. The definition of the ductility demand ratios for the bridge portfolio is a gap in the study, since values suggested in the literature are adopted for other bridge configurations. The results of the parametric analyses enable the generation of linear relations between the yield curvature and the reinforcement ratios. Such relations are useful to estimate capacity models for probabilistic or deterministic vulnerability assessments ([11]-[17] and [53]) or displacement-based design procedures [54]. The former is particularly useful in Brazil, given the lack of studies that developed such relations, and the variety of old and new bridges designed according to different codes (consequently, different reinforcement ratios).

The capacity limit states obtained herein are valuable information to perform a vulnerability analysis of the bridge portfolio by several different hazard sources, such as earthquakes, hurricanes and explosions. In addition, these results may be used in other bridge portfolios with geometric and physical characteristics similar to the bridge bents analyzed herein.

## ACKNOWLEDGEMENTS

This study was financed in part by the Coordenação de Aperfeiçoamento de Pessoal de Nível Superior - Brasil (CAPES) - Finance Code 001; and by the São Paulo Research Foundation (FAPESP) - Finance Code 2018/23304-9. The opinions, findings, and conclusions or recommendations expressed in this paper are those of the authors only and do not necessarily reflect the views of the sponsors or affiliates.

## REFERENCES

[1] F. Schanack, G. Valdebenito, and J. Alvial, "Seismic damage to bridges during the 27 February 2010 magnitude 8.8 Chile earthquake," *Earthq. Spectra*, vol. 28, no. 1, pp. 301–315, 2012, http://dx.doi.org/10.1193/1.3672424.

[2] A. Palermo et al., "Performance of road bridges during the 14 November 2016 Kaikoura earthquake," *Bull. N. Zeland Soc. Earthq. Eng.*, vol. 50, no. 2, pp. 253–270, 2017, http://dx.doi.org/10.5459/bnzsee.50.2.253-270.

[3] Y. Alberto, M. Otsubo, H. Kyokawa, T. Kiyota, and I. Towhata, "Reconnaissance of the 2017 Puebla, Mexico earthquake," *Soil Found.*, vol. 58, no. 5, pp. 1073–1092, 2018, http://dx.doi.org/10.1016/j.sandf.2018.06.007.

[4] N. Ataei and J. E. Padgett, "Probabilistic modeling of bridge deck unseating during hurricanes events," *J. Bridge Eng.*, vol. 18, no. 4, pp. 275–286, 2013, http://dx.doi.org/10.1061/(ASCE)BE.1943-5592.0000371.

[5] N. Ataei and J. E. Padgett, "Fragility surrogate models for coastal bridges in hurricane prone zones," *Eng. Struct.*, vol. 103, pp. 203–213, 2015, http://dx.doi.org/10.1016/j.engstruct.2015.07.002.

[6] G. P. Balomenos, S. Kameshwar, and J. E. Padgett, "Parameterized fragility models for multi-bridges' classes subjected to hurricane loads," *Eng. Struct.*, vol. 208, pp. 110213, 2020, http://dx.doi.org/10.1016/j.engstruct.2020.110213.

[7] F. H. B. Alves "Sistema de previsão de enchentes: integração de modelos de previsão de chuva, simulação hidrológica e hidrodinâmica," M.S. thesis, Universidade Federal de Pernambuco, UFPE, Pernambuco, Brasil, 2017.

[8] F. H. B. Alves "Análise dos níveis de solicitação gerados por explosivos sobre os pilares do viaduto da BR-020 em Caucaia, Ceará, aliada à verificação de segurança e dimensionamento preventivo," B.S. thesis, Universidade Federal do Ceará, UFCE, Ceará, Brasil, 2019.

[9] J. E. Padgett and R. DesRoches, "Methodology for the development of analytical fragility curves for retrofitted bridges," *Earthquake Eng. Struct. Dynam.*, vol. 37, no. 8, pp. 1157–1174, 2008, http://dx.doi.org/10.1002/eqe.801.

[10] Federal Emergency Management Agency, *Earthquake Loss Estimation Methodology, HAZUS-MH 2.1: Technical Manual*. Washington, DC, USA: FEMA, 1997.

[11] B. G. Nielson and R. DesRoches, "Seismic fragility methodology for highway bridges using a component level approach," *Earthquake Eng. Struct. Dynam.*, vol. 36, no. 6, pp. 823–839, 2007, http://dx.doi.org/10.1002/eqe.655.

[12] H. Pahlavan, B. Zakeri, G. G. Amiri, and M. Shaianfar, "Probabilistic vulnerability assessment of horizontally curved multiframe RC box-girder highway bridges," *J. Perform. Constr. Facil.*, vol. 30, no. 3, pp. 04015038, 2016, http://dx.doi.org/10.1061/(ASCE)CF.1943-5509.0000780.

[13] E. Choi, R. DesRoches, and B. Nielson, "Seismic fragility of typical bridges in moderate seismic zones," *Eng. Struct.*, vol. 26, pp. 187–199, 2004, http://dx.doi.org/10.1016/j.engstruct.2003.09.006.

[14] K. Ramanathan, R. DesRoches, and J. E. Padgett, "Analytical fragility curves for multispan continuous steel girder bridges in moderate seismic zones," *Transp. Res. Rec.*, vol. 2202, no. 1, pp. 173–182, 2010, http://dx.doi.org/10.3141/2202-21.

[15] H. Pahlavan, B. Zakeri, G. G. Amiri, and M. Shaianfar, "Probabilistic vulnerability assessment of horizontally curved multiframe RC box-girder highway bridges," *J. Perform. Constr. Facil.*, vol. 30, no. 3, pp. 04015038, 2016, http://dx.doi.org/10.1061/%28ASCE%29CF.1943-5509.0000780.

[16] S. Mangalathu, F. Soleimani, and J.-S. Jeon, "Bridge's classes for regional seismic risk assessment: Improving hazus models," *Eng. Struct.*, vol. 148, pp. 755–766, 2017, http://dx.doi.org/10.1016/j.engstruct.2017.07.019.

[17] J. E. Padgett and R. DesRoches, "Bridge functionality relationships for improved seismic risk assessment of transportation networks," *Earthq. Spectra*, vol. 23, no. 1, pp. 115–130, 2007, http://dx.doi.org/10.1193/1.2431209.

[18] A. Dutta and J. B. Mander, "Seismic fragility analysis of highway bridges," in *Proceedings of the Center-to-Center Project Workshop on Earthquake Engineering in Transportation System*, Tokyo, Japan, 1999.

[19] H. Hwang, J. B. Liu, and Y.-H. Chiu, *Seismic Fragility Analysis of Highway Bridges* (Mid-America Earthquake Center Tech. Rep. MAEC RR-4 Project), USA: University of Memphis, 2001.

[20] E. Hernández-Montes and M. Aschleim, "Estimates of the yield curvature for design of reinforced concrete columns," *Mag. Concr. Res.*, vol. 55, no. 4, pp. 337–383, 2003, http://dx.doi.org/10.1680/macr.2003.55.4.373.

[21] I. Brachmann, J. Browning, and A. Matamoros, "Drift-dependent confinement requirements for reinforced concrete columns under cyclic loading," *ACI Struct. J.*, vol. 101, no. 5, pp. 669–677, 2004, http://dx.doi.org/10.14359/13389.

[22] M. N. Priestley, G. M. Calvi, and M. J. Kowalsky, *Displacement Based Seismic Design of Structures*, 1st ed. Pavia: IUSS Press, 2007.

[23] M. N. Sheik, H. S. Tsang, T. J. McCarthy, and N. T. K. Lam, "Yield curvature for seismic design of circular reinforced concrete columns," *Mag. Concr. Res.*, vol. 62, no. 10, pp. 741–748, 2010, http://dx.doi.org/10.1680/macr.2010.62.10.741.

[24] D. H. Tavares, J. R. Suescun, P. Paultre, and J. E. Padgett, "Seismic fragility of a highway bridge in Quebec," *J. Bridge Eng.*, vol. 18, no. 11, pp. 1131–1139, 2013, http://dx.doi.org/10.1061/(asce)be.1943-5592.0000471.

[25] B. R. Aryal and N. C. Sharma, "Development of fragility curves for seismic performance comparison of hammerhead and multicolumn bridge pier," *Int. J. Sci. Res.*, vol. 9, no. 3, pp. 3–8, 2020, http://dx.doi.org/10.21275/SR20209224222.

[26] H. Krawinkler and G. D. P. K. Seneviratna, "Pros and cons of a pushover analysis of seismic performance evaluation," *Eng. Struct.*, vol. 20, no. 4-6, pp. 452–464, 1998, http://dx.doi.org/10.1016/s0141-0296(97)00092-8.

[27] T. Isakovic and M. Fischinger, "Higher modes in simplified inelastic seismic analysis of single column bent viaducts," *Earthquake Eng. Struct. Dynam.*, vol. 35, no. 1, pp. 95–114, 2006, http://dx.doi.org/10.1002/eqe.535.

[28] M. S. C. Garcia, G. H. Siqueira, L. C. M. Vieira Jr., and I. Vizotto, "Evaluation of structural capacity of triangular and hexagonal reinforced concrete free-form shells," *Eng. Struct.*, vol. 188, pp. 519–537, 2019, http://dx.doi.org/10.1016/j.engstruct.2019.03.044.

[29] H. Rodrigues, H. Varum, A. Arêde, and A. Costa, "Comparative efficiency analysis of different nonlinear modelling strategies to simulate the biaxial response of RC columns," *Earthq. Eng. Eng. Vib.*, vol. 11, no. 4, pp. 553–566, 2012, http://dx.doi.org/10.1007/s11803-012-0141-1.

[30] H. Rodrigues, A. Arêde, H. Varum, and A. Costa, "Experimental evaluation of rectangular reinforced concrete column behaviour under biaxial cyclic loading," *Earthquake Eng. Struct. Dynam.*, vol. 42, no. 2, pp. 239–259, 2012, http://dx.doi.org/10.1002/eqe.2205.

[31] D. Giardini, P. Basham, and M. Bery, "The global seismic hazard assessment program (GSHAP) – 1992/1999," *Ist. Naz. Geofis. Vulcanologia*, vol. 42, no. 6, pp. 957–974, 1999, http://dx.doi.org/10.4401/ag-3780.

[32] M. Assumpção, M. Pirchiner, J. Dourado, and L. Barros, "Terremotos no Brasil: preparando-se para eventos raros," *Boletim SBGf*, no. 96, pp. 25-29, 2016.

[33] M. D. Petersen et al., "Seismic hazard, risk, and design for South America," *Bull. Seismol. Soc. Am.*, vol. 108, no. 2, pp. 781–800, 2018, http://dx.doi.org/10.1785/0120170002.

[34] C. B. L. Oliveira, M. Greco, and T. N. Bittencourt, "Analysis of the Brazilian federal bridge inventory," *IBRACON Struct. Mater. J.*, vol. 12, no. 1, pp. 1–13, 2019, http://dx.doi.org/10.1590/s1983-41952019000100002.

[35] G. H. F. Cavalcante, E. M. V. Pereira, I. D. Rodrigues, L. C. M. Vieira Jr., J. E. Padgett, and G. H. Siqueira "Proposal of representative porfolios for federal roadway bridges in Northeastern Brazil," Preprint arXiv:2108.00934, 2021.

[36] Associação Brasileira de Normas Técnicas, *Projeto de Estruturas de Concreto - Procedimento,* NBR 6118, 2014.

[37] S. A. Mirza and J. G. MacGregor, "Variability of mechanical properties of reinforcing bars," *J. Struct. Div.*, vol. 105, no. 5, pp. 921–937, 1979.

[38] W. Santiago and A. Beck, "A new study of Brazilian concrete strength conformance," *IBRACON Struct. Mater. J.*, vol. 10, no. 4, pp. 906–923, 2017, http://dx.doi.org/10.1590/s1983-41952017000400008.

[39] C. G. Nogueira "Desenvolvimento de modelos mecânicos de confiabilidade e de otimização para aplicação em estruturas de concreto armado," Ph.D. thesis, Departamento de Engenharia, Universidade de São Paulo, USP, São Paulo, Brasil, 2010.

[40] J. E. Padgett and R. DesRoches, "Retrofitted bridge fragility analysis for typical classes of multispan bridges," *Earthq. Spectra*, vol. 25, no. 1, pp. 117–141, 2009, http://dx.doi.org/10.1193/1.3049405.

[41] S. Mazzoni et al., "Open system for earthquake engineering simulation: OpenSees Command Language Manual*."* https://opensees.berkeley.edu/OpenSees/manuals/usermanual/OpenSeesCommandLanguageManual.pdf (accessed Jan. 26, 2021).

[42] G. A. Chang and J. B. Mander, *Seismic Energy Based Fatigue Damage Analysis of Bridge Columns: Part 1 – Evaluation of Seismic Capacity* (Tech. Rep. NCEER-94-006). Buffalo NY, USA: National Center for Earthquake Engineering Research, 1994.

[43] F. C. Filippou, V. V. Bertero, and E. P. Popov, *Effects of Bond Deterioration on Hysteretic Behavior of Reinforced Concrete Joints* (Tech. Rep. NSF/CEE-83032). Berkeley, CA, USA: Earthquake Engineering Research Center, 1983.

[44] H. Tanaka, "Effect of lateral confining reinforcement on the ductile behavior of reinforced concrete columns," Ph.D. thesis, University of Canterburry, New Zeland, 1990.

[45] P. Morandi, S. Hak, and G. Magenes, "Perfomance-based interpretation of in-plane cyclic tests on RC frames with strong masonry infills," *Eng. Struct.*, vol. 156, pp. 503–521, 2018, http://dx.doi.org/10.1016/j.engstruct.2017.11.058.

[46] E. M. V. Pereira, "Estudo da fragilidade sísmica de pórticos de concreto armado com irregularidades estruturais," M.S. thesis, Unicamp, Campinas, SP, 2021. [Online]. Available: http://repositorio.unicamp.br/Busca/Download?codigoArquivo=464788

[47] E. M. V. Pereira, G. H. F. Cavalcante, I. D. Rodrigues, L. C. M. Vieira Jr., and G. H. Siqueira, "Seismic reliability assessment of a non-seismic reinforced concrete framed structure designed according to ABNT NBR 6118:2014," *IBRACON Struct. Mater. J.*, vol. 15, no. 1, pp. e15110, 2022, http://dx.doi.org/10.1590/S1983-41952022000100010.

[48] A. T. Beck, *Confiabilidade e Segurança das Estruturas*, 1th ed. Elsevier, Brasil, 2019.

[49] M. D. Mckay, R. J. Beckham, and W. J. Conover, "Comparison of three methods for selecting values of input variables in the analysis of output from a computer code," *Technometrics*, vol. 21, no. 2, pp. 239–245, 1979, http://dx.doi.org/10.2307/1271432.

[50] O. Avsar, "Fragility based seismic vulnerability assessment of ordinary highway bridges in Turkey," Ph.D. thesis, Middle East Technical University, Ancara, Turkey, 2009.

[51] M. A. Belkacem, H. Bechtoula, N. Bourahla, and A. A. Belkacem, "Effect of axial load and transverse reinforcements on the seismic performance of reinforced concrete columns," *Front. Struct. Civ. Eng.*, vol. 13, no. 4, pp. 831–851, 2019, http://dx.doi.org/10.1007/s11709-018-0513-3.

[52] D. Domenico, D. Falliano, and G. Ricciardi, "Confinement effect of different arrangements of transverse reinforcement on axially loaded concrete columns: An experimental study," *J. Mech. Behav. Mater.*, vol. 28, no. 1, pp. 13–19, 2019, http://dx.doi.org/10.1515/jmbm-2019-0003.

[53] A. Deb, A. L. Zha, Z. A. Caamaño-Withall, J. P. Conte, and J. I. Restrepo, "Updated probabilistic seismic performance assessment framework of ordinary standard bridges in California," *Earthquake Eng. Struct. Dynam.*, vol. 50, no. 9, pp. 2551–2570, 2021, http://dx.doi.org/10.1002/eqe.3459.

[54] R. W. Soares, S. S. Lima, and S. H. C. Santos, "Reinforcement concrete bridge pier ductility analysis for different levels of detailing," *IBRACON Struct. Mater. J.*, vol. 10, no. 5, pp. 1042–1050, 2017, http://dx.doi.org/10.1590/s1983-41952017000500006.

**Author contributions:** GHFC: conceptualization, data curation, methodology, formal analysis, software, writing-original draft; EMVP: methodology, formal analysis, writing-original draft; IDR: methodology, formal analysis, writing-original draft; LCMVJ: Project administration; GHS: Project administration, formal analysis, supervision, writing-review & editing.

**Editors:** Mauricio Ferreira, Guilherme Aris Parsekian.

IBRACON Structures and Materials Journal
Revista IBRACON de Estruturas e Materiais
ISSN 1983-4195 ismj.org

ORIGINAL ARTICLE

# Shear-torsion-bending interaction in RC beams according to NBR 6118/2014 and AASHTO LRFD 2014

## *Interação entre torção, flexão e cortante em vigas de concreto armado segundo NBR 6118/2014 e AASHTO LRFD 2014*

Vinícius Belarmino Almeida[a]
Bernardo Horowitz[a]

[a]Universidade Federal de Pernambuco – UFPE, Centro de Tecnologia e Geociências, Programa de Pós-Graduação em Engenharia Civil, Recife, PE, Brasil

Received 4 October 2021
Accepted 7 March 2022

**Abstract:** Reinforced concrete beams are subjected to bending, torsion and shear simultaneously. The interaction of combined loading is complex and demands a unified model for analysis and design. Using the models from NBR 6118/2014 (variable angle truss model with parallel chords) and AASHTO LRFD Bridge Design Specifications 2014 (Modified Compression Field Theory), an algorithm was created, converting the resistance problem into a constrained optimization problem and generating an interaction surface that also displays the active constraints for each degree of interaction. Applying it to three beams previously tested, the experimental data was plotted against the surface obtained by the standards. The procedure and its optimization approach were efficient and effective in predicting the beams' resistance. Comparison between the interaction surfaces, empirical data and existing literature showed the procedure and the standards were consistent and its application simple and practical.

**Keywords:** reinforced concrete, bending, torsion, shear, interaction, optimization, NBR 6118, AASHTO LRFD.

**Resumo**: Vigas de concreto armado estão sujeitas a esforços de flexão, torção e cortante, muitas vezes simultaneamente. A interação entre esses é um fenômeno complexo, que exige um modelo unificado de análise e dimensionamento. Seguindo os modelos da NBR 6118/2014 (treliça generalizada de banzos paralelos) e AASHTO LRFD Bridge Design Specifications 2014 (Teoria do Campo de Compressão Modificada), implementou-se um algoritmo que transforma o problema de resistência em um problema de otimização com restrições, gerando uma superfície de interação com indicações das restrições ativas em cada grau de interação. Aplicando o procedimento para três vigas ensaiadas anteriormente, plotaram-se os resultados experimentais sobre a superfície obtida pelas normas. O procedimento e sua abordagem de otimização foram eficientes e eficazes em prever a resistência das vigas analisadas. A comparação das superfícies de interação com dados experimentais e resultados da literatura mostrou a consistência do procedimento e das normas, e sua aplicação se mostrou prática e simples.

**Palavras-chave:** concreto armado, flexão, torção, cortante, interação, otimização, NBR 6118, AASHTO LRFD.

**How to cite:** V. B. Almeida and B. Horowitz, "Shear-torsion-bending interaction in RC beams according to NBR 6118/2014 and AAASHTO LRFD 2014," *Rev. IBRACON Estrut. Mater.*, vol. 16, no. 1, e16102, 2023, https://doi.org/10.1590/S1983-41952023000100002

Corresponding author: Vinícius Belarmino Almeida. E-mail: vinicius.almeida@ufpe.br
**Financial support:** This study was financed in part by the Coordenação de Aperfeiçoamento de Pessoal de Nível Superior (CAPES) – Finance Code 001.
**Conflict of interest:** Nothing to declare.
**Data Availability:** The data that support the findings of this study are openly available in https://doi.org/10.48331/scielodata.ZGNEIO

## 1 INTRODUCTION

Reinforced concrete beams are subjected to bending, torsion and shear forces, with several mechanical and empirical models available for design and analysis considering each one of these separately. Most structural elements withstand a combined action, however. In order to analyze this interaction, many engineers resort to simplified procedures or completely ignore this phenomena, due to the complexity of standards procedures and the lack of unanimity around a straightforward mechanical and rational model [1].

While flexure theory has been around since the 17th century and is well established for reinforced concrete since the 1960s, the most popular model for shear and torsion (truss/strut-and-tie model) is relatively new, developed by Ritter and Morsch in the beginning of the 20th century. Even the most modern and complete models still carry some empiricism and needs some validation for some situations [2], [3]. Other than generalized truss models using equilibrium or compatibility, recent research has suggested different models such as trusses with crack friction, disturbed stress fields, finite element applications, simplified model for combined stress resultants and shear friction [4], [5].

The sheer number of variables involved in the shear problem make it very difficult for experiments to be interpreted. Also, shear and interaction tests are hard to perform in a practical and reliable manner. These factors combined hinder the proposal of a simple and complete method for analysis and design [6]. Compared to the flexure procedure, standards still use too many equations, suggest overconservative simplifications, or require the use of iterative methods for shear. The goal of this paper is to show an automatic method with an optimization approach that allows the use of the complete procedures proposed by two standards: NBR 6118/2014 and AASHTO LRFD 2014. The proposed algorithm generates full shear-torsion- bending interaction surfaces, allowing the verification of the standards consistency with experimental data from the literature.

## 2 PROPOSED METHOD

Given: $T$, $M$ and $V$ (torsion moment, bending moment and shear force) acting on a beam; $r$ an action multiplier (a non-dimensional variable between 0 and 1 - the "magnitude" of forces); and $F_{max}$ the maximum resistance of the force $F$ acting alone; the geometric relationship shown in Figure 1 is obtained. $\alpha_r$ $and$ $\beta_r$ control the interaction between the actions, obtained by Equations 1, 2 e 3. To obtain the resistance of the section for an interaction degree ($\alpha_r$ $and$ $\beta_r$), $r$ must be maximized, increasing the actions until failure. This results in Problem 1 (Figure 2), where a constraint A (action) < R (resistance) represents a standard's verification.

$$M = M_{max} r sin\beta_r \tag{1}$$

$$T = T_{max} r cos\beta_r sin\alpha_r \tag{2}$$

$$V = V_{max} r cos\beta_r cos\alpha_r \tag{3}$$

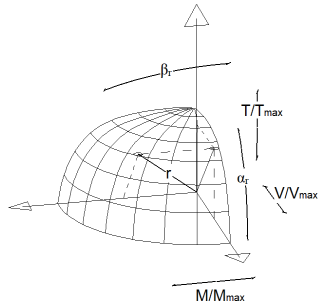


**Figure 1:** Relationship between torsion moment, bending moment and shear force.

| | |
|---|---|
| **Maximize** | $\mathrm{r} = f(r, \alpha_r, \beta_r)$ |
| $\mathrm{r} \in \mathbb{R} \mid \alpha_r, \beta_r \in [0, \frac{\pi}{2}]$ | |
| **Subject to:** | $S(r, \alpha_r, \beta_r) \leq \mathrm{R}(r, \alpha_r, \beta_r)$ |

**Figure 2:** Subroutine for Problem 1.

This approach was taken from Obel [7], extended to 3D and solved using a SQP algorithm from commercial software MATLAB. The algorithms are available on SciELO Data [8].

## 3 STANDARDS' PROCEDURES

### 3.1 NBR 6118/2014

NBR 6118/2014 uses load and resistance factored design, with statistical coefficients for each limit state to consider variability, uncertainty, precision, simultaneity and importance of the phenomena analyzed. Thus, in the ultimate limit state, design must ensure the design action $F_{Sd}$ is inferior to design resistance $F_{Rd}$. This section shows its prescriptions for shear, torsion, flexure and interaction in beams [9].

#### Shear

The standard allows two calculation models based on the generalized truss with parallel chords, considering concrete struts inclined at $\theta$ and transverse steel ties inclined at $\alpha$ with some concrete contribution in tension. Model II permits a variation of the inclination of the struts $\theta$ between 30º and 45º, while model I sets the angle of the diagonals at 45º, in a conservative simplification. Thus, this article will focus on the demonstration of Model II [9].

To check the **inclined concrete struts** between the diagonal cracks, vertical equilibrium is applied on the left section of Figure 3a and 3b, finding $R_{cw}$, the force on the struts as a function of the shear force $V_{Sd}$ (Equation 4). The compression stress on the struts $\sigma_{cw}$ is shown in Figure 3c and is given by Equation 5, using the beam width $b_w$ and lever arm $z$.

$$R_{cw} = V_{Sd} / \, sin\theta \tag{4}$$

$$\sigma_{cw} = \frac{R_{cw}}{b_w \times z \times (cot\theta + cot\alpha) \times sin\theta} \tag{5}$$

Substituting Equation 4 in Equation 5, Equation 6 is obtained. At failure, the compression stress on the strut reaches concrete compression resistance, which is 70% of the usual maximum $0.85 f_{cd}$, due to the biaxial stress nature of the truss model. A reduction factor $\alpha_{v2}$ is considered, to adapt the cylinder test result that originates $f_{cd}$ to the shape of the concrete struts (Equation 7). Assuming the lever arm z is 90% of the effective depth d, Equation 6 turns to Equation 8 (shear force. $V_{Sd}$ reaches the strut shear resistance $V_{Rd2}$).

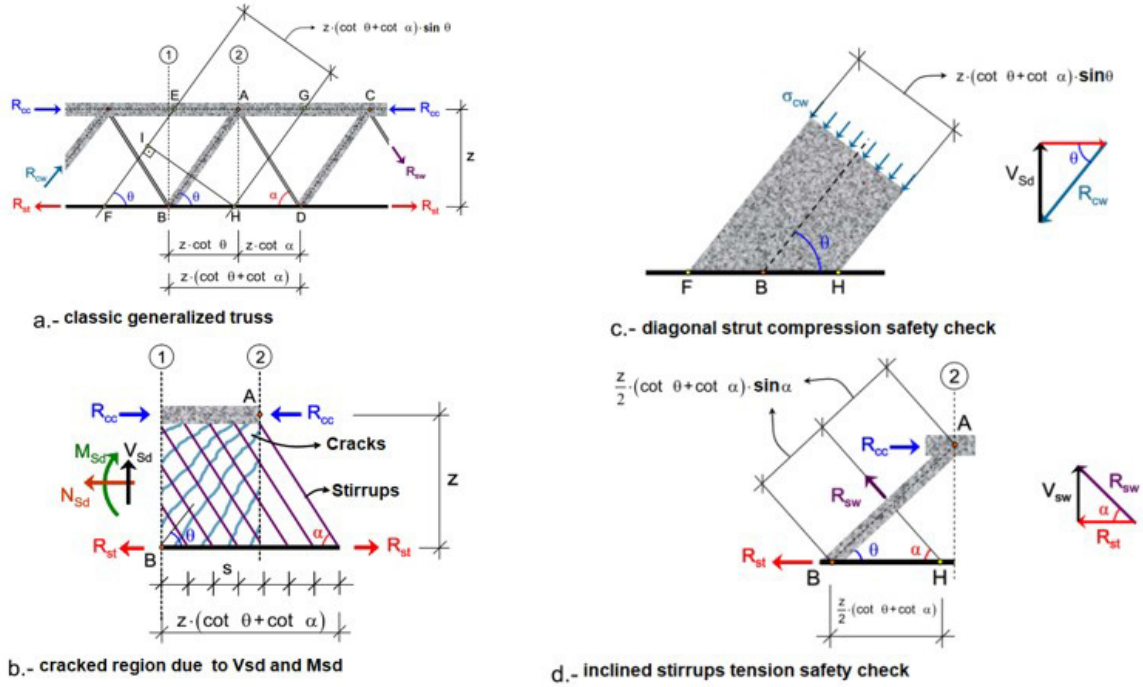


**Figure 3:** Generalized truss model with parallel chords [10].

$$\sigma_{cw} = \frac{V_{Sd}}{bw \times z \times (cot\theta + cot\alpha) \times sin^2\theta} \tag{6}$$

$$\alpha_{v2} = 1 - \frac{f_{ck}}{250} \tag{7}$$

$$V_{Sd} = V_{Rd2} = 0.54 \times \alpha_{v2} \times f_{cd} \times b_w \times d \times sin\,\theta^2 \times (cot\,\theta + cot\,\alpha) \tag{8}$$

The **ties** resist shear though a steel contribution $V_{sw}$ and a concrete contribution $V_{cw}$. The force acting on the stirrups $R_{swt}$ is obtained by vertical equilibrium on the right section of Figure 3b e 3d, resulting in Equation 9. Being the number of stirrups (spaced at s distance) crossing a diagonal crack $n_{bars}$ given by Equation 10 and considering them to yield at $f_{yd}$ stress, the maximum force developed by the vertical hoops is given by Equation 11. At failure, the force on the stirrups reaches the maximum possible force developed by the steel (Equation 12).

$$R_{swt} \times sin\alpha = V_{sw} \tag{9}$$

$$n_{bars} = \frac{z \times (cot\theta + cot\alpha)}{s} \tag{10}$$

$$R_{swt} = \frac{A_{sw} \times f_{yd} \times 0.9d \times (cot\theta + cot\alpha)}{s} \tag{11}$$

$$V_{sw} = \frac{A_{sw} \times f_{yd} \times 0.9d \times (cot\theta + cot\alpha) \times sin\alpha}{s} \quad (12)$$

Using a similar procedure on the sections from Figure 4, the concrete contribution $V_{cw}$, is given by Equation 13, as a function of the concrete tension design resistance $f_{ctd}$. This must be diminished, however, to account for the cracking of the section depending on the bending moment and relative shear force, according to Equations 14, 15 and 16. At failure, shear design force equals the shear resistance of the ties $V_{Rd3}$ given by Equation 17, adding steel and concrete contribution.

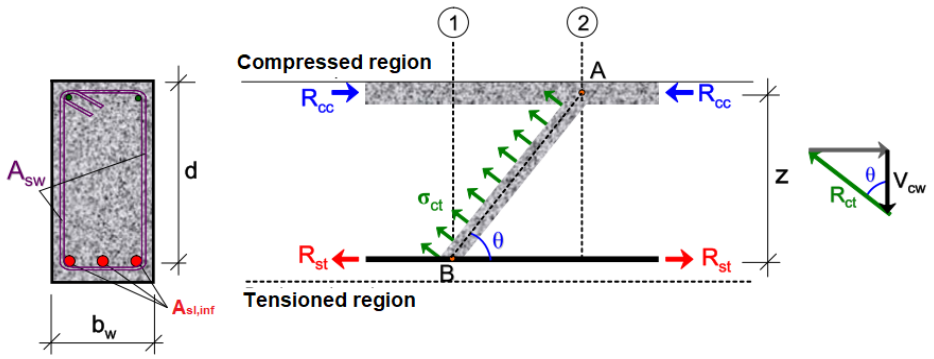


**Figure 4:** Concrete contribution to the ties [10].

$$V_{cw} = b_w \times 0.9d \times f_{ctd} \times \frac{cos\theta}{sin\theta} \quad (13)$$

$$V_{c0} = 0.6 \times f_{ctd} \times b_w \times d \quad (14)$$

$$V_{c1} = V_{c0} \times \frac{(V_{Sd} - V_{Rd2})}{(V_{c0} - V_{Rd2})} \quad (15)$$

$$V_c = \begin{cases} 0, for\ fully\ tensioned\ sections\ under\ flexure - tension \\ V_{c1}, for\ partially\ tensioned\ sections\ under\ flexure - tension \\ V_{c1} + \left(1 + \frac{M_0}{M_{Sd}}\right), for\ flexure - compression, being\ M_0\ the\ decompression\ bending \end{cases} \quad (16)$$

$$V_{Sd} = V_{Rd3} = V_{sw} + V_c \quad (17)$$

To verify the **parallel chords**, horizontal equilibrium is observed in Figure 3b, finding the force on the tensioned chord $R_{st,v}$ in Equation 18, which generates Equation 19 using previous equations. Also, the bending moment induces a tension force on the bottom chord, given by Equation 20. Thus, the bottom chord is tensioned by a force given by Equation 21. This force must be inferior to the yielding force of the bottom steel area $A_{sl,inf}$ (Equation 22).

$$2R_{st,v} = R_{cw} \times cos\theta - R_{sw} \times cos\alpha \tag{18}$$

$$R_{st,v} = V_{Sd}(cot\,\theta - cot\,\alpha)/2 \tag{19}$$

$$R_{st,m} = \frac{M_{Sd}}{z} \tag{20}$$

$$R_{st} = \frac{M_{Sd}}{z} + V_{Sd}(cot\,\theta - cot\,\alpha)/2 \tag{21}$$

$$\frac{M_{Sd}}{z} + 0.5V_{Sd}(cot\,\theta - cot\,\alpha) < f_{yd} \times A_{sl,inf} \tag{22}$$

**Torsion**

For torsion, NBR 6118/2014 considers a similar model: generalized space truss with parallel chords, considering inclined concrete struts and transverse steel ties without concrete contribution. The space truss geometry is obtained using the thin-walled tube analogy (Figure 5). The struts inclination must be compatible with the one assumed for shear, using either Model I or Model II, but the latter will be the focus of this article, for generalization [9].

The equivalent section is comprised of four perpendicular walls, comprised of connected plane trusses with diagonal struts, transverse steel ties and longitudinal steel parallel chords. Considering spalling of the section under torsion, the equivalent section is a function of the original dimensions, section perimeter $u$ and the distance from the corner steel centroid to the lateral face ($c_1$). Its thickness $h_e$ spans between values from Equation 23 and Equation 24. Its middle line perimeter $u_e$ is given by Equation 25 and its enclosed area $A_e$ is obtained from Equation 26.

$$h_{e,min} = \begin{cases} min\left(\frac{A_c}{u}, b_w - 2c_1\right), if\ \frac{A_c}{u} < 2c_1 \\ 2c_1, otherwise \end{cases} \tag{23}$$

$$h_{e,max} = \begin{cases} h_{e,min}, if\ \frac{A_c}{u} < 2c_1 \\ \frac{A_c}{u}, otherwise \end{cases} \tag{24}$$

$$u_e = \begin{cases} u - 8c_1, if\ \frac{A_c}{u} < 2c_1 \\ u - 4h_e, otherwise \end{cases} \tag{25}$$

$$A_e = \begin{cases} (b_w - 2c_1) \times (h - 2c_1), if\ \frac{A_c}{u} < 2c_1 \\ (b_w - h_e) \times (h - h_e), otherwise \end{cases} \tag{26}$$

Considering the shear flow on the wall $q$ is the ratio of the shear stress over the wall thickness $t$ and applying moment equilibrium, Equation 27 gives the relation between torsion and shear flow. The shear force is the product between the shear flow and its length, which leads to Equation 28 giving the shear force on the walls due to torsion.

Using a section of the vertical wall like Figure 6, and considering that the $n_{bars}$ ties crossing a diagonal crack (Equation 29) yield at $f_{ywd}$, vertical equilibrium gives the maximum shear force resisted by each vertical wall (Equation 30). Applying Equation 28, the maximum torsion resisted by each leg $A_t$ of the **stirrups** is given by Equation 31. The shear path enclosed area is taken as $A_e$. Concrete under tension doesn't contribute, due to cracking caused by torsion [11].

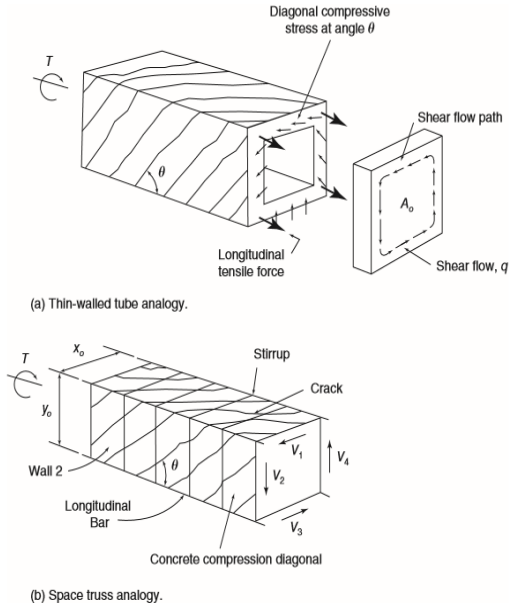


**Figure 5:** Thin-walled tube analogy and generalized space truss [12].

$$T = 2qA_0 \tag{27}$$

$$V1 = V3 = \frac{T}{2A_o} \times x_o \; e \; V2 = V4 = \frac{T}{2A_o} \times y_o \tag{28}$$

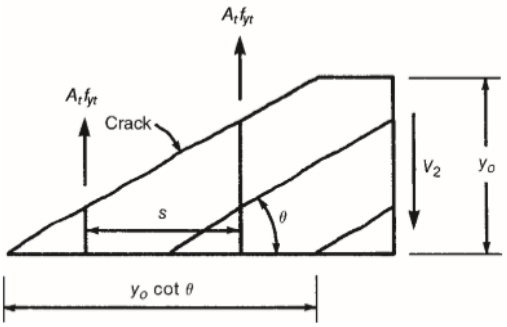


**Figure 6:** Section of the vertical wall detailing the stirrups force [12].

$$n_{bars} = \frac{y_o}{s} \times cot\theta \tag{29}$$

$$V_2 = \frac{A_t f_{ywd} y_o}{s} \times cot\theta \tag{30}$$

$$T_{Rd3} = \frac{2A_e A_t f_{ywd}}{s} \times cot\theta \tag{31}$$

Using a different section of the vertical walls (Figure 7), and using vertical and horizontal equilibrium, it is possible to obtain the compression force on struts $D_2$ (Equation 32) and the tension force on the chords $N$ (Equation 33). Using Equation 28, these actions can be related to the torsion, resulting in (Equation 34) and (Equation 35). At failure, total steel area $A_{s,tot}$ of the **parallel chords** yield, giving the maximum torsion resisted by them $T_{Rd4}$ (Equation 36). Assuming the same as for shear, at failure the **concrete struts** reach its strength, which gives its torsion resistance $T_{Rd2}$ (Equation 37) [13].

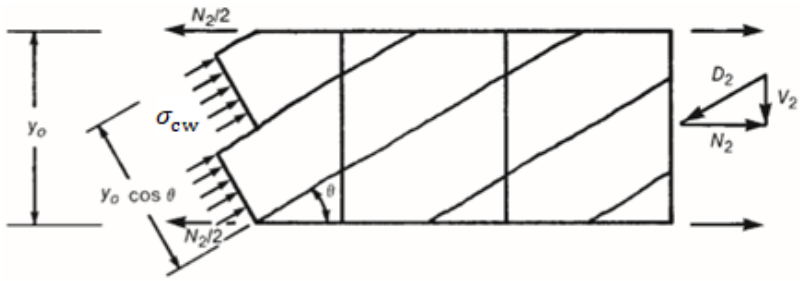


**Figure 7:** Section of a vertical wall of the truss detailing the chords and struts forces [12].

$$D_2 = \frac{V_2}{sin\theta} \tag{32}$$

$$N = 2(V_1\, cot\,\theta + V_2\, cot\,\theta) \tag{33}$$

$$N = \frac{T}{2A_0} 2(x_0 + y_0)\, cot\,\theta = \frac{T}{2A_0} p_o\, cot\,\theta \tag{34}$$

$$\sigma_{cw} = \frac{V_2}{t y_0\, cos\,\theta\, sin\,\theta} = \frac{\frac{T}{2A_0} \times y_o}{t y_0\, cos\,\theta\, sin\,\theta} = \frac{T}{2tA_0\, cos\,\theta\, sin\,\theta} \tag{35}$$

$$T_{Rd4} = \frac{2A_e A_{s,tot} f_{yd}\, tan\,\theta}{u_e} \tag{36}$$

$$T_{Rd2} = 0.5 \times \alpha_{v2} \times f_{cd} \times t \times A_e \times sin\,2\theta \quad (37)$$

In summary, torsion design according to NBR 6118/2014 aims to ensure that torsion design load $T_{Sd}$ is inferior to the struts, ties and chords resistance $T_{Rd2}$, $T_{Rd3}$ and $T_{Rd4}$.

**Bending moment and interaction**

The Brazilian standard uses flexure basic assumptions: plane sections remain plane, perfect steel-concrete bond and constitutive relationships for concrete and steel, neglecting the cracked concrete under tension. Failure is considered to happen under certain domains, where concrete maybe crushed, steel may yield or a combination of both (Figure 8) [9].

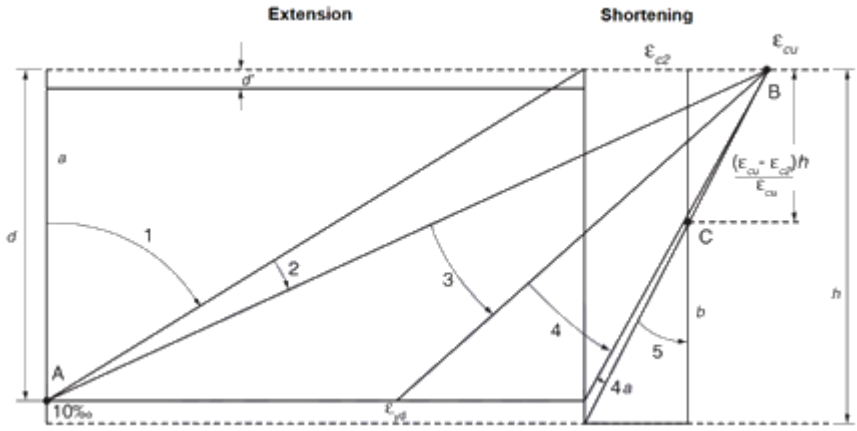


**Figure 8:** Failure domains for flexure [9].

In this article, domains 2 and 3 will be used to obtain bending resistance, where compressed concrete is crushed, and steel is beyond yielding strain. Maximum compression stress is approximated by a stress block and its height $a$ is a fraction of the neutral line height $c$. The acting design bending moment $M_{Sd}$ must be inferior to the bending developed by the compression-tension couple that act on the lever arm $z$. This may be considered 90% of the effective height $d$ or a function of the stress block height, which gives the design bending resistance $M_{Rd}$ (Equation 38). This process is illustrated by Figure 9 [14]

$$M_{Rd} = z \times f_{yd} A_{s,inf} = 0.9d \times f_{yd} A_{s,inf} \; or \; (d - \tfrac{a}{2}) \times f_{yd} A_{s,inf} \quad (38)$$

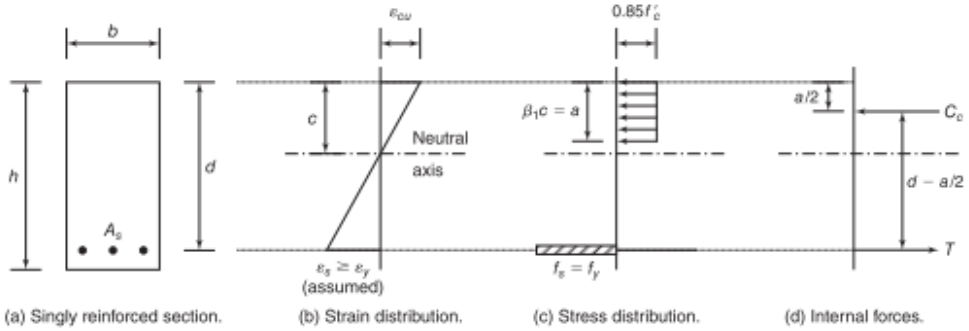


**Figure 9:** RC concrete cross section under flexure [12].

Due to the interaction of combined action, a triaxial stress state arises, with different levels of cracking, softening and strength for each region of the section, which would require a complex 3D model for an exact analysis. The model used by the Brazilian standard, however, is able to capture the phenomenon with a reasonable accuracy, combining the generalized space truss with parallel chords for shear and torsion with the flexure theory [13].

In the **diagonal concrete struts**, flexure influences only the inclination and the cracking level, reducing rigidity and strength. Torsion induces circulatory shear stress around the section, whereas shear force causes shear stress distributed on the web. In hollow sections, only the most critical wall is verified, where shear and torsion effects are added Figure 10a. In solid sections, this separation is impossible, and the real interaction is quite complex (Figure 10b). NBR 6118/2014 considers a linear interaction, as shown in Equation 39 [13].

Only shear and torsion induce stresses on the **ties**. These effects are added on one leg of the hoops and this linear superposition is accounted by Equation 40 simply adding the portion of the steel used by torsion (first term) and by shear ($A_{sv}$, where an relieve of the effect is considered in Equation 41, due to the concrete contribution to shear resistance) [7].

The **top chord** steel $A_{s,sup}$ is tensioned by shear and torsion and compressed by flexure (Equation 42), whereas the **bottom chord** steel $A_{s,inf}$ is tensioned by all actions (Equation 43) [12]. In highly compressed hollow sections, the principal stresses induced by the torsion shear stress and flexure compression becomes relevant and needs to be checked. Using Mohr's circle, the maximum principal stress $\sigma_{cmax}$ is given by Equation 44, as a function of the average normal stress caused by bending $\sigma_{cmed}$ (Equation 45) and shear stress due to torsion $\tau_t$ (Equation 46). The compression strength $\bar{f}_{cd12}$ can be taken as an average between strut-and-tie resistances $f_{cd1}$ (only struts node) e $f_{cd2}$ (strut and ties node), resulting in Equation 47. At failure, the principal stress must be smaller than the strength Equation 48.

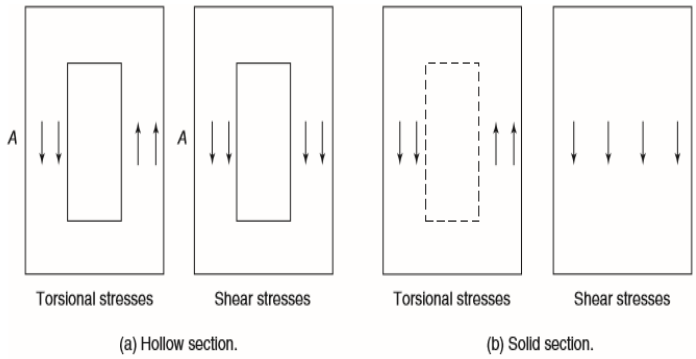


**Figure 10:** Shear and torsion stresses on a hollow and solid section [12].

$$\frac{T_{Sd}}{T_{Rd2}} + \frac{V_{Sd}}{V_{Rd2}} < 1 \tag{39}$$

$$\frac{T_{Sd}}{f_{ywd} \times A_e \times cot\,\theta} + A_{sv} < A_{sw}/s \tag{40}$$

$$A_{sv} = max(V_{Sd} - V_c, 0)/(f_{ywd} \times z \times cot\theta) \tag{41}$$

$$-\frac{M_{Sd}}{0.9d} + (0.5V_{Sd} + T_{Sd} \times u_e/4A_e)\, cot\,\theta < f_{yd} \times A_{s,sup} \tag{42}$$

$$\frac{M_{Sd}}{0.9d} + (0.5V_{Sd} + T_{Sd} \times u_e/4A_e)\, cot\, \theta < f_{yd} \times A_{s,inf} \tag{43}$$

$$\sigma_{cmax} = \frac{\sigma_{cmed}}{2} + \sqrt{\left(\frac{\sigma_{cmed}}{2}\right)^2 + \tau_t^2} \tag{44}$$

$$\sigma_{cmed} = \frac{M_{Sd}}{0.9d \times b_w \times 2(d - 0.9d)} \tag{45}$$

$$\tau_t = \frac{T_{Sd}}{2 \times t \times A_0} \tag{46}$$

$$\bar{f}_{cd12} = \lambda f_{cd1} + (1 - \lambda) f_{cd2}, where\ \lambda = cos\,\gamma\ \ and\ \gamma = arctan\left(\frac{{}^{T_{Sd}}/_{T_{max}}}{{}^{M_{Sd}}/_{M_{max}}}\right) \tag{47}$$

$$\sigma_{cmax} < \bar{f}_{cd12} \tag{48}$$

### 3.2 AASHTO LRFD Bridge Design Specifications 2014

The AASHTO LRFD 2014 standard uses a similar design approach to the Brazilian standard, with statistical coefficients that major loads and reduces resistance, aiming to ensure factored action $F_u$ is inferior to the nominal resistance $F_n$. This section shows its prescriptions for shear, torsion, flexure and interaction, taken from the standard's chapters 5.7 e 5.8 [15].

#### Shear

The standard's model for shear is based on the Modified Compression Field Theory (MCFT), which is a set of equilibrium, compatibility and constitutive relations created to give the complete response of cracked concrete under shear in the generalized truss. It considers parallel chords, tensioned ties and a continuous field of diagonal compression. Assuming the direction of principal stresses is the same of the strains and using both average and local stresses and strain, it achieves the set of equations in Figure 11. AASHTO uses a simplified version of MCFT, assuming the stresses in the cracked region are critical to failure and steel must yield to ensure ductility at failure. Shear resistance is then given by Equation 49, which accounts for a **stirrup's contribution** and a **concrete contribution** (using the $\beta$ parameter for "aggregate interlock" and compression field inclination $\theta$). Due to the nature of the "aggregate interlock" mechanism, this equation is restricted to $f'_c$< 64 MPa and a lightweight-aggregate reduction factor $\lambda$ is considered. The lever arm may be taken as the maximum between 0.9d e 0.72h. To ensure stirrups yield before **crushing of struts**, an upper bound of 25% of the concrete compression resistance $f'_c$ is set for shear stress [16]. These simplifications allow the equation to emulate the empirical "concrete and steel" contribution formula ($V_c + V_s$), traditional in the American standards and practice [1].

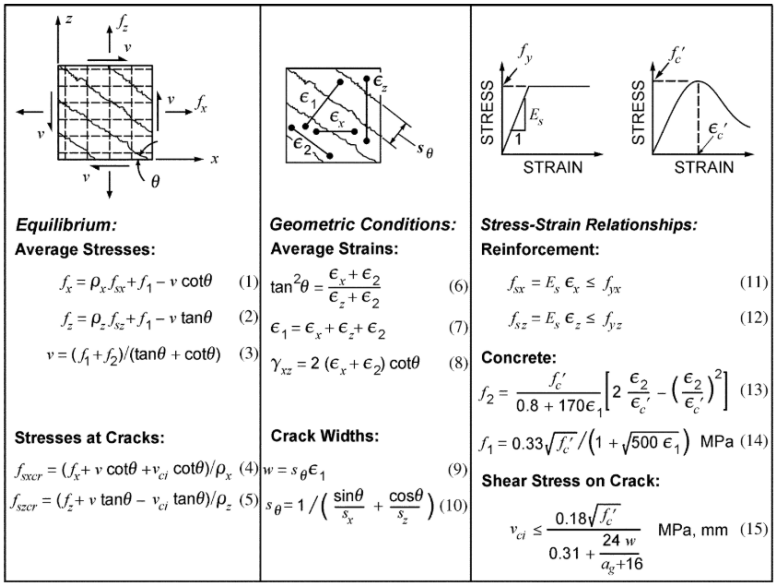


**Figure 11:** MCFT equilibrium, compatibility and constitutive relationships [16].

$$\frac{V_u}{b_w z} < \frac{V_n}{b_w z} = \frac{V_c + V_s}{b_w z} = \lambda\beta\sqrt{f'_c} + \frac{A_{sw} f_{ywd} cot\theta}{b_w s} < 0.25 f'_c \tag{49}$$

The $\beta$ parameter accounts for several effects. Steel longitudinal strain $\varepsilon_s$ accounts for the "strain effect", section's reinforcement ratio, level of shear, compression and bending action and rigidity $E_s$. It is obtained by Equation 50 using horizontal equilibrium (Figure 12), considering the compressed concrete to be uncracked and taking, conservatively, $0.5cot\theta$ as 1. Spacing between diagonal cracks $s_x$ increases the crack width $w$ and reduces the "aggregate interlock". This is called "size effect" and is given by Equation 51. Considering an aggregate size correction factor, $s_{xe}$ is obtained, as shown in Equation 52. For high strength concrete, another correction is necessary, as the cracks tend to form through the aggregate. Based on empirical evidence for a diagonally cracked standard beam, the crack width is given as a function of longitudinal strain in Equation 53. To avoid negative values in this equation, a lower bound is set to Equation 50. Correcting Equation 53 to consider "size effect" and using it into the shear stress on crack considered my MCFT, Equation 54 is obtained [17].

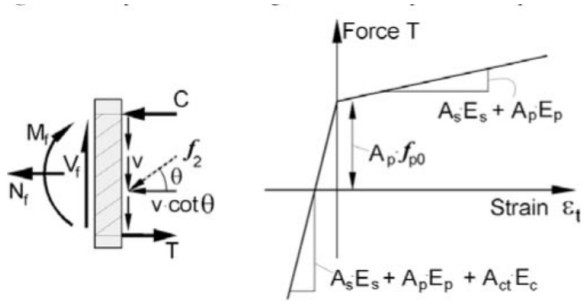


**Figure 12:** Acting and resisting forces and strains on a section [16].

$$-4 \times 10^{-4} < \varepsilon_s = \frac{\frac{M_u}{z} + 0.5V_u cot\theta + 0.5N_u}{A_{s,inf} \times E_s} = \frac{\frac{M_u}{z} + V_u + 0.5N_u}{A_{s,inf} \times E_s} < 6 \times 10^{-3} \tag{50}$$

$$s_x = \begin{cases} z, without\ stirrups \\ 0.3m, with\ stirrups \end{cases} \quad (51)$$

$$s_{xe} = s_x \times \frac{0.035}{0.016 + a_g} > 0.85 s_x \quad (52)$$

$$w = 0.2 + 2000\varepsilon_s \quad (53)$$

$$\beta = \frac{4.8}{(1+750\varepsilon_s)} \times \frac{1.3}{1+s_{xe}} \quad (54)$$

The compression field inclination $\theta$ defines the truss' capacity to redistribute forces to the ties and chords. For the steel to yield before the concrete crushes at failure, this angle must be within the limits shown in Figure 13. The inclination is assumed a linear function of the longitudinal strain, as in Equation 55. To control this redistribution in the truss, an upper bound is set to the angle, though the maximum limit on Equation 50.

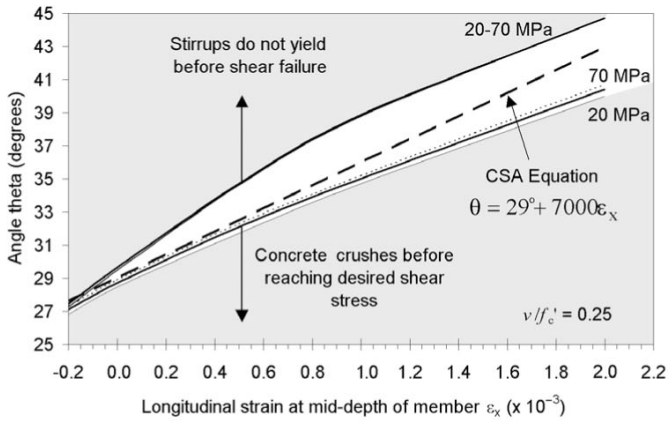


**Figure 13:** Inclination of the compression field as a function of longitudinal deformation [17].

$$\theta = 29° + 3500\varepsilon_s \quad (55)$$

The **bottom chord** of the truss must also be checked, ensuring tension due to shear and flexure aren't higher than the reinforcement's yield, which leads to Equation 56 [16].

$$f_{yd} \times A_{s,inf} > \frac{M_u}{z} + (V_u - 0.5V_s)cot\theta + 0.5N_u \quad (56)$$

## Torsion

Simplified MCFT also accounts for torsion, aided by the thin-walled tube analogy. Its geometry considers spalling of the concrete cover and is a function of the original dimensions and the distance from the stirrups to the lateral face

of the section ($c_2$). Based on that, the enclosed area $A_0$ and perimeter $p_0$ of the shear flow middle line are taken respectively as 85% and 90% of the enclosed area $A_{\mathrm{oh}}$ and perimeter $p_{\mathrm{h}}$ of the hoops. AASHTO [15] uses the equilibrium of the generalized space truss to check for tension on the **ties** and **chords** (Equations 57 and 58). Crushing of the concrete **struts** is verified using a factored equivalent shear $V_{u,eq}$, considering a quadratic interaction between torsion and shear, that must be lower than $0.25f'_c b_w z$ (Equation 59). Since MCFT doesn't consider a concrete contribution to torsion resistance, only the parameters $\varepsilon_s$ e $\theta$ are needed, calculated as previously shown for shear [18].

$$T_n = \frac{2A_o A_t f_{yt}}{s} \times cot\theta \tag{57}$$

$$\frac{M_u}{z} + \frac{0.45T_u p_h}{2A_o} \times cot\theta < f_{yd} \times A_{s,inf} \tag{58}$$

$$V_{u,eq} = \sqrt{{V_u}^2 + \left(\frac{0.9T_u p_h}{2A_o}\right)^2} < 0.25 \times f'_c \times b_w \times z \tag{59}$$

**Flexure and interaction**

Flexure is checked similarly to the Brazilian standard, resulting in Equation 60 [15].

$$M_n = z \times f_{yd} A_{s,inf} = 0.9d \times f_{yd} A_{s,inf} \; or \; 0.72h \times f_{yd} A_{s,inf} \tag{60}$$

Interaction on AASHTO affects the equilibrium verifications and β and θ, through the longitudinal strain. However, it uses a simplified version of MCFT. Spalling is rarely observed in sections with smaller cover, which leads to overestimated torsional stresses. The shear stress limit on the struts is also overconservative for beams with lower longitudinal strains [19].

Crushing of the **struts** in interaction is already verified in Equation 59. Tension on the **ties** is checked by superposition of shear and torsion in Equations 61 e 62. On the **chords**, a quadratic interaction is considered between shear and torsion, added to the compression or the tension caused by bending, as in Equations 63 e 64 [18]. Principal stresses are not checked on the top chord for solid sections, leaving such verification for a specific hollow section topic.

$$\frac{T_u}{f_{ywd} \times A_o \times cot\,\theta} + A_{sv} < A_{sw}/s \tag{61}$$

$$A_{sv} = max(V_u - V_c, 0)/(f_{ywd} \times z \times cot\theta) \tag{62}$$

$$\frac{M_u}{z} + \left(\sqrt{\left(\frac{0.45T_u p_h}{2A_o}\right)^2 + (V_u - 0.5 \times V_s)^2}\right) \times cot\theta < f_{yd} \times A_{s,inf} \tag{63}$$

$$-\frac{M_u}{z} + \left(\sqrt{\left(\frac{0.45T_u p_h}{2A_o}\right)^2 + (V_u - 0.5 \times V_s)^2}\right) \times cot\theta < f_{yd} \times A_{s,sup} \tag{64}$$

### 3.3 Optimization problem for each standard

**NBR 6118/2014**

For an interaction degree $\alpha_r$ and $\beta_r$, with unity values for resistance and load factors:

1) Given a RC beam with the following parameters:
   a. Longitudinal and transverse reinforcement yield stresses: $f_{yd}, f_{ywd}$
   b. Concrete compressive strength: $f_{cd} = f_{ck}$
   c. Cross section dimensions: $b_w$, h, $d$, $c_1$
   d. Longitudinal and transverse reinforcement detailing $A_{s,inf}, A_{s,sup}, A_{sw}, s$
2) Auxiliary parameters are calculated:
   a. Concrete average tensile strength (Equation 65):

$$f_{ct,m} = \begin{cases} 0.3 \times {f_{ck}}^{2/3}, if\ f_{ck} \leq 50MPa \\ 2.12 \times ln(1 + 0.11 f_{ck}), otherwise \end{cases} \quad (65)$$

   b. Concrete minimum tensile strength (Equation 66):

$$f_{ctk,inf} = 0.7 f_{ct,m} \quad (66)$$

   c. Concrete struts strength reduction factor $\alpha_{v2}$ - Equation 7
   d. Cross section's area $A_c$, moment of inertia $I_c$ and perimeter $u$
   e. Thin-walled tube thicknesses ($h_{e,min}$) and ($h_{e,max}$) - Equations 23 and 24
3) Max resistance $V_{max}$, $T_{max}$ e $M_{max}$ are calculated as $V_{Rd2}$ (Equation 8), $T_{Rd2}$ (Equation 37) and $M_{Rd}$ (Equation 38)
4) Objective function is defined as the action multiplier *r* (Equation 67):

$$f(r, \alpha_r, \beta_r, h_e, \theta) = r \quad (67)$$

5) The following variables are defined:
   a. Actions $M_{Sd}$, $T_{Sd}$ *e* $V_{Sd}$ according to Equations 1, 2 and 3
   b. Average strut-and-tie compressive resistance $\bar{f}_{cd12}$ as in Equation 47
   c. Thin-walled tube's middle line perimeter ($u_e$) and enclosed area ($A_e$) according to Equations 25 and 26
6) Constraints on the optimization variables are defined (Equations 68 and 69):

$$30° \leq \theta \leq 45° \quad (68)$$

$$h_{e,min} \leq h_e \leq h_{e,max} \quad (69)$$

7) Resistance constraints are defined:
   a. $T_{Sd} < T_{Rd2}, T_{Rd3}, T_{Rd4}$ according to Equation 31, Equation 35 and Equation 37
   b. $V_{Sd} < V_{Rd2}, V_{Rd3}$ according to Equation 8 and Equation 17
   c. Flexure and interaction check on the chords according to Equation 42 and Equation 43
   d. Verification of struts and ties according to Equation 39 and Equation 40
   e. Principal compressive stress check (Equation 48)
8) The objective function is maximized subject to constraints, using actions normalized by the maximum resistance. This procedure is shown on Problem 2 (Figure 14) and its MATLAB algorithm is available on SciELO Data RIEM repository as *Otim_R_NBR* [8].

**Given**: $f_{yd}, f_{ywd}, f_{cd}, b_w, \mathrm{h}, c_1, A_{s,inf}, A_{s,sup}, A_{sw}, s$

**Considering:**

$$V_{Rd2} = 0.54 \times \alpha_{v2} \times f_{cd} \times b_w \times d \times \sin\theta^2 \times (\cot\theta + \cot\alpha)$$

$$V_{Rd3} = V_{sw} + V_c = \frac{A_v f_{yt} 0.9d}{s} \times cot\theta + 0.6 \times f_{ct} \times b_w \times d$$

$$h_{e,min} = \begin{cases} \min\left(\frac{A_c}{u}, b_w - 2c_1\right), if\ \frac{A_c}{u} < 2c_1 \\ 2c_1,\ otherwise \end{cases}$$

$$h_{e,max} = \begin{cases} h_{e,min}, if\ \frac{A_c}{u} < 2c_1 \\ \frac{A_c}{u},\ otherwise \end{cases}$$

$$T_{Rd2} = 0.5 \times \alpha_{v2} \times f_{cd} \times A_e \times h_e \times \sin 2\theta$$

$$T_{Rd3} = A_{sw} \times f_{ywd} \times A_e \times \cot\theta / s$$

$$T_{Rd4} = 4 \times A_s \times f_{yd} \times A_e \times \frac{\tan\theta}{u_e}$$

$$\sigma_{cmax} = \frac{\sigma_{cmed}}{2} + \sqrt{\left(\frac{\sigma_{cmed}}{2}\right)^2 + \tau_t^2}$$

$$\bar{f}_{cd12} = \lambda f_{cd1} + (1-\lambda) f_{cd2}, where\ \lambda = cos\,\gamma\ and\ \gamma = arctg\left(\frac{T_{Sd}/T_{max}}{M_{Sd}/M_{max}}\right)$$

$$A_{sv} = \max(V_{Sd} - V_c, 0)/(f_{ywd} \times z \times cot\theta)$$

**Maximize**

$$f(\mathrm{r}, \alpha_r, \beta_r, h_e, \theta) = \mathrm{r}$$

$\mathrm{r}, h_e, \theta \in \mathbb{R}$
$\alpha_r, \beta_r \in [0, \pi/2]$

$$M_{Sd} = M_{max}\, r sin\beta_r; T_{Sd} = T_{max}\, r cos\beta_r sin\alpha_r; V_{Sd} = V_{max}\, r cos\beta_r cos\alpha_r$$

**Subject to:**

$$30° \le \theta \le 45°$$

$$h_{e,min} \le h_e \le h_{e,max}$$

$$T_{Sd} < T_{Rd2}, T_{Rd3}, T_{Rd4}$$

$$V_{Sd} < V_{Rd2}, V_{Rd3}$$

$$-M_{Sd}/0.9d + (0.5V_{Sd} + T_{Sd} \times u_e/4A_e)\cot\theta < f_{yd} \times A_{s,\,superior}$$

$$M_{Sd}/0.9d + (0.5V_{Sd} + T_{Sd} \times u_e/4A_e)\cot\theta < f_{yd} \times A_{s\,inferior}$$

$$\frac{T_{Sd}}{T_{Rd2}} + \frac{V_{Sd}}{V_{Rd2}} < 1$$

$$\sigma_{cmax} < f_{cd1-2}$$

$$\frac{T_{Sd}}{f_{ywd} \times A_e \times \cot\theta} + A_{sv} < A_{sw}/s$$

**Figure 14:** Subroutine for Problem 2.

## AASHTO LRFD BRIDGE DESIGN SPECIFICATIONS 2014

For an interaction degree $\alpha_r$ and $\beta_r$, with unity values for resistance and load factors:

1) Given a RC beam with the following parameters:
   a. Longitudinal and transverse reinforcement yield stresses and Young's Modulus: $f_y, f_{yw}, E_s (\cong 210GPa)$
   b. Concrete compressive strength: $f'_c$
   c. Cross section dimensions: $b_w, \mathrm{h}, d, c_2$
   d. Longitudinal and transverse reinforcement detailing $A_{s,inf}, A_{s,sup}, A_{sw}, s$
   e. Max aggregate size $a_g$ (linearly reduced if $60\mathrm{MPa} < f'_c < 70\mathrm{MPa}$)
2) Auxiliar parameters are calculated:
   a. Stirrup's enclosed area $A_{oh}$ and perimeter $p_h$
   b. Thin-walled tube's middle line enclosed area $A_o$ and perimeter $p_o$ taken respectively as 85% of $A_{oh}$ and 90% of $p_h$
   c. Lever arm $z$ taken as max between 90% of $d$ and 72% of $h$
   d. Effective diagonal cracks spacing $s_{xe}$ according to Equation 52

3) Max resistance $V_{max}$, $T_{max}$ e $M_{max}$ are taken as the upper bound of (Equation 49) for shear and torsion and maximum of (Equation 38) for the bending moment
4) Objective function is defined as the action multiplier *r* (Equation 70):

$$f(r, \alpha_r, \beta_r) = r \tag{70}$$

5) The following variables are defined:
   a. Factored actions $M_u$, $T_u$ *e* $V_u$ according to Equations 1, 2 and 3
   b. Factored equivalent shear force $V_{u,eq}$ according to Equation 59
   c. Longitudinal reinforcement strain $\varepsilon_s$ (Equation 50), struts inclination $\theta$ (Equation 55) and "aggregate interlock" parameter β (Equation 54)
6) Resistance constraints are defined:
   a. Flexure and interaction check on the chords according to Equation 63 and Equation 64
   b. Shear, torsion and interaction verifications on the ties and the struts according to Equations 59 and 61
7) The objective function is maximized subject to constraints, using actions normalized by the maximum resistance. This procedure is shown on Problem 3 (Figure 15) and its implementation on MATLAB is available on the SciELO Data RIEM repository as *Otim_R_AASHTO* [8].

**Given**: $f_{yd}, f_{ywd}, f_{cd}, b_w, h, c_2, A_{s,inf}, A_{s,sup}, A_{sw}, s, a_g$

**Considering:**

$$A_o = 0.85 A_{oh} \text{ and } p_o = 0.9 p_h$$

$$A_{sv,min} = 0.083 \times \sqrt{f'_c} \times b_w \times s / f_{ywd}$$

$$s_x = \begin{cases} z, \text{ if } A_{sw} \geq A_{sv,min} \\ 0.3m, \text{if } A_{sw} < A_{sv,min} \end{cases}$$

$$s_{xe} = s_x \times \frac{0.035}{0.016 + a_g} > 0.85 s_x$$

$$V_{u,eq} = \sqrt{{V_u}^2 + \left(\frac{0.9 T_u p_h}{2A_o}\right)^2}$$

$$-4 \times 10^{-4} \leq \varepsilon_s = \frac{\frac{M_u}{z} + V_{u,eq}}{A_{s,inf} \times E_s} \leq 6 \times 10^{-3}$$

$$\beta = \frac{4.8}{(1 + 750\varepsilon_s)} \times \frac{1.3}{1 + s_{xe}}$$

$$\theta = 29° + 3500\varepsilon_s$$

$$V_c = 0.083 \times \beta \times \sqrt{f'_c} \times b_w \times z | V_s = \frac{A_{sw} f_{ywd} \cot\theta}{b_w s}$$

$$A_{sv} = \max(V_u - V_c, 0) / (f_{ywd} \times z \times \cot\theta)$$

**Maximize** $f(r, \alpha_r, \beta_r) = r$

$r \in \mathbb{R} \mid \alpha_r, \beta_r \in [0, \pi/2]$ $\quad M_u = M_{max} r \sin\beta_r ; T_u = T_{max} r \cos\beta_r \sin\alpha_r ; V_u = V_{max} r \cos\beta_r \cos\alpha_r$

**Subject to:**

$$\frac{T_u}{A_o f_{ywd} \cot\theta} + A_{sv} < \frac{A_v}{s}$$

$$V_{u,eq} < 0.25 \times f'_c \times b_w \times z$$

$$\frac{M_u}{z} + \left(\sqrt{\left(\frac{0.45 T_u p_h}{2A_o}\right)^2 + (V_u - 0.5 \times V_s)^2}\right) \times \cot\theta < f_{yd} \times A_{s,inf}$$

$$-\frac{M_u}{z} + \left(\sqrt{\left(\frac{0.45 T_u p_h}{2A_o}\right)^2 + (V_u - 0.5 \times V_s)^2}\right) \times \cot\theta < f_{yd} \times A_{s,sup}$$

**Figure 15:** Subroutine for Problem 3.

### 3.4 Post-processing

Based on the optimization's solution point and previous equations, the trio of resistance values for each interaction degree $\alpha_r$ and $\beta_r$ is obtained. These values are then divided by the maximum resistance found for each kind. For each beam, several $\alpha_r$ and $\beta_r$ are evaluated, ranging from 0º to 90º in 6º steps, obtaining enough points to plot a smooth interaction surface using interpolation. For comparison, experimental data points from the analyzed tests are plotted along with hidden lines starting from the origin. These were normalized using the maximum predicted resistance based on the tested beam's parameters, which may differ from nominal values. The scaling values were obtained by the programs *MVTmax_NBR* e *MVTmax_AASHTO*, available in [8]. Also, the algorithm calculates the value of the constraints at the solution, indicating the active one on the plot using a color code.

This post-processing procedure was also implemented in MATLAB and is available on the author's SciELO Data RIEM repository as *Pos_OtimR_NBR_AASHTO* [8].

## 4 COMPARISON WITH EXPERIMENTS

### 4.1 Analyzed tests

The first analyzed experiment was done by Badawy et al. [20], in which seven straight beams (S1 to S7) were tested under combined action until failure, as shown in Figure 16. The test region of the beams had the cross section shown in Figure 17. Other parameters are summarized on Table 1 and test results are shown in Table 2.

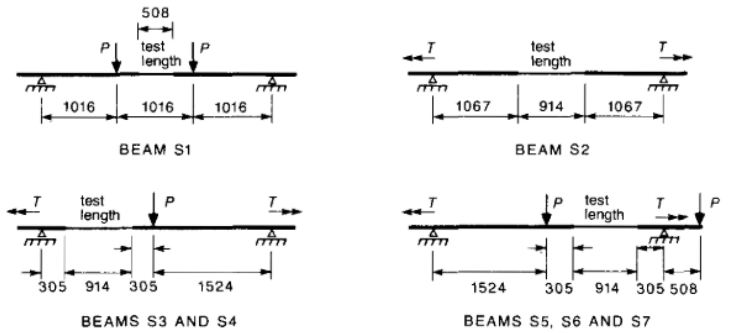


**Figure 16:** Test setup for combined action on beams S1 to S7 (dimensions in mm) [20].

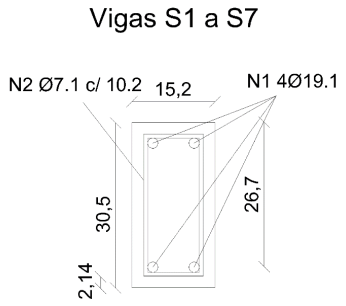


**Figure 17:** S1 to S7 beams cross section (dimensions in cm and bars diameter in mm).

The second analyzed experiment was done by McMullen and Warwaruk [21], in which 34 beams were tested under combined action until failure, comprising 7 groups with different reinforcement. Groups 5, 6 and 7, hereby called M5, M6 and M7 were the only tested under torsion, shear and bending. They were setup as shown in Figure 18 and had cross sections like those of Figure 19. As top and bottom reinforcement had different steel grades, the top reinforcement area will be multiplied by $\frac{f_{y,sup}}{f_{y,inf}}$ and bottom reinforcement strength will be used. Other parameters are summarized on Table 1 and test results are shown in Table 2.

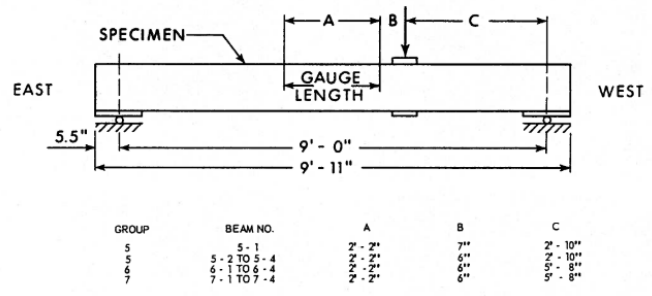


**Figure 18:** Test setup for combined action on beams M5 a M7 [21].

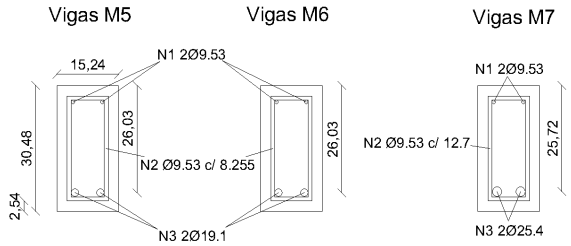


**Figure 19:** M5 to M7 beams cross section (dimensions in cm and bars diameter in mm).

**Table 1:** Other beams' parameters [20], [21]. *Areas multiplied by $\frac{fydsup}{fydinf}$

| Beams | S1 a S7 | M5 | M6 | M7 |
|---|---|---|---|---|
| $f_{yd,inf}$ (MPa) | 475 | 323.4 | 323.4 | 302.0 |
| $f_{yd,sup}$ (MPa) | 475 | 365.4 | 365.4 | 365.4 |
| $f_{ywd}$ (MPa) | 300.3 | 370.25 | 370.25 | 370.25 |
| $f_{cd}$ (MPa) | 30 | 34.47 | 34.47 | 34.47 |
| $b_w$ (cm) | 15.2 | 15.24 | 15.24 | 15.24 |
| h (cm) | 30.5 | 30.48 | 30.48 | 30.48 |
| d (cm) | 26.7 | 26.03 | 26.03 | 25.72 |
| $c_1$ (mm) | 38 | 44.75 | 44.75 | 47.63 |
| $c_2$ (mm) | 24.95 | 30.16 | 30.16 | 30.16 |
| $A_{s,inf}$ (cm2) | 5.73 | 5.73 | 5.73 | 10.13 |
| $A_{s,sup}$ (cm2) | 5.73 | 1.61* | 1.61* | 1.73* |
| $A_{sw}$ (cm2) | 0.79 | 1.43 | 1.43 | 1.43 |
| s (cm) | 10.2 | 8.255 | 8.255 | 12.7 |
| $A_g$ (mm) | 19 | 19 | 19 | 19 |

**Table 2:** Test results [20], [21].

| Beams | $M_{exp}$ (kN · m) | $T_{exp}$ (kN · m) | $V_{exp}$ (kN) | $b_{w,exp}$ (cm) | $h_{exp}$ (cm) | $f_{ccexp}$ (MPa) |
|---|---|---|---|---|---|---|
| S1 | 76.82 | 0.00 | 0.00 | 15.2 | 30.5 | 30 |
| S2 | 0.00 | 13.56 | 0.00 | 15.2 | 30.5 | 30 |
| S3 | 18.81 | 12.42 | 23.13 | 15.2 | 30.5 | 30 |
| S4 | 51.51 | 10.73 | 50.71 | 15.2 | 30.5 | 30 |
| S5 | 0.00 | 0.00 | 151.20 | 15.2 | 30.5 | 30 |
| S6 | 0.00 | 8.93 | 93.41 | 15.2 | 30.5 | 30 |
| S7 | 0.00 | 11.65 | 48.93 | 15.2 | 30.5 | 30 |
| M5-1 | 7.34 | 14.46 | 3.38 | 15.88 | 30.81 | 39.37 |
| M5-2 | 16.16 | 15.93 | 8.41 | 16.21 | 30.81 | 43.92 |
| M5-3 | 31.41 | 14.69 | 17.21 | 15.24 | 30.81 | 41.78 |
| M5-4 | 43.95 | 11.19 | 24.51 | 15.88 | 30.81 | 39.99 |
| M6-1 | 7.34 | 14.57 | 8.05 | 15.88 | 30.81 | 40.40 |
| M6-2 | 16.83 | 16.38 | 18.99 | 15.09 | 30.81 | 40.89 |
| M6-3 | 29.83 | 14.91 | 34.12 | 15.88 | 30.81 | 39.30 |
| M6-4 | 48.24 | 12.09 | 55.38 | 16.21 | 30.81 | 39.44 |
| M7-1 | 6.33 | 12.65 | 6.94 | 15.09 | 30.81 | 41.92 |
| M7-2 | 12.99 | 12.99 | 14.77 | 15.88 | 30.81 | 35.92 |
| M7-3 | 31.07 | 14.91 | 36.07 | 16.21 | 30.81 | 39.30 |
| M7-4 | 57.06 | 14.12 | 66.59 | 15.09 | 30.81 | 36.82 |

### 4.2 Results and discussion

#### S1 to S7 beams

Running the optimization and post-processing algorithms for the beams from Badawy et al. [20], the interaction surfaces were obtained for both standards (Figure 20). These were compared with the AASHTO interaction diagram for the same beams taken from Rahal [19] for validity, shown in Figure 21. The shape and magnitude of the surface is similar, although the drawing projection and the scaling factors were different from the ones used in this article. Due to some inconsistencies between Rahal's interaction surface and Badawy's experimental results, results S5, S6 and S7 were omitted from Rahal's interaction surface when used for validation.

Most of the surface is limited by yielding of ties, with an almost "conical" interaction (circular shear-torsion interaction, with decreasing radius following bending increase). Only with high flexure levels, chord resistance is critical. On AASHTO surface, the active constraint is yielding on the bottom chord. On the NBR diagram, the principal compressive stress check on the top chord was critical. This "extra" constraint prescribed by NBR 6118 chops the tip of the interaction surface when compared to the AASHTO's surface.

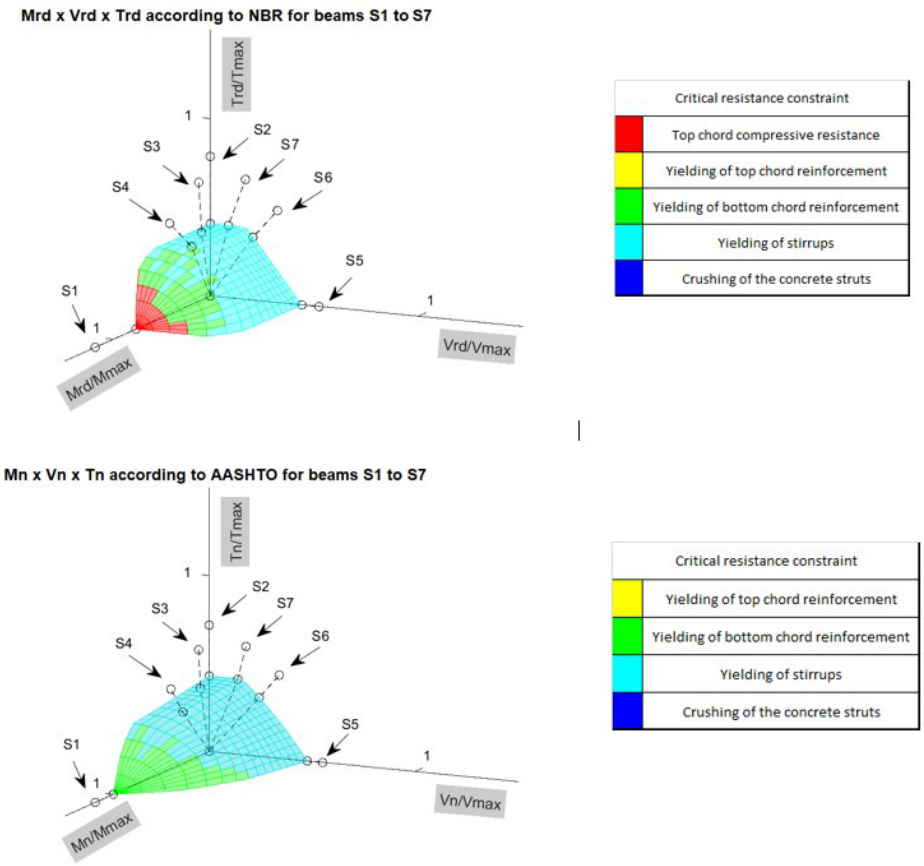


**Figure 20:** Interaction surface according to NBR and AASHTO for beams S1-S7.

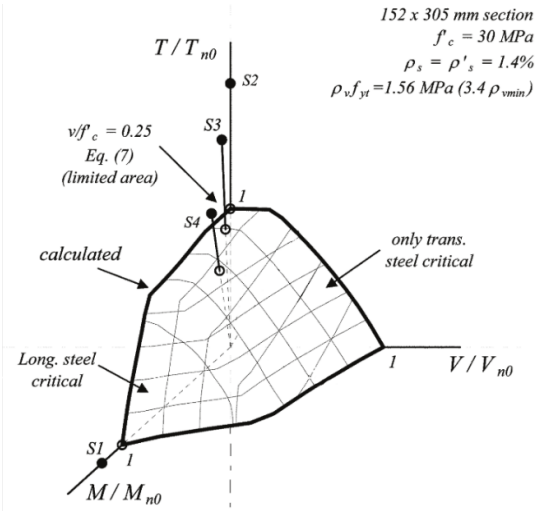


**Figure 21:** Adapted from Rahal's AASHTO surface for beams S1-S4 [19].M5 to M7 beams.

Running the optimization and post-processing algorithms for the beams from McMullen and Warwaruk [21], the interaction surfaces were obtained for both standards (Figure 22 for groups M5 and M6 and Figure 23 for group M7). On these beams, it

was observed a region on the surface (for low levels of flexure) which was limited by the yielding of the top chord, due to a weak top reinforcement. At this area, small increments on the bending moment led to an increase in torsion resistance, as the flexure compression alleviates the tension on the chord. This had been observed in similar situations by Onsongo [22].

For medium levels of flexure, resistance is limited by yielding of ties according to both standards. Beams M5 and M6, with weaker longitudinal reinforcement, show yielding of the bottom chord as critical even on this region, whereas beams M7 have this constraint as critical only in high levels of flexure. On either case, this interaction rapidly escalates for higher bending moments, causing a drastic reduction in shear and torsion resistance. For beams M7, the verification of compressive principal stresses on the top chord is once again critical according to NBR, predicting lower flexure resistance than AASHTO.

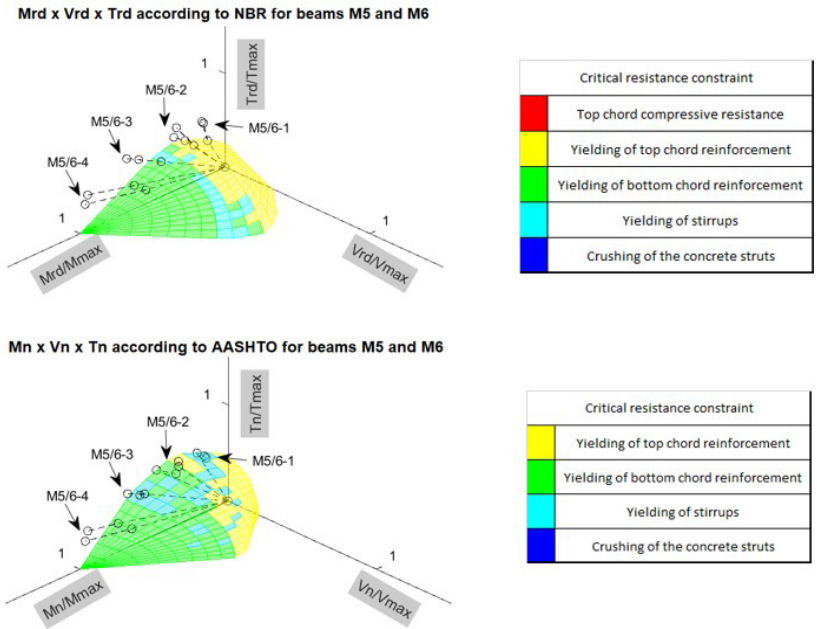


**Figure 22:** Interaction surface according to NBR and AASHTO for beams M5 e M6.

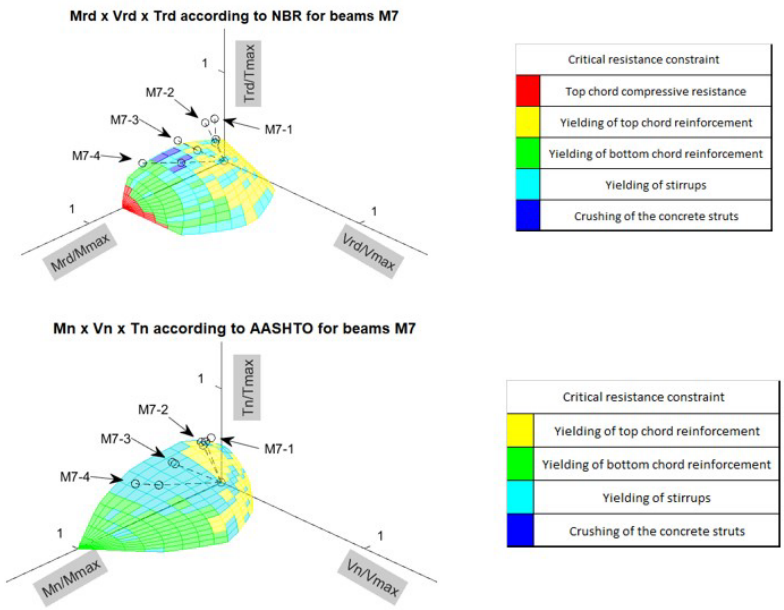


**Figure 23:** Interaction surface according to NBR and AASHTO for beams M7.

## 5 CONCLUSIONS

The proposed optimization method development and application for tested beams using prescriptions from NBR 6118/2014 and AASHTO LRFD 2014 allowed to demonstrate its practicality and validity against results from the literature:

- The procedure was efficient and effective in predicting RC beams resistance under combined action for torsion, flexure and shear.
- The program also illustrated the critical resistance mechanism under interaction, aiding the engineer's decision making.
- The performance of both standards on predicting the interaction response of the RC beams was satisfactory when confronted against experimental data.
- NBR 6118/2014 has a much bigger number of equations, which makes its use more complex and may lead to the application of simplified methods.
- AASHTO LRFD 2014, on the other hand, shows a simple and direct general procedure, that analyzes not only failure but the action-strain response.

## REFERENCES


[1] E. C. Bentz and M. P. Collins, "Updating the ACI shear design provisions," *Concr. Int.*, vol. 39, no. 9, pp. 33–38, 2017. Accessed: Oct. 4, 2021. [Online]. Available: https://www.concrete.org/publications/internationalconcreteabstractsportal.aspx?m=details&ID=51701012

[2] ACI-ASCE 445 Joint Committee, *Recent Approaches to Shear Design of Structural Concrete*. Farmington Hills, MI, USA: American Concrete Institute, 2000.

[3] ACI-ASCE 445 Joint Committee, *Report on Torsion in Structural Concrete*. Farmington Hills, MI, USA: American Concrete Institute, 2012.

[4] T. T. C. Hsu and Y. L. Mo, *Unified Theory of Concrete Structures.* Hoboken, NJ, USA: Wiley, 2010.

[5] K. N. Rahal, "A unified approach to shear and torsion in reinforced concrete," *Struct. Eng. Mech.*, vol. 77, no. 5, pp. 691–703, 2021, http://dx.doi.org/10.12989/sem.2021.77.5.691.

[6] M. P. Collins, E. C. Bentz, E. G. Sherwood, and L. Xie, "An adequate theory for the shear strength of reinforced concrete structures," *Mag. Concr. Res.*, vol. 60, no. 9, pp. 635–650, 2008, http://dx.doi.org/10.1680/macr.2008.60.9.635.

[7] W. Obel, "Interação torque – cortante: avaliação da NBR-6118," M.S. thesis, Universidade Federal de Pernambuco, Recife, Brasil, 2019.

[8] V. B. Almeida, "Data for: Shear-Torsion-Bending Interaction in RC Beams according to NBR 6118/2014 and AASHTO LRFD 2014." 2022. Accessed: Apr. 15, 2022. [Online]. Available: https://doi.org/10.48331/scielodata.ZGNEIO.

[9] Associação Brasileira de Normas Técnicas, *Projeto de Estruturas de Concreto - Procedimento,* NBR 6118*,* 2014.

[10] J. S. Giongo, *Concreto Armado: Dimensionamento de Elementos Estruturais Fletidos Solicitados por Força Cortante*, 1st ed. São Carlos, Brasil: EESC - Departamento de Engenharia de Estruturas, 2011.

[11] M. S. Ibrahim, E. Gebreyouhannes, A. Muhdin, and A. Gebre, "Effect of concrete cover on the pure torsional behavior of reinforced concrete beams," *Eng. Struct.*, vol. 216, p. 110790, 2020, https://doi.org/10.1016/j.engstruct.2020.110790.

[12] J. K. Wight, *Reinforced Concrete - Mechanics and Design*, 7th ed., Hoboken, NJ, USA: Pearson, 2016.

[13] L. M. Pinheiro, C. D. Muzardo, and S. P. Santos, *Estruturas de Concreto*, 1st ed. São Carlos, Brasil: EESC - Departamento de Engenharia de Estruturas, 2003.

[14] J. S. Giongo, *Dimensionamento Considerando o Estado Limite Último de Elementos Estruturais Lineares Submetidos à Ação de Momento Fletor*, 1st ed. São Carlos, Brasil: EESC - Departamento de Engenharia de Estruturas, 2009.

[15] American Association of State Highway and Transportation Officials, *AASHTO LRFD Bridge Design Specifications,* 7th ed. Washington, DC, USA: AASHTO; 2015.

[16] E. C. Bentz, F. J. Vecchio, and M. P. Collins, "Simplified modified compression field theory for calculating shear strength of reinforced concrete elements," *ACI Struct. J.*, vol. 103, no. 4, pp. 614–624, 2006, http://dx.doi.org/10.14359/16438.

[17] E. C. Bentz and M. P. Collins, "Development of the 2004 Canadian Standards Association (CSA) A23.3 shear provisions for reinforced concrete," *Can. J. Civ. Eng.*, vol. 33, no. 5, pp. 521–534, May 2006, http://dx.doi.org/10.1139/L06-005.

[18] M. P. Collins and D. Mitchell, *Prestressed Concrete Structures.* Englewood Cliffs, NJ, USA: Prentice Hall, 1991.

[19] K. N. Rahal, "Evaluation of AASHTO-LRFD general procedure for torsion and combined loading," *ACI Struct. J.*, vol. 103, no. 5, pp. 683–692, 2006., http://dx.doi.org/10.14359/16920.

[20] H. E. I. Badawy, A. E. McMullen, and I. J. Jordaan, "Experimental investigation of the collapse of reinforced concrete curved beams," *Mag. Concr. Res.*, vol. 29, no. 99, pp. 59–69, 1977, http://dx.doi.org/10.1680/macr.1977.29.99.59.

[21] A. E. McMullen and J. Warwaruk, *The Torsional Strength of Rectangular Reinforced Concrete Beams Subjected to Combined Loading*. Edmonton, Canada: The Univ. Alberta, Dep. Civ. Eng.; 1967. Accessed: Oct. 4, 2021. [Online]. Available: https://era.library.ualberta.ca/items/5086dede-150c-43e1-8a0a-8a0a27d5605f/download/04ed74f7-789e-486d-ba8d-aa3b0ddc554b.

[22] W. M. Onsongo, "Failure interaction curves for combined loading involving torsion, bending, and axial loading," *J. S. Afr. Inst. Civ. Eng.*, vol. 49, no. 1, pp. 17–24, 2007.

**Author contributions:** V. B. Almeida: Data curation, Formal analysis, Investigation, Methodology, Visualization, Writing-original draft; B. Horowitz: Conceptualization, Project administration, Resources, Supervision, Validation, Writing-review & editing.

**Editors:** Tulio N. Bittencourt, Guilherme Aris Parsekian

IBRACON Structures and Materials Journal
Revista IBRACON de Estruturas e Materiais
ISSN 1983-4195 ismj.org

REVIEW

# UAV-based inspection of bridge and tunnel structures: an application review

## *Inspeção de estruturas de pontes e túneis baseada em VANTs: uma revisão das aplicações*

Fabio Yukio Toriumi[a]
Túlio Nogueira Bittencourt[a]
Marcos Massao Futai[a]

[a]Universidade de São Paulo – USP, Escola Politécnica, São Paulo, SP, Brasil

Received 08 November 2021
Accepted 09 March 2022

**Abstract:** Bridges and tunnels are large and complex structures that demand periodic inspections to assess their physical conditions. Although both have different designs and constructions from each other, a common problem they share is the drawbacks that their conventional inspections face. Moreover, conventional procedures not only are laborious, time-consuming, and costly, but also involve high and/or hard-to-reach places, often exposing the specialized inspectors to danger. To overcome these problems, the Unmanned Aerial Vehicle (UAV) is being explored to automate these inspections. Recently, the number of researches employing it within the civil infrastructure condition assessment has been growing in recent years, especially for the inspection of large and complex structures. Unlike the UAV-based bridge inspection that already has some review articles available in the literature, there are none yet for the tunnel inspection, to the best of authors' knowledge. Therefore, this article intends to conduct not only a review of the few UAV-based tunnel inspection researches available in the literature, but also an up-to-date review of UAV-based bridge inspection researches. Finally, the key challenges and future trends of the UAV-based inspection of these two structures are discussed, followed by the review conclusions.

**Keywords:** unmanned aerial vehicle, bridge, tunnel, inspection, applications.

**Resumo:** Pontes e túneis são estruturas complexas e largas que exigem inspeções periódicas para avaliar suas condições físicas. Embora ambos possuam projetos e construções diferentes entre si, um problema comum que eles compartilham são as desvantagens que suas inspeções convencionais enfrentam. Além disso, procedimentos convencionais não só são trabalhosos, demorados e dispendiosos, mas também envolvem lugares altos e/ou de difícil acesso, muitas vezes expondo os inspetores especializados a perigos. Para superar estes problemas, o Veículo Aéreo Não Tripulado (VANT) está sendo explorado para automatizar essas inspeções. Recentemente, o número de pesquisas que o empregam na avaliação da condição de infraestruturas civis vem crescendo nos últimos anos, especialmente para a inspeção de estruturas complexas e largas. Ao contrário da inspeção de pontes com VANT que já possui alguns artigos de revisão disponíveis na literatura, não há nenhum ainda para a inspeção de túneis com VANT, até onde os autores saibam. Portanto, este artigo pretende conduzir não somente uma revisão das poucas pesquisas disponíveis na literatura sobre inspeção de túneis com VANT, como também uma revisão atualizada das pesquisas sobre inspeção de pontes com VANT. Finalmente, os principais desafios e as tendências futuras da inspeção com VANT dessas duas estruturas são discutidas, seguidas das conclusões da revisão.

**Palavras-chave:** veículo aéreo não tripulado, ponte, túnel, inspeção, aplicações.

**How to cite:** F. Y. Toriumi, T. N. Bittencourt, and M. M. Futai, "UAV-based inspection of bridge and tunnel structures: an application review," *Rev. IBRACON Estrut. Mater.*, vol. 16, no. 1, elocation, 2023, https://doi.org/10.1590/S1983-41952023000100003

**Corresponding author:** Fabio Yukio Toriumi. E-mail: fabioyt@usp.br
**Financial support:** FDTE, proc. nº BP 1924.04.21.
**Conflict of interest:** Nothing to declare.
**Data Availability:** Data-sharing is not applicable to this article as no new data were created or analyzed in this study.

## 1 INTRODUCTION

Bridges and tunnels are often complex large structures that demand specialized inspectors to perform their inspection and assessment in a nondestructive way, which are performed on-site by visual and physical measurement approaches, whose employment depends on the bridge/tunnel type and the material of its structure.

The visual inspection is the predominant non-contact approach used for these structures, as it will at first indicate any visual changes in their surface, such as the crack existence, which is a primary key sign of a structure failure [1], [2]. As its name says, the structure condition is visually reviewed on-site by the inspector, who will register any visual changes with images taken by a camera.

Other approach examples are the acoustic inspection, where hammers or chains are used to detect delamination or hollow areas in concrete components by analyzing the sound changes across its surface; and the infrared (IR)/thermal imaging inspection, or also referred to as infrared thermography (IRT), which may also be used to detect these defects and indicate material degradation by analyzing the infrared radiation changes along the concrete surface, collected by an IR thermal camera.

Regulations and practices vary worldwide, but for example, the manual bridge inspection in the U.S., administered and regulated by Federal Highway Administration (FHWA), usually requires a local traffic control, where the inspectors need to coordinate an inspection date with the traffic controller in order to ensure safety precautions. It is executed by 2 or 3 inspectors on average, depending on the length and complexity of the bridge, where they visually examine all the components by eyesight and prior experience to look for any defects, flaws or potential problem areas that require maintenance [3]. If any of these failures are identified, they are registered by pictures taken during the visual inspection and a physical inspection with equipment or tools is performed afterwards to quantify the damage. The FHWA requires each bridge to be inspected in a biennial routine, unless that the bridge is rated as structurally deficient, then it is recommended at least an annual routine.

This bridge conventional inspection procedure faces some drawbacks, being the main ones listed below:

- existence of inaccessible areas, usually at height;
- high-costly, as generally requires heavy machinery rental (usually aerial work platforms) to provide temporary access to these areas, in addition to affect the local traffic, as it may require lane closures in the highway bridge/tunnel cases;
- laborious, demanding a great effort from the inspectors to get near some hard-to-reach places;
- dangerous, exposing the inspectors to high and complex places, besides the weather conditions and local environment (as gale, dust, and the nearness of water environment, e.g., above lakes and rivers);
- time-consuming task, since these structures are usually large and complex.

In addition, its inspection results are subjective (dependent on the inspector's knowledge and experience), yielding to low reliability due to possible inaccuracies and failing defect detection [4]. It is worth noting that tunnel conventional inspection procedure face pretty much these same drawbacks.

To deal with them, some solutions are being explored in the literature and applied to aid or even replace some manual activities within the conventional inspection. One of them that is getting more attention is the use of Unmanned Aerial Vehicles (UAVs).

Although some reviews involving the UAV-based bridge inspection topic are already available in the literature, some of them explore a wider area within the civil infrastructure. In contrast, this article not only intends to provide an extensive up-to-date survey focused on previous works that explored the use of UAVs for bridge inspection, including both non-contact and contact based methods, but also includes the UAV-based tunnel inspection topic, about which there is no literature review available yet, to the best of authors' knowledge.

Considering all the above statements, the key goals of this review article are as follows:

1. To review the researches of bridge and tunnel inspections using UAVs, where the main applications are identified.
2. To identify the best practices and solutions to address the UAV-based inspection of this kind of structures.
3. To update this topic by presenting emerging commercial off-the-shelf (COTS) UAVs that are promising and have not yet been considered in the literature.
4. To provide both current key challenges and potential future trends of the UAV-based research in bridge and tunnel inspections.

Totally, 142 literature documents (including journal/conference papers, master's/PhD theses, technical reports, to name a few) were compiled (retrieved mainly from Web of Science, ScienceDirect, and Google Scholar databases, considering a publication year period of 2000 to 2021), being 132 related to bridge topic and 10 to tunnel. Their year of publication are gathered in a clustered bar chart (Figure 1), showing that there was a large increase of published

documents from 2018 onward, indicating a growing interest on UAV employment for inspection of these large structures and its importance in the civil infrastructure field.

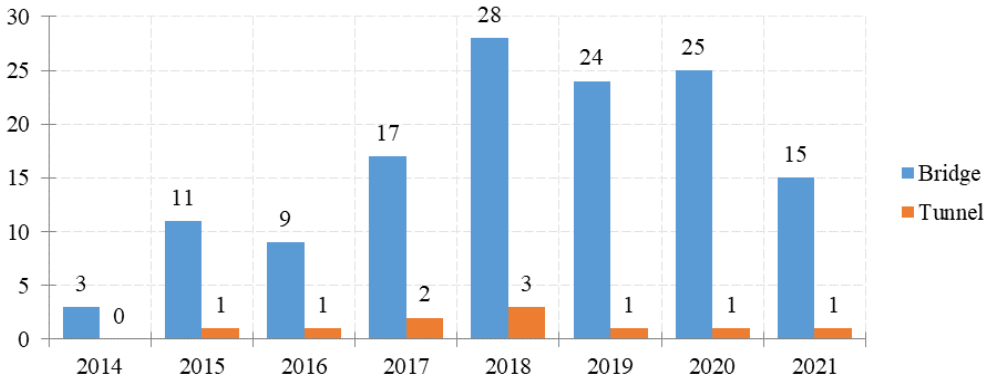


**Figure 1.** Number of documents published through the years concerning bridge and tunnel inspections using UAVs.

## 2 UAV EMPLOYMENT IN LARGE STRUCTURE INSPECTIONS

Besides the usual expressions "UAV" and "drone", there are also other correlated expressions found in the literature, as "Micro Aerial Vehicle" (MAV) and "Unmanned Aerial System" (UAS), this latter being usually composed of an UAV with its payload (the equipment it carries) and the ground control system, accordingly to the Unmanned Aerial Vehicle System Association (UAVSA) [5]. These expressions will be used accordingly to those adopted in each cited reference.

The use of UAVs, especially the multi-rotor types, bring some advantages over the conventional inspection procedure:

- it is safer, as the UAV operator control it remotely in a near safe place, together with the specialized inspector that can conduct the inspection by monitoring the UAV video broadcast or by accessing the collected images/videos later on a device (pc, tablet, to name a few);
- offers more accessibility, since the UAV can easily access hard-to-reach places when compared to the conventional procedure;
- has a relatively lower cost, as UAVs are compact, portable, and low-priced devices in contrast to the rented heavy machinery, as well as the indirect savings, such as the cost reduction associated with traffic control (e.g., lessened lane closure during highway bridge/tunnel inspection, especially the high traffic ones);
- yields reduced time inspection, due to the UAVs high mobility.

Although the research publications concerning the use of UAVs for bridge inspection begin in 2014, as stated in Figure 1, there are other few documents that were previously published, e.g.:

- Metni and Hamel [6], in 2007, that was the first step towards the UAV-based bridge inspection. It evaluated an UAV dynamics for structure monitoring and bridge maintenance, where a control scheme was developed for it under some practical restrictions, and validated the concept of inspecting bridge defects with an UAV equipped with a visual device in an on-site experiment using a small helicopter that flew around a viaduct, in France, while taking a video sequence, from which some pictures have been extracted and presented to bridge inspection experts for evaluation;
- and Moller [7], in 2008, that developed a twin-motor aerial robot called "Aerobot" to carry video cameras up to approximately 61m height to perform close inspection of elevated highway structures (including bridges), but due to some implementation issues, the device was not deployed within the schedule and the project was terminated.

Meanwhile, the UAV technology has had a major breakthrough, especially the multi-rotor types, which are more stable and produce less vibration when compared to single-rotor helicopters [8], being them essential features to collect high quality images.

This way, it was in 2014 that Brooks et al. [8] and Hallermann and Morgenthal [9] demonstrated the multi-rotor UAV capability for large structure inspections in civil engineering field, where all the aforementioned advantages (over the conventional procedure) were also stated. Brooks et al. [8] used a 6-rotor UAV (Bergen hexacopter), mounted with a Nikon D800 camera and a FLIR Tau 2 IR camera, to analyze two overpass bridges in Livonia, Michigan, whose

presented significant structural defects (i.e., spall, crack, and delamination); and Hallermann and Morgenthal [9] tested an 8-rotor UAV (AscTec Falcon 8), equipped with two cameras (Sony NEX-5 and Panasonic Lumix TZ22), to inspect an 80m long concrete arch bridge, whose arch is approx. 40m high, showing that it was possible to fly at short distance from its structure, even at high heights, although the wind played the major role together with the changing lighting conditions along the structure.

After this, the UAV potential for visual inspection assistance became more and more clear as reported in the literature, e.g., Otero et al. [10] showed that the collected images from the UAS, during field tests, and by inspectors, during previous inspections, were of similar quality, and Seo et al. [11] demonstrated that the UAV-enabled inspection of an arch timber stringer bridge provided results almost identical to the conventional inspection report.

Furthermore, recent researches are also exploring the application of the UAV system for contact based inspection procedures, which brings additional challenges involving the development of inspection devices, and the UAV control, once it might interact with the target structure, generating a complex dynamic for the UAV stabilization.

In the following, all these applications are presented through the reviewed documents, which were separated into the tunnel topic (Section 3) and the bridge topic (Section 4).

## 3 UAV-BASED TUNNEL INSPECTION

Although UAV application for tunnel inspections is still unusual (due to the main issues of this kind of environment, e.g., lack of both lighting and global positioning system (GPS) signal), as demonstrated by the lower number of published documents, it has potential since it avoids the mobility limitations [12] as recent technology innovations on UAVs and photographic equipment are continuously being introduced to the field [13], allowing a faster inspection performance, which will be required in the future [14].

A common characteristic found in these few UAV-based tunnel inspection documents is that all of them used custom-built UAVs, needed to overcome the aforementioned issues, e.g., developed UAVs mounted with light detection and ranging (LiDAR), multiple/rotating camera system, lighting source, and GPS-free navigation system. Their information is briefly described in Table 1.

**Table 1.** UAV-based tunnel inspection research efforts.

| Ref. | Custom-built UAV (platform) | Custom-built UAV (payload) | Application scale | Findings |
|---|---|---|---|---|
| [15] | 4-rotor AscTec Pelican | · 1 Hokuyo LiDAR;<br>· LED lights;<br>· 1 inertial measurement unit (IMU);<br>· 1 1.6 GHz Atom Intel processor. | · published in 2015, was the first literature study (to their knowledge) that focused on UAV localization and autonomous control in featureless three-dimensional (3D) tunnel-like environments;<br>· performed field experiments in three different sites:<br>§ in penstocks of both Carter and Allatoona Dams, in Georgia<br>§ in a long building hallway at the University of Pennsylvania. | · although a camera was not used in this research, the experimental results showed the feasibility of the UAV-based inspection of tunnel-like environments, making it a reasonable choice for future inspections by equipping the UAV with onboard cameras;<br>· the proposed approach can be used for other tunnels, as those in transportation networks, besides the penstocks in dams and hydroelectric power plants that were explored in the experiments. |
| [16] | 6-rotor KMel Robotics KHex | · 2 Hokuyo UST-20LX 2D LiDARs;<br>· 4 VGA resolution BlueFox cameras;<br>· 8 10W Cree power-LEDs;<br>· 1 IMU;<br>· 1 Intel i7 NUC board;<br>· other sensors. | · proposed a complete system design to collect detailed images of dark, featureless, symmetric and GPS-denied environments (as inside penstocks and tunnels) for their inspection using fully autonomous MAV;<br>· performed field experiments in penstocks of both Carters and Glen Canyon Dams, from which a 360º panoramic image reconstruction and its 3D visualization were obtained. | · the 360º panoramic image reconstruction and its 3D visualization aid for a convenient inspection of inner penstock and tunnel environments;<br>· a safe autonomy was achieved in dark, featureless, symmetric and GPS-denied environment by fusing the data obtained from the four VGA resolution cameras and the two LiDARs. |
| [17] | 6-rotor DJI-F550 | · 1 Velodyne Puck LITE LiDAR;<br>· 4 Chameleon3 cameras (each rectified with four Cree XHP-50 high-power LEDs);<br>· 1 PixHawk onboard controller (with IMU);<br>· 1 Intel i7 NUC board. | · presented a new approach to achieve autonomous UAV-based inspection of tunnels and penstocks by addressing the navigation, mapping, estimation, and control problems;<br>· performed field experiments in a penstock of Center Hill Dam, where the autonomous and shared control navigation, environment mapping, and state estimation are demonstrated. | · the autonomous navigation was executed by the onboard controller that receives feedback from the proposed estimator while allowing the shared control navigation with an operator even when the UAV is out of his sight, provided by a visual interface that shows him the UAV sensory data in real-time. |

**Table 1.** Continued...

| Ref. | Custom-built UAV (platform) | Custom-built UAV (payload) | Application scale | Findings |
|---|---|---|---|---|
| [18] | 4-rotor DJI-F330 | · measurement component (hammering device and microphone);<br>· traversing component (Zumo Robot platform for Arduino);<br>· control component (wireless communication device, DJI Naza-M Lite flight controller, and a microcomputer);<br>· positioning system (camera). | · developed an onboard hammering device for their custom-built UAV to perform tunnel inspection with the impact acoustic method, where the UAV thrust component push it along a concrete wall and the traversing component enable its movement across the structure, while the impact sounds made by the onboard hammering device are acquired by a microphone for later analysis. | · the proposed mechanism was tested in inclined composite panels, achieving free movement in an angle of inclination up to 15º, and its inspection performance was evaluated with experimental results, where the peak frequency of the impact sound (collected by hitting concrete pieces during flight) was successfully detected, validating the proposed mechanism. |
| [19] | 4-rotor custom frame | · 1 LiDAR;<br>· onboard computers;<br>· other components (not specified). | · aimed to develop a railway culvert inspection tool, composed of the custom-built UAV and the developed control algorithm for semi-autonomous navigation and autonomous alignment of the UAV centroid with the culvert cross section center;<br>· performed field experiments in a built 2.4m long small tunnel with an inner rectangular cross section of 1.38m x 1.5m, where the UAV achieved self-stabilization. | · despite some portion of the LiDAR field of view being obstructed by the UAV frame (as it is positioned in the middle of the frame), it had insignificant impact on the overall system performance;<br>· an adjustment on the UAV flight altitude was required during the experiments to avoid the ground effect (an air cushion generated below the UAV), originated while hovering close to the ground, which was aggravated by the confined space and disturbed the UAV stable flight. |
| [20] | 4-rotor custom collision tolerant frame | · 1 Hokuyo UST-20LX 2D LiDAR;<br>· 1 Kodak PIXPRO SP360 4K omnidirectional camera;<br>· 1 high power LED;<br>· 1 StereoLab ZED stereo camera;<br>· 6 TeraRanger One range sensors;<br>· other components. | · attempted to address the inspection problem of human inaccessible tunnels with UAV autonomous navigation and collection of visual data inside these environments;<br>· performed both simulations in gazebo and field experiments in a hydraulic tunnel. | · the autonomous navigation was achieved by using the stereo camera, even when losing communication over long tunnel stretches;<br>· the omnidirectional camera with ultra-wide view angle was able to capture visual image of the inner tunnel wall condition, even inside dark environments. |
| [21] | 4-rotor custom frame | · 1 developed rotating camera system (integrated with high luminance LEDs);<br>· 6 TeraRanger One range sensors;<br>· 1 LightWare SF11/C laser altimeter (down-pointing);<br>· 1 Pixhawk 2.1 flight controller (with IMU);<br>· 1 Intel Edison (as a companion computer);<br>· other sensors. | · designed and developed a novel UAV (called "SWIRL" - Surveyor With Intelligent Rotating Lens) and imaging system for deep tunnel network inspection, where a novel rotating camera system perform spiral panoramic imaging (tested and validated in a field experiment at Connaught Drive underpass, Singapore);<br>· performed both simulations using Gazebo and two field experiments to evaluate the UAV autonomous flight:<br>§ in a covered section at Eu Tong Sen Canal (to evaluate the horizontal traveling through a poor illuminated tunnel);<br>§ in an entry shaft of the Deep Tunnel Sewerage System in Singapore (to evaluate the vertical traveling in shafts). | · the limited data required by the proposed location method resulted in a relative lower UAV payload and power consumption, yielding to more than 35min of autonomous flight time;<br>· during the field experiment in the entry shaft, its constant high velocity updraft, together with the turbulence generated by its enclosed environment, acted negatively on the UAV flight performance, rising its positioning error. |
| [22] | 4-rotor custom frame | · 1 GoPro Hero4 camera (mounted on a rotating system with light source);<br>· other components (not specified). | · proposed a method that exploits Bundle Adjustment, Structure-from-Motion and available geometry priors to robustly estimate the GoPro Hero4 camera pose, which is rotated 360º around the shaft of the custom-built UAV, to take a sequence of images while the UAV traverses tunnel-like environments, in order to perform panoramic cylindrical views and fully-dense 3D reconstructions;<br>· performed field experiments in an underpass, where the rotating camera system was mounted on a tripod stand and three different datasets were collected to evaluate the proposed method, whose results were compared with the Multi-View Reconstruction Environment method. | · the proposed method allowed the use of as few images as possible to reconstruct a fully-dense 3D scene by using the prior knowledge of local geometry (e.g., the tunnel cross section diameter), enabling this way a pre-configuration of the UAV speed for an efficient image capture. |

**Table 1.** Continued...

| Ref. | Custom-built UAV (platform) | Custom-built UAV (payload) | Application scale | Findings |
|---|---|---|---|---|
| [23] | 4-rotor custom frame | · 1 2D rotating RPLIDAR (range measurement);<br>· 1 LIDAR-lite v3 (height measurement);<br>· 1 GoPro Hero7 camera;<br>· 2 10W LED light bars;<br>· 1 PX4Flow optical flow sensor (velocity estimation);<br>· 1 Aaeon UP-Board processing unit (with an Intel Atom x5-Z8350 processor, and ROSflight controller). | · used a ROSflight based custom-built MAV (developed by Luleå University of Technology) to rapidly explore unknown areas while providing feedback to the operator, for which a framework focusing on MAV navigation, control and vision is proposed;<br>· performed field experiments in a dark underground mine in Sweden, located at 790m deep, where three different test cases (in a 150m long tunnel area with a cross section of 6m x 4m) evaluated the feasibility and adaptability of the proposed framework. | · the proposed framework allowed flexibility and modularity on the MAV system by proposing two different approaches for its navigation (one depending on the 2D LiDAR measurements, and the other on the camera image streams), which accomplished the autonomous flight, and by assigning different sensors to the state estimation;<br>· the field experiments demonstrated the capability of low-cost and resource-constrained MAVs to navigate in tunnel confined environments. |
| [24] | not specified | · 1 high definition camera;<br>· 1 fill light;<br>· other components (not specified). | · presented a real-time defect detection (focused on exposed rebar) of spillway tunnels using UAV and deep learning;<br>· performed field experiments in a spillway tunnel of a hydro-power station in the Minjiang River, where the UAV collected images within a specified area, whose siltation, stagnant water, and light conditions yielded to challenges for image collection. | · the proposed deep learning method allowed a relative reduction of its model size and parameter numbers, yielding to a better real-time performance, which is a key feature for future onboard UAV application. |

Among them, only Iwamoto et al. [18] focused their UAV development research for a contact based inspection (impact acoustic method), while the other authors regarded the camera-based visual inspection [16], [20]–[22], [24] and concerned the UAV positioning/localization and/or environment mapping, based on LiDAR [15], [17], [19], [23].

## 4 UAV-BASED BRIDGE INSPECTION

Regarding now the UAVs used for bridge inspections in the literature, they can be divided into three groups: 1) the literature review articles, 2) the ones that made initial evaluation studies of the topic (or were at early research stage), and 3) the ones that performed case studies with practical tests.

Beginning with the review papers, nine addressed literature reviews involving UAV-based bridge inspections:

- Dorafshan and Maguire [5] presented the state of practice for the U.S. bridge inspection programs, where the autonomous navigation, 3D model reconstruction, and automated damage inspection were some of the covered topics, together with a summary of both U.S. Department of Transportation (DOT) investigations and the Federal Aviation Administration regulations on UASs. It concluded that despite the existing challenges involving UAS-assisted bridge inspections, it has the potential to improve inspection accuracy at a relatively lower cost;
- Duque et al. [25] provided a review on visual inspection, monitoring, and analysis of infrastructure using UAVs, where the bridge inspection topic was also summarized. It concluded from the findings that the UAV results are satisfactory, leading to a more efficient visual inspection in a lower time when compared with the conventional inspection procedure;
- Agnisarman et al. [26] reviewed literature publications that investigated automated visual inspection technologies applied for civil infrastructures, including the UAV-based bridge inspection. It identified that the inspection of bridges is the most frequently addressed domain among the automation-assisted inspection applications (20 of 53 reviewed studies), reflecting the importance of its structure maintenance and repair;
- Greenwood et al. [27] summarized the UAV development efforts on civil infrastructure applications, where one of the discussed topics was the key cases of UAVs being used in bridge inspection and monitoring. It stated that, among the civil infrastructure monitoring, bridge inspection is the most widely approached topic for UAV integration;
- Sony et al. [28] presented a review of next-generation smart sensing technology (such as UAVs, robotic sensors, cameras, and smartphones) applied for structural health monitoring, where the bridge inspection topic was discussed within the UAV-based literature section;
- Ahmed et al. [29] examined recent developments in autonomous robotic platforms for NDE and structural health monitoring of bridges, where UAV-based non-destructive inspections were addressed. It stated that it is a relatively new field of research, where its flexibility and versatility need to be exploited in order to access and monitor the distinct bridge infrastructure parts;

- Outay et al. [30] concerned three major domains of transportation: road safety, traffic monitoring, and highway infrastructure management; where the advancements of key feature extraction from UAV collected images/videos by computer vision algorithms were addressed. Within the highway infrastructure management topic, some research efforts that used UAVs for bridge inspection and monitoring were briefly summarized;
- Jeong et al. [31] summarized the literature central findings on UAV techniques for bridge inspection and damage quantification, where both conventional UAV-enabled visual inspection and damage detection algorithm studies were briefly described. It concluded that UAV can be considered for bridge inspection as a feasible and efficient tool, and a continued interest in it is expected;
- and Feroz and Abu Dabous [32] conducted a review of UAV applications in bridge condition monitoring, based on remote sensing technologies (such as LiDAR, IR and visual imagery, in addition to other sensors), where sixty-five journal and conference papers were compiled and summarized. It concluded that the use of UAVs improved the cost efficiency and accessibility, while reducing safety hazards and avoiding traffic closures during the inspection process.

Within the group that made initial evaluation studies, composed of [33]–[42], although they were at early stage from a practical point of view, some important details were discussed, such as the necessary specifications and payloads of the UAV, the flight mission planning considerations (including the on-site risk evaluation, the protocols to be followed by the operator, and the bridge data collection), together with the main advantages and challenges of the UAV-based bridge inspection applications.

Lastly, considering the ones that performed practical inspection tests, the used UAVs were identified and listed in Table 2, together with their models, approximate flight time (depending on the UAV series model, its payload, battery lifetime, and environmental conditions, as temperature and weather), and the used cameras.

**Table 2.** UAVs used for bridge inspection found in the literature.

| Model (type) | Cameras (resolution) | Flight time (approx.) | References |
|---|---|---|---|
| SenseFly Albris (4-rotors) | Int.* (38MP /1280x720 video); IR (80x60 video). | up to 22min | [43]–[45] |
| 3DR Iris (4-rotors) | GoPro Hero 3 or 4 Series (5~12MP/ 1080p~4K video). | 10~13min | [46]–[49] |
| DJI Mavic Series (4-rotors) | Int. (12~48MP/ 1080p~4K video). | 21~31min | [46]–[56] |
| DJI Phantom 3 Series (4-rotors) | Int. (12~12.4MP/ 1080p~4K video). | 23~25min | [45], [57]–[59] |
| DJI Phantom 4 Series (4-rotors) | Int. (20MP/ 4K video). | 27~30min | [11], [50], [51], [55], [60]–[70] |
| DJI Inspire Series (4-rotors) | Zenmuse X Series (12.4~24MP/ 4K video); IR - FLIR Vue Pro (640x512 video). | 18~27min | [71]–[75] |
| DJI Matrice 100 Series (4-rotors) | Zenmuse X Series or Zenmuse Z3 (3.5x Optical Zoom). | 19~40min | [76], [77] |
| DJI Matrice 200 Series (4-rotors) | Zenmuse X Series or Zenmuse Z30 (30x Optical Zoom). | 13~38min | [78]–[82] |
| DJI Matrice 600 Series (6-rotors) | Zenmuse X Series; Fujifilm GFX 50S (51.4MP/ 1080p video). | 16~40min | [50], [51], [55], [83]–[87] |
| Bergen Hexacopter (6-rotors) | Nikon D800 (36.3MP/ 1080p video); IR - FLIR Tau 2 (640x512 video). | 18~30min | [8], [88], [89] |
| Intel/AscTec Falcon 8 (8-rotors) | Sony NEX-5 (14.2MP/ 1080i video); Sony Alpha 7R (36.4MP/ 1080p video); Panasonic Lumix TZ22 (14.1MP/ 1080i video). | 12~20min | [9], [90], [91] |
| Other COTS | ---------- | ---------- | [92]–[104] |
| Custom-built | ---------- | ---------- | [10], [47]–[49], [105]–[131] |
| Not specified | ---------- | ---------- | [132]–[151] |

* IR = infrared camera; Int. = Integrated camera.

One can see from Table 2 that the COTS DJI models [152] are predominant in the applications, together with the custom-built ones, whose were developed by researches within academic institutions or by collaborating companies, not to mention the UAVs that were not specified in their papers.

These UAV applications can be divided into two main groups, the non-contact and contact based methods, described in the sequence.

### 4.1 Non-contact based inspection applications

The majority of the applications, listed in Table 2, are non-contact based methods, where the predominant one is the visual imagery, which consists in acquiring images, videos, and other visual information. Within it, there are two main approaches: the visual and the infrared inspections.

#### 4.1.1 Visual inspection applications

In the visual inspection, considering the UAV application, the inspector search for any visual structural changes in the images/videos collected by the UAV cameras, either on-site or later in a device. Although this type of application has all the UAV benefits listed in Section 2, the defect detection still relies on the specialized inspectors, whose similar subjective and inaccurate results from the conventional procedure still remain unsolved. Another method used to tackle this problem is the automatic inspection (or the term "vision" is also commonly used), where image processing techniques are specifically developed to detect and/or identify the structural defects in the images/videos collected by the UAV cameras.

All these visual inspection applications are listed in Table 3, where they are separated within the structure material of the bridge and their related defect types.

**Table 3.** Structural defect detection researches in UAV-based bridge visual inspection applications.

| Structure material | Defect type | Inspection type | |
|---|---|---|---|
| | | (manual) | (automatic) |
| Concrete | Crack | [10], [11], [43], [45], [54], [58], [62]–[65], [67], [80], [81], [117], [130], [137] | [46]–[48], [50]–[53], [55], [56], [60], [61], [68], [71], [74], [76], [78], [90], [96], [104]–[112], [115], [116], [131]–[136], [143], [150] |
| | Spalling | [11], [62]–[65], [67], [81] | [60], [61], [105], [106], [108], [115], [132], [134] |
| | Efflorescence | [10], [11], [43], [45], [54], [58], [62]–[65], [67], [81] | [60], [132] |
| | Exposed rebar | [11], [62], [64], [65], [67], [70] | [60], [108], [115], [150] |
| | Generic/others | [10], [11], [54], [62]–[65], [67], [80], [81] | [60], [108], [132], [150] |
| Steel | Corrosion | [10], [11], [45], [54], [62]–[65], [67], [70], [101], [102] | [96], [100], [109], [138], [147], [150], [151] |
| | Crack | [49], [54] | [48], [100], [138] |
| | Paint failure | [45], [80], [149] | [138] |

It can be seen that the most explored defect type:

- in concrete structures is the crack, as expected, since it is the main visual warning for a possible failure;
- and in steel structures is the corrosion, as it is one of the main defects that arise in this type of material due to its exposure to environmental conditions (as temperature and humidity, to name a few);

and the most employed technique within the automatic inspection is the deep learning, whose popularity in the literature has been increasing due to its advantages, such as the simultaneous detection of multiple different defect types, e.g., [60], [100], [108], [115], [150].

Despite the defect detection/identification, there are other UAV applications for aiding visual inspection, such as 3D reconstructions [43], [45], [48], [50], [51], [55], [60], [66], [70], [71], [74], [76], [90], [91], [98], [99], [105], [106], [118], [142] and damage quantification [63], [66], [67], [69], [71], [80], [81], [81], [96], [108], [131], [136], [140], [143].

Another emerging imaging-based application with UAVs is the displacement/deformation measurement techniques of bridge structure, e.g., photogrammetric computer vision [9], [83], [89], [97], [146] and digital image correlation (DIC) [79], [92]–[95], [148]. Despite these imaging-based techniques, it is also worth mentioning the use of Laser Doppler Vibrometers (LDV) in UAVs as a non-contact sensor to measure bridge displacements [84]–[86].

#### 4.1.2 Infrared inspection applications

Unlike the aforementioned great number of visual applications, the IR inspection is still underexplored within the UAV applications, although IR images of bridge decks are already commonly used during conventional bridge

inspections to obtain information on subsurface defects, like concrete delamination [103]. Some few researches that explore this nondestructive method are briefly described below:

- Brooks et al. [8] and Escobar-Wolf et al. [88] used the FLIR Tau 2 IR camera, installed on the Bergen Hexacopter, to detect six delamination areas on the inspected bridge deck, where a total of seven delamination areas (all without visible signs) had been spotted before with a handheld FLIR SC 640 IR camera, whose presence were confirmed with a hammer test, i.e., only one delamination area was not found with the UAV IR imagery. Then, their proposed method improves the classification by also including the images collected by a Nikon D800 camera (also installed on the UAV) in the analysis;
- Zink and Lovelace [103] tested the integrated IR camera from the Aeyron Skyranger UAV in one of the evaluated bridges, where the collected IR images clearly showed the thermal gradient at the deck beam locations;
- Khan et al. [119] and Ellenberg et al. [120] performed experimental investigations on a mock-up concrete bridge, where a hexacopter based on DJI F550 frame (equipped with a GoPro Hero3 camera and a FLIR TAU2 IR camera) was used to map it using a multispectral approach, consisted of visual and IR imaging. While Khan et al. [119] presented the collected UAV images that clearly showed three delaminated regions on the mock-up, Ellenberg et al. [120] used a gradient following algorithm to identify the delaminated regions;
- Ellenberg et al. [141] used a commercially available six-rotor UAV equipped with both GoPro Hero3+ silver edition camera and IR camera (FLIR Tau 2) to collect real-time video imagery from a bridge deck mock-up (an eight inch thick concrete slab, supported by three structural steel I-beams) with multiple pre-manufactured defects (including delamination instances) for field testing, in which the collected IR images/videos were sufficiently clear for their developed image post-processing algorithm to identify the delamination locations;
- Omar and Nehdi [72], [75] mounted an IR camera (FLIR Vue Pro) on a DJI UAV (Inspire 1 Pro) to detect subsurface delamination in concrete bridge decks, where the feasibility of the proposed system was investigated in two full-scale in-service reinforced concrete bridge decks and demonstrated by comparing its results with other nondestructive testing technique results (including hammer sounding and half-cell potential testing), where the defect regions identified by the proposed system were confirmed;
- Wells and Lovelace [44] detected deck delamination with good accuracy in one of the on-field bridge inspections with an onboard thermal sensor of the SenseFly Albris UAV, whose results were validated by comparing them with the ones obtained by a handheld FLIR thermal camera, where the delamination areas were previously located and marked with the chain dragging method;
- Hiasa et al. [57] tested a FLIR T420 IR camera (a handheld IR camera that is not intended for UAV application) attached to a DJI Phantom 3 Advanced UAV using gummed tape, where it was examined if the vibration of the UAV during a hovering flight would affect the images taken from the IR camera (e.g., generate blurred images). They showed that it was possible to capture clearly lattice pattern squares from 1m to 5m range, concluding that if even in this test was possible to capture the target without blurry, then other IR cameras meant for UAV application are also capable, as they are typically used with a gimbal (that mitigates the vibration effects). It is worth noticing that the test was made during hovering flight, i.e., the flying speed during UAV motion may still affect the IRT results, e.g., for a video application;
- Mac et al. [82] conducted experiments on a concrete specimen (emulating a bridge deck surface) with artificial delamination, where two methods were employed to capture its surface temperature: a professional handheld IR camera (FLIR SC660) and a DJI M200 UAV equipped with IR camera (FLIR Zenmuse XT2). A good agreement was observed between their results, which validated the UAV application;
- Jang et al. [153] presented a deep learning based concrete crack detection using hybrid images, where a hybrid image scanning system was developed to combine vision and IRT images for unmanned vehicle, in which an integration with UAVs is in progress by the process of miniaturization and packaging of the developed system to reduce its size and weight for mounting it onto a custom-built sticking-type UAV;
- and Cheng et al. [87] developed a customized deep learning model based on encoder-decoder to segment concrete delamination areas in thermal images at the pixel level. This model is validated with experiments conducted in an in-service concrete bridge, where two UAV configurations were employed to take both thermal and visible images, being the thermal camera (FLIR A8300) mounted on a DJI Matrice 600.

Most of them involved automatic inspection methods, where distinct image processing algorithms were developed to mainly detect the delamination areas, being on the other hand [44], [57], [82], [103], [119] based on manual inspection or other analysis methods.

### 4.2 Contact based inspection applications

Although UAVs are being widely used for non-contact inspections, especially the image-based ones, as can be noticed above by the number of documents available in the literature, they are also still underexplored for contact inspection tasks. It is mainly due to the challenges that this type of methods involves, requiring specific device developments to be installed onboard the UAV, hampered by its limited payload capacity, along with the requirement of a more sophisticated control algorithm to deal with the complex dynamics derived by the interaction between UAV and target structure.

There is still no COTS UAV available for contact based inspection and both research and development are necessary to overcome these challenges. Thus, there are few documents in the literature that developed custom-built UAVs focused on dealing with this problem.

An example is the displacement or strain measurement application, for which the custom-built UAVs in Sanchez-Cuevas et al. [113], [114] and Jimenez-Cano et al. [122] were developed. Different from the previously visual-based ones, these UAVs rely on a reflector prism (360º miniprisms) installed in their structure, to perform the bridge inspection while in contact with its ceiling, where a total station (Leica Geosystem MS50) continuously tracks the prism position, from which an estimation of the bridge deformation can be obtained. Additionally, the ceiling effect (arisen when the UAV gets close to the bridge ceiling) is exploited to improve the UAV flight performance, where the increment in rotor thrust (derived from this effect) is explored by the developed UAV control while keeping the UAV stable and preventing it from crashing into the ceiling.

Another example is the acoustic inspection application, performed by the custom-built UAVs developed in Chun et al. [109], Mason et al. [144], and Moreu et al. [145], whose onboard hammering device systems were developed to perform both impact and sound recording for post-processing analyses of concrete structure assessment. Besides that, the implementation of onboard manipulators on UAVs, both 1 Degree-of-Freedom (DoF) ones (explored in Ikeda et al. [124] and Ichikawa et al. [126]) and 3 DoF ones (in Jimenez-Cano et al. [123] and Ikeda et al. [125]), may not only be employed for this kind of test, but also for other contact based inspection applications, where a specific device may be manipulated by these UAVs.

## 5 DISCUSSION OF THE REVIEWED LITERATURE

Following the above description of UAV-based application researches for bridge and tunnel inspection, it would be interesting to have an overview of these main applications. To aid this, the following pie charts (Figure 2) are presented.

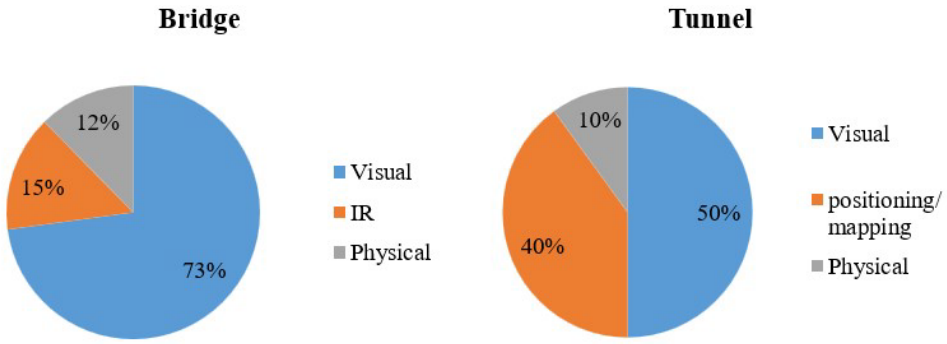


**Figure 2.** Percentage of the main UAV-based applications for bridge and tunnel inspection.

It is evident that the most employed application is the visual inspection, corroborating with the statements made previously in Subsection 4.1. It was expected since this is also the main employed method in the conventional procedure and the availability of lightweight high-definition cameras (especially the on-board/integrated ones on COTS UAV platforms) enable a good quality inspection. Although in the tunnel case it is not as expressive as in the bridge case, the visual inspection still represents half of UAV-based tunnel applications, followed by the ones focused on LiDAR-based UAV positioning/localization and/or environment mapping, since the lack of GPS signal in this environment is still a main challenge.

Note that, within all the UAV-based inspection applications, it was employed either manual or automatic flight navigation, where in the former the operator manually controls the UAV position during the inspection process, and in

the latter a pre-determined trajectory is programmed and uploaded in the UAV, so that it can automatically navigate on-site, where the operator supervise it during all the inspection and may intervene it by taking the UAV control, if any unexpected external event occurs.

It is worth emphasizing the difference between automatic and autonomous flight navigation. While the former is developed to reduce the human intervention during its operation to a minimum, the latter does not allow any human intervention during its flight mission, being independent and self-governing while coping with all unforeseen and unpredictable situations that may happen during its navigation. Currently, UAV regulations of many countries do not allow autonomous flight navigation in open airspace since it is still immature and may pose risk to itself and to all of its surroundings. However, this may change as this development becomes more mature and ensures more security during its operation.

Despite the flight navigation mode, it was shown in Section 2 that UAVs provide several advantages over the conventional inspection of bridge and tunnel structures, overcoming the main drawbacks related to their procedures (described in Section 1), e.g., the UAV enable the access and assess of dangerous and/or tight spots that are inaccessible to humans [20], [130].

However, the use of this type of technology also brings some challenges, as described in the following.

### 5.1 Key challenges

The use of UAVs presents some challenges/limitations as:

- the flight planning, which requires a specialized UAV operator (who needs to be trained and certified to ensure a safe UAV operation) to conduct a manual flight or even to attend an automatic flight (which requires a previously developed path planning) to inspect the on-site structure, along with the evaluation of the environment and weather conditions, which may preclude the flight mission, e.g., gale and heavy rain;
- limited flight time and payload capacity, which varies for each UAV platform, requiring some extra batteries for long structure inspections;
- the noise on collected images, derived mainly from the local conditions, e.g., dust, changing lighting conditions along the structure, and wind disturbances during UAV flight (that may lead to blurry images);
- the existence of GPS-denied areas, whose hinder the UAV navigation, precluding the inspection of structure components at these areas, e.g., at tunnel environments and underneath large bridges;
- and the regulations of governing authorities for UAV operation, which varies from country to country [34].

However, they are continuously being dealt with by the researchers of the area, as the research and development of autonomous flight that provide high accuracy positioning to collect images without blurry effects, along with the UAV technology advancement (e.g., energy-efficient UAV platform designs, enhanced batteries, and GPS-free flight capability) and also the regulations improvement by the associated government agencies in charge.

Concerning the UAV-based tunnel inspection, as stated in Section 2, the major challenges are the lack of both light and GPS-signal, which were mainly overcome by custom-built UAVs developed in the few literature documents (see Table 1), besides some of them being inaccessible by humans, where the UAV must do its inspection out of the operator view, making the task even more challenging (e.g., problem tackled by Özaslan et al. [17] and Hongyu [20]).

Likewise, among the main challenges of UAV-based bridge inspection, the underside deck can be mentioned, which is one of the most problematic areas to perform the inspection by an UAV. Some few examples that designed UAVs to overcome this problem are Sanchez-Cuevas et al. [113], [114] and Jimenez-Cano et al. [122], whose UAV platforms explore the ceiling effect when in contact with it in a fixed position during an under-bridge inspection, and Wang et al. [112], whose tethered creeping UAV platform ensures the distance between the camera and the bottom of the bridge for an accurate crack detection. Other examples related to this problem are Yang et al. [117] and Peng et al. [131] that mounted a camera in an upward gimbal on the top of their UAVs (solution that are also being provided by some specific COTS UAVs, mentioned in Subsection 5.2).

However, its main issue is again the lack of GPS signal, especially at large bridges. Dorafshan et al. [48] not only summarized some instances during state DOT missions, but also underwent it during their field experiments, where though the built-in sonar sensors, installed on the bottom of their DJI Mavic, allowed the operator to substantially control it while flying under the bridge (in absence of GPS signal), some instability occurred when flying over the river, precluding the under-bridge inspection over this region. Other authors have also reported this issue, e.g., [5], [103], [113], [117], [127], [128], for which an auxiliary positioning system is required, such as other position estimation approaches (as optical flow and visual odometry techniques) and/or other technologies (as LiDARs and image based navigational sensors).

At last, but not least, the success of the UAV-based inspection task rely on the UAV flight parameters (e.g., the distance between the UAV and the structure), the payload choice (the sensors and instruments carried by the UAV) and their parameter configuration (e.g., the high definition camera settings, as the shutter speed, aperture, and ISO), which may be cumbersome even for experienced UAV operators.

### 5.2 Future trends

Throughout the survey, an identified trend regarding the UAV-based inspection of both tunnels and bridges is the development of automatic flights and even semi-autonomous navigation that are being explored by some of the research studies. This will lead to a future trend of completely autonomous UAV navigation, which will play an important role to enable the automation of the inspection procedure.

Seeing this and the rapid advance on UAV and remote sensing technologies, together with the development of advanced control and navigation, another expected future trend is the multi-UAV cooperation, whose collected multi-data will not only improve the efficiency and performance of the inspection, but also decrease the execution time.

Before this, a trend provided by the rapid advancement of UAV technology is the emerging of COTS models focused on inspection tasks, which are probably already being used in current researches of UAV-based inspection of this kind of structures. Some examples of these 4-rotors UAVs are:

- the DJI Mavic 2 Enterprise Series (launched on October 29, 2018) [154], which is based on the Mavic 2 flight platform (with same 31min flight time), but with new features, as the modular accessories (spotlight, speaker, and beacon), the camera upgrades (in which the IR camera addition, available in Dual and Advanced series, is highlighted here), and the add-on Real Time Kinematics (RTK) module for the Advanced series only;
- the collision-resistant Flyability Elios 2 (launched on April 29, 2019) [155] (with up to 10min flight time) that has a protective frame as a distinctive feature (a carbon fiber spherical cage that encloses the UAV, protecting it from collisions up to 1.5 m/s), in addition to embeds both 12.3MP camera (that records 4K videos) and Lepton 3.5 FLIR IR camera (160x120 video), together with onboard LEDs that provide 10K lumens of light with a remotely adjustable intensity;
- and the DJI Matrice 300 Series (launched on May 7, 2020) [156] (with up to 55min flight time), compatible with more Zenmuse Series cameras (including powerful full-frame, optical zoom, and IR options) and supporting an upward gimbal, in addition to have the RTK module available.

Although some UAV model comparatives were made in the literature, e.g., [5], [25], [51], the aforementioned models had not been released yet.

Considering all the presented UAV models (Table 2 and the aforementioned ones), the authors highlight here two of them: the DJI Matrice 210 RTK V2 and the DJI Matrice 300 RTK, since they support not only both IR camera and RTK module (which are desirable features for this kind of inspection), but also an upward gimbal, which is a highly recommended feature for both tunnel and underside bridge deck inspections. Although DJI Mavic 2 Enterprise Advanced also provide both IR camera and RTK module, it does not offer the upward gimbal option, but its relative lower price makes it a good alternative. At last, but not least, it is worth mentioning the Flyability Elios 2, whose protective frame and GPS-free flight capability are strong features to also inspect complex and confined indoor spaces, being a great option especially for tunnel inspections.

The IR camera availability is emphasized since the use of hybrid image processing (in this case, the fusion of infrared and visible images) will provide more information to the inspection process, where their individual advantages can be explored to improve the defect detection. Moreover, other sensors may also be explored in this kind of approach, such as the ultrasonic displacement sensor (to provide a distance measurement from the target structure) [157].

## 6 CONCLUSIONS

There has been a rapid increase in the number of researches on UAV-based inspection applications in civil infrastructure field, especially for large and complex structures, promoted by the fast advancing electronics technology that is aiding the development of powerful custom-built UAV platforms and also enabling the emergence of COTS UAV solutions focused on inspection tasks. They bring several benefits over the conventional procedures of bridge and tunnel inspection, such as more accessibility and safety, along with a reduced cost and inspection time, overcoming the main drawbacks faced by them, which are practically the same for both.

This review article has gathered and surveyed both UAV-based inspection researches of bridges and tunnels, and the main applications have been identified, whose relevant information were summarized in detailed tables to provide

a convenient overview of their state-of-art. This includes the several identified COTS UAV platforms that were employed for bridge visual inspection and the diverse custom-built UAVs developed specifically for tunnel inspection.

Although the challenges for both bridge and tunnel UAV-based inspections are practically the same, it is worth to emphasize that the lack of lighting and GPS signal in tunnel environments are far more critical when compared to the bridge case, as in the latter these regions are relatively smaller (usually under its deck), where it is still possible to collect images with some UAV platforms that can point the camera in an angular way towards the bottom of the deck. Consequently, the percentage of researches focusing on positioning and mapping in tunnel environments is still expressive (see Figure 2).

It also has shown that the current main employed application is the visual inspection, boosted by the great number of available lightweight high-definition cameras, especially the on-board/integrated ones on COTS UAV platforms, which provide high quality images and enable an inspection result of similar quality from the conventional procedures.

Despite the still existence of some limitations that hinder the applications of UAV-based inspection of large structures, such as the existence of diverse UAV regulations that vary for each country and the weather conditions that may preclude and delay the on-site inspection execution, some other challenges are being overcome by the fast advancing of UAV and remote sensing technologies, together with the development of advanced control and navigation, which may enable some new future possibilities such as the automatic condition monitoring of these structures, where an UAV will autonomously execute a periodic inspection with a precise positioning during the path-planned trajectory, and the collected data from different sensors will be evaluated and compared with the previous ones, yielding to a shorter-time assessment and a better maintenance management.

## ACKNOWLEDGEMENTS

The authors would like to thank Fundação para o Desenvolvimento Tecnológico da Engenharia (FDTE) for their support.

## REFERENCES

[1] B. M. Phares, D. D. Rolander, B. A. Graybeal, and G. A. Washer, "Reliability of visual bridge inspection," *Public Roads*, vol. 64, no. 5, pp. 22–29, 2001. Accessed: Mar. 30, 2021. [Online]. Available: https://trid.trb.org/view/683631.https://trid.trb.org/view/683631

[2] S. Stent, R. Gherardi, B. Stenger, K. Soga, and R. Cipolla, "Visual change detection on tunnel linings," *Mach. Vis. Appl.*, vol. 27, no. 3, pp. 319–330, 2016, http://dx.doi.org/10.1007/s00138-014-0648-8.

[3] A. Zulifqar, M. Cabieses, A. Mikhail, and N. Khan, *Design of a Bridge Inspection System (BIS) to Reduce Time and Cost.* Farifax, VA, USA: George Mason Univ., 2014.

[4] B. A. Graybeal, B. M. Phares, D. D. Rolander, M. Moore, and G. Washer, "Visual inspection of highway bridges," *J. Nondestruct. Eval.*, vol. 21, no. 3, pp. 67–83, 2002, http://dx.doi.org/10.1023/A:1022508121821.

[5] S. Dorafshan and M. Maguire, "Bridge inspection: human performance, unmanned aerial systems and automation," *J. Civ. Struct. Health Monit.*, vol. 8, no. 3, pp. 443–476, 2018, http://dx.doi.org/10.1007/s13349-018-0285-4.

[6] N. Metni and T. Hamel, "A UAV for bridge inspection: Visual servoing control law with orientation limits," *Autom. Construct.*, vol. 17, no. 1, pp. 3–10, 2007, http://dx.doi.org/10.1016/j.autcon.2006.12.010.

[7] P. S. Moller, *CALTRANS Bridge Inspection Aerial Robot* |(Tech. Rep. CA 08-0182). Sacramento, CA: California Dept. Transp., 2008. Accessed: Mar. 30, 2021. [Online]. Available: https://trid.trb.org/view/917744

[8] C. Brooks et al., *Evaluating the Use of Unmanned Aerial Vehicles for Transportation Purposes* (Tech. Rep. RC-1616). Lansing, MI: Michigan Dept. Transp., 2014, Accessed: Mar. 30, 2021. [Online]. Available: https://trid.trb.org/view/1352503

[9] N. Hallermann and G. Morgenthal, "Visual inspection strategies for large bridges using unmanned aerial vehicles (UAV)," in *Proc. 7th Int. Conf. Bridge Maint., Saf. Manage. (IABMAS)*, Shanghai, China, 2014, pp. 661–667.

[10] L. D. Otero, N. Gagliardo, D. Dalli, W.-H. Huang, and P. Cosentino, *Proof of Concept for Using Unmanned Aerial Vehicles for High Mast Pole and Bridge Inspections* (Tech. Rep. BDV28-TWO-977-02). Tallahassee, FL: Florida Dept. Transp., Res. Center, 2015, http://dx.doi.org/10.13140/RG.2.1.4567.2166.

[11] J. Seo, L. Duque, and J. Wacker, "Glued-laminated timber arch bridge inspection using UAV," in *Comput. Civ. Eng. 2019: Smart Cities, Sustainability, and Resilience*, Reston, 2019, pp. 336–342.

[12] R. Montero, J. G. Victores, S. Martínez, A. Jardón, and C. Balaguer, "Past, present and future of robotic tunnel inspection," *Autom. Construct.*, vol. 59, pp. 99–112, 2015, http://dx.doi.org/10.1016/j.autcon.2015.02.003.

[13] L. Attard, C. J. Debono, G. Valentino, and M. Di Castro, "Tunnel inspection using photogrammetric techniques and image processing: A review," *ISPRS J. Photogramm. Remote Sens.*, vol. 144, pp. 180–188, 2018, http://dx.doi.org/10.1016/j.isprsjprs.2018.07.010.

[14] Y. Xue, S. Zhang, M. Zhou, and H. Zhu, "Novel SfM-DLT method for metro tunnel 3D reconstruction and visualization," *Undergr. Space*, vol. 6, no. 2, pp. 134–141, 2021, http://dx.doi.org/10.1016/j.undsp.2020.01.002.

[15] T. Özaslan, S. Shen, Y. Mulgaonkar, N. Michael, and V. Kumar, "Inspection of penstocks and featureless tunnel-like environments using micro UAVs," in *Field and Service Robotics*, L. Mejias, P. Corke, and J. Roberts, Eds., Cham: Springer International Publishing, 2015, pp. 123–136, http://dx.doi.org/10.1007/978-3-319-07488-7_9.

[16] T. Özaslan et al., "Towards fully autonomous visual inspection of dark featureless dam penstocks using MAVs," in *2016 IEEE/RSJ Int. Conf. Intell. Robots Syst. (IROS)*, Daejeon, Korea, 2016, pp. 4998–5005.

[17] T. Özaslan et al., "Autonomous navigation and mapping for inspection of penstocks and tunnels with MAVs," *IEEE Robot. Autom. Lett.*, vol. 2, no. 3, pp. 1740–1747, 2017, http://dx.doi.org/10.1109/LRA.2017.2699790.

[18] T. Iwamoto, T. Enaka, and K. Tada, "Development of testing machine for tunnel inspection using multi-rotor UAV," *J. Phys. Conf. Ser.*, vol. 842, no. 1, pp. 012068, 2017, http://dx.doi.org/10.1088/1742-6596/842/1/012068.

[19] C. H. Vong, R. Ravitharan, P. Reichl, J. Chevin, and H. Chung, "Small scale unmanned aerial system (UAS) for railway culvert and tunnel inspection," in *ICRT 2017: Railway Develop., Operations, Maint.*, Reston, VA, 2018, pp. 1024–1032, http://dx.doi.org/10.1061/9780784481257.102.

[20] T. Hongyu, "Inspection of human inaccessible tunnel using unmanned aerial vehicle," M.S. thesis, Dept. Elect. Comput. Eng., Nat. Univ. Singap., Singapore, 2018.

[21] C. H. Tan et al., "A smart unmanned aerial vehicle (UAV) based imaging system for inspection of deep hazardous tunnels," *Water Pract. Technol.*, vol. 13, no. 4, pp. 991–1000, 2018, http://dx.doi.org/10.2166/wpt.2018.105.

[22] R. S. Pahwa, K. Y. Chan, J. Bai, V. B. Saputra, M. N. Do, and S. Foong, "Dense 3D reconstruction for visual tunnel inspection using unmanned aerial vehicle," in *2019 IEEE/RSJ Int. Conf. Intell. Robots Syst. (IROS)*, Macau, China, 2019, pp. 7025–7032.

[23] S. S. Mansouri, C. Kanellakis, D. Kominiak, and G. Nikolakopoulos, "Deploying MAVs for autonomous navigation in dark underground mine environments," *Robot. Auton. Syst.*, vol. 126, pp. 103472, 2020, http://dx.doi.org/10.1016/j.robot.2020.103472.

[24] C. Feng, H. Zhang, Y. Li, S. Wang, and H. Wang, "Efficient real-time defect detection for spillway tunnel using deep learning," *J. Real-Time Image Process.*, vol. 18, no. 6, pp. 1–11, 2021, http://dx.doi.org/10.1007/s11554-021-01130-x.

[25] L. Duque, J. Seo, and J. Wacker, "Synthesis of unmanned aerial vehicle applications for infrastructures," *J. Perform. Constr. Facil.*, vol. 32, no. 4, pp. 04018046, 2018, http://dx.doi.org/10.1061/(ASCE)CF.1943-5509.0001185.

[26] S. Agnisarman, S. Lopes, K. Chalil Madathil, K. Piratla, and A. Gramopadhye, "A survey of automation-enabled human-in-the-loop systems for infrastructure visual inspection," *Autom. Construct.*, vol. 97, pp. 52–76, 2019, http://dx.doi.org/10.1016/j.autcon.2018.10.019.

[27] W. W. Greenwood, J. P. Lynch, and D. Zekkos, "Applications of UAVs in civil infrastructure," *J. Infrastruct. Syst.*, vol. 25, no. 2, pp. 04019002, 2019, http://dx.doi.org/10.1061/(ASCE)IS.1943-555X.0000464.

[28] S. Sony, S. Laventure, and A. Sadhu, "A literature review of next-generation smart sensing technology in structural health monitoring," *Struct. Contr. Health Monit.*, vol. 26, no. 3, e2321, 2019, http://dx.doi.org/10.1002/stc.2321.

[29] H. Ahmed, H. M. La, and N. Gucunski, "Review of non-destructive civil infrastructure evaluation for bridges: State-of-the-art robotic platforms, sensors and algorithms," *Sens.*, vol. 20, no. 14, pp. 3954, 2020, http://dx.doi.org/10.3390/s20143954.

[30] F. Outay, H. A. Mengash, and M. Adnan, "Applications of unmanned aerial vehicle (UAV) in road safety, traffic and highway infrastructure management: recent advances and challenges," *Transp. Res. Part A Policy Pract.*, vol. 141, pp. 116–129, 2020, http://dx.doi.org/10.1016/j.tra.2020.09.018.

[31] E. Jeong, J. Seo, and J. Wacker, "Literature review and technical survey on bridge inspection using unmanned aerial vehicles," *J. Perform. Constr. Facil.*, vol. 34, no. 6, pp. 04020113, 2020, http://dx.doi.org/10.1061/(ASCE)CF.1943-5509.0001519.

[32] S. Feroz and S. Abu Dabous, "Uav-based remote sensing applications for bridge condition assessment," *Remote Sens.*, vol. 13, no. 9, pp. 1809, 2021, http://dx.doi.org/10.3390/rs13091809.

[33] Z. Yin, *A Quadcopter with Heterogeneous Sensors for Autonomous Bridge Inspection* (Tech. Rep. 25-1121-0003-197). Lincoln, NE: Mid-America Transp. Center, 2014. [Online]. Available: https://trid.trb.org/view/1331073

[34] B. Chan, H. Guan, J. Jo, and M. Blumenstein, "Towards UAV-based bridge inspection systems: a review and an application perspective," *Struct. Monit. Maint.*, vol. 2, no. 3, pp. 283–300, 2015, http://dx.doi.org/10.12989/smm.2015.2.3.283.

[35] K. Cunningham et al., "UAS-based inspection of the placer river trail bridge: a data-driven approach," in *Struct. Congr. 2015*, Portland, OR, USA, 2015, pp. 607–615, http://dx.doi.org/10.1061/9780784479117.053.

[36] N. Bolourian, M. M. Soltani, A. Albahri, and A. Hammad"High level framework for bridge inspection using LiDAR-equipped UAV," in *2017 Proc. 34th Int. Symp. Automat. Robot. Constr. (ISARC)*, Taipei, Taiwan, 2017, pp. 683–688.

[37] H.-J. Jung, J.-H. Lee, and I.-H. Kim, "Challenging issues and solutions of bridge inspection technology using unmanned aerial vehicles," in *Proc. SPIE 10598, Sens. Smart Struct. Technol. Civ., Mech., Aerosp. Syst.*, Denver, CO, USA, 2018, pp. 1–6.

[38] Y. Z. Ayele and E. L. Droguett, "Application of UAVs for bridge inspection and resilience assessment," in *Proc. 29th Eur. Saf. Rel. Conf.*, Hannover, Germany, 2019, pp. 1328–1335.

[39] D. Cheyne, B. Merrill, and J. Boggs, *Use of Small Unmanned Aerial Systems for Bridge Inspection* (Tech. Rep. FHWA-HIF-19-056). Washington, DC: Fed. Hig. Adm. (FHWA), 2019, [Online]. Available: https://trid.trb.org/view/1749103

[40] K. K. Jena, S. Mishra, S. Mishra, and S. K. Bhoi, "Unmanned aerial vehicle assisted bridge crack severity inspection using edge detection methods," in *2019 3rd Int. Conf. I-SMAC (IoT in Social, Mobile, Analytics and Cloud) (I-SMAC)*, Palladam, India, 2019, pp. 284–289.

[41] Y. Zou, V. Gonzalez, J. Lim, R. Amor, B. Guo, and M. Babaeian Jelodar, "Systematic framework for postearthquake bridge inspection through UAV and 3D BIM reconstruction," in *Proc. CIB World Build. Congr.*, Hong Kong, China, 2019, pp. 1–9.

[42] S. HekmatiAthar, N. Goudarzi, A. Karimoddini, A. Homaifar, and D. Divakaran, "A systematic evaluation and selection of UAS-enabled solutions for bridge inspection practices," in *2020 IEEE Aerosp. Conf.*, Big Sky, MT, USA, 2020, pp. 1–11, http://dx.doi.org/10.1109/AERO47225.2020.9172795.

[43] J. Wells and B. Lovelace, *Improving the Quality of Bridge Inspections Using Unmanned Aircraft Systems (UAS)* (Tech. Rep. MN/RC 2018-26). St. Paul, MN: Minnesota Dept. Transp., 2018. [Online]. Available: https://trid.trb.org/view/1539868

[44] B. Lovelace, *Unmanned Aircraft System Bridge Inspection Demonstration Project Phase II* (Tech. Rep. MN/RC 2017-18). St. Paul, MN: Minnesota Dept. Transp., June 2017, [Online]. Available: https://trid.trb.org/view/1475149

[45] M. N. Gillins, "Unmanned aircraft systems for bridge inspection: testing and developing end-to-end operational workflow," M.S. thesis, Oregon State Univ., Corvallis, OR, USA, 2016. [Online]. Available: http://hdl.handle.net/1957/60001

[46] S. Dorafshan, R. J. Thomas, C. Coopmans, and M. Maguire, "Deep learning neural networks for sUAS-assisted structural inspections: feasibility and application," in *2018 Int. Conf. Unmanned Aircr. Syst. (ICUAS)*, Dallas, TX, USA, 2018, pp. 874–882.

[47] S. Dorafshan, M. Maguire, N. V. Hoffer, and C. Coopmans, "Challenges in bridge inspection using small unmanned aerial systems: results and lessons learned," in *2017 Int. Conf. Unmanned Aircr. Syst. (ICUAS)*, Miami, FL, USA, 2017, pp. 1722–1730.

[48] S. Dorafshan, M. Maguire, N. V. Hoffer, and C. Coopmans, *Fatigue Crack Detection Using Unmanned Aerial Systems in Under-Bridge Inspection* (Tech. Rep. FHWA-ITD-17-256). Boise, Idaho: Idaho Transp. Dept., 2017.

[49] S. Dorafshan, R. J. Thomas, and M. Maguire, "Fatigue crack detection using unmanned aerial systems in fracture critical inspection of steel bridges," *J. Bridge Eng.*, vol. 23, no. 10, pp. 04018078, 2018, http://dx.doi.org/10.1061/(ASCE)BE.1943-5592.0001291.

[50] B. J. Perry, "Streamlined bridge inspection framework utilizing unmanned aerial vehicles (UAVs)," M.S. thesis, Dept. Civ. Environ. Eng., Colorado State Univ., Fort Collins, CO, USA, 2019. [Online]. Available: https://hdl.handle.net/10217/197417

[51] B. J. Perry, Y. Guo, R. Atadero, and J. W. van de Lindt, "Streamlined bridge inspection system utilizing unmanned aerial vehicles (UAVs) and machine learning," *Meas.*, vol. 164, pp. 108048, 2020, http://dx.doi.org/10.1016/j.measurement.2020.108048.

[52] Y. Turkan, *Bridge structural inspections using bridge information modeling (BrIM) and unmanned aerial vehicles (UAVs)* (Pacific Northwest Transp. Consortium, Seattle, WA, USA, Tech. Rep. 2017-S-OSU-2, 2019. [Online]. Available: http://hdl.handle.net/1773/45581

[53] Y. Xu and Y. Turkan, "BrIM and UAS for bridge inspections and management," *Eng. Constr. Archit. Manage.*, vol. 27, no. 3, pp. 785–807, 2020, http://dx.doi.org/10.1108/ECAM-12-2018-0556.

[54] S. Dorafshan, R. J. Thomas, C. Coopmans, and M. Maguire, "A practitioner's guide to small unmanned aerial systems for bridge inspection," *Infrastruct.*, vol. 4, no. 4, pp. 72, 2019, http://dx.doi.org/10.3390/infrastructures4040072.

[55] B. J. Perry, Y. Guo, R. Atadero, and J. W. van de Lindt, "Unmanned aerial vehicle (UAV)-enabled bridge inspection framework," in *Bridge Maintenance, Safety, Management, Life-Cycle Sustainability and Innovations*, H. Yokota and D.M. Frangopol, Eds., London: CRC Press, 2021, pp. 158–165.

[56] B. J. Perry, Y. Guo, R. Atadero, and J. W. van de Lindt, "Tracking bridge condition over time using recurrent UAV-based inspection," in *Bridge Maintenance, Safety, Management, Life-Cycle Sustainability and Innovations*. CRC Press, 2021, pp. 286–291.

[57] S. Hiasa, E. Karaaslan, W. Shattenkirk, C. Mildner, and F. N. Catbas, "Bridge inspection and condition assessment using image-based technologies with UAVs," in *Struct. Congr. 2018: Bridges, Transp. Struct., Nonbuild. Struct.*, Fort Worth, TX, USA, 2018, pp. 217–228.

[58] M. N. Gillins, D. T. Gillins, and C. Parrish, "Cost-effective bridge safety inspections using unmanned aircraft systems (UAS)," in *Geotech. Struct. Eng. Congr.*, Phoenix, AZ, USA, 2016, pp. 1931–1940.

[59] H. Yoon, J. Shin, and B. F. Spencer Jr, "Structural displacement measurement using an unmanned aerial system," *Comput. Aided Civ. Infrastruct. Eng.*, vol. 33, no. 3, pp. 183–192, 2018, http://dx.doi.org/10.1111/mice.12338.

[60] J. J. Lin, A. Ibrahim, S. Sarwade, and M. Golparvar-Fard, "Bridge inspection with aerial robots: Automating the entire pipeline of visual data capture, 3D mapping, defect detection, analysis, and reporting," *J. Comput. Civ. Eng.*, vol. 35, no. 2, pp. 04020064, 2021, http://dx.doi.org/10.1061/(ASCE)CP.1943-5487.0000954.

[61] W. Wu, M. A. Qurishee, J. Owino, I. Fomunung, M. Onyango, and B. Atolagbe, "Coupling deep learning and UAV for infrastructure condition assessment automation," in *2018 IEEE Int. Smart Cities Conf. (ISC2)*, Kansas City, MO, USA, 2018, pp. 1–7.

[62] J. Seo, L. Duque, and J. Wacker, "Drone-enabled bridge inspection methodology and application," *Autom. Construct.*, vol. 94, pp. 112–126, 2018, http://dx.doi.org/10.1016/j.autcon.2018.06.006.

[63] L. Duque, J. Seo, and J. Wacker, "Timber bridge inspection using UAV," in *Struct. Congr. 2018: Bridges, Transp. Struct., Nonbuild. Struct.*, Fort Worth, TX, USA, 2018, pp. 186–196, http://dx.doi.org/10.1061/9780784481332.017.

[64] J. Seo, J. P. Wacker, and L. Duque, *Evaluating the Use of Drones for Timber Bridge Inspection* (Tech. Rep.). Madison, WI: US Dept. Agriculture, Forest Service, Forest Products Lab., 2018.

[65] J. Seo, L. Duque, and J. P. Wacker, "Field application of UAS-based bridge inspection," *Transp. Res. Rec.*, vol. 2672, no. 12, pp. 72–81, 2018, http://dx.doi.org/10.1177/0361198118780825.

[66] S. Chen, D. F. Laefer, E. Mangina, S. M. I. Zolanvari, and J. Byrne, "UAV bridge inspection through evaluated 3D reconstructions," *J. Bridge Eng.*, vol. 24, no. 4, pp. 05019001, 2019, http://dx.doi.org/10.1061/(ASCE)BE.1943-5592.0001343.

[67] L. Duque, "UAV-based bridge inspection and computational simulations," M.S. thesis, Dept. Civ. Environ. Eng., South Dakota State Univ., Brookings, SD, USA, 2017.

[68] A. Humpe, "Bridge inspection with an off-the-shelf 360º camera drone," *Drones*, vol. 4, no. 4, pp. 67, 2020, http://dx.doi.org/10.3390/drones4040067.

[69] L. Duque, J. Seo, and J. Wacker, "Bridge deterioration quantification protocol using UAV," *J. Bridge Eng.*, vol. 23, no. 10, pp. 04018080, 2018, http://dx.doi.org/10.1061/(ASCE)BE.1943-5592.0001289.

[70] E. Ciampa, L. D. Vito, and M. R. Pecce, "Practical issues on the use of drones for construction inspections," *J. Phys. Conf. Ser.*, vol. 1249, no. 1, pp. 012016, May 2019, http://dx.doi.org/10.1088/1742-6596/1249/1/012016.

[71] I.-H. Kim, H. Jeon, S.-C. Baek, W.-H. Hong, and H.-J. Jung, "Application of crack identification techniques for an aging concrete bridge inspection using an unmanned aerial vehicle," *Sens.*, vol. 18, no. 6, pp. 1881, 2018, http://dx.doi.org/10.3390/s18061881.

[72] T. Omar and M. L. Nehdi, "Remote sensing of concrete bridge decks using unmanned aerial vehicle infrared thermography," *Autom. Construct.*, vol. 83, pp. 360–371, 2017, http://dx.doi.org/10.1016/j.autcon.2017.06.024.

[73] J. Hackl, B. T. Adey, M. Woźniak, and O. Schümperlin, "Use of unmanned aerial vehicle photogrammetry to obtain topographical information to improve bridge risk assessment," *J. Infrastruct. Syst.*, vol. 24, no. 1, pp. 04017041, 2018, http://dx.doi.org/10.1061/(ASCE)IS.1943-555X.0000393.

[74] Y.-F. Liu, X. Nie, J.-S. Fan, and X.-G. Liu, "Image-based crack assessment of bridge piers using unmanned aerial vehicles and three-dimensional scene reconstruction," *Comput. Aided Civ. Infrastruct. Eng.*, vol. 35, no. 5, pp. 511–529, 2020, http://dx.doi.org/10.1111/mice.12501.

[75] T. Omar and M. L. Nehdi, "Thermal detection of subsurface delaminations in reinforced concrete bridge decks using unmanned aerial vehicle," *Spec. Publ.*, vol. 331, pp. 1–14, 2019.

[76] Y. Z. Ayele, M. Aliyari, D. Griffiths, and E. L. Droguett, "Automatic crack segmentation for UAV-assisted bridge inspection," *Energies*, vol. 13, no. 23, pp. 6250, 2020, http://dx.doi.org/10.3390/en13236250.

[77] M. Aliyari, B. Ashrafi, and Y. Z. Ayele, "Hazards identification and risk assessment for UAV-assisted bridge inspections," *Struct. Infrastruct. Eng.*, vol. 18, no. 3, pp. 412–428, 2022, http://dx.doi.org/10.1080/15732479.2020.1858878.

[78] Z. Yu, Y. Shen, and C. Shen, "A real-time detection approach for bridge cracks based on YOLOv4-FPM," *Autom. Construct.*, vol. 122, pp. 103514, 2021, http://dx.doi.org/10.1016/j.autcon.2020.103514.

[79] E. Jeong, J. Seo, and J. Wacker, "New bridge inspection approach with joint UAV and DIC system," in *Struct. Congr. 2020*, 2020, pp. 349–359.

[80] J. Seo, E. Jeong, and J. Wacker, "Visual bridge damage measurement using drone-captured image quality optimization," in *Eur. Workshop Struct. Health Monit.*, P. Rizzo and A. Milazzo, Eds., Cham: Springer International Publishing, 2021, pp. 503–513, http://dx.doi.org/10.1007/978-3-030-64908-1_47.

[81] E. Jeong, J. Seo, and J. Wacker, "Grayscale drone inspection image enhancement framework for advanced bridge defect measurement," *Transp. Res. Rec.*, vol. 2675, no. 8, pp. 603–612, 2021.

[82] V. H. Mac, Q. H. Tran, J. Huh, N. S. Doan, C. Kang, and D. Han, "Detection of delamination with various width-to-depth ratios in concrete bridge deck using passive IRT: Limits and applicability," *Mater.*, vol. 12, no. 23, pp. 3996, 2019, http://dx.doi.org/10.3390/ma12233996.

[83] D. Erdenebat and D. Waldmann, "Application of the DAD method for damage localisation on an existing bridge structure using close-range UAV photogrammetry," *Eng. Struct.*, vol. 218, pp. 110727, 2020, http://dx.doi.org/10.1016/j.engstruct.2020.110727.

[84] P. Garg et al., "Measuring transverse displacements using unmanned aerial systems laser doppler vibrometer (UAS-LDV): Development and field validation," *Sens.*, vol. 20, no. 21, pp. 6051, 2020, http://dx.doi.org/10.3390/s20216051.

[85] P. Garg, "Displacement measurement using a laser doppler vibrometer mounted on an unmanned aerial vehicles," M.S. thesis, Dept. Elect. Comput. Eng., Univ. New Mex., Albuquerque, NM, USA, 2017.

[86] P. Garg, F. Moreu, A. Ozdagli, M. R. Taha, and D. Mascareñas, "Noncontact dynamic displacement measurement of structures using a moving laser doppler vibrometer," *J. Bridge Eng.*, vol. 24, no. 9, pp. 04019089, 2019, http://dx.doi.org/10.1061/(ASCE)BE.1943-5592.0001472.

[87] C. Cheng, Z. Shang, and Z. Shen, "Automatic delamination segmentation for bridge deck based on encoder-decoder deep learning through UAV-based thermography," *NDT Int.*, vol. 116, pp. 102341, 2020, http://dx.doi.org/10.1016/j.ndteint.2020.102341.

[88] R. Escobar-Wolf, T. Oommen, C. N. Brooks, R. J. Dobson, and T. M. Ahlborn, "Unmanned aerial vehicle (UAV)-based assessment of concrete bridge deck delamination using thermal and visible camera sensors: a preliminary analysis," *Res. Nondestruct. Eval.*, vol. 29, no. 4, pp. 183–198, 2018, http://dx.doi.org/10.1080/09349847.2017.1304597.

[89] F. Jalinoos, M. Amjadian, A. K. Agrawal, C. Brooks, and D. Banach, "Experimental evaluation of unmanned aerial system for measuring bridge movement," *J. Bridge Eng.*, vol. 25, no. 1, pp. 04019132, 2020, http://dx.doi.org/10.1061/(ASCE)BE.1943-5592.0001508.

[90] G. Morgenthal et al., "Framework for automated UAS-based structural condition assessment of bridges," *Autom. Construct.*, vol. 97, pp. 77–95, 2019, http://dx.doi.org/10.1016/j.autcon.2018.10.006.

[91] K. W. Lee and J. K. Park, "Modeling and management of bridge structures using unmanned aerial vehicle in korea," *Sens. Mater.*, vol. 31, no. 11, pp. 3765–3772, 2019, http://dx.doi.org/10.18494/SAM.2019.2467.

[92] D. Reagan, A. Sabato, and C. Niezrecki, "Feasibility of using digital image correlation for unmanned aerial vehicle structural health monitoring of bridges," *Struct. Health Monit.*, vol. 17, no. 5, pp. 1056–1072, 2018, http://dx.doi.org/10.1177/1475921717735326.

[93] D. Reagan, A. Sabato, and C. Niezrecki, "Unmanned aerial vehicle acquisition of three-dimensional digital image correlation measurements for structural health monitoring of bridges," in *Proc. SPIE 10169, Nondestruct. Charact. Monit. Adv. Mater., Aerosp., Civ. Infrastruct.*, Portland, OR, USA, 2017, pp. 68–77, http://dx.doi.org/10.1117/12.2259985.

[94] D. Reagan, "Unmanned aerial vehicle measurement using three dimensional digital image correlation to perform bridge structural health monitoring," M.S. thesis, Dept. Mech. Eng., Univ. Massachusetts Lowell, Lowell, MA, USA, 2017.

[95] D. Reagan, A. Sabato, C. Niezrecki, T. Yu, and R. Wilson, "An autonomous unmanned aerial vehicle sensing system for structural health monitoring of bridges," in *Proc. SPIE 9804, Nondestruct. Charact. Monit. Adv. Mater., Aerosp., Civ. Infrastruct.*, Las Vegas, NV, USA, 2016, pp. 244–252, http://dx.doi.org/10.1117/12.2218370.

[96] A. Ellenberg, A. Kontsos, F. Moon, and I. Bartoli, "Bridge related damage quantification using unmanned aerial vehicle imagery," *Struct. Contr. Health Monit.*, vol. 23, no. 9, pp. 1168–1179, 2016, http://dx.doi.org/10.1002/stc.1831.

[97] A. Ellenberg, L. Branco, A. Krick, I. Bartoli, and A. Kontsos, "Use of unmanned aerial vehicle for quantitative infrastructure evaluation," *J. Infrastruct. Syst.*, vol. 21, no. 3, pp. 04014054, 2015, http://dx.doi.org/10.1061/(ASCE)IS.1943-555X.0000246.

[98] D. Lattanzi and G. R. Miller, "3D scene reconstruction for robotic bridge inspection," *J. Infrastruct. Syst.*, vol. 21, no. 2, pp. 04014041, 2015, http://dx.doi.org/10.1061/(ASCE)IS.1943-555X.0000229.

[99] K. W. Franke et al., "Reconnaissance of two liquefaction sites using small unmanned aerial vehicles and structure from motion computer vision following the april 1, 2014 chile earthquake," *J. Geotech. Geoenviron. Eng.*, vol. 143, no. 5, pp. 04016125, 2017, http://dx.doi.org/10.1061/(ASCE)GT.1943-5606.0001647.

[100] R. Ali, D. Kang, G. Suh, and Y.-J. Cha, "Real-time multiple damage mapping using autonomous UAV and deep faster region-based neural networks for GPS-denied structures," *Autom. Construct.*, vol. 130, pp. 103831, 2021, http://dx.doi.org/10.1016/j.autcon.2021.103831.

[101] P. Darby, W. Hollerman, and J. Miller, "Exploring the potential utility of unmanned aerial vehicles for practical bridge inspection in Louisiana," *MATEC Web Conf.*, vol. 271, pp. 01001, 2019, http://dx.doi.org/10.1051/matecconf/201927101001.

[102] P. Darby and V. Gopu, *Bridge Inspecting with Unmanned Aerial Vehicles R&D* (Tech. Rep. 17STLSU11). Baton Rouge, LA: Transp. Consortium of South-Central States (Tran-SET), 2018.

[103] J. Zink and B. Lovelace, *Unmanned Aerial Vehicle Bridge Inspection Demonstration Project* (Tech. Rep. MN/RC 2015-40). St. Paul, MN: Minnesota Dept. Transp., 2015, [Online]. Available: https://trid.trb.org/view/1410491

[104] Q. Zhu, T. H. Dinh, M. D. Phung, and Q. P. Ha, "Hierarchical convolutional neural network with feature preservation and autotuned thresholding for crack detection," *IEEE Access*, vol. 9, pp. 60201–60214, 2021.

[105] L. Yang, B. Li, W. Li, H. Brand, B. Jiang, and J. Xiao, "Concrete defects inspection and 3D mapping using CityFlyer quadrotor robot," IEEE/CAA J," *Autom. Sin.*, vol. 7, no. 4, pp. 991–1002, 2020, http://dx.doi.org/10.1109/JAS.2020.1003234.

[106] L. Yang, B. Li, W. Li, Z. Liu, G. Yang, and J. Xiao, "A robotic system towards concrete structure spalling and crack database," in *2017 IEEE Int. Conf. Robot. Biomimetics (ROBIO)*, Macau, China, 2017, pp. 1276–1281.

[107] M. R. Saleem, J.-W. Park, J.-H. Lee, H.-J. Jung, and M. Z. Sarwar, "Instant bridge visual inspection using an unmanned aerial vehicle by image capturing and geo-tagging system and deep convolutional neural network," *Struct. Health Monit.*, vol. 20, no. 4, pp. 1760–1777, 2021, http://dx.doi.org/10.1177/1475921720932384.

[108] X. Peng, X. Zhong, C. Zhao, Y. F. Chen, and T. Zhang, "The feasibility assessment study of bridge crack width recognition in images based on special inspection UAV," *Adv. Civ. Eng.*, vol. 2020, pp. 1–17, 2020., http://dx.doi.org/10.1155/2020/8811649.

[109] P. Chun et al., "Utilization of unmanned aerial vehicle, artificial intelligence, and remote measurement technology for bridge inspections," *J. Robot. Mechatron.*, vol. 32, no. 6, pp. 1244–1258, 2020, http://dx.doi.org/10.20965/jrm.2020.p1244.

[110] B. Lei, N. Wang, P. Xu, and G. Song, "New crack detection method for bridge inspection using UAV incorporating image processing," *J. Aerosp. Eng.*, vol. 31, no. 5, pp. 04018058, 2018, http://dx.doi.org/10.1061/(ASCE)AS.1943-5525.0000879.

[111] Z. Yin, Y. Mao, and C. Seto, *Develop a UAV Platform for Automated Bridge Inspection* (Tech. Rep. 25-1121-0003-295). Lincoln, NE: Mid-America Transp. Center, Mar. 2015. [Online]. Available: https://trid.trb.org/view/1522949

[112] H.-F. Wang, L. Zhai, H. Huang, L.-M. Guan, K.-N. Mu, and G. Wang, "Measurement for cracks at the bottom of bridges based on tethered creeping unmanned aerial vehicle," *Autom. Construct.*, vol. 119, pp. 103330, 2020, http://dx.doi.org/10.1016/j.autcon.2020.103330.

[113] P. J. Sanchez-Cuevas, G. Heredia, and A. Ollero, "Multirotor UAS for bridge inspection by contact using the ceiling effect," in *2017 Int. Conf. Unmanned Aircr. Syst. (ICUAS)*, Miami, FL, USA, 2017, pp. 767–774.

[114] P. J. Sanchez-Cuevas, P. Ramon-Soria, B. Arrue, A. Ollero, and G. Heredia, "Robotic system for inspection by contact of bridge beams using UAVs," *Sens.*, vol. 19, no. 2, pp. 305, 2019, http://dx.doi.org/10.3390/s19020305.

[115] S. Yoon, G.-H. Gwon, J.-H. Lee, and H.-J. Jung, "Three-dimensional image coordinate-based missing region of interest area detection and damage localization for bridge visual inspection using unmanned aerial vehicles," *Struct. Health Monit.*, vol. 20, no. 4, pp. 1462–1475, 2021, http://dx.doi.org/10.1177/1475921720918675.

[116] B. Lei, Y. Ren, N. Wang, L. Huo, and G. Song, "Design of a new low-cost unmanned aerial vehicle and vision-based concrete crack inspection method," *Struct. Health Monit.*, vol. 19, no. 6, pp. 1871–1883, 2020, http://dx.doi.org/10.1177/1475921719898862.

[117] C.-H. Yang, M.-C. Wen, Y.-C. Chen, and S.-C. Kang, "An optimized unmanned aerial system for bridge inspection," in *2015 Proc. 32nd Int. Symp. Automat. Robot. Constr. (ISARC)*, Oulu, Finland, 2015, pp. 1–6.

[118] A. Khaloo, D. Lattanzi, K. Cunningham, R. Dell'Andrea, and M. Riley, "Unmanned aerial vehicle inspection of the placer river trail bridge through image-based 3D modelling," *Struct. Infrastruct. Eng.*, vol. 14, no. 1, pp. 124–136, 2018.

[119] F. Khan et al., "Investigation on bridge assessment using unmanned aerial systems," in *Struct. Congr. 2015*, Portland, OR, USA, 2015, pp. 404–413.

[120] A. Ellenberg, A. Kontsos, F. Moon, and I. Bartoli, "Low-cost, quantitative assessment of highway bridges through the use of unmanned aerial vehicles," in *Proc. SPIE 9805, Health Monit. Struct. Biol. Syst.*, Las Vegas, NV, USA, 2016, pp. 612–621, http://dx.doi.org/10.1117/12.2219741.

[121] L. Yoder and S. Scherer, "Autonomous exploration for infrastructure modeling with a micro aerial vehicle," in *Field and Service Robotics*, D. S. Wettergreen and T. D. Barfoot, Eds., Cham: Springer International Publishing, 2016, pp. 427–440, http://dx.doi.org/10.1007/978-3-319-27702-8_28.

[122] A. E. Jimenez-Cano, P. J. Sanchez-Cuevas, P. Grau, A. Ollero, and G. Heredia, "Contact-based bridge inspection multirotors: design, modeling, and control considering the ceiling effect," *IEEE Robot. Autom. Lett.*, vol. 4, no. 4, pp. 3561–3568, 2019.

[123] A. E. Jimenez-Cano, J. Braga, G. Heredia, and A. Ollero, "Aerial manipulator for structure inspection by contact from the underside," in *2015 IEEE/RSJ Int. Conf. Intell. Robots Syst. (IROS)*, Hamburg, Germany, 2015, pp. 1879–1884.

[124] T. Ikeda et al., "Wall contact by octo-rotor UAV with one DoF manipulator for bridge inspection," in *2017 IEEE/RSJ Int. Conf. Intell. Robots Syst. (IROS)*, British Columbia, Canada, 2017, pp. 5122–5127.

[125] T. Ikeda et al., "Stable impact and contact force control by UAV for inspection of floor slab of bridge," *Adv. Robot.*, vol. 32, no. 19, pp. 1061–1076, 2018, http://dx.doi.org/10.1080/01691864.2018.1525075.

[126] A. Ichikawa et al., "UAV with manipulator for bridge inspection: hammering system for mounting to UAV," in *2017 IEEE/SICE Int. Symp. Syst. Integration (SII)*, Taipei, Taiwan, 2017, pp. 775–780.

[127] S. Jung et al., "Toward autonomous bridge inspection: a framework and experimental results," in *2019 16th Int. Conf. Ubiquitous Robots (UR)*, Jeju, Korea, 2019, pp. 208–211.

[128] A. P. Tomiczek, T. J. Whitley, J. A. Bridge, and P. G. Ifju, "Bridge inspections with small unmanned aircraft systems: case studies," *J. Bridge Eng.*, vol. 24, no. 4, pp. 05019003, 2019, http://dx.doi.org/10.1061/(ASCE)BE.1943-5592.0001376.

[129] C. J. O. Salaan et al., "Close visual bridge inspection using a UAV with a passive rotating spherical shell," *J. Field Robot.*, vol. 35, no. 6, pp. 850–867, 2018, http://dx.doi.org/10.1002/rob.21781.

[130] M. Yamada, M. Nakao, Y. Hada, and N. Sawasaki, "Development and field test of novel two-wheeled UAV for bridge inspections," in *2017 Int. Conf. Unmanned Aircr. Syst. (ICUAS)*, Miami, FL, USA, 2017, pp. 1014–1021.

[131] X. Peng, X. Zhong, C. Zhao, A. Chen, and T. Zhang, "A UAV-based machine vision method for bridge crack recognition and width quantification through hybrid feature learning," *Constr. Build. Mater.*, vol. 299, pp. 123896, 2021, http://dx.doi.org/10.1016/j.conbuildmat.2021.123896.

[132] H.-J. Jung, J.-H. Lee, S. Yoon, and I.-H. Kim, "Bridge inspection and condition assessment using unmanned aerial vehicles (UAVs): major challenges and solutions from a practical perspective," *Smart Struct. Syst.*, vol. 24, no. 5, pp. 669–681, 2019, http://dx.doi.org/10.12989/sss.2019.24.5.669.

[133] D. Kang and Y.-J. Cha, "Damage detection with an autonomous UAV using deep learning," in *Proc. SPIE 10598, Sens. Smart Struct. Technol. Civ., Mech., Aerosp. Syst.*, Denver, CO, USA, 2018, pp. 7–14, http://dx.doi.org/10.1117/12.2295961.

[134] Z. Ma, E. Zhao, G. Granello, and G. Loporcaro, "Drone aided machine-learning tool for post-earthquake bridge damage reconnaissance," in *17th World Conf. Earthq. Eng. (WCEE)*, Sendai, Japan, 2020, pp. 1–12. [Online]. Available: https://hdl.handle.net/10092/101461

[135] M. M. Karim, C. H. Dagli, and R. Qin, "Modeling and simulation of a robotic bridge inspection system," *Procedia Comput. Sci.*, vol. 168, pp. 177–185, 2020, http://dx.doi.org/10.1016/j.procs.2020.02.276.

[136] J.-H. Lee, S.-S. Yoon, I.-H. Kim, and H.-J. Jung, “Study on image quality assessment and processing, damage diagnosis of crack for bridge inspection based on unmanned aerial vehicle,” in *ACEM18/Struct. 18*, Incheon, Korea, 2018, pp. 1–6. [Online]. Available: http://hdl.handle.net/10203/247365

[137] P. J. Sarkis and J. M. Sarkis, “Uso de drone em inspeção e definição de recuperação em OAEs,” in *9th Cong. Bras. Pontes e Estrut. (CBPE)*, Rio de Janeiro, Brazil, 2016, pp. 1–10.

[138] T. Harweg, A. Peters, D. Bachmann, and F. Weichert, "CNN-based deep architecture for health monitoring of civil and industrial structures using UAVs," *Proc.*, vol. 42, no. 1, pp. 69, 2020, http://dx.doi.org/10.3390/ecsa-6-06640.

[139] E. Bianchi, A. L. Abbott, P. Tokekar, and M. Hebdon, "COCO-bridge: structural detail data set for bridge inspections," *J. Comput. Civ. Eng.*, vol. 35, no. 3, pp. 04021003, 2021, http://dx.doi.org/10.1061/(ASCE)CP.1943-5487.0000949.

[140] J.-H. Lee, S.-S. Yoon, H.-J. Jung, and I.-H. Kim, “Diagnosis of crack damage on structures based on image processing techniques and R-CNN using unmanned aerial vehicle (UAV),” in *Proc. SPIE 10598, Sens. Smart Struct. Technol. Civ., Mech., Aerosp. Syst.*, Denver, CO, USA, 2018, pp. 265–272.

[141] A. Ellenberg, A. Kontsos, F. Moon, and I. Bartoli, "Bridge deck delamination identification from unmanned aerial vehicle infrared imagery," *Autom. Construct.*, vol. 72, pp. 155–165, 2016, http://dx.doi.org/10.1016/j.autcon.2016.08.024.

[142] C. Eschmann and T. Wundsam, "Web-based georeferenced 3D inspection and monitoring of bridges with unmanned aircraft systems," *J. Surv. Eng.*, vol. 143, no. 3, pp. 04017003, 2017., http://dx.doi.org/10.1061/(ASCE)SU.1943-5428.0000221.

[143] J.-W. Kim, S.-B. Kim, J.-C. Park, and J.-W. Nam, “Development of crack detection system with unmanned aerial vehicles and digital image processing,” in *2015 World Congr. Adv. Struct. Eng. Mechanics (ASEM)*, Incheon, Korea, 2015, pp. 1–11.

[144] J. D. Mason, E. T. Ayorinde, D. D. Mascarenas, and F. Moreu, *Tap Testing Hammer Using Unmanned Aerial Systems (UASs)* (Tech. Rep. LA-UR-16-26204). Los Alamos, NM: Los Alamos Nat. Lab. (LANL), 2016.

[145] F. Moreu, E. Ayorinde, J. Mason, C. Farrar, and D. Mascarenas, "Remote railroad bridge structural tap testing using aerial robots," *Int. J. Intell. Robot. Appl.*, vol. 2, no. 1, pp. 67–80, 2018, http://dx.doi.org/10.1007/s41315-017-0041-7.

[146] O. Özcan and O. Özcan, "Multi-hazard assessment of RC bridges using unmanned aerial vehicle-based measurements," *Balt. J. Road Bridge Eng.*, vol. 13, no. 3, pp. 192–208, 2018, http://dx.doi.org/10.7250/bjrbe.2018-13.412.

[147] A. Marchewka, P. Ziółkowski, and V. Aguilar-Vidal, "Framework for structural health monitoring of steel bridges by computer vision," *Sens.*, vol. 20, no. 3, pp. 700, 2020, http://dx.doi.org/10.3390/s20030700.

[148] G. Chen, Q. Liang, W. Zhong, X. Gao, and F. Cui, "Homography-based measurement of bridge vibration using UAV and DIC method," *Meas.*, vol. 170, pp. 108683, 2021, http://dx.doi.org/10.1016/j.measurement.2020.108683.

[149] J. Dang et al., "Arial patrol for bridge routine and post-earthquake emergency inspection using small aerial photography UAV,” in *Proc. 5th Int. Symp. Adv. Civ. Environ. Eng. Practises Sustain. Develop. (ACEPS)*, Galle, Sri Lanka, 2017, pp. 260–267.

[150] J. Dang and P. Chun, "Mixed training of deep convolutional neural network for bridge deterioration detection with UAV and inspection report sourced images,” in *Bridge Maintenance, Safety, Management, Life-Cycle Sustainability and Innovations*. CRC Press, 2021, pp. 308–312.

[151] J. Shi, J. Dang, and R. Zuo, "Bridge damage cropping-and-stitching segmentation using fully convolutional network based on images from UAVs,” in *Bridge Maintenance, Safety, Management, Life-Cycle Sustainability and Innovations*. CRC Press, 2021, pp. 264–270.

[152] DJI Official. https://www.dji.com (accessed Sept. 21, 2021).

[153] K. Jang, N. Kim, and Y.-K. An, "Deep learning–based autonomous concrete crack evaluation through hybrid image scanning," *Struct. Health Monit.*, vol. 18, no. 5-6, pp. 1722–1737, 2019, http://dx.doi.org/10.1177/1475921718821719.

[154] DJI Official. "DJI Unveils Mavic 2 Enterprise." https://www.dji.com/newsroom/news/dji-mavic-2-enterprise (accessed June 4, 2021).

[155] M. Gandillon. "Flyability Launches Elios 2 for Intuitive Indoor Inspections." Flyability.com. https://www.flyability.com/news/flyability-elios-2-indoor-inspections (accessed June 10, 2021).

[156] DJI. "DJI Defines a New Standard for Industrial Tools by Unveiling the Most Advanced Commercial Drone Platform and its First Hybrid Camera Series." DJI Official. https://www.dji.com/newsroom/news/matrice-300-rtk-zenmuse-h20-series (accessed June 4, 2021).

[157] H. Kim, J. Lee, E. Ahn, S. Cho, M. Shin, and S.-H. Sim, "Concrete crack identification using a UAV incorporating hybrid image processing," *Sens.*, vol. 17, no. 9, pp. 2052, 2017, http://dx.doi.org/10.3390/s17092052.

**Author contributions:** FYT: conceptualization, writing, formal analysis, revision; TNB, MMF: supervision, proofreading.

**Editors:** Luís Oliveira Santos, Guilherme Aris Parsekian.

IBRACON Structures and Materials Journal
Revista IBRACON de Estruturas e Materiais
ISSN 1983-4195 ismj.org

ORIGINAL ARTICLE

# Flexural and direct tensile strength ratio for concrete unusual cross-sections

## *Relação entre as resistências à tração na flexão e direta para seções transversais não usuais de concreto*

José Anchiêta Damasceno Fernandes Neto[a]
Vladimir Guilherme Haach[a]

[a]Universidade de São Paulo – USP, Escola de Engenharia de São Carlos, Departamento de Engenharia de Estruturas, São Carlos, SP, Brasil

Received 28 April 2021
Accepted 10 March 2022

**Abstract:** The relationship between flexural and direct tensile strength ($\alpha_{fl}$ ratio) has been explored in evaluations of the cracking moment for concrete structural elements. However, most results for $\alpha_{fl}$ can be applied only for rectangular cross-sections. This manuscript addresses its obtaining for unusual cross-sections largely used in precast concrete elements. A theoretical analysis was performed in thirty-two different cross-sections regarding the compressive strength of concrete and the aggregate type used in the concrete composition. The results showed a smooth increase in $\alpha_{fl}$ for higher strength concretes and lower elastic modulus aggregates. The theoretical procedure showed a good correlation with experimental data and prediction models and can be an interesting alternative for the obtaining of the $\alpha_{fl}$ of unusual cross-sections.

**Keywords:** flexural tensile strength, direct tensile strength, cracking moment, precast concrete, theoretical analysis.

**Resumo:** A relação entre a resistência à tração na flexão e tração direta (razão $\alpha_{fl}$) tem sido explorada na avaliação do momento de fissuração para elementos estruturais de concreto. No entanto, a maioria dos resultados relatados para $\alpha_{fl}$ podem ser aplicados apenas para seções transversais retangulares. Este artigo aborda a obtenção da relação $\alpha_{fl}$ para seções transversais não usuais amplamente utilizadas em elementos de concreto pré-moldado. Uma análise teórica foi realizada em trinta e duas diferentes seções transversais em termos da resistência à compressão do concreto e o tipo de agregado utilizado na composição do concreto. Os resultados apresentaram um suave aumento em $\alpha_{fl}$ para concretos de maior resistência e agregados com menor módulo de elasticidade. O procedimento teórico exibiu uma boa correlação com dados experimentais e modelos de previsão, e pode ser uma alternativa interessante para a obtenção da relação $\alpha_{fl}$ de seções transversais não usuais.

**Palavras-chave:** resistência à tração na flexão, resistência à tração direta, momento de fissuração, concreto pré-moldado, análise teórica.

**How to cite:** J. A. D. Fernandes Neto, and V. G. Haach, "Flexural and axial tensile strength ratio for precast concrete structures," *Rev. IBRACON Estrut. Mater.*, vol. 16, no. 1, 16104, 2023, https://doi.org/10.1590/S1983-41952023000100004

## 1 INTRODUCTION

Concrete is a material of quasi-brittle behavior evaluated predominantly in compression due to its high compressive strength and limited tensile strength. Such low tensile strength property is, therefore, neglected in the design of reinforced concrete structures, and steel reinforcement is used to support tensile stresses [1]. On the other hand, the tensile strength of concrete is an important property in assessments of both cracking formation and deflections at the

**Corresponding author:** José Anchiêta Damasceno Fernandes Neto.E-mail: anchietafernandes@usp.br
**Financial support:** Coordenação de Aperfeiçoamento de Pessoal de Nível Superior – Brasil (CAPES) – Finance Code 001 and Conselho Nacional de Desenvolvimento Científico e Tecnológico (Processo 302479/2017-1).
**Conflict of interest:** Nothing to declare.
**Data Availability:** The data that support the findings of this study are available from the corresponding author, J. A. D. Fernandes Neto, upon reasonable request.

serviceability limit state [2], and cracking moment in prestressed elements, punching shear, concrete/steel bond strength, shrinkage, control of crack width in early-ages, and development of moment-curvature diagrams [3]. It can be obtained by three different test methods, namely direct tensile test, splitting tensile test, and flexural test.

Splitting and flexural tensile strengths have been widely used and defined from the indirect application of tensile stresses according to EN 12390-6 [4] and EN 12390-5 [5], respectively. However, studies on the determination of the direct tensile strength are limited, since this property is susceptible to testing techniques, such as boundary conditions, loading ratio, and size and shape of the specimens tested [6], [7]. According to Chen et al. [8], although uniaxial tensile tests are challenging, their results are easily interpreted. Contrarily, flexural tests show a nonuniform stress-strain distribution in the cross-section of the specimen, thus hampering the analysis of results. Both tensile strengths (direct, splitting, and flexural) are usually correlated by some standard codes. Although the direct tensile strength is the true tensile strength of concrete, the splitting tensile strength is useful and reliable to estimate the conventional strength due to its simplicity execution. On the other hand, flexural tensile strength can be used to obtain the tensile strength in structural elements subjected to bending. For example, the ABNT NBR 6118 [9] indicates values for the correlation between flexural and direct tensile strength to be used on the verification of the cracking moment for rectangular, I-, T- and inverted T sections.

In general, the direct tensile strength is acquired through correlations between other properties. Figure 1a displays the difference between the tensile behavior for both direct tensile and flexural tests. Direct tensile tests exhibit a linear hardening up to the direct tensile strength ($f_{ct}$) when a brittle failure occurs. Unlike direct tensile tests, flexural tests show nonlinear hardening after the tensile strength of concrete has been reached and a smooth failure when the flexural tensile strength ($f_{ct,fl}$) has been achieved (see Figure 1a). A typical nonlinear flexural behavior of plain concrete is shown by a moment-curvature relationship (see Figure 1b). Hillerborg et al. [10] proposed a plain concrete behavior under tensile loading based on a fictitious crack model, which considers the presence of a fracture process zone when the maximum stress reaches the tensile strength of concrete (Figures 1c-1d). Such a zone is characterized by a gradual softening of concrete due to micro-cracking and interlocking of the aggregates, cement, or fibers [11], [12]. A fictitious crack is formed in this region simultaneously with a tensile stress decrease in the bottom fiber. When the tensile stress is assumed zero, a real crack is installed, and its width increases according to the softening stress-strain relationship [13] (Figures 1d-1e).

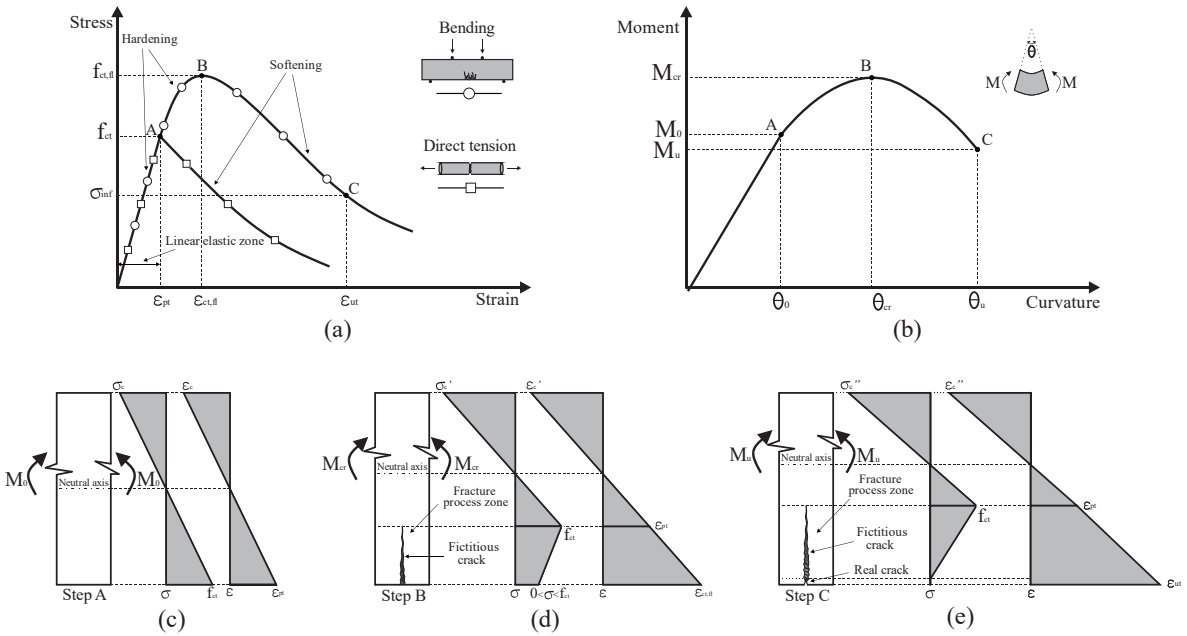


**Figure 1.** Plain concrete behavior under tensile loading: (a) stress-strain relationship, (b) moment-curvature relationship, and (c-e) stress-strain distribution diagrams along the uncracked and cracked sections.

Flexural tensile strength is essential for evaluations of the cracking moment of concrete elements (Equation 1). In particular, ABNT NBR 6118 [9] recommends the cracking moment verification by Equation 2 with a relationship between flexural and direct tensile strengths, shown in Equation 3:

$$M_{cr} = \frac{f_{ct,fl} \cdot I_g}{y_t} \tag{1}$$

$$M_{cr} = \frac{\alpha_{fl} \cdot f_{ct} \cdot I_g}{y_t} \tag{2}$$

$$\alpha_{fl} = \frac{f_{ct,fl}}{f_{ct}} \tag{3}$$

where $M_{cr}$ is the cracking moment, $f_{ct,fl}$ is the flexural tensile strength, $f_{ct}$ is the direct tensile strength, $I_g$ is the moment of inertia of the gross concrete section, $y_t$ is the distance from the centroidal axis of the gross section, and $\alpha_{fl}$ is the flexural and direct tensile strength ratio.

Some researchers have addressed the flexural and direct tensile strength ratio ($\alpha_{fl}$) due to differences between the flexural and direct tensile behaviors of concrete and the significance of their correlation. Maalej and Li [13] developed an analytical model to evaluate the flexural strength of fiber cementitious composites and observed the flexural and direct tensile strength ratio depends on the brittleness ratio and is affected by stress distribution in the fracture process zone. Ratio $\alpha_{fl}$ is a function of the specimen geometry and should decrease as the specimen height increases [13], [14]. Sorelli et al. [15] performed bending and uniaxial tensile tests in hybrid fiber-reinforced concretes, and the results indicated both type and fiber geometry highly influence their post-cracking behavior. $\alpha_{fl}$ was 1.46 for plain concrete and increased to 1.86 for macro fiber reinforced concrete.

Wu et al. [6] and Chen et al. [8] studied the effects of strain rate and testing method on the tensile strength of concrete and experimentally compared three methods, namely direct tensile, splitting tensile, and flexural tests for measuring it. The results confirmed the specimens tested under flexure showed higher tensile strength than those subjected to direct and splitting tension. The authors concluded the tensile strength increases and $\alpha_{fl}$ decreases with a strain rate increment, reaching 2.1 to 2.5 values for plain concrete of 37 MPa compressive strength [6], [8]. Balbo [16] evaluated a relationship between splitting tensile strength and flexural strength for dry and plastic concretes used in pavements bases. The experimental data showed the flexural strength is usually 92% and 49% higher than the splitting tensile strength of dry and plastic concretes, respectively. Lin et al. [17] proposed a testing method with embedded steel bars that was considered suitable for assessing the direct tensile strength of normal strength concrete specimens. The results were approximately 50% lower than the flexural tensile strength. $\alpha_{fl}$ varied between 1.92 and 2.02 in tensile tests performed in Ultra-High Performance Fiber Reinforced Cementitious Composites [18].

The studies addressed are limited and report results only for rectangular cross-sections. On the other hand, structural elements with unusual cross-sections have been largely used in several precast concrete industries due to their versatility, production speed, durability, and safety [19]. Besides, such studies usually disregard the influence of strength and aggregate type of the concrete, which are important factors in tensile behavior [20], [21].

This paper evaluates the flexural and direct tensile strength ratio for unusual cross-sections used mainly in precast concrete elements. A theoretical analysis was performed in thirty-two different cross-sections regarding the compressive strength of concrete and the aggregate type used in the mixture. A discussion on the influence of ultimate tensile strain and a comparison between prediction models are also addressed.

## 2 ANALYTICAL SOLUTION

Ananthan et al. [22] investigated the fracture behavior of plain concrete slender beams subjected to flexural loading using equilibrium equations, and proposed a one-dimensional model, called softening beam model, which accurately predicts the maximum load of rectangular concrete specimens under bending. The model was developed from uncracked ligament equilibrium and use of the strain softening modulus, calculated by Equation 4:

$$E_T = \frac{f_{ct}}{\varepsilon_{ut} - \varepsilon_{pt}} \tag{4}$$

where $E_T$ is the strain softening modulus (MPa), and $\varepsilon_{ut}$ and $\varepsilon_{pt}$ are the ultimate and peak strains of concrete in tension, respectively.

The relationship between strain softening modulus and elastic modulus is given by

$$E^* = \frac{E_T}{E} \tag{5}$$

where E* is the relation between strain softening modulus and initial modulus and E is the elastic modulus of concrete (MPa).

According to Ananthan et al. [22], ratio E* features the failure mechanism in concrete specimens through the slope of the post-peak softening branch of the tensile stress-strain diagram. The material displays a perfectly brittle behavior when $E^* = \infty$ and perfectly ductile behavior for $E^* = 0$ (see Figure 2a). Figures 2b and 2c show the stress distribution for both perfectly brittle and perfectly ductile behaviors, respectively. The ultimate moment capacity can be obtained from the moment equilibrium of cross-section for both cases, and $\alpha_{fl}$ assumes values of 1.0 and 3.0 for brittle and ductile materials, respectively. Such results indicate the limit range where $\alpha_{fl}$ can be considered [22], [23].

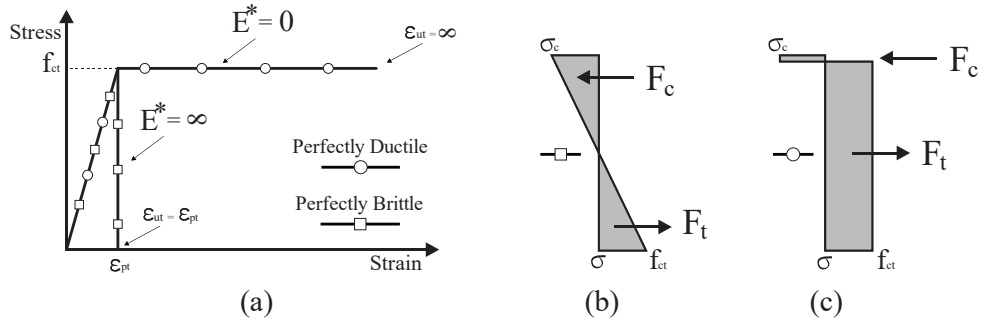


**Figure 2.** (a) Idealized stress-strain relationship in tension and stress distribution diagrams for (b) perfectly brittle material and (c) perfectly ductile material.

Since a strain softening in tension characterizes the concrete, the idealized stress-strain relationships (Figure 2a) do not apply to an uncracked-ligament real behavior, whose description considers a slope of strain-softening modulus with $0 < E^* < \infty$ (Figure 3a). The softening beam model assumes the stress-strain relationship of concrete in tension can be indicated by a bilinear diagram (Figure 3a). The plane section remains plane after deformation, and the compression behavior simulated is linearly proportional. The equilibrium conditions should be satisfied up to the fracture onset, represented in the stress-strain distribution diagrams in Figure 3b [22].

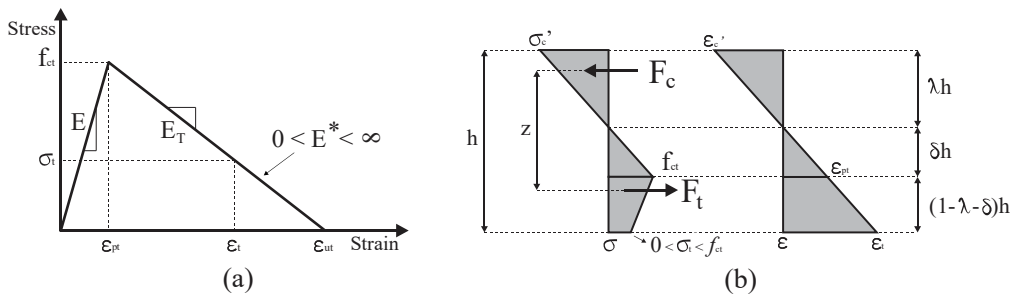


**Figure 3.** (a) Stress-strain relationship for concrete in tension and (b) stress-strain distribution diagram on the uncracked ligament.

According to the stress-strain relationship in Figure 3a, the stress in the post-peak softening branch is given by

$$\sigma_t = f_{ct} - E_T(\varepsilon_t - \varepsilon_{pt}) \quad (6)$$

where $\sigma_t$ is the tensile stress (MPa), and $\varepsilon_t$ is the corresponding tensile strain.

$\varepsilon_t$ can be obtained by Equation 7, derived from the relationships depicted in Figure 3b.

$$\varepsilon_t = \left(\frac{1 - \lambda}{\delta}\right)\varepsilon_{pt} \quad (7)$$

where $\lambda$ and $\delta$ are variable factors from 0 to 1 that characterize the stress-strain distribution diagrams.

Substituting Equation 7 in Equation 6 yields

$$\sigma_t = f_{ct} - \frac{E_T \varepsilon_{pt}(1 - \lambda - \delta)}{\delta} \quad (8)$$

Because of the linear hardening of the stress-strain relationship, the peak strain of concrete in tension can be written as

$$\varepsilon_{pt} = \frac{f_{ct}}{E} \quad (9)$$

Replacing Equations 9 and 5 in Equation 8, the tensile stress in softening portion is given by

$$\sigma_t = f_{ct}\left[1 - E^* \frac{(1 - \lambda - \delta)}{\delta}\right] \quad (10)$$

According to the stress distribution diagram (Figure 3b), the compressive stress can be obtained by:

$$\sigma_c' = f_{ct} \cdot \frac{\lambda}{\delta} \quad (11)$$

where $\sigma_c$' is the compressive stress (MPa).

The compressive and tensile horizontal forces acting on the uncracked ligament (Equations 12 and 13, respectively) are defined multiplying the tensile strength of concrete by the area of the stress distribution diagram:

$$F_c = \frac{\sigma_c' \cdot \lambda \cdot h \cdot b_w}{2} \quad (12)$$

$$F_t = \frac{f_{ct} \cdot \delta \cdot h \cdot b_w}{2} + \frac{(f_{ct} + \sigma_t)}{2}(1 - \lambda - \delta) \cdot h \cdot b_w \quad (13)$$

where $F_c$ is the horizontal compressive force (N), $F_t$ is the horizontal tensile force (N), h is the rectangular section height (mm), and $b_w$ is a rectangular section width (mm).

The first equilibrium condition should be satisfied, since no external horizontal forces act on the section, thus:

$$F_c + F_t = 0 \tag{14}$$

$$\frac{1}{2}\left(\sigma_c' \cdot \lambda \cdot h \cdot b_w\right) = \frac{1}{2}\left(f_{ct} \cdot \delta \cdot h \cdot b_w\right) + \frac{1}{2}(f_{ct} + \sigma_t)(1 - \lambda - \delta) \cdot h \cdot b_w \tag{15}$$

Substituting Equations 10 and 11 in Equation 15, the first equilibrium condition is defined as

$$\lambda^2\left(1 + E^*\right) + 2\lambda\left(\delta + E^*\delta - E^*\right) + \left[\delta^2\left(1 + E^*\right) - 2\delta\left(1 + E^*\right) + E^*\right] = 0 \tag{16}$$

The solution to the quadratic equation is given by

$$\lambda = \frac{-\left(\delta + E^*\delta - E^*\right) \pm \sqrt{2E^*\delta + 2\delta - E^*}}{\left(1 + E^*\right)} \tag{17}$$

The moment equilibrium condition is accepted when the external bending moment is equal to the ultimate moment capacity generated by the horizontal tensile force on the compression center, and can be written as

$$M_{cr} = \frac{b_w \cdot h^2}{6}\left[2f_{ct} \cdot \delta\left(\lambda + \delta\right) + \sigma_t\left(1 - \lambda - \delta\right)\left(\lambda + 3\delta + 3\right) + (f_{ct} - \sigma_t)(1 - \lambda - \delta)\left(\lambda + 2\delta + 1\right)\right] \tag{18}$$

Finally, applying properties $I_g$ and $y_t$ for rectangular cross-section, and replacing Equation 18 in Equation 2, Ananthan et al. [22] defined $\alpha_{fl}$ as

$$\alpha_{fl} = 3 - 2\lambda + E^*\frac{(\delta + 2)}{\delta}(2\delta + 2\lambda - 1) - (\delta + \lambda)^2\left[1 + \frac{E^*(\delta + 2)}{\delta}\right] \tag{19}$$

Equation 19 represents $\alpha_{fl}$ for a rectangular cross-section. It is noteworthy that the characterization of the stress distribution diagram and knowledge of the stress-strain relationship in tension are sufficient to obtain $\alpha_{fl}$.

## 3 SOLUTION FOR UNUSUAL CROSS-SECTIONS

The theoretical analysis was developed in two phases. The first involved the definition of the geometry of the cross-sections and mechanical parameters employed, whereas in the second, the ultimate moment capacity of the cross-sections was calculated by the moment-curvature diagram, and $\alpha_{fl}$ was obtained for normal and high strength concretes of 20 to 90 MPa. Six different aggregate types, namely basalt, diabase, granite, gneiss, limestone, and sandstone were considered in each series.

### 3.1 Geometry of the cross-sections of precast concrete structures

Thirty-two cross-sections usually applied in precast concrete structures were employed. They were divided into four groups of eight and coined according to both structural element type and application position in situ. The BCS Group was comprised of one-dimensional structural elements frequently used in precast concrete buildings, such as beams, columns, and piles, and the FLS Group considered structural elements of one and two dimensions employed in buildings and bridge floors (e.g., slabs, rails, filler blocks, and double tees). Structural elements, such as U and Y-beams and tiles used in roofs of commercial and industrial buildings were inserted in the RFS group. Finally, the BRS Group was comprised of buried large structural elements employed in waterway and highway infrastructures (e.g., culverts and tunnels). Figure 4 illustrates the geometry of the cross-sections evaluated.

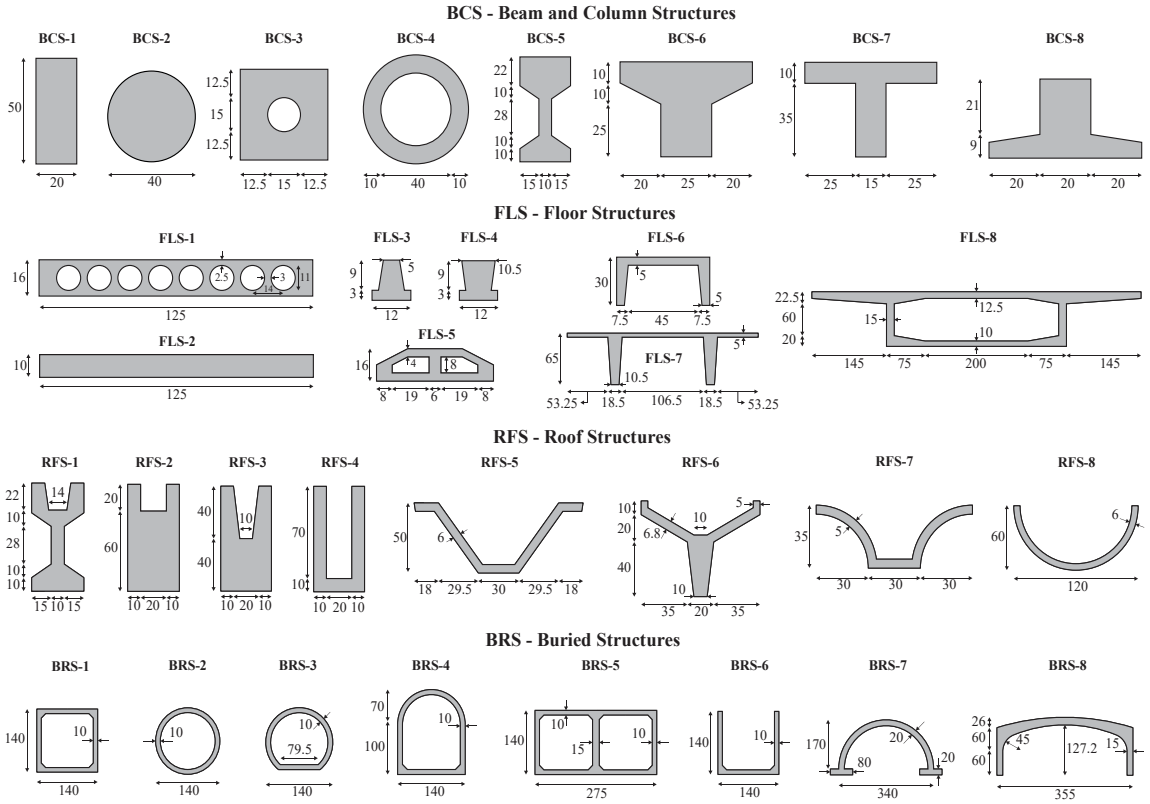


**Figure 4.** Geometry of the cross-sections of precast concrete groups (dimensions in cm).

### 3.2 Mechanical parameters

The compressive behavior of concrete was described from a parabola-rectangle stress-strain relationship recommended by ABNT NBR 6118 [9], which shows an initial parabolic branch, and a constant branch between the strain at the maximum compressive strength and the ultimate compressive strain. [9]. The tensile behavior of concrete is represented by a bilinear stress-strain relationship proposed by Bažant and Oh [24]. This law considers a linear hardening characterized by the elastic modulus, and a linear softening after the tensile strength of concrete has been reached. Its ultimate tensile strain was 10 times greater than the peak tensile strain ($\varepsilon_{ut} = 10\varepsilon_{pt}$) according to ACI 224.2R [25]. Safety factors $\beta$ and $\gamma_c$ were considered in stress-strain diagrams and assumed values of 0.85 and 1.4, respectively, in accordance with ABNT NBR 6118 [9]. In this paper, the steel reinforcement contribution was not considered because only the portion of tensile strength of concrete is employed to assess the cracking moment of the structural elements. Figure 5 shows the compressive and tensile behaviors of concrete.

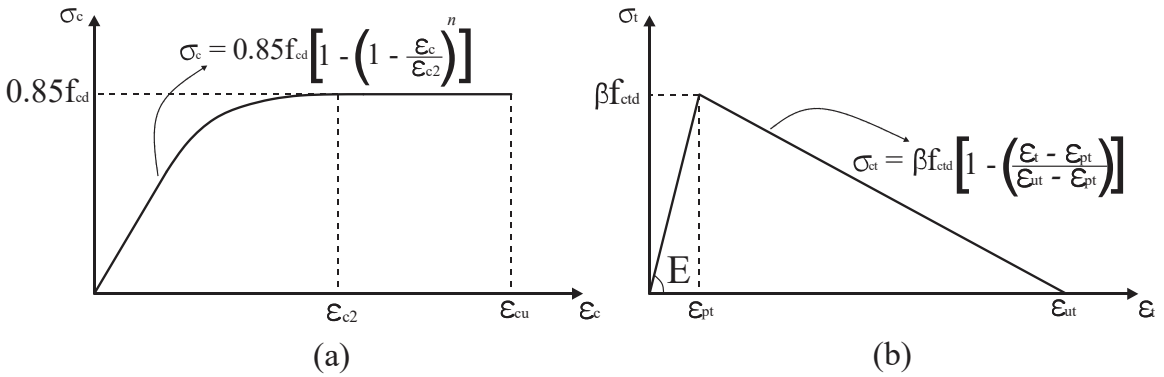


**Figure 5.** Mechanical behavior of concrete: (a) Compression and (b) tension.

The mechanical properties were obtained from the characteristic compressive strength of concrete ($f_{ck}$) using relationships indicated in ABNT NBR 6118 [9], leading to valid results. Table 1 displays the relationships employed for the mechanical properties of concrete.

**Table 1.** Summary of the mechanical properties of concrete.

| Property | $f_{ck} \leq 50$ MPa | $f_{ck} > 50$ MPa |
|---|---|---|
| $f_{cd}$ | $f_{ck}/\gamma_c$ | $f_{ck}/\gamma_c$ |
| $f_{ctd}$ | $0.21f_{ck}^{2/3}/\gamma_c$ | $0.7\left[2.12\ln\left(1+0.11f_{ck}\right)\right]/\gamma_c$ |
| E | $5600\alpha_e f_{ck}^{1/2}$ | $21500\alpha_e\left(0.1f_{ck}+1.25\right)^{1/3}$ |
| $\varepsilon_{c2}$ | 2.0‰ | $2.0‰ + 0.085‰\left(f_{ck}-50\right)^{0.53}$ |
| $\varepsilon_{cu}$ | 3.5‰ | $2.6‰ + 35‰\left[\left(90-f_{ck}\right)/100\right]^4$ |
| n | 2.0 | $1.4 + 23.4\left[\left(90-f_{ck}\right)/100\right]^4$ |
| $\varepsilon_{pt}$ | $\beta f_{ctd}/E$ | $\beta f_{ctd}/E$ |
| $\varepsilon_{ut}$ | $10\varepsilon_{pt}$ | $10\varepsilon_{pt}$ |

Note: $f_{ck}$ is the characteristic compressive strength of concrete (MPa), $f_{cd}$ is the design compressive strength of concrete (MPa), $f_{ctd}$ is the design tensile strength of concrete (MPa), E is the elastic modulus of concrete (MPa), $\alpha_e$ is the correction factor of elastic modulus according to aggregate type, $\varepsilon_{c2}$ is the strain at the maximum compressive strength, $\varepsilon_{cu}$ is the ultimate compressive strain, $\varepsilon_{ut}$ is the ultimate tensile strain, $\varepsilon_{pt}$ is the peak tensile strain, n is the exponent of compressive stress law, and $\beta$ and $\gamma_c$ are safety factors.

The ultimate moment capacity was determined by the moment-curvature relations from a section analysis of the precast concrete elements. The geometry of the cross-sections, mechanical properties, stress-strain diagrams of concrete, force equilibrium, and strain compatibility were used for the obtaining of the moment-curvature relationships, assuming plane sections remained plane after bending. The neutral axis depth was adjusted for a given compressive strain of concrete, for satisfying the equilibrium of the internal forces, and the moment was calculated. The moment-curvature curves exhibited a linear branch up to the peak tensile strain of concrete, with a subsequent nonlinear behavior until the ultimate tensile strain had been achieved. The elastic modulus was multiplied by a correction factor ($\alpha_e$) that assumed values of 1.2, 1.0, 0.9 and 0.7 for mix compositions with basalt/diabase, granite/gneiss, limestone and sandstone, respectively, for consideration of the different aggregate types, thus changing the peak and ultimate tensile strain of concrete. Finally, Equation 20 determined $\alpha_{fl}$.

$$\alpha_{fl} = \frac{M_{cr} \cdot y_t}{\beta \cdot f_{ctd} \cdot I_g} \tag{20}$$

## 4 RESULTS AND DISCUSSIONS

Firstly, the theoretical model was compared with a combination of experimental results from flexural and uniaxial tensile tests conducted by Sorelli et al. [15], Lin et al. [17] and Wee et al. [26] in rectangular cross-section specimens. Different samples were tested under direct tensile and four- or three-point bending. The tensile strength of concrete was evaluated in models with 3 to 90-day curing time and 10 to 70 MPa compressive strength for distinct mix compositions.

The experimental and theoretical results of the comparison of $\alpha_{fl}$ (Figure 6) show the theoretical model reasonably agreed with the experimental data. The higher differences were observed in tests performed at early ages, which showed small compressive strength. Numerous operations are performed on the specimens at this stage, and their properties are widely influenced by temperature, humidity, and curing conditions [1]. Besides, the drying shrinkage occurs by the imposition of tensile stress fields on concrete [16]. The difference between experimental and theoretical results was approximately 10%, considering normal and high strength concretes above 20 MPa. Therefore, the theoretical model showed a good fit for the strengths scope considered in this study.

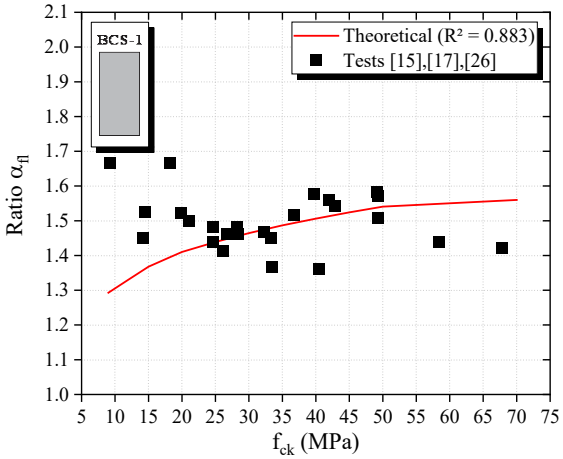


**Figure 6.** Comparison between theoretical and experimental results.

The results were also divided into two topics. Firstly, $\alpha_{fl}$ was addressed in terms of compressive strength of concrete, aggregate type used in the mixture, and ultimate tensile strain, and in the second topic, it was compared according to different prediction models.

### 4.1 Influence of compressive strength of concrete and aggregate type

An extensive theoretical analysis evaluated the influence of the compressive strength of concrete and aggregate type on $\alpha_{fl}$. Table 2 shows $\alpha_{fl}$ calculated for a typical concrete with $f_{ck}$ = 40 MPa and different types of aggregates. The results indicate the aggregate type used in the mix composition exerts a moderate influence on $\alpha_{fl}$. Low-stiffness aggregates provided greater deformability to the concrete [27], and compositions obtained higher values for $\alpha_{fl}$. The use of basaltic aggregates as reference promoted up to 12.9%, 6.9% and 4.3% increases for concretes that used sandstone, limestone, and granite aggregates, respectively, for all series analyzed. The difference decreased in function of the increase in the compressive strength of concrete.

**Table 2.** Variation in $\alpha_{fl}$ according to aggregate type for $f_{ck}$ = 40 MPa.

| Group | Section | Aggregate type | | | | Mean | CV (%) |
|---|---|---|---|---|---|---|---|
| | | Basalt or Diabase | Granite or Gneiss | Limestone | Sandstone | | |
| BCS | BCS-1 | 1.46 | 1.51 | 1.54 | 1.61 | 1.53 | 4.10 |
| | BCS-2 | 1.68 | 1.75 | 1.79 | 1.87 | 1.77 | 4.48 |
| | BCS-3 | 1.40 | 1.45 | 1.46 | 1.52 | 1.46 | 3.38 |
| | BCS-4 | 1.43 | 1.46 | 1.50 | 1.54 | 1.48 | 3.23 |
| | BCS-5 | 1.19 | 1.22 | 1.23 | 1.26 | 1.23 | 2.36 |
| | BCS-6 | 1.40 | 1.44 | 1.47 | 1.52 | 1.46 | 3.47 |
| | BCS-7 | 1.38 | 1.41 | 1.42 | 1.46 | 1.42 | 2.33 |
| | BCS-8 | 1.37 | 1.41 | 1.43 | 1.49 | 1.43 | 3.51 |
| FLS | FLS-1 | 1.26 | 1.29 | 1.31 | 1.33 | 1.30 | 2.30 |
| | FLS-2 | 1.46 | 1.51 | 1.54 | 1.61 | 1.53 | 4.10 |
| | FLS-3 | 1.40 | 1.45 | 1.48 | 1.55 | 1.47 | 4.27 |
| | FLS-4 | 1.38 | 1.42 | 1.45 | 1.51 | 1.44 | 3.80 |
| | FLS-5 | 1.32 | 1.35 | 1.37 | 1.42 | 1.37 | 3.08 |
| | FLS-6 | 1.42 | 1.46 | 1.47 | 1.51 | 1.47 | 2.52 |
| | FLS-7 | 1.44 | 1.48 | 1.49 | 1.53 | 1.49 | 2.49 |
| | FLS-8 | 1.08 | 1.09 | 1.10 | 1.12 | 1.10 | 1.56 |
| RFS | RFS-1 | 1.22 | 1.24 | 1.26 | 1.29 | 1.25 | 2.38 |
| | RFS-2 | 1.48 | 1.54 | 1.57 | 1.66 | 1.56 | 4.80 |

**Table 2.** Continued...

| Group | Section | Aggregate type | | | | Mean | CV (%) |
|---|---|---|---|---|---|---|---|
| | | Basalt or Diabase | Granite or Gneiss | Limestone | Sandstone | | |
| | RFS-3 | 1.51 | 1.57 | 1.60 | 1.68 | 1.59 | 4.45 |
| | RFS-4 | 1.31 | 1.35 | 1.38 | 1.44 | 1.37 | 4.00 |
| | RFS-5 | 1.27 | 1.31 | 1.33 | 1.38 | 1.32 | 3.46 |
| | RFS-6 | 1.53 | 1.59 | 1.62 | 1.70 | 1.61 | 4.39 |
| | RFS-7 | 1.23 | 1.26 | 1.27 | 1.32 | 1.27 | 2.95 |
| | RFS-8 | 1.37 | 1.42 | 1.44 | 1.51 | 1.44 | 4.04 |
| BRS | BRS-1 | 1.12 | 1.14 | 1.16 | 1.19 | 1.15 | 2.59 |
| | BRS-2 | 1.29 | 1.32 | 1.34 | 1.39 | 1.34 | 3.15 |
| | BRS-3 | 1.17 | 1.21 | 1.22 | 1.26 | 1.22 | 3.04 |
| | BRS-4 | 1.13 | 1.16 | 1.18 | 1.22 | 1.17 | 3.22 |
| | BRS-5 | 1.11 | 1.13 | 1.14 | 1.18 | 1.14 | 2.58 |
| | BRS-6 | 1.14 | 1.17 | 1.19 | 1.24 | 1.19 | 3.55 |
| | BRS-7 | 1.18 | 1.21 | 1.23 | 1.27 | 1.22 | 3.09 |
| | BRS-8 | 1.40 | 1.44 | 1.46 | 1.51 | 1.45 | 3.15 |

Figure 7 more clearly shows the influence of the aggregate type on $\alpha_{fl}$. According to the correlations between the mechanical properties of concrete in Table 1, the elastic modulus reduction due to the aggregate type caused more deformability and improved the ultimate tensile strain of the concrete. Additionally, for the same tensile strength of concrete, the increase in the ultimate tensile strain reduced the softening branch slope and the strain softening modulus ($E_T$), increasing $\alpha_{fl}$. On the other hand, the $\alpha_{fl}$ ratio of concretes with aggregates of lower elastic modulus showed a smaller increment than concretes with aggregates of larger elastic modulus (Figure 7). $\alpha_{fl}$ can be sequentially higher in concretes with basalt, granite, limestone and sandstone, respectively, for the same ultimate tensile strain value.

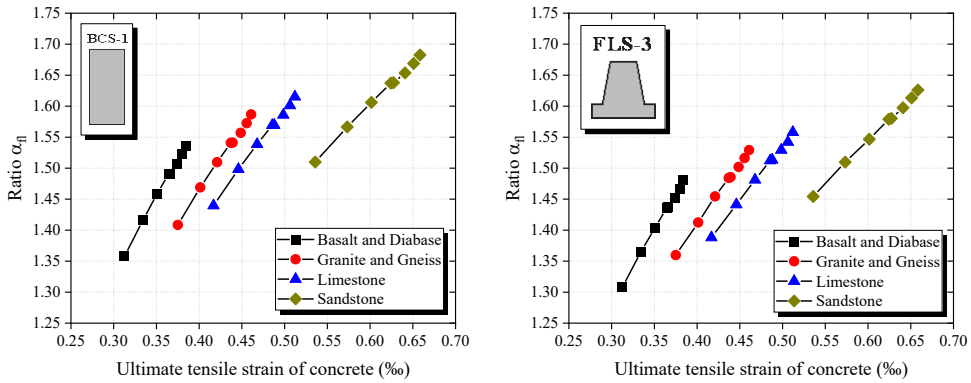


**Figure 7.** Variation in $\alpha_{fl}$ with ultimate tensile strain for BCS-1 and FLS-3.

The increase in the compressive strength of concrete conduct to an increase in the tensile strength of the concrete reducing the neutral axis depth ($\lambda$) in structural elements subjected to bending (see Figure 4b), which smoothly increases the $\alpha_{fl}$ ratio, according to Equation 19. The $\alpha_{fl}$ value increased to 9.5% on average when the compressive strength of concrete improved from 20 MPa to 90 MPa. However, normal strength concretes (20 MPa to 50 MPa) showed an up to 7% increase against only 2.5% of high strength ones (60 MPa to 90 MPa).

Figures 8, 9, 10 and 11 show $\alpha_{fl}$ in terms of compressive strength of concrete and aggregate type for BCS, FLS, RFS and BRS groups, respectively.

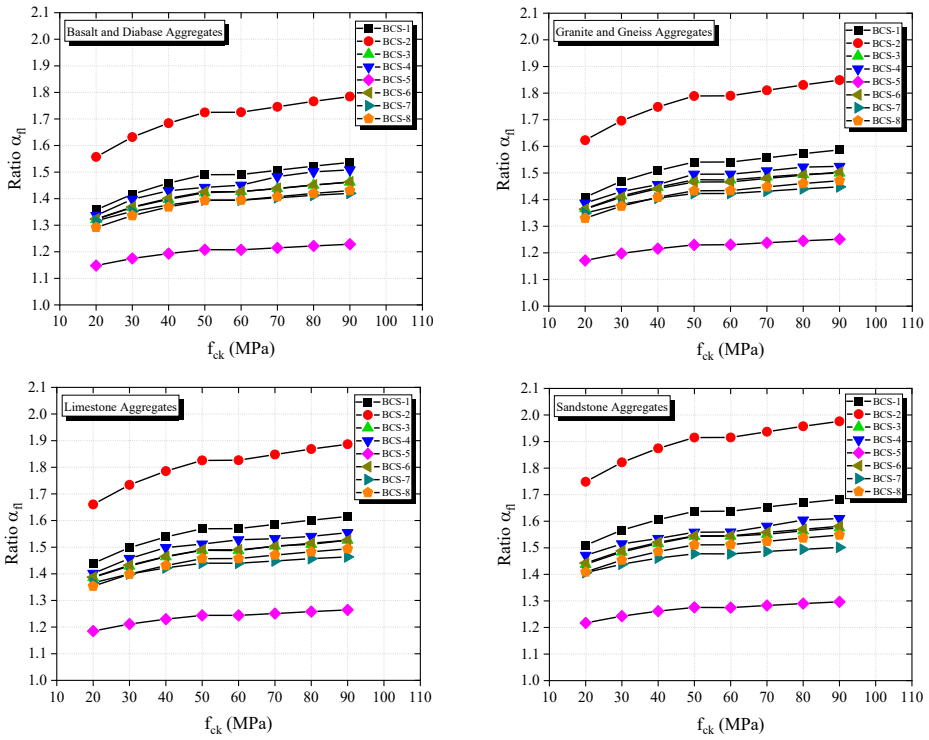


**Figure 8.** Variation in $\alpha_{fl}$ with compressive strength for BCS Group.

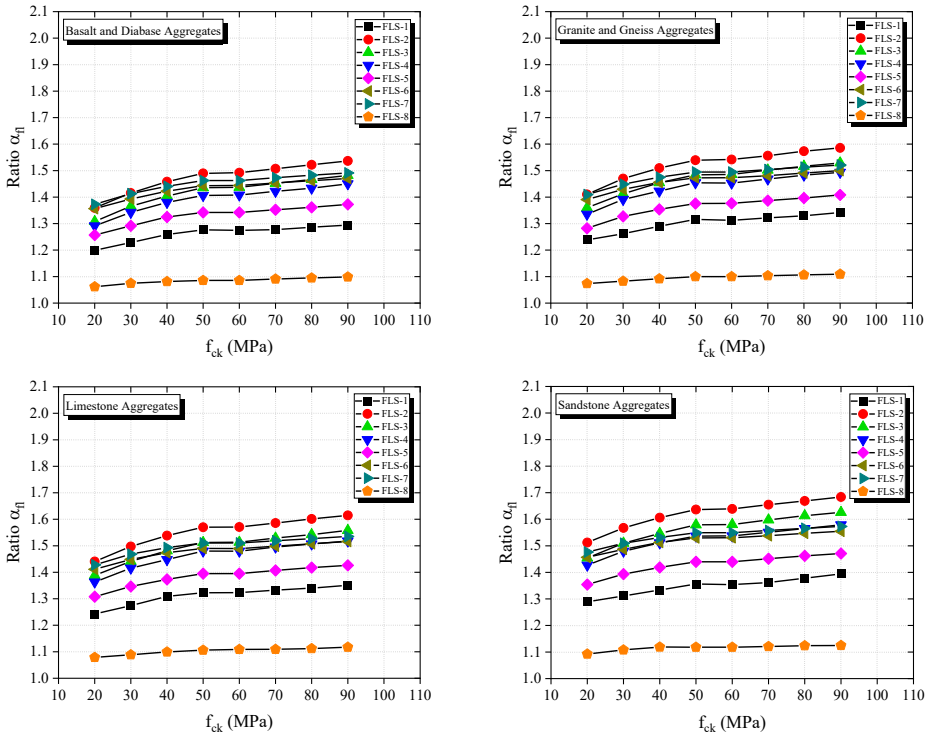


**Figure 9.** Variation in $\alpha_{fl}$ with compressive strength for FLS Group.

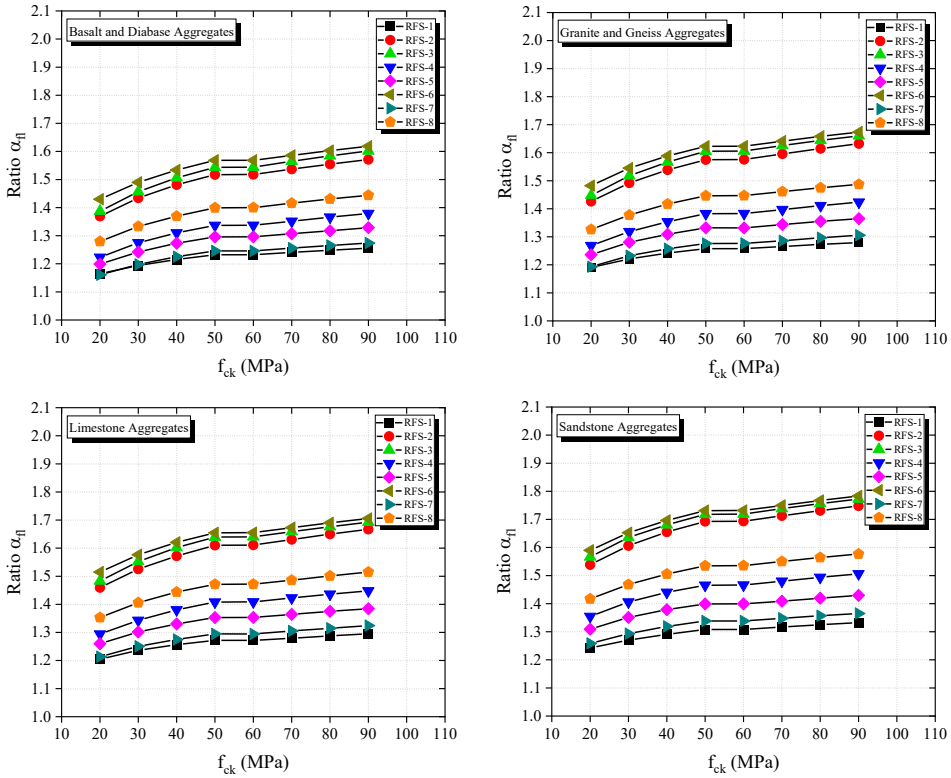


**Figure 10.** Variation in $\alpha_{fl}$ with compressive strength for RFS Group.

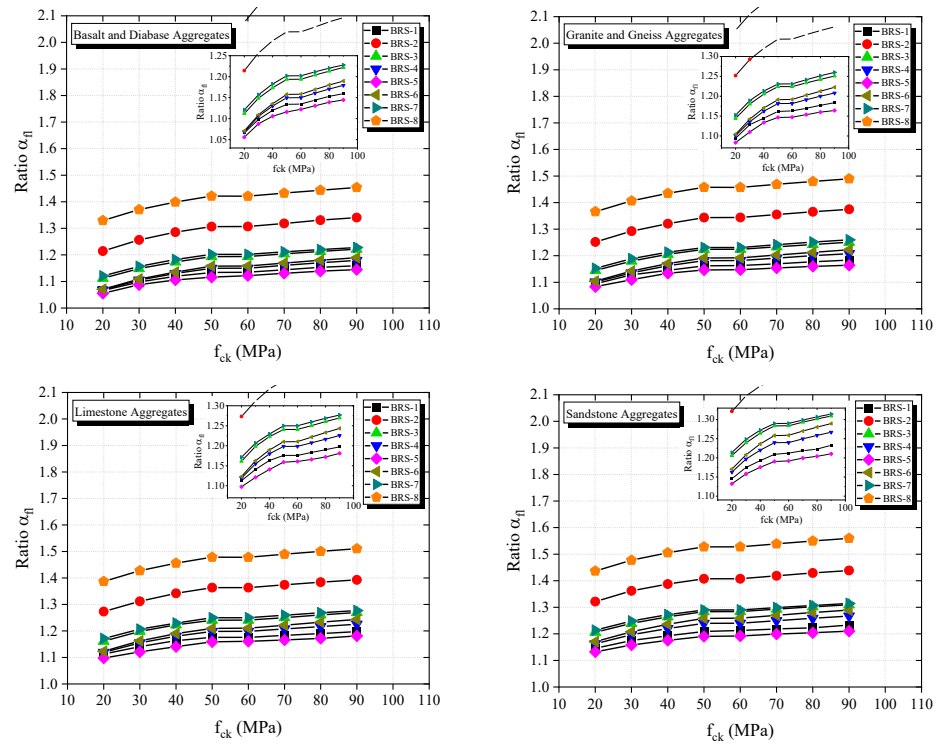


**Figure 11.** Variation in $\alpha_{fl}$ with compressive strength for BRS Group.

The $\alpha_{fl}$ variation in terms of compressive strength of concrete showed constant values for 50 MPa and 60 MPa compressive strengths due to the distinct mechanical parameters adopted for normal and high strength concretes (Table 1). Regarding mechanical properties, the linear compressive stress-strain relationship employed in the analytical solution proposed by Ananthan et al. [22] was different from the parabola-rectangle stress-strain one used in this study. However, the ultimate moment capacity produces small compressive stresses in the top fiber of the cross-section, and the stress-strain relationship in compression exerts a small influence on $\alpha_{fl}$.

According to the results, 75.1% of the calculated values of $\alpha_{fl}$ remained between 1.20 and 1.60. Values above this range were mostly obtained by circular cross-section (BCS-2), rectangular cross-sections (BCS-1 and FLS-2), and U and Y-beams (RFS-2/3/6) used as roof structural elements. On the other hand, 14.6% of the results ($\alpha_{fl} < 1.20$) were associated with large structural elements, such as cross-sections for box culverts (BRS-1/3/4/5) and box girder bridges (FLS-8). The $\alpha_{fl}$ decrease in such structural elements may be related to the size effect phenomenon. According to [28]-[30], the flexural tensile strength of specimens of large dimensions is reduced due to an increase in the cross-section height. In this study, the size effect was milder in elements with circular segments, such as cross-sections for tunnels (BRS-2/7/8).

### 4.2 Comparison with prediction models

The theoretical results of $\alpha_{fl}$ were compared with different prediction models from the literature. Codes for the design of concrete structures have shown fixed values or simple expressions for $\alpha_{fl}$. According to Model Code [14], $\alpha_{fl}$ depends only on the cross-section height and is reduced with its increase. In contrast, ABNT NBR 6118 [9] recommends the use of fixed values for $\alpha_{fl}$. Both models disregard the mechanical characteristics of the structural element.

Based on nonlinear fracture mechanics, Buchaim [23], Müller and Hilsdorf [31] and Rokugo et al. [32] proposed analytical models considering the influence of the characteristic length ($l_{ch}$) on the flexural behavior, defined by Hillerborg et al. [10] according to both fracture energy and mechanical properties of concrete. Although this parameter has no direct physical meaning, it is a property that determines the fracture process zone size [13]. Table 3 shows the summarized expressions of the codes and authors for the prediction of $\alpha_{fl}$.

**Table 3.** Summary of the expressions for $\alpha_{fl}$.

| Model | Ratio $\alpha_{fl}$ |
|---|---|
| Model Code [14] | $\alpha_{fl} = \frac{1+0.06h^{0.7}}{0.06h^{0.7}}$ |
| Müller and Hilsdorf [31] | $\alpha_{fl} = \frac{\left[1 + \alpha_{mh}\left(0.01h\right)^{0.7}\right]}{\left(\alpha_{mh}\left(0.01h\right)^{0.7}\right)}$; with $\alpha_{mh} = 0.8 + \frac{5}{\left(0.01l_{ch}\right)^{1.5}}$ and $l_{ch} = \frac{G_f E}{{f_{ct}}^2}$ |
| ABNT NBR 6118 [9] | $\alpha_{fl}$ = 1.5, 1.3 or 1.2 for rectangular, I and T beams, respectively. |
| Buchaim [23] | $\alpha_{fl} = 1 + 2\eta\left[\frac{3 - 6\eta + 3\left(1 - B\right)\eta^2 + 2B\eta^3}{3 - 6\eta + \left(B + 3\right)\eta^2}\right]$; with $\eta = \frac{a_d}{h}$ and $B = \frac{{f_{ct}}^2 L}{2G_f E}$ |
| Rokugo et al. [32] | $\alpha_{fl} = \frac{\left[1 + 0.85 + 4.5\left(h/l_{ch}\right)\right]}{\left[0.85 + 4.5\left(h/l_{ch}\right)\right]}$; with $l_{ch} = \frac{G_f E}{{f_{ct}}^2}$ |

Note: $\lambda$ and $\delta$ are factors of the characterization of the stress-strain distribution diagram, h is the cross-section height (mm), $l_{ch}$ is the characteristic length (mm), $G_f$ is the fracture energy of concrete (N.mm), E is the elastic modulus of concrete (MPa), $f_{ct}$ is the direct tensile strength of concrete (MPa), $a_d$ is the fictitious crack height (mm), and L is the structural element length (mm).

Figure 12 shows $\alpha_{fl}$ for each prediction model compared to theoretical results for rectangular cross-section (BCS-1). The energy fracture was obtained according to the Model Code [14], and a 0.10 h/L ratio was considered. Predictions of design codes do not compute the concrete composition and show constant values for $\alpha_{fl}$. The results ranged between 1.22 and 1.50 for Model Code [14] and ABNT NBR 6118 [9], respectively, whereas in the other prediction models, they varied up to 10% due to an increase in the compressive strength of concrete. The largest variations between the prediction models evaluated ranged between 36.8% and 26.5% for normal and high strength concretes, respectively.

Although most prediction models are defined only for rectangular cross-sections, ABNT NBR 6118 [9] establishes $\alpha_{fl}$ for I and T beams – see Figure 13 for a comparison of $\alpha_{fl}$ for rectangular, and I and T beams.

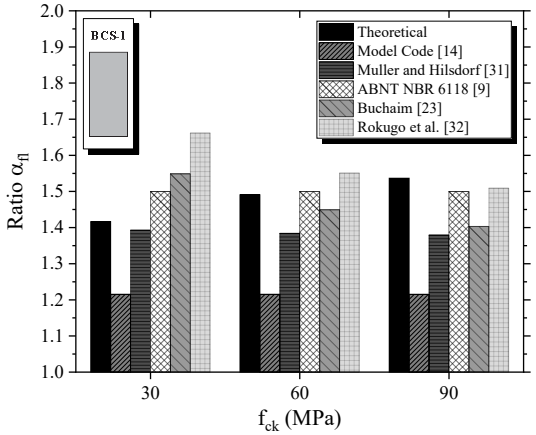


**Figure 12.** Comparison of $\alpha_{fl}$ obtained by different prediction models.

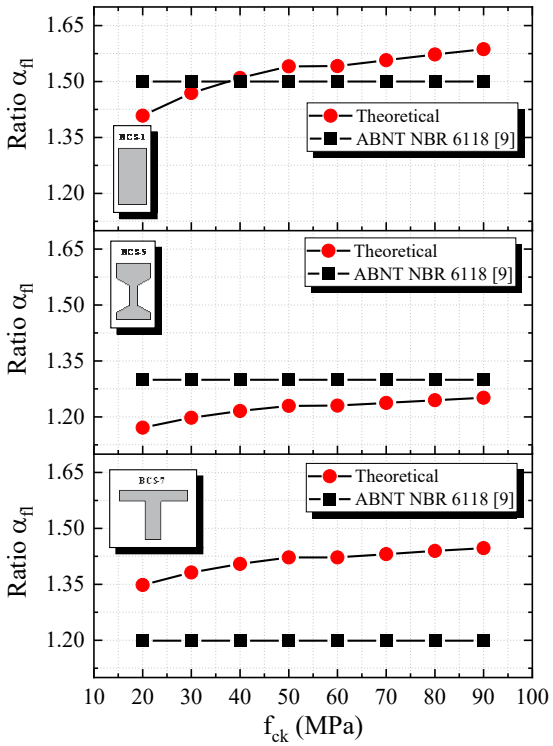


**Figure 13.** $\alpha_{fl}$ for rectangular, I and T beams: Theoretical results vs. ABNT NBR 6118 [9].

In general, the theoretical procedure used in this study showed a good agreement with the prediction models described, except for Model Code [14], which was more conservative. A greater disparity was observed for low strength concretes, which subsequently balanced $\alpha_{fl}$ with the increase in the compressive strength.

## 5 CONCLUSIONS

This study reported a theoretical analysis of ratio $\alpha_{fl}$ for unusual cross-sections widely used in precast concrete structures. Thirty-two different cross-sections were evaluated and divided into four groups of elements commonly

employed in beams, columns, floors, roofs, and buried structures. Fictitious crack model considerations were used in the theoretical analysis for the obtaining of the ultimate moment capacity of precast concrete elements. Parametric studies investigated the effects of the compressive strength of concrete and aggregate type of the mix composition on $\alpha_{fl}$. Normal and high strength concretes of 20 MPa to 90 MPa compressive strength and six aggregate types were considered in the analysis.

An increment in the compressive strength of concrete smoothly increased $\alpha_{fl}$. Similarly, lower elastic modulus aggregates caused a greater deformability in the concrete and increased $\alpha_{fl}$. Such an increment in $\alpha_{fl}$ due to the compressive strength and aggregate type was higher in normal strength concretes than in high strength ones. The analyses revealed 75.1% of ratio $\alpha_{fl}$ results ranged between 1.20 and 1.60, highlighting its higher values for circular, rectangular, and U and Y beams. On the other hand, buried large cross-sections showed a significant decrement in $\alpha_{fl}$ due to the size effect.

The proposed methodology was compared with experimental results, and prediction models from the literature showed a reasonable agreement, with more significant differences observed concerning the Model Code [14]. According to the results, the theoretical procedure has proven a viable alternative and can be a consistent way for assessing the $\alpha_{fl}$ of precast concrete elements with unusual cross-sections.

## ACKNOWLEDGEMENTS

This study was partially financed by the Coordenação de Aperfeiçoamento de Pessoal de Nível Superior – Brasil (CAPES) – Finance Code 001 and CNPq (Brazilian government agency for research - Finance Code Nº 302479/2017-1).

## REFERENCES

[1] P. K. Mehta and P. J. M. Monteiro, *Concrete: Microstructure, properties and materials*, 3rd ed. New York, United States: McGraw-Hill, 2006.

[2] American Concrete Institute, *Building code requirements for structural concrete*, ACI Committee 318, 2019.

[3] R. V. Silva, J. de Brito, and R. K. Dhir, "Tensile strength behaviour of recycled aggregate concrete," *Constr. Build. Mater.*, vol. 83, pp. 108–118, May 2015, http://dx.doi.org/10.1016/j.conbuildmat.2015.03.034.

[4] European Committee for Standardization, *Testing hardened concrete: Tensile splitting strength of test specimens*, EN 12390-6, 2009.

[5] European Committee for Standardization, *Testing hardened concrete: Flexural strength of test specimens*, EN 12390-5, 2019.

[6] S. Wu, X. Chen, and J. Zhou, "Tensile strength of concrete under static and intermediate strain rates: Correlated results from different testing methods," *Nucl. Eng. Des.*, vol. 250, pp. 173–183, Sep 2012, http://dx.doi.org/10.1016/j.nucengdes.2012.05.004.

[7] J. Á. López, P. Serna, J. Navarro-Gregori, and E. Camacho, "An inverse analysis method based on deflection to curvature transformation to determine the tensile properties of UHPFRC," *Mater. Struct.*, vol. 48, pp. 3703–3718, Oct 2015, http://dx.doi.org/10.1617/s11527-014-0434-0.

[8] X. Chen, S. Wu, J. Zhou, Y. Chen, and A. Qin, "Effect of testing method and strain rate on stress-strain behavior of concrete," *J. Mater. Civ. Eng.*, vol. 25, no. 11, pp. 1752–1761, Nov 2013, http://dx.doi.org/10.1061/(ASCE)MT.1943-5533.0000732.

[9] Associação Brasileira de Normas Técnicas, *Projeto de estruturas de concreto: Procedimento*, ABNT NBR 6118, 2014.

[10] A. Hillerborg, M. Modéer, and P.-E. Petersson, "Analysis of crack formation and crack growth in concrete by means of fracture mechanics and finite elements," *Cement Concr. Res.*, vol. 6, no. 6, pp. 773–781, Nov 1976. http://dx.doi.org/10.1016/0008-8846(76)90007-7.

[11] A. R. Murthy, B. L. Karihaloo, N. R. Iyer, and B. K. R. Prasad, "Bilinear tension softening diagrams of concrete mixes corresponding to their size-dependent specific fracture energy," *Constr. Build. Mater.*, vol. 47, pp. 1160–1166, Oct 2013., http://dx.doi.org/10.1016/j.conbuildmat.2013.06.004.

[12] M. Maalej and V. C. Li, "Flexural/tensile-strength ratio in engineered cementitious composites," *J. Mater. Civ. Eng.*, vol. 6, no. 4, pp. 513–528, Nov 1994, http://dx.doi.org/10.1061/(ASCE)0899-1561(1994)6:4(513).

[13] M. Maalej and V. C. Li, "Flexural strength of fiber cementitious composites," *J. Mater. Civ. Eng.*, vol. 6, no. 3, pp. 390–406, Nov 1994, http://dx.doi.org/10.1061/(ASCE)0899-1561(1994)6:3(390).

[14] International Federation for Structural Concrete, *fib Model Code 2010*, MC2010, 2010.

[15] L. G. Sorelli, A. Meda, and G. A. Plizzari, "Bending and uniaxial tensile tests on concrete reinforced with hybrid steel fibers," *J. Mater. Civ. Eng.*, vol. 17, no. 5, pp. 519–527, Oct 2005, http://dx.doi.org/10.1061/(ASCE)0899-1561(2005)17:5(519).

[16] J. T. Balbo, "Relations between indirect tensile and flexural strengths for dry and plastic concretes," *Rev. IBRACON Estrut. Mater.*, vol. 6, no. 6, pp. 854–874, Dec 2013, http://dx.doi.org/10.1590/S1983-41952013000600003.

[17] W. T. Lin, A. Cheng, R. Huang, and T. C. Cheng, "A method for testing the strength of concrete using uniaxial direct tension," *J. Chin. Inst. Eng.*, vol. 36, no. 3, pp. 295–303, Jul 2013, http://dx.doi.org/10.1080/02533839.2012.725912.

[18] F. L. Monte and L. Ferrara, "Tensile behaviour identification in Ultra-High Performance Fibre Reinforced Cementitious Composites: indirect tension tests and back analysis of flexural test results," *Mater. Struct.*, vol. 53, no. 145, pp. 1–12, Nov 2020, http://dx.doi.org/10.1617/s11527-020-01576-8.

[19] V. G. Haach and M. A. C. Paiva, "Application of the rebound test for the technological control of concrete hollow-core slabs," *Rev. IBRACON Estrut. Mater.*, vol. 13, no. 4, pp. 1–14, Aug 2020, http://dx.doi.org/10.1590/S1983-41952020000400006.

[20] K. P. Vishalakshi, V. Revathi, and S. S. Reddy, "Effect of type of coarse aggregate on the strength properties and fracture energy of normal and high strength concrete," *Eng. Fract. Mech.*, vol. 194, pp. 52–60, May 2018, http://dx.doi.org/10.1016/j.engfracmech.2018.02.029.

[21] S. J. Choi, K. H. Yang, J. I. Sim, and B. J. Choi, "Direct tensile strength of lightweight concrete with different specimen depths and aggregate sizes," *Constr. Build. Mater.*, vol. 63, pp. 132–141, Jul 2014, http://dx.doi.org/10.1016/j.conbuildmat.2014.04.055.

[22] H. Ananthan, B. K. Raghuprasad, and K. T. Sundara Raja Iyengar, "Influence of strain softening on the fracture of plain concrete beams," *Int. J. Fract.*, vol. 45, pp. 195–219, Sep 1990, http://dx.doi.org/10.1007/BF00693349.

[23] R. Buchaim, “A influência da não-linearidade física do concreto armado na rigidez à flexão e na capacidade de rotação plástica,” Ph.D dissertation, Dept. Eng. Estrut. Fund., Univ. São Paulo, São Paulo, 2001.

[24] Z. P. Bažant and B. H. Oh, "Crack band theory for fracture of concrete," *Mater. Struct.*, vol. 16, no. 145, pp. 155–177, May 1983, http://dx.doi.org/10.1007/BF02486267.

[25] American Concrete Institute, *Cracking of concrete members in direct tension*, ACI Committee 224.2R, 1997.

[26] T. H. Wee, H. R. Lu, and S. Swaddiwudhipong, "Tensile strain capacity of concrete under various state of stress," *Mag. Concr. Res.*, vol. 52, no. 3, pp. 185–193, Jun 2000. http://dx.doi.org/10.1680/macr.2000.52.3.185.

[27] R. W. Sun and G. C. Fanourakis, "An assessment of factors affecting the elastic modulus of concrete," *Struct. Concr.*, vol. 22, no. 1, pp. 1–11, Feb 2021. http://dx.doi.org/10.1002/suco.202000553.

[28] A. Carpinteri and G. Ferro, "Size effects on tensile fracture properties: A unified explanation based on disorder and fractality of concrete microstructure," *Mater. Struct.*, vol. 27, pp. 563–571, Dec 1994, http://dx.doi.org/10.1007/BF02473124.

[29] M. Herbrand, A. Stark, and J. Hegger, "Size effect in unnotched concrete specimens in bedding: An analytical approach," *Struct. Concr.*, vol. 20, no. 2, pp. 660–669, Feb 2019, http://dx.doi.org/10.1002/suco.201800136.

[30] Z. P. Bažant and D. Novak, "Proposal for standard test of modulus of rupture of concrete with its size dependence," *ACI Mater. J.*, vol. 98, no. 1, pp. 79–87, Jan 2001.

[31] H. S. Müller and H. K. Hilsdorf, “Constitutive relations of structural concrete,” *CEB Bullet. Inf.*, no. 217, pp. 17-65, Apr, 1993.

[32] K. Rokugo, Y. H. Katoh, and W. Koyanagi, "Fracture mechanics approach to evaluation of flexural strength of concrete," *ACI Mater. J.*, vol. 92, no. 5, pp. 561–566, Jan 1993.

**Author contributions:** JADFN: conceptualization, methodology, validation, data curation, formal analysis, writing – original draft; VGH: conceptualization, methodology, project administration, supervision, writing – review & editing.

**Editors:** Luís Oliveira Santos, Guilherme Aris Parsekian.

IBRACON Structures and Materials Journal
Revista IBRACON de Estruturas e Materiais
ISSN 1983-4195 ismj.org

ORIGINAL ARTICLE

# Influence of concrete strength on the distribution of bending moment in widened curved bridges

## *Influência da resistência do concreto na distribuição do momento fletor em pontes curvas alargadas*

Yngrid Rayane Freitas Nascimento[a]
José Neres da Silva Filho[a]
Arthur da Silva Rebouças[b]
Rodrigo Barros[a]
Joel Araújo do Nascimento Neto[a]

[a]Universidade Federal do Rio Grande do Norte – UFRN, Programa de Pós-graduação em Engenharia Civil – PEC, Natal, RN, Brasil
[b]Instituto Federal de Educação, Ciência e Tecnologia do Rio Grande do Norte – IFRN, São Paulo do Potengi, RN, Brasil

Received September 13, 2021
Accepted April 22, 2022

**Abstract:** The study proposes to analyze the distribution of bending moment due to live load in curved bridges that have undergone a process of widening, considering the influence of concrete's strength variation. The results show that the bending moment redistribution is more significant the higher the stiffness in the widenings. In addition, the redistribution induced by the variation of stiffness depends on the live load positioning but, generally, it results in the migration of bending moments to the stiffer regions, relieving the original girders. The curvature did not significantly alter the response induced by the stiffening of the widened segments. Also, the divergences found between the MEF and the V-load Method results for models with uniform and variable stiffness were similar. Finally, the Modification Factors (MF) proved to be more sensitive to the influence of curvature than to the concrete strength in the widenings.

**Keywords:** bridge widening, widening stiffness, live loads, FEM, V-load method.

**Resumo:** Esta pesquisa propõe analisar a distribuição de momentos fletores devido à carga móvel entre longarinas de pontes curvas de concreto armado que passaram por um processo de alargamento da superestrutura. Como principais conclusões foi constatado que a redistribuição de momentos é tanto mais significativa quanto mais elevada for a rigidez dos alargamentos. Ademais também foi observado que a redistribuição induzida pela variação da rigidez está condicionada à posição do carregamento móvel, porém, em geral, resultam na migração de esforços para os trechos mais rígidos, aliviando as longarinas originais. Constatou-se ainda que a variação da curvatura pouco altera a redistribuição de esforços induzida pelo aumento da rigidez no alargamento. Ademais, as divergências entre os resultados do MEF e do Método *V-Load* para os modelos com rigidez variável não divergiram significativamente daqueles obtidos nos modelos de rigidez constante. Por fim, os Fatores de Modificação (FM) mostraram-se mais sensíveis à variação do raio de curvatura do que à resistência do concreto nos alargamentos.

**Palavras-chave:** pontes alargadas, resistência do concreto, cargas móveis, MEF, método V-load.

**How to cite:** Y. R. F. Nascimento, J. N. Silva Filho, A. S. Rebouças, R. Barros, and J. A. Nascimento Neto, "Influence of concrete strength on the distribution of bending moment in widened curved bridges," *Rev. IBRACON Estrut. Mater.*, vol. 16, no. 1, e16105, 2023, https://doi.org/10.1590/S1983-41952023000100005

**Corresponding author:** Yngrid Rayane Freitas Nascimento. E-mail: yngrid.rayane.eng@gmail.com
**Financial support:** None.
**Conflict of interest:** Nothing to declare.
**Data Availability:** The data that support the findings of this study are available from the corresponding author, Y. N., upon reasonable request.

## 1 INTRODUCTION

The structural analysis of horizontally curved bridges and viaducts presents a higher complexity level when compared to similar structures with straight layouts since, due to the curvature and stiffness of the deck, some geometric parameters directly affect the structural behavior. Regardless, curved bridges have become increasingly competitive, given their structural efficiency, stability, economy, and aesthetics.

One of the most prominent subjects related to the analysis of curved bridges is the live load distribution on the deck, particularly the influence of the curvature on this mechanism. Studies such as Kim et al. [1] and Zhang et al. [2] highlight the curvature as a key parameter in the distribution of bending moments. Although relevant advances have been achieved in this field, the collected research concerning load distribution in widened curved structures is still significantly limited.

In Brazil, the geometric standards for highway bridges have been evolving since the 1940s. For the first bridges, the recommended total width was 8.30 m (27.3 ft), without considering the addition of shoulders. Nowadays, the standard width for bridges of one roadway is 12.80 m (42 ft), comprehending two lanes as well as shoulders on each side [3]. In addition to changes in the standards governing the geometric characteristics of highway bridges, the constant increase in traffic volume and, therefore, in the loads to which these structures are subjected, are factors that contribute to their poor performance. For a significant portion of Brazilian highway bridges, the need for interventions directed to the recovery, widening, or strengthening is substantial, under the risk of becoming critical points for the occurrence of accidents [4].

According to Barros and Vitório [5], the "C*onventional Widening Method with Reinforced Concrete*" is the most employed in the country. It entails the addition of reinforced concrete beams and slabs that are incorporated into the original deck. The solidarization between the original and the widened sections is usually accomplished through a slab cast in place, executed on the upper part of the deck. When using this method, the concrete in the widened section often has a higher characteristic compressive strength and, therefore, higher stiffness than the material of the original structure. Fontana [6] proposed to analyze the impact of variable stiffness in a widened straight cellular bridge, noting the significant influence of this parameter on the distribution of bending moments. Consequently, in curved bridges widened by this method, in addition to the curvature, another aspect that should considerably impact the load distribution would be the variation of stiffness along the cross section.

Thus, the main purpose of this research is to analyze the distribution of bending moments due to live loads in curved reinforced concrete bridges, considering the implementation of deck widening, to assess the effect of variable stiffness in widened sections. Furthermore, the study evaluates the influence of the curvature and the number of girders in these structures. The analysis was based primarily on the results obtained from numerical models, using the Finite Element Method, enabling the attainment of the Bending Moment Distribution Factors (BMDF) due to the live load. Additionally, the applicability of the approximate analytical method V-Load was analyzed by comparing its results with those of the FEM. In complement, the bending moments were analyzed according to an artifice proposed by Acosta and González [7], called the Modification Factor.

## 2 STRUCTURAL BEHAVIOR IN CURVED BRIDGES

The radius is the parameter that determines the deviation between the structural behavior of bridges with straight and curved layouts. In curved bridges, the curvature is responsible for setting an eccentricity between the center of gravity of the deck and the axis connecting the end supports. Thus, when the deck is subject to vertical loads, this eccentricity gives rise to torsional moments whose magnitude cannot be neglected as occurs in the analysis of straight bridges.

In a curved beam subjected to vertical loads, the actions of bending and torsional forces occur in a coupled way. Figure 1 shows an infinitesimal element of a curved beam loaded only in the direction normal to the horizontal plane by load $p$ (dead load), as well as the internal forces generated by this loading. By balancing the forces on the Y-axis is possible to obtain Equation 1:

$$\frac{dV}{ds} = -p \tag{1}$$

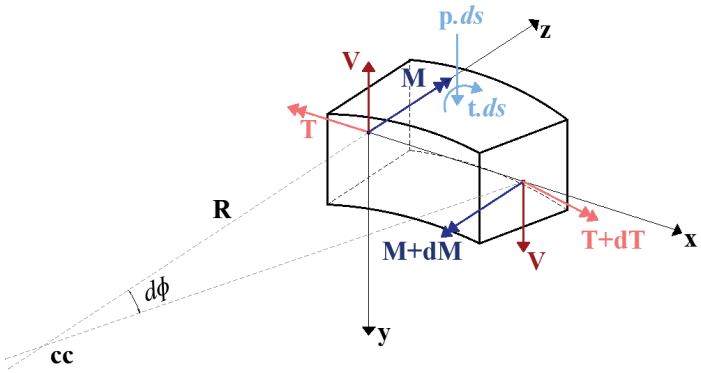


**Figure 1.** Internal forces in a curved beam element. Adapted from Barbosa [8].

Equation 1 shows that the shear force on an infinitesimal curved element does not depend on any geometric component of the beam. Therefore, one may conclude that there is no difference between a curved beam and a straight beam regarding the magnitude of the shear force, since the variation of the shear V along the segment *ds* results in the constant *p*.

From the balance of moments about the Z-axis (Figure 1) results Equation 2:

$$\frac{dM}{ds} = V - \frac{T}{R} \tag{2}$$

From the balance of moments about the X-axis results Equation 3:

$$\frac{dT}{ds} = t + \frac{M}{R} \tag{3}$$

Therefore, it is verified that there is an interaction between bending moment and torsional moment, since, according to Equations 2 and 3, the bending moment generates torsion, and the torsional moment causes longitudinal bending in the beam. It is important to highlight that both aforementioned equations are also functions of the geometric parameter radius of curvature (R). This correlation allows one to see that there is a variation of both bending moment and torsional moment along the segment *ds*, due to the radius of the curved segment.

## 3 APPROXIMATE ANALYSIS OF CURVED BRIDGES: V-LOAD METHOD

Fu and Wang [9] and AASHTO [10] classify structural analysis methods in refined and approximate. With the advance of technology, it has become much more practical and advantageous to employ refined methods, which comprises analyses in two (2D) or three dimensions (3D), instead of approximate methods, *i.e.*, a one-dimensional (1D) analysis. Although a wide variety of refined methods for structural analysis are available, among them FEM, approximate methods should not be disregarded.

Besides being simple to apply, approximate methods can be used in preliminary design, or they can serve as a parameter to validate results from more complex analysis methods. Furthermore, these methods often allow a better understanding of the structural behavior of the structures to which they are applied. For curved steel girder bridges, AASHTO [10] allows the use of the V-Load Method.

According to Fiechtl et al. [11], V-Loads result from the equilibrium, as a function of the radius of curvature (R), the bridge width (D), and the diaphragm spacing (d). Figure 2a shows the segment of curved bridge with two girders and five diaphragms spaced radially. Considering that the girders sections resist the bending moment entirely by longitudinal forces applied on the flanges, as shown in Figure 2b, the force on each flange of girder 1 is $M_1/h_1$, where $h_1$ is the distance between the points of application of the forces and $M_1$ is the bending moment.

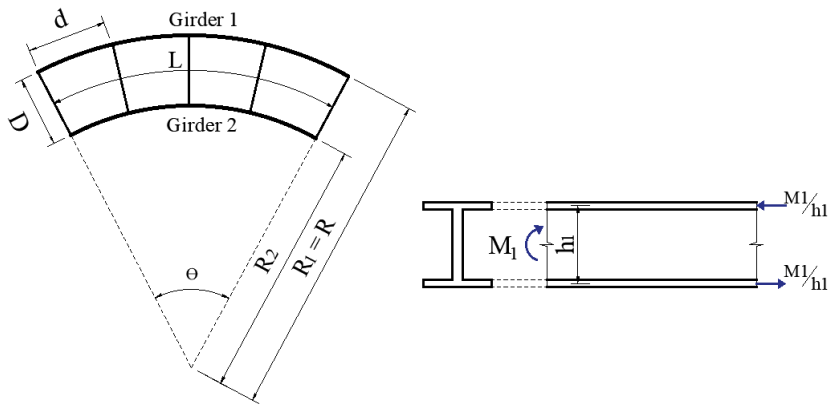


**Figure 2.** (a) Segment of a curved bridge with two girders; (b) Longitudinal bending and flange forces acting on girder 1. Adapted from Fiechtl et al. [11].

However, since the girders are curved, the longitudinal forces due to bending in different sections are not in equilibrium. Therefore, to ensure radial equilibrium on the flanges, there must be a force acting in the direction of the diaphragm, indicated by $H_1$. Similar forces must appear on the bottom flange.

The forces $H_1$ and $H_2$ generate a rotation tendency and, to ensure the stability of the diaphragm, vertical forces must appear, as indicated in Figure 3. These shear forces are called V-Loads, indicated by $V$. The force $H_1$ is determined by Equation 4, and the force $H_2$ can be obtained analogously.

$$H_1 = \frac{M_1 \cdot \theta}{h_1} \tag{4}$$

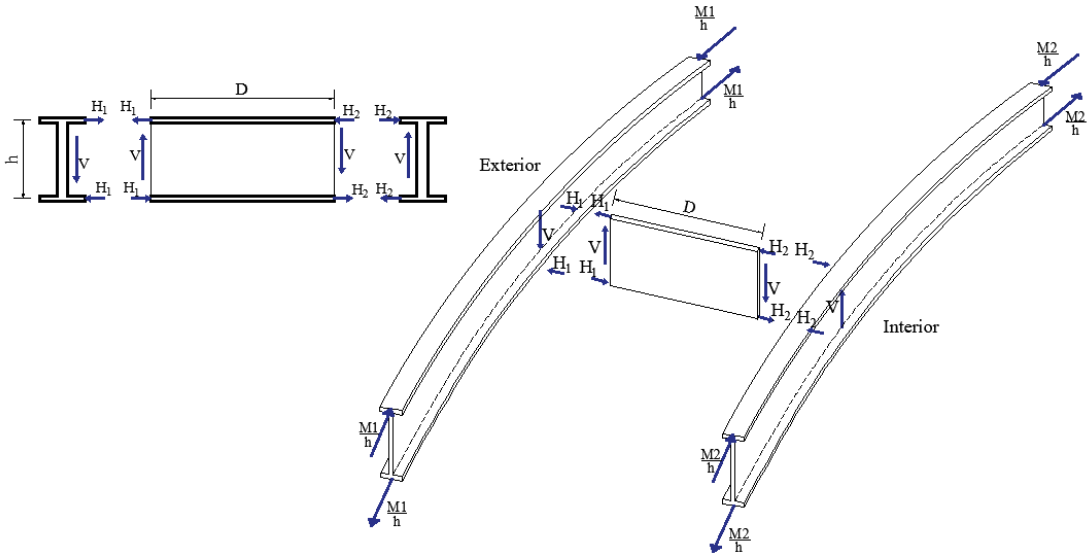


**Figure 3.** View of the bridge focusing on the diaphragms. Adapted from Fiechtl et al. [11].

In Equation 4, $\theta$ is the angle between adjacent diaphragms, which is assumed to be small. Thus, considering the arc length and substituting the value of $\theta$, $H_1$ can be given by:

$$H_1 = \frac{M_1 \cdot d_1}{h_1 \cdot R_1} \tag{5}$$

To maintain the equilibrium of moments in the diaphragm, the vertical force must be:

$$V = (H_1 + H_2) \cdot \frac{h}{D} \tag{6}$$

In Equation 6, the term $h$ refers to the diaphragm height. Considering the two girders and the diaphragm with the same height, so that $h = h_1 = h_2$, we obtain:

$$V = \frac{M_1 \cdot \frac{d_1}{R_1} + M_2 \cdot \frac{d_2}{R_2}}{D} \tag{7}$$

Since $d_1/R_1 = d_2/R_2 = d/R$, the shear force on the diaphragm is:

$$V = \frac{M_1 + M_2}{R \cdot D/d} \tag{8}$$

The bending moments due to external loads (those that were applied to the bridge) are called "primary moments" and will be identified by the index "*p*". The additional bending moments due to the curvature, represented by the vertical forces (V-Loads), will be denoted by the index "*v*". Thus, the total bending moment is given by:

$$M_1 = M_{1p} + M_{1v} \tag{9}$$

According to Monzon et al. [12], the same procedure can be followed for bridges with three or more girders. However, in these cases, beyond summing the bending moments due to external loads, a coefficient that depends on the number of girders must be applied. Therefore, the V-Load is calculated by:

$$V = \frac{\sum_{i=1}^{N_g} M_{ip}}{C \cdot R \cdot D} d \tag{10}$$

Where $M_{ip}$ is the primary moment on the girder "*i*"; $D$ is the distance between the axis of the inner girder and that of the outer girder; $R$ is the radius of curvature; $d$ is the spacing between the bracing or diaphragms; $C$ is the coefficient that considers the linear distribution of the V-Loads according to the number of $N_g$ stringers in the cross section.

## 4 BENDING MOMENT DISTRIBUTION FACTOR AND MODIFICATION FACTOR

Brockenbrough [13] was one of the pioneers in the study of live load distribution factors in curved bridges. In his research, the author proposes to obtain the distribution factors through the ratio between the bending moment obtained by a refined three-dimensional model and those resulting from a simplified girder model. Based on this concept, in this paper, the distribution factors are determined through the ratio between the moment at the most solicited section (mid-span section) for each girder, obtained from 3D models, and the bending moment for the whole bridge, obtained by modeling the bridge as a beam (1D). Thus, the bending moment distribution factors are attained through Equation 11.

$$BMDF = \frac{M^{MEF,3D}{}_{girder}}{M^{1D}{}_{bridge}} \tag{11}$$

In addition to bending moment distribution factors, this study also had its analyses based on the Modification Factor (MF), developed by Acosta and González [7], obtained by the ratio between the maximum bending moment on the girders of a curved bridge (CB) and the maximum bending moment on the equivalent girders of a straight bridge (SB) (Equation 12). According to the authors, the purpose of Modification Factors is to serve as a reference in design

situations, as it allows to estimate the internal forces in a curved bridge from the results of a straight bridge with equivalent dimensions, *i.e.*, same span length and cross-section.

$$MF = \frac{Max.girder\ bending\ moment\ (curved\ bridge)}{Max.girder\ bending\ moment\ (\ straight\ bridge)} = \frac{M_{CB}}{M_{SB}} \tag{12}$$

## 5 MODELS

The preexisting bridge has a total width of 8.30 m, supported by three girders. After the widening, the deck will be 12.80 m wide. The analysis will consider two different scenarios:

— Scenario: 1: Widening performed through symmetric addition of two girders (one on each side), amounting to five girders;

— Scenario 2: Widening performed through symmetric addition of four girders (two on each side), amounting to seven girders;

The preexisting structure was generated admitting concrete compressive characteristic strength ($f_{ck}$) equal to 25 MPa. In regards to the widenings, models with uniform and variable stiffness along the cross section were developed. The models with uniform stiffness had their widenings modeled with the same $f_{ck}$ of the original structure and served for comparison with the models with variable stiffness. In these models, the widened regions were modeled either considering a concrete compressive strength of 40 MPa or of 60 MPa.

In curved bridges, the curvature is usually established by fixating the radius or central angle along the entire length of the bridge. In terms of curvature, the models were classified into three groups:

— Group 01 (G1): Infinite radius of curvature (straight bridge);

— Group 02 (G2): Radius of 150 meters (central angle equals to 12.25°);

— Grupo 03 (G3): Radius of 50 meters (central angle equals to 36.6°).

A total of 18 models were analyzed, as shown in Table 1. The models were identified according to the number of girders, radius, and concrete compressive strength in the widened section. Thus, model 7LG2-40R, for example, consists of a 7-girder bridge with a radius of 150 meters and concrete compressive strength in the widened section of 40 MPa.

**Table 1.** Summary of developed models

| Number of girders | Group | Compressive strength of concrete in the widening region | Model identification |
|---|---|---|---|
| 5 | G1 | 25 | 5LG1-25R |
| | | 40 | 5LG1-40R |
| | | 60 | 5LG1-60R |
| | G2 | 25 | 5LG2-25R |
| | | 40 | 5LG2-40R |
| | | 60 | 5LG2-60R |
| | G3 | 25 | 5LG3-25R |
| | | 40 | 5LG3-40R |
| | | 60 | 5LG3-60R |
| 7 | G1 | 25 | 7LG1-25R |
| | | 40 | 7LG1-40R |
| | | 60 | 7LG1-60R |
| | G2 | 25 | 7LG2-25R |
| | | 40 | 7LG2-40R |
| | | 60 | 7LG2-60R |
| | G3 | 25 | 7LG3-25R |
| | | 40 | 7LG3-40R |
| | | 60 | 7LG3-60R |

### 5.1 Geometry

Figure 4 shows the cross sections adopted, considering the widening performed by adding two (Figure 4a) and four girders (Figure 4b).

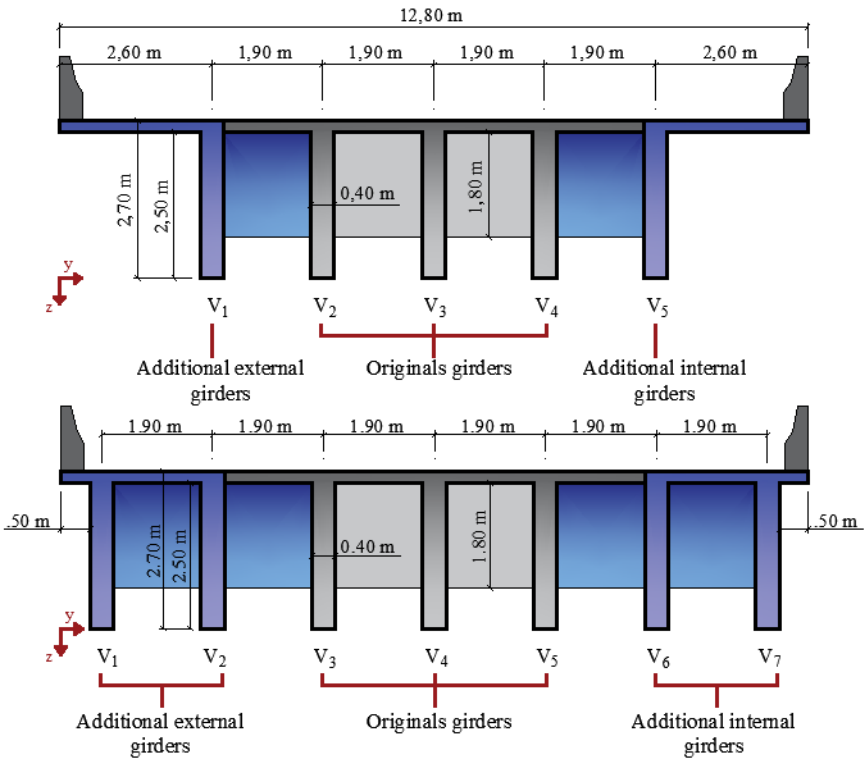


**Figure 4.** Cross sections after widening: (a) 5-girder model; (b) 7-girder model.

### 5.2 Materials

In all models, the material properties were determined following ABNT NBR 6118 [14]. To assess the influence exerted by the stiffness variation in the distribution of bending moments, the elasticity modulus ($E_{cs}$), calculated using the characteristic compressive strength of concrete, will be admitted. The elasticity moduli for the three types of concrete considered in the research are presented in Table 2. Considering that the expressions used in determining the elasticity modulus are related to the type of aggregate used in the concrete, it is relevant to emphasize that the values shown were determined admitting the use of granite aggregate.

**Table 2.** Material properties

| $f_{ck}$ (MPa) | $E_{cs}$ (MPa) |
|---|---|
| 25 | 24150 |
| 40 | 31875 |
| 60 | 41208 |

### 5.3 Load cases and boundary conditions

This research only considers the live loads of the design truck TB-450 as defined by the ABNT NBR 7188 [15]. As established by this code, the TB-450 is a three-axle vehicle that weighs 450 kN, and occupies an area of 18 m$^2$, as shown in Figure 5. Outside the region occupied by the design truck, a 5.0 kN/m$^2$ uniformly distributed load is applied.

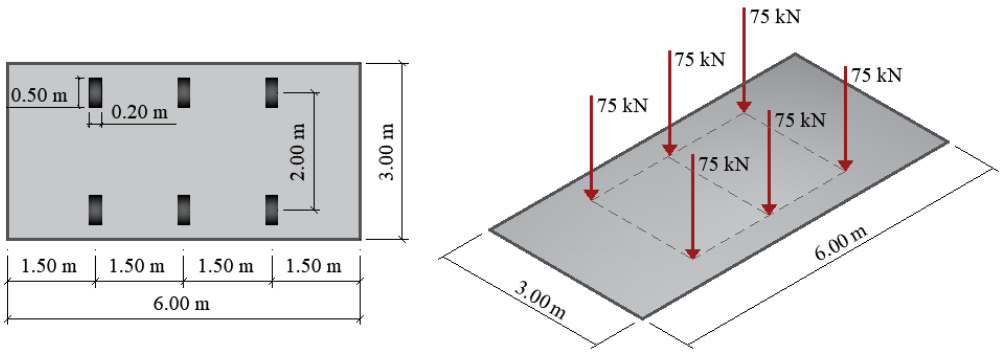


**Figure 5.** Vehicle type TB-450. Adapted from ABNT NBR 7188 [15].

Each girder absorbs a percentage of the total bending moment and to determine accurately this effect, the design vehicle was fixated in strategic transversal positions, moving only along the length of the bridge. They were called load cases 01 and 02. In load case 01, the design vehicle is fixed at the outermost position of the deck, while in load case 02 it is positioned on the centerline of the deck (Figure 6).

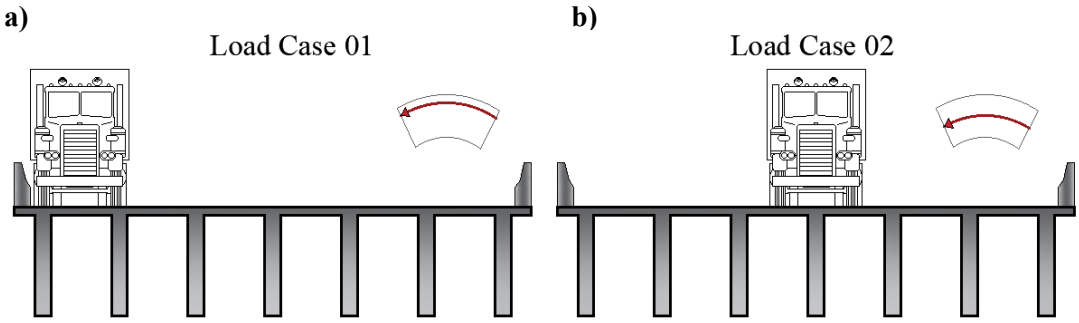


**Figure 6.** (a) Load case 01 – vehicle positioned at the outside of the curve. (b) Load case 02 – vehicle positioned at the curve centerline.

The boundary conditions, in turn, were defined following what was proposed by Samaan et al. [16]. The authors identified that the *tangential method of restriction*, in which the translations are restrained only in the directions tangential or radial to the curve, produces results consistent with experimental data, besides being easier to execute. In all models, the girders are directly supported on the abutments, restraining vertical translations in all supports. However, to ensure the global equilibrium of the structure, in one of the girders, the boundary conditions are slightly different. In addition to the vertical constraint, the support at one end also constrains the tangential displacement, while the other extremity constrains tangential and radial displacements. Rebouças et al. [17] successfully applied these conditions in order to perform a similar analysis.

## 6 3D MEF MODELS

The numerical modeling was performed through the software CSIBridge® (version 21), which utilizes FEM. Fu and Wang [9] state that the level of accuracy of bridge modeling depends on the desired results and recommend the generation of three-dimensional models with two-dimensional elements. Studies such as Kim et al. [1] and Nevling et al. [18] show that this methodology provides highly satisfactory results, similar to data obtained in the field.

This research developed three-dimensional models, with four nodes shell elements representing the slabs, girders, abutment, and diaphragms (Figures 7 and 8). In the development of the models, through consideration of boundary conditions and finite element analysis, it was decided to fixate the element dimension along the length of the bridge to 1.00 meter. Furthermore, the aspect ratio was limited to 2.5, since the use of smaller elements required too much time in computational work for little gain in precision. It is worth noting that according to Logan [19], and with the corroboration of Fu and Wang [9] and Fatemi et al. [20], aspect ratios over 4 generate processing errors higher than 15%.

The determination of the bending moment distribution factors from the numerical models developed in CSIBridge® was done by the ratio between the maximum bending moment of each girder and the total bending moment acting on the bridge.

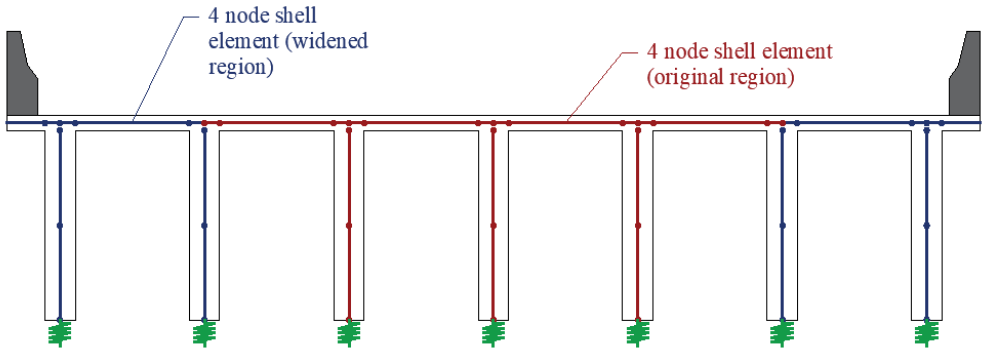


**Figure 7.** Discretization of bridge cross section in numerical model.

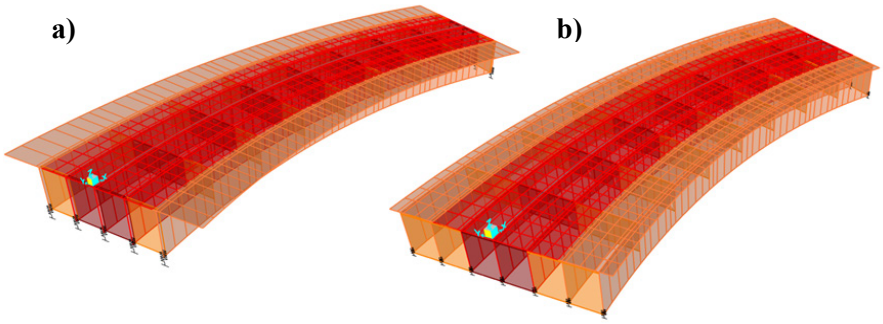


**Figure 8.** Three-dimensional finite element bridge model adopted in the analysis: (a) 5-girder model; (b) 7-girder model.

## 7 ANALYSES OF RESULTS

To assess the behavior of the bending moment distribution factors, the percentage variations between the BMDF's were calculated through two separate approaches: Global Analysis and Local Analysis. In the Global Analysis, the percentage difference captures the variation of the bending moment distribution factors (due to live load) that reaches the girders ($V_i$, $V_{i+1}$, $V_{i+2}$, $V_{i+3}$) compared to the factor in the reference girder within the same model (Figure 9). This approach provides a better understanding of the general behavior of bending moment distribution per model since the comparison occurs between girders. In all cases, the percentages have the innermost girder (right side of the deck) as reference.

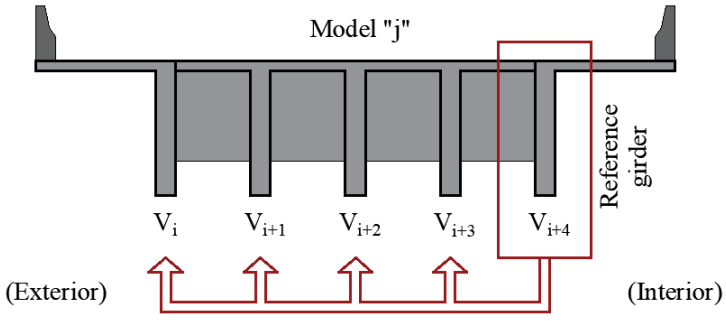


**Figure 9.** Methodology for Global Analysis.

In Local Analysis, the percentage reflects the magnitude of increase or decrease in the BMDF's of a girder $V_i^{\,j}$ compared to the factor of a girder of the same local position ($V_i^{\,j+1}$, $V_i^{\,j+2}$) but of a different model (Figure 10). Thus, greater emphasis will be given to this approach since it enables the direct analysis of the influence of the considered parameters. In the terms that identify the girders, shown in Figures 9 and 10, the index "*i*" specifies the girder while the index "*j*" refers to the model.

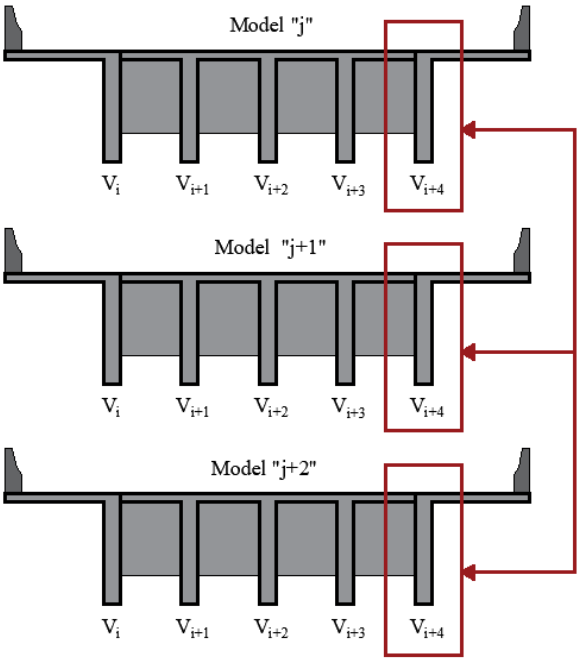


**Figure 10.** Methodology for Local Analysis

### 7.1 Bending Moment Distribution Factors

Figure 11 presents the percentual differences for global analysis obtained for the BMDF's from group G3 models (R = 50 m), considering the load cases 01 and 02. The reference girder is always the innermost one (V5 in 5-girder models, and V7 in 7-girder models). First, it is verified that the maximum percentages occur in the outermost girder (V1) for both load cases, regardless of the stiffness of the widened regions. That indicates that said girder absorbs the majority of the total bending moment.

According to the Precast Concrete Institute (PCI) [21], the bending stresses in the outermost girder tend to be substantially higher than in the other girders. One of the reasons for this behavior is that the arc length in the axis of the outermost girder is longer than the centerline of the bridge. This increases the bending moments in the external girder by approximately the square of the ratio between the arch lengths. Additionally, there is the fact that the girders transfer a portion of their torsional moments to the adjacent beam. This transfer develops to the external direction of the curve (from inside to outside). Thus, the outermost girder receives the contribution of the adjacent beam, but without redistributing a portion of these internal forces. In general, the direction of growth of the BMDF's is from inside to outside. Since all the percentage variations obtained are positive, one may conclude that the BMDF's are minimum in the innermost girder, that is, V5 in 5-girder models and V7 in 7-girder models.

Still considering the values obtained through load case 01, regarding the additional external girders, the rise in widening stiffness amplifies the global percentage. Thus, it is possible to deduce that the increase in stiffness heightens the differences between the BMDF's of the additional external girders and the reference girder. For example, the percentage increase of the BMDF for girder V1 compared to V5, considering the widened section with $f_{ck}$ of 60 MPa, is 509.2%, while in the model with uniform stiffness, this variation is 418.6% (Figure 11a).

In the original girders, the behavior is the opposite. In the 5-girder model (Figure 11-a), for girders V2 and V3, the increase of stiffness in the widening reduces the percentage differences. In the girder V4, increases in the percentages

are registered, although the variation rate is low. In the 7-girder model (Figure 11b), the original girders (V3, V4, and V5) behave consistently, presenting reductions with increasing stiffness.

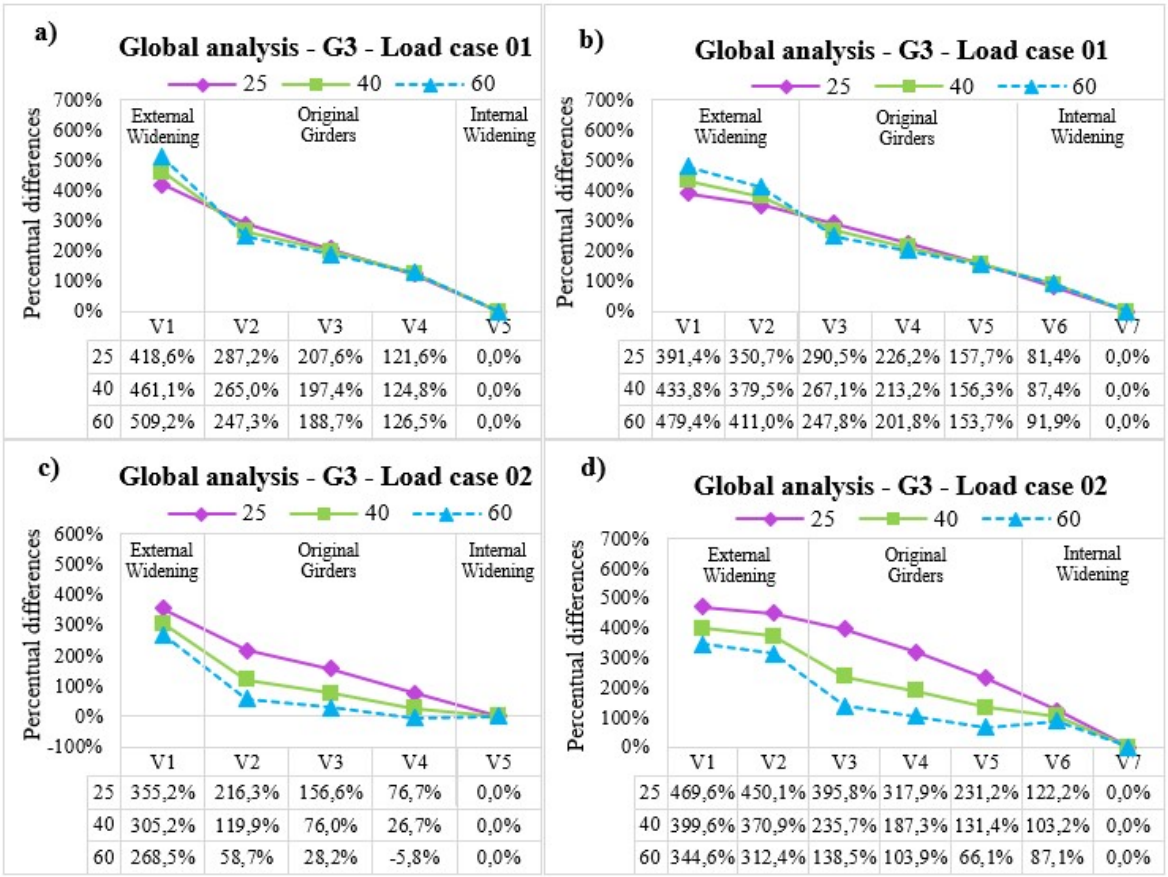


| a) | V1 | V2 | V3 | V4 | V5 |
|---|---|---|---|---|---|
| 25 | 418,6% | 287,2% | 207,6% | 121,6% | 0,0% |
| 40 | 461,1% | 265,0% | 197,4% | 124,8% | 0,0% |
| 60 | 509,2% | 247,3% | 188,7% | 126,5% | 0,0% |

| b) | V1 | V2 | V3 | V4 | V5 | V6 | V7 |
|---|---|---|---|---|---|---|---|
| 25 | 391,4% | 350,7% | 290,5% | 226,2% | 157,7% | 81,4% | 0,0% |
| 40 | 433,8% | 379,5% | 267,1% | 213,2% | 156,3% | 87,4% | 0,0% |
| 60 | 479,4% | 411,0% | 247,8% | 201,8% | 153,7% | 91,9% | 0,0% |

| c) | V1 | V2 | V3 | V4 | V5 |
|---|---|---|---|---|---|
| 25 | 355,2% | 216,3% | 156,6% | 76,7% | 0,0% |
| 40 | 305,2% | 119,9% | 76,0% | 26,7% | 0,0% |
| 60 | 268,5% | 58,7% | 28,2% | -5,8% | 0,0% |

| d) | V1 | V2 | V3 | V4 | V5 | V6 | V7 |
|---|---|---|---|---|---|---|---|
| 25 | 469,6% | 450,1% | 395,8% | 317,9% | 231,2% | 122,2% | 0,0% |
| 40 | 399,6% | 370,9% | 235,7% | 187,3% | 131,4% | 103,2% | 0,0% |
| 60 | 344,6% | 312,4% | 138,5% | 103,9% | 66,1% | 87,1% | 0,0% |

**Figure 11.** Global analysis of the BMDF's for the models with 25, 40, and 60 MPa widening, in comparison to the innermost girder: (a) 5L-G3 (Load case 01); (b) 7L-G3 (Load case 01); (c) 5L-G3 (Load case 02); (d) 7L-G3 (Load case 02).

Moving on to the analysis of the percentages resulting from load case 02, in the case of the 5-girder models (Figure 11c), once again, the BMDF's are minimal in the reference girder (V5). The only exception is the model in which the widening has $f_{ck}$ of 60 MPa, in which the minimum BMDF occurs in the girder V4, although the percentage is of little importance (-5.8%). Analogously, in the 7-girder model (Figure 11d), all percentages are positive, indicating that the minimum BMDF's occur in the girder V7. It is important to note that the percentage variations related to load case 01 are higher than those obtained by load case 02. This behavior stem from the fact that, despite the asymmetry inherent to curved bridges, positioning the type-vehicle on the centerline of the deck, associated with the presence of diaphragms, contributes to a more homogeneous distribution. Furthermore, unlike what was verified for load case 01, the global percentages from load case 02 tend to reduce with the stiffening of the widening areas.

As for the influence of stiffness, generally, the variations tend to be smaller in models with stiffer widenings. According to the data presented in Figures 11c,d, the global percentages behavior is approximately linear in models with uniform stiffness. However, in models with variable stiffness, the reduction rate of the global percentages caused by raising the stiffness is higher in the original girders, being more subtle in the widened sections.

### 7.2 Analysis of the influence of stiffness in the widenings by means of concrete compressive strength

Figure 12 summarizes the local percentage differences calculated for the group G3 models (R = 50 m), considering load cases 01 and 02. These results will be used to assess the effects induced in each girder by raising the widening stiffness.

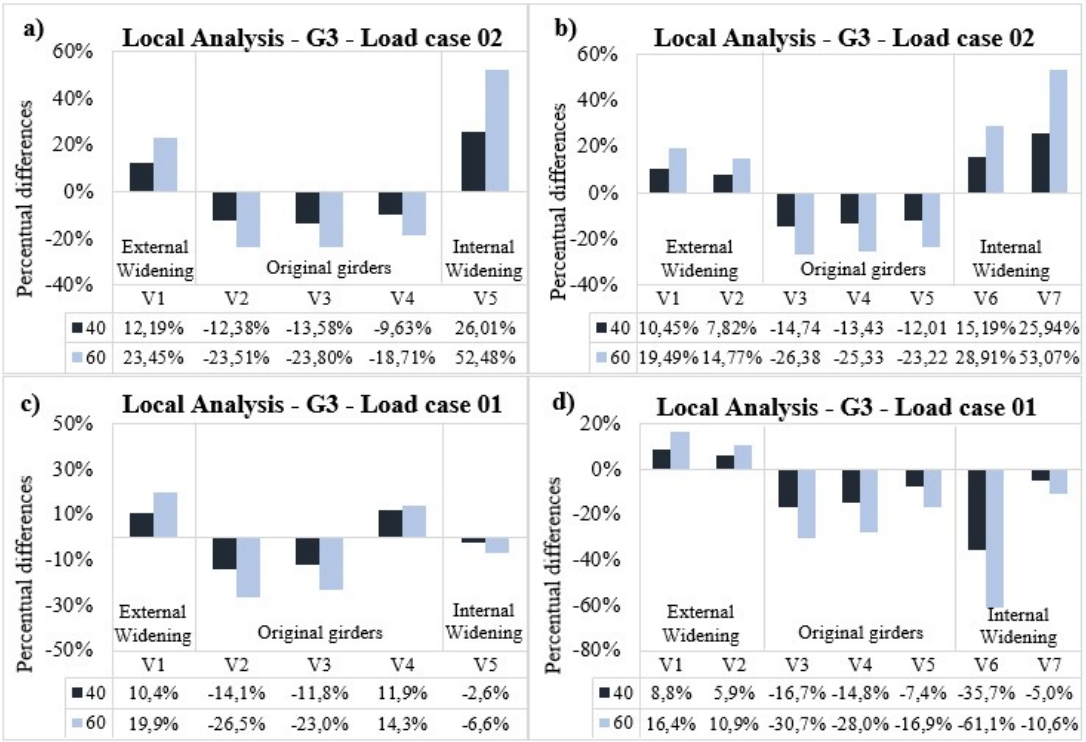


**Figure 12.** Local analysis of the BMDF's for models with 40 and 60 MPa widening, compared to the models with uniform stiffness.: (a) 5L-G3 (Load case 02); (b) 7L-G3 (Load case 02); (c) 5L-G3 (Load case 01); (d) 7L-G3 (Load case 01).

When studying the effect of widening in straight box bridges, Fontana [6] observed that the stiffer widenings began to support a higher percentage of loading, which led to an increase in the distribution factors in these areas. As a result, the distribution factors in the girder corresponding to the original deck suffered reductions. The author also verified that the loading decreases registered in the original girders, as well as the loading increases in the additional girders, tend to be higher the stiffer is the widening. Accordingly, this was the behavior verified in the values for load case 02 (Figure 12a,b).

In all cases, the percentages are higher for the models where the widening performed with characteristic compressive strength of 60 MPa. For the 5-girder models (Figure 12a), the increments in the additional girder V5 are higher than in the girder V1. Similarly, in the 7-girder model, the percentages attained for the additional internal girders (V6 and V7) are higher than those of the external girders V1 and V2. For both cases, in the original girders, the percentages decrease, in absolute value, towards the inner side of the curve, although the observed variation is low.

When it comes to curved bridges, the position of the load has a significant influence on the load distribution. In Figures 12c,d, related to load case 01, the additional external girders (V1 in the 5-girder model, V1, and V2 in the 7-girder model) experiences loading increases. For the 5-girder model, girders V2 and V3 show reductions, while in the 7-girder model, decreases occur in girders V3, V4, and V5. So far, the observations are within the expected behavior considering only the effect of stiffening the widening. However, in the 5-girder model, the original girder V4 experiences an increase in loading, while in the additional girder V5 occurs a reduction. In the 7-girder model, the additional internal girders (V6 and V7) present reductions, particularly the girder V6, in which the decrease reaches -61.1%.

Executing widenings with a higher stiffness than that of the original deck should relieve the pre-existing girders, not overload them. The behavior observed in the BMDF's attained from load case 01 is highly problematic since it has original girders receiving additional loading while widening girders, with concrete of higher compressive strength, receive less load than they would in a deck with uniform stiffness. This inconvenience is mitigated by the fact that the BMDF's on the girders positioned in the inner side of the deck (right side) tend to be smaller.

### 7.3 Analysis of the influence of curvature

Kim et al. [1] and Zhang et al. [2] presented the curvature as one of the most influential parameters in the distribution of bending moments in curved bridges. For this reason, it is relevant to evaluate the effect that varying the radius has on the distribution of bending moments in the widened deck.

In the previous subsection, the percentages resulted from the comparison of the BMDF's of the models of variable stiffness in relation to those of uniform stiffness, considering the models of group G3 (Figure 12). Deepening this analysis, Figure 13 introduces the percentages obtained from a similar analysis applied to the models of groups G1 and G2. It should be noted that, although Figure 13 shows the local percentage differences only for the 7-girder models, the behavior verified in the 5-girder models was analogous.

The first noteworthy aspect is that the variation in curvature does not significantly affect the local percentages. This allows for the conclusion that the effects of stiffness variation in the widened sections are independent of the bridge radius of curvature.

Preliminarily, one can see that the increases and decreases fit the observations made in the analysis of the percentages obtained for group G3 (Figure 12). For load case 01 (Figure 13a,c), as expected, loading increases happen in the additional external girders V1 and V2, while the original girders experience decreases. In the additional internal girder V7, contrary to expectations, reductions are verified.

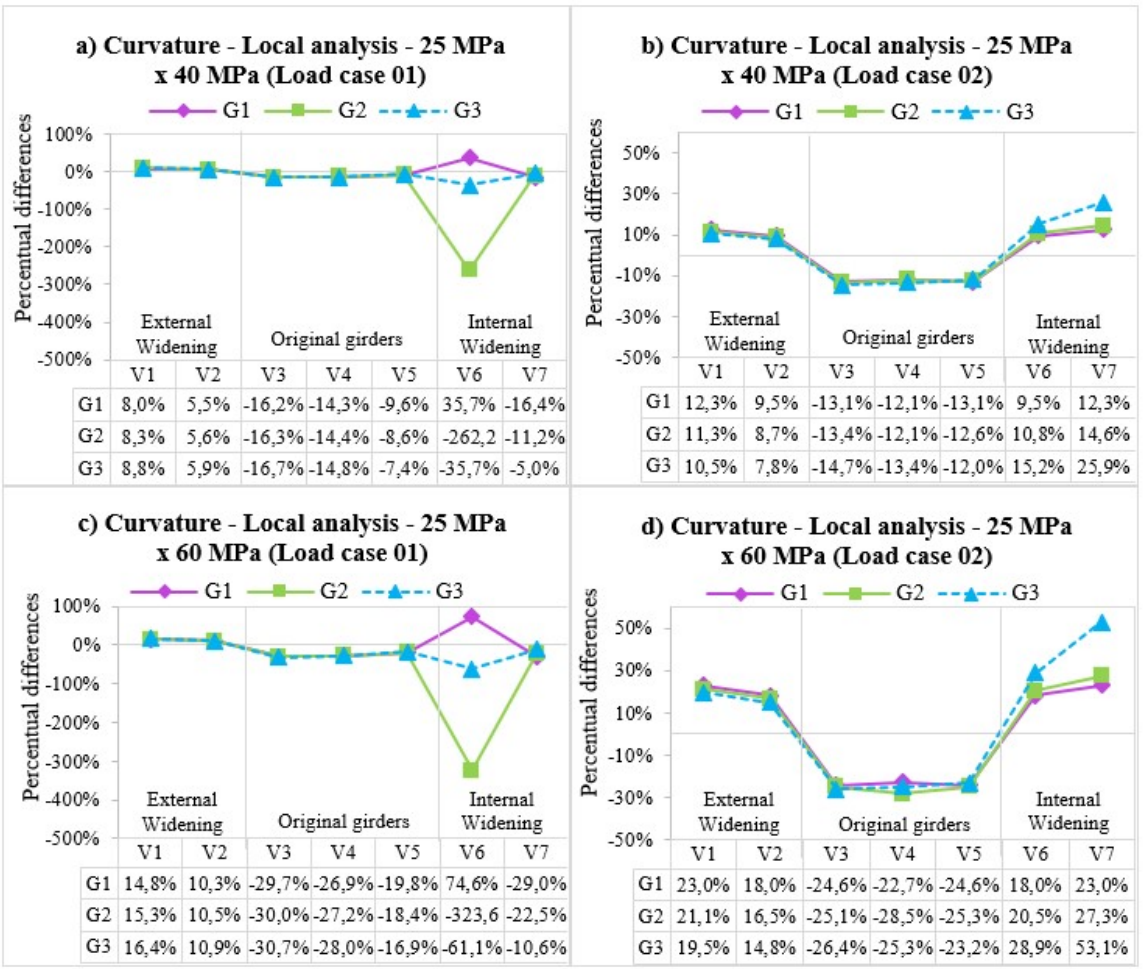


**Figure 13.** Local analysis of the BMDF's as a function of the radius for the 7-girder models: (a) widening of 40 MPa (Load case 01); (b) widening of 40 MPa (Load case 02); (c) widening of 60 MPa (Load case 01); (d) widening of 60 MPa (Load case 02);

The girder V6, however, experiences increases in the straight model (G1) and decreases in the curved models (G2 and G3). These reductions are notably high for the models with the greater radius (G2), and these discrepancies occur mainly due to two reasons. Firstly, for load case 01, the bending moments tended to concentrate on the outermost girders. The values of the BMDF's attained for the innermost girders (the girders V6 and V7 in particular) were in general very low. Thus, the percentages calculated by dividing the BMDF variation by the corresponding distribution factor in the model with uniform stiffness (reference model) contributed to producing high values. In addition to that,

in the model with uniform stiffness, contrary to the expectations, the bending moment direction caused tension on the upper fibers of the girder. However, when analyzing the models with variable stiffness, the influence exerted by the widening stiffening caused the inversion of the bending moment direction, which, as in the other girders, tensioned the lower fibers of the girder V6. Since the obtained data considered the difference between the load factor of the model with variable stiffness and the load factor on the reference model, the percentages in question reflected the total amplitude of the variation that led to the inversion of bending moment direction and not the occurrence of expressive variations in load distribution.

It is worth noting that the phenomenon of reversal of moment direction only occurred in the girder V6 of the group G2 models. Although after the inversion, the modulus of the acting moment became lower, the inversion on its own represents an issue since, aside from causing relief of the original reinforcement, it creates a demand for new reinforcement in a different region.

For the percentages obtained through load case 02 (Figure 13b,d), the effect of the curvature variation also proves to be negligible, and the highest impact is registered on the innermost girder (V7). In these girders, the increments rise with the reduction of the radius, being maximum for the group G3 models.

### 7.4 Analysis of the influence of the number of girders

Works such as Zhang et al. [2] highlight the number of girders as a factor of high impact on the load distribution in curved bridges. According to this study, for bridges with more than three girders, the addition of girders causes a significant reduction in the load distribution factors. In this sense, this analysis examines the effect of adding girders, comparing the results obtained from 5-girder models with those from 7-girder models. To achieve that, this assessment compares the sum of the factors in the original girders (O.G.), additional external (Ext. G.), and internal (Int. G.) between the 5-girder and 7-girder models. To better explain, the sum of the BMDF's from girders V2, V3, and V4 (5-girder model) will be compared to the sum of the factors from girders V3, V4, and V5 (the 7-girder model). Similarly, the BMDF of girder V1 will be compared to the sum of the factors from girders V1 and V2, while the factor from girder V5 will be compared to the sum of BMDF's from girders V6 and V7. These comparisons resulted in local percentage variations, as shown in Figure 14, considering the group G2 models (R = 150 m).

For both load cases, in response to the increase in the number of girders, increments are observed in the quantity of bending moment absorbed by the external widened section (Ext. G.). Although these values indicate that the total moment absorbed in this section is higher in models with 7 girders, it should be noted that this section includes two girders, which share this loading and, therefore, are relieved. With the stiffening of the widening, these increments drop. In the original section, the portion of bending moment absorbed is smaller in the 7-girder model, indicating that the increase in the number of girders relieved the pre-existing girders, and said relief is more expressive the higher the stiffness of the widening.

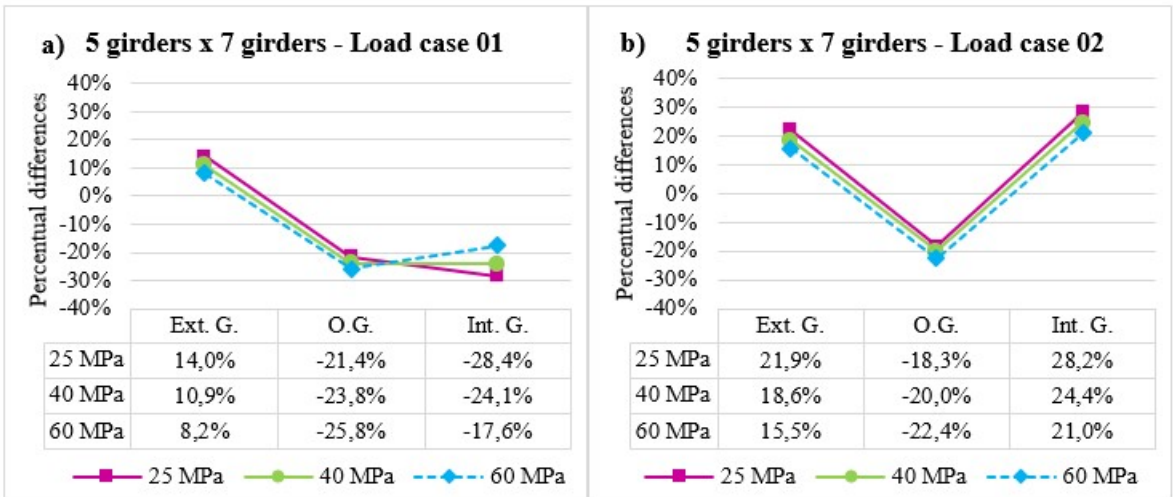


**Figure 14.** Local analysis between the BMDF's of the 5-girder and 7-girder models: (a) Load case 01; (b) Load case 02.

In the internal widened section, reductions are registered for load case 01 (Figure 14a), while increases occur for load case 02 (Figure 14b). However, for both load cases, in response to the widening stiffening, the differences between the total bending moment absorbed by the widenings reduce.

### 7.5 Comparison between numerical models and the V-Load method

In order to assess its applicability, the results obtained using the V-Load Method were compared with those generated through FEM. The comparison is based on percentage differences, obtained through local analysis. Therefore, the percentage reflects the variation between the BMDF calculated by the V-Load method compared to the value generated by FEM. This methodology was applied to models with uniform stiffness, as well as to those with variable stiffness along the cross-section. Figure 15 presents the data generated through this analysis.

Figures 16a,b show the local percentage variations for the group G2 models ($R$ = 150 m). For the girders included in the widened outermost section (V1 for the 5-girder model, V1 and V2 for the 7-girder model), decreases are registered, indicating that the BMDF's obtained by the V-Load Method in these girders are lower than those resulting from the FEM. In the central girders on both 5 and 7-girder models, reductions are also verified. In the 5-girder model, the percentages are higher, considering absolute value, in the girder V5. Similarly, the variations for the 7-girder model tend to be higher in the innermost girders and are maximum in the girder V7.

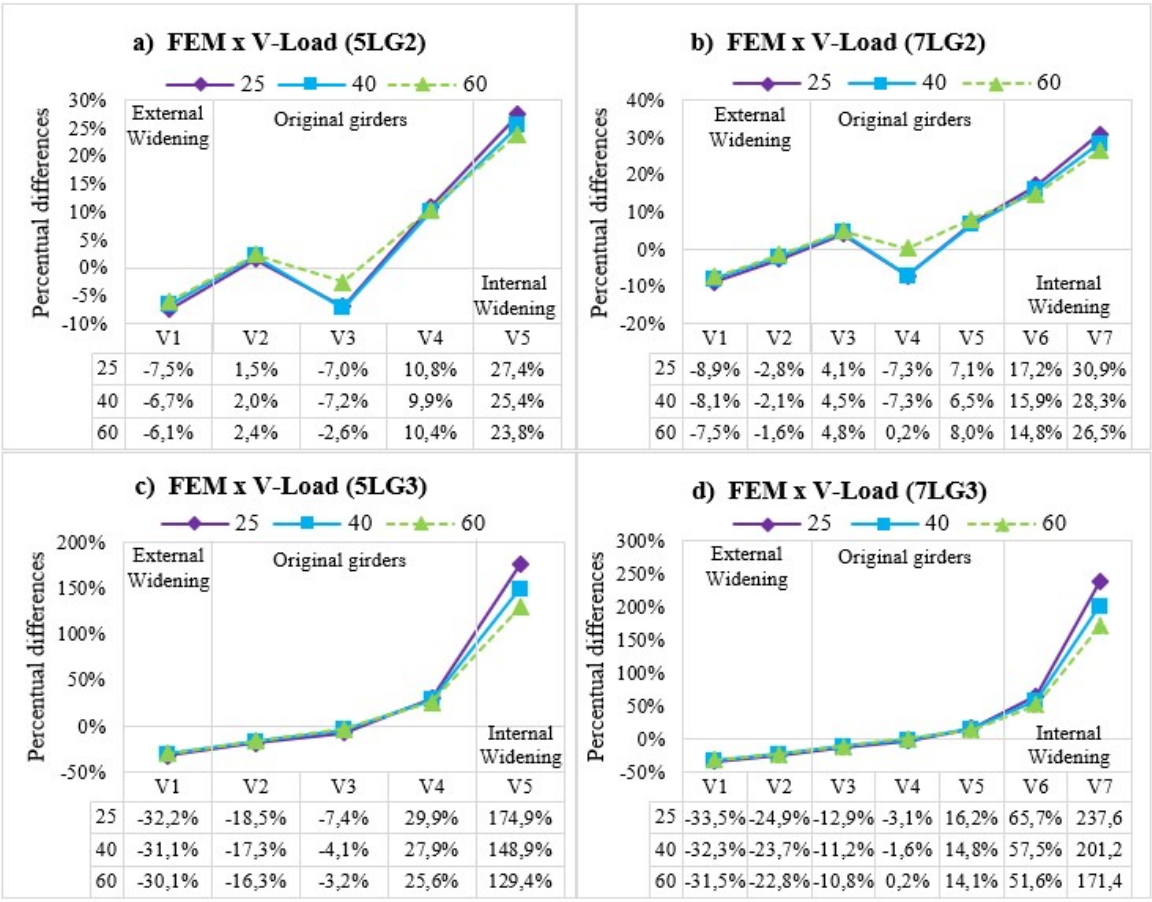


a) FEM x V-Load (5LG2)

| | V1 | V2 | V3 | V4 | V5 |
|---|---|---|---|---|---|
| 25 | -7,5% | 1,5% | -7,0% | 10,8% | 27,4% |
| 40 | -6,7% | 2,0% | -7,2% | 9,9% | 25,4% |
| 60 | -6,1% | 2,4% | -2,6% | 10,4% | 23,8% |

b) FEM x V-Load (7LG2)

| | V1 | V2 | V3 | V4 | V5 | V6 | V7 |
|---|---|---|---|---|---|---|---|
| 25 | -8,9% | -2,8% | 4,1% | -7,3% | 7,1% | 17,2% | 30,9% |
| 40 | -8,1% | -2,1% | 4,5% | -7,3% | 6,5% | 15,9% | 28,3% |
| 60 | -7,5% | -1,6% | 4,8% | 0,2% | 8,0% | 14,8% | 26,5% |

c) FEM x V-Load (5LG3)

| | V1 | V2 | V3 | V4 | V5 |
|---|---|---|---|---|---|
| 25 | -32,2% | -18,5% | -7,4% | 29,9% | 174,9% |
| 40 | -31,1% | -17,3% | -4,1% | 27,9% | 148,9% |
| 60 | -30,1% | -16,3% | -3,2% | 25,6% | 129,4% |

d) FEM x V-Load (7LG3)

| | V1 | V2 | V3 | V4 | V5 | V6 | V7 |
|---|---|---|---|---|---|---|---|
| 25 | -33,5% | -24,9% | -12,9% | -3,1% | 16,2% | 65,7% | 237,6 |
| 40 | -32,3% | -23,7% | -11,2% | -1,6% | 14,8% | 57,5% | 201,2 |
| 60 | -31,5% | -22,8% | -10,8% | 0,2% | 14,1% | 51,6% | 171,4 |

**Figure 15.** Local analysis between the FEM and the V-Load Method: (a) 5L-G2; (b) 7L-G2; (c) 5L-G3; (d) 7L-G3.

For the models belonging to group G3 (Figure 15c,d), regardless of the number of girders, reductions are observed from the outermost (V1) to the central girder. The main difference between the percentage's behavior from group G2 and G3 models is that, for the latter, the variations at the girder adjacent to the left widened section (V2 for the 5-girder model, V3 for the 7-girder model) is negative. Furthermore, the percentages are, in general, higher for the G3 group

models. According to Monzon et al. [12], the V-Load method is better suited to bridges with larger radii. As observed for group G2, the percentages in the girders on the inner side of the bridge tend to be higher, being maximum in the innermost girders V5 and V7. Ribeiro [22] also observed the incremental effect exerted by the radius on the divergences between the FEM and the V-Load method and, corroborating what was verified in these assessments, the author found that the highest discrepancies tend to occur in the innermost girders.

Regarding the effect of stiffness variation in the widened regions, in general, for the external girders, the higher the stiffness, the smaller the discrepancies compared to the FEM results. For the internal girders, the same behavior is observed. For the external additional and the original girders, the stiffness variation in the widened regions does not significantly affect the differences between analytical and numerical models. It is valid to point out that the V-Load method was conceived for bridges in which all girders have the same bending stiffness [11].

### 7.6 Modification Factors Analysis

In order to complement the analyses presented so far, this item presents the Modification Factors obtained for the curved models, considering the variation of the radius and widening stiffness.

According to the concepts previously discussed, the MF result from the ratio between the maximum value of the bending moment obtained for a curved bridge and a straight bridge, considering the same girder. To limit the data volume, for both 5-girder and the 7-girder models, the MF analysis only involved the external, central, and internal girders, as shown in Figure 16.

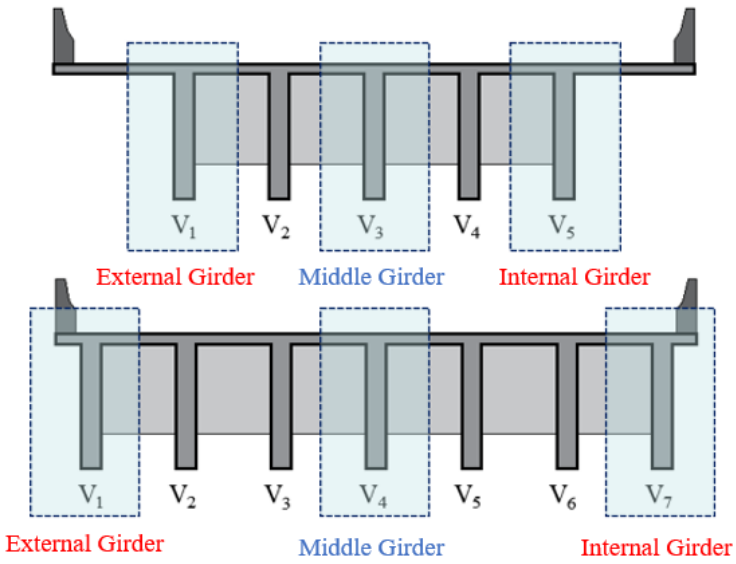


**Figure 16.** Girders considered for the attainment of Modification Factors.

Figure 17 shows the MF's obtained by applying load case 01 for the 5-girder and 7-girder models, each graphic as a function of widening stiffness. In general, for this load case, the factors are similar for the external and central girders while increasing noticeably for the internal girders, especially in the MF obtained for group G3 models (Figure 17c,d).

The comparison between the results for groups G2 and G3 shows that the MF's are higher for models with greater curvature, and this disparity is particularly relevant considering the factors of the internal girders. These behavioral aspects of the MF's indicate that, concerning load case 01, inserting a curvature affects the internal stringers more expressively, and its influence is more intense the higher the radius. When considering the effect of the compressive strength variation in the widened sections, the data shows that the most relevant repercussions are felt only in the internal girders, especially in the group G3 models, with no significant variations for the other girders.

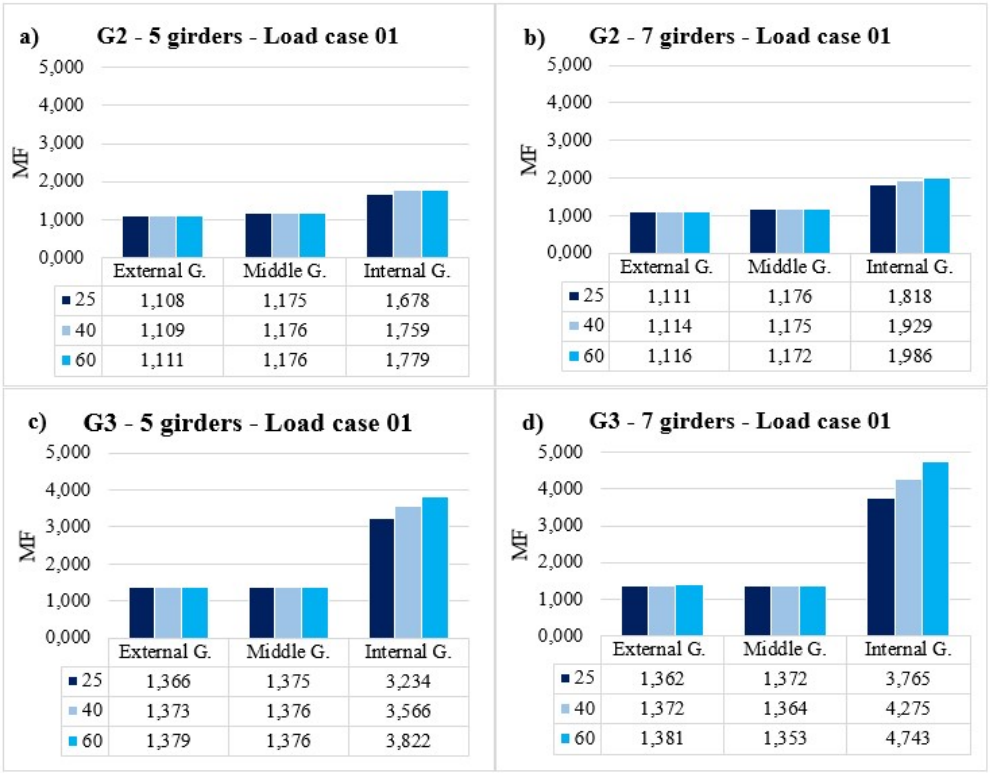


**Figure 17.** Modifications Factors for load case 01: (a) 5L-G2; (b) 7L-G2; (c) 5L-G3; (d) 7L-G3.

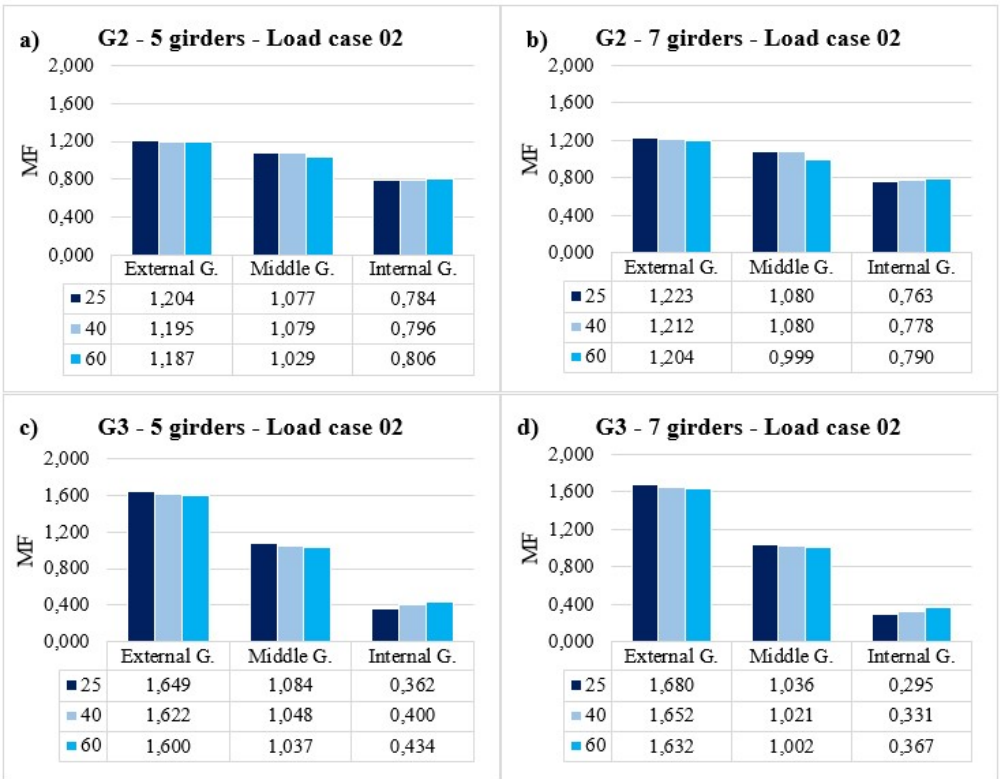


**Figure 18.** Modifications Factors for load case 02: (a) 5L-G2; (b) 7L-G2; (c) 5L-G3; (d) 7L-G3.

Figure 18, in turn, introduces the MF's obtained from the bending moments resulting from load case 02. Firstly, the growth tendency of the MF's, in this case, is opposed to the behavior exhibited by the values pertaining the load case 01 since they reduce towards the internal girder. Another aspect identified is that, compared to the results of load case 01, the MF's tend to be smaller for load case 02, except for the external girders. It is interesting to note that, regardless of the number of girders or the radius, the MF's attained for the central girders are very close to the unity, indicating that there is no significant divergence between the bending moments obtained in the straight and curved models for the girder in question. Contrary to what occurred in the analysis of factors from load case 01, the internal girders have the lowest MF's, being, in all cases, lesser than 1.0.

Considering the influence of curvature, although the MF's in the central girders are not affected by the change of radius, the factors in the external girders increase while decreasing in the internal girders. This behavior is compatible with what was verified by Acosta and González [7] and Rebouças et al. [17]. Furthermore, regarding the widening stiffness, there are no relevant changes due to the variation of this parameter.

## 8 CONCLUSIONS

This paper sought to analyze the transverse distribution of bending moments in curved bridges considering the execution of widenings with concrete of variable compressive strength. The analysis shows that the effects of this parameter depend not only on the magnitude of the stiffness but also on the live load positioning. In all cases, the percentage variations are greater the higher the stiffness of the widenings. For load case 02, consistently, the bending moment distribution factors in the widened regions tend to grow with the stiffening. As a consequence, the distribution factors from the original girders reduce. For load case 01, while the external widened sections experience increases, and the original girders are relieved, this relief also occurs in the internal widened regions.

Regarding the curvature effect, the radius variation did not significantly alter the percentages calculated for bending moment distribution. This behavior allows deducing that, although the curvature is a key parameter for load distribution in curved bridges, changing the radius does not change the effect of load redistribution induced by the widening stiffness variation.

Comparing the models with 5 and 7 girders, for load case 02, the load fraction absorbed by the original section of the deck with 7 girders reduced, while the widened regions experienced increases. However, for load case 01, not only the original girders were relieved, but the bending moments of the internal widened section also suffered reductions. Therefore, the addition of girders produced a similar effect to that induced by the stiffening of the widenings. This similarity is probably related to the fact that the addition of the girders, even when maintaining the concrete compressive strength, reduces the overhang length and stiffens the widening. Furthermore, the analysis shows that the higher the stiffness in the widened sections, the greater the percentage reduction, *i.e*., the higher the relief experienced by the original region of a 7-girder model compared to the loading in the same area on a 5-girder model. However, for the models with variable stiffness, the discrepancy between the loading in the widened sections of the 5 and 7-girder models tends to decrease.

The comparison of bending moments obtained from FEM and those calculated by the approximate analytical V-Load method shows that the percentage differences are higher in the innermost girders, which are even more significant for the group G3 models. Moreover, although the V-Load method was idealized considering the hypothesis of girders with uniform stiffness, the percentages for models with variable stiffness did not diverge significantly from those obtained in models with uniform stiffness.

Finally, given the analyses of the Modification Factors, regarding the effect of the increase in curvature, the factor attained with load case 01 increased in general, particularly in the internal girders. However, for load case 02, while the central girders were hardly affected, the MF's of the external and internal girders increased and decreased, respectively. Compared to the curvature effect, the variation of widening stiffness only produced relevant changes for the internal girders of the group G3 models, considering load case 01, while being negligible in the other cases.

## 9 REFERENCES

[1] W. S. Kim, J. A. Laman, and D. G. Linzell, "Live load radial moment distribution for horizontally curved bridges," *J. Bridge Eng.*, vol. 12, no. 6, pp. 727–736, Nov 2007, http://dx.doi.org/10.1061/(ASCE)1084-0702(2007)12:6(727).

[2] H. Zhang, D. Huang, and T. Wang, "Lateral load distribution in curved Steel I-girder bridges," *J. Bridge Eng.*, vol. 10, no. 3, pp. 281–290, 2005, http://dx.doi.org/10.1061/(ASCE)1084-0702(2005)10:3(281).

[3] Departamento Nacional de Infraestrutura de Transportes, *Manual de Inspeção de Pontes Rodoviárias*, 2ª ed. Rio de Janeiro: IPR, 2004.

[4] J. A. P. Vitório, “Um estudo comparativo sobre métodos de alargamento de pontes rodoviárias de concreto armado com a utilização das normas brasileiras e eurocódigos,” Ph.D. dissertation, FEUP, Porto, 2013.

[5] R. M. C. Barros, J. A. P. Vitório, “Análise paramétrica de projetos de alargamento e reforço de pontes rodoviárias de concreto armado,” in *Jorn. Sul Am. Eng. Estrut.*, Rio de Janeiro, set. 2012.

[6] P. Fontana, “Análise de modelos de distribuição transversal de cargas em superestruturas de viga em seção caixão de pontes e viadutos alargados,” M.S. thesis, PPGEC, UFTPR, Curitiba, 2016.

[7] R. Acosta and J. V. González, "Structural response of plan-curved steel i-girder bridges from an equivalent straight bridge analysis," *J. Bridge Eng.*, vol. 23, no. 3, Mar 2018, http://dx.doi.org/10.1061/(ASCE)BE.1943-5592.0001187.

[8] R. L. Barbosa, “Pontes curvas unicelulares em regime elástico,” M.S. thesis, PEF, USP, São Paulo, 1997.

[9] C. C. Fu and S. Wang, *Computational Analysis and Design of Bridge Structures*, 1st ed. Boca Raton, USA: CRC Press, 2015.

[10] American Association of State Highway and Transportation Officials, *AASHTO LRFD Bridge Design Specifications*, 7th ed. Washington, DC, USA: AASHTO, 2014.

[11] A. L. Fiechtl, G. L. Fenves, and K. H. Frank, *Approximate Analysis of Horizontally Curved Girder Bridges* (Rep. 360-2F), UT, Austin, TX, USA, 1987.

[12] E. V. Monzon, A. M. Itani, and M. L. Reno, “Horizontally curved girder bridges,” in *Bridge Engineering Handbook*, 2nd ed. Boca Raton, USA: CRC Press, 2014, ch. 6, pp. 259-281.

[13] R. L. Brockenbrough, "Distribution Factors for Curved I-Girder Bridges," *J. Struct. Eng.*, vol. 112, no. 10, pp. 2200–2215, Oct 1986, http://dx.doi.org/10.1061/(ASCE)0733-9445(1986)112:10(2200).

[14] Associação Brasileira de Normas Técnicas, *Projeto de Estruturas de Concreto – Procedimento*, NBR 6118, 2014.

[15] Associação Brasileira de Normas Técnicas, *Carga Móvel Rodoviária e de Pedestres em Pontes, Viadutos, Passarelas e Outras Estruturas*, NBR 7188, 2013.

[16] M. Samaan, K. Sennah, and J. B. Kennedy, "Positioning of bearings for curved continuous spread-box girder bridges," *Can. J. Civ. Eng.*, vol. 29, no. 5, pp. 641–652, Oct 2002, http://dx.doi.org/10.1139/l02-049.

[17] A. Rebouças, J. Silva Fo, R. Barros, Y. Nascimento, and P. Coutinho, "Curved bridges live load bending moment distribution using straight and curved girders," *Rev. IBRACON Estrut. Mater.*, vol. 15, no. 2, e15208, Apr 2022, http://dx.doi.org/10.1590/s1983-41952022000200008.

[18] D. Nevling, D. Linzell, and J. Laman, "Examination of level of analysis accuracy for curved I-girder bridges through comparisons to field data," *J. Bridge Eng.*, vol. 11, no. 2, pp. 160–168, Mar 2006, http://dx.doi.org/10.1061/(ASCE)1084-0702(2006)11:2(160).

[19] D. L. Logan, *A First Course in the Finite Element Method*, 5th ed. Stamford, CT, USA: Cengage Learn., 2012.

[20] S. J. Fatemi, M. S. Mohamed Ali, and A. H. Sheikh, "Load distribution for composite steel-concrete horizontally curved box girder bridge," *J. Construct. Steel Res.*, vol. 116, pp. 19–28, Jan 2016, http://dx.doi.org/10.1016/j.jcsr.2015.08.042.

[21] Precast Concrete Institute, *Bridge Design Manual*, 3th ed. Chicago, IL, USA: Precast/Prestressed Concr. Inst., 2011.

[22] V. A. Ribeiro, “Avaliação da influência das curvaturas e das transversinas na distribuição do momento fletor devido à carga móvel em pontes curvas de concreto armado,” M.S. thesis, PEC, UFRN, Natal, 2019.

**Author contributions:** YN: conceptualization, methodology, data curation, software, formal analysis, writing; JN: formal analysis, project administration, supervision, writing-review and editing; AR: data curation, writing-review and editing; RB: conceptualization, supervision, visualization; JN: conceptualization, supervision.

**Editors:** Mauro de Vasconcellos Real, Guilherme Aris Parsekian.

IBRACON Structures and Materials Journal
Revista IBRACON de Estruturas e Materiais
ISSN 1983-4195 ismj.org

ORIGINAL ARTICLE

# Shear in reinforced concrete beams with continuous internal transverse reinforcement

## *Cisalhamento em vigas de concreto armado com armadura transversal interna contínua*

Diego Ferreira de Souza[a]
Jedson Henryque Correa Abrantes[a]
Luamim Sales Tapajós[b]
Mauricio de Pina Ferreira[c]
Aarão Ferreira Lima Neto[a]

[a]Universidade Federal do Pará – UFPA, Nucleus of Amazonian Development in Engineering, Postgraduate Program in Infrastructure Engineering and Energy Development, Tucurui, PA, Brasil
[b]Universidade Federal do Oeste do Pará – UFOPA, Faculty of Civil Engineering, Itaituba, PA, Brasil
[c]Universidade Federal do Pará – UFPA, Institute of Technology, Faculty of Civil Engineering, Belém, PA, Brasil

**Received** 22 January 2021
**Accepted** 04 May 2022

**Abstract:** Reinforced concrete elements with a high longitudinal and transverse reinforcement ratio may present conflicts on both of them, resulting in reduced labor productivity and a poor job when assembling the transversal reinforcement, reducing its effectiveness. Thus, this research presents a type of internal transverse reinforcement as an alternative to mitigate this conflict between the transverse and longitudinal bars. A total of 5 reinforced concrete wide beams were made, one of them as a reference with closed stirrups, and the other ones with internal stirrups, varying the inclination of the internal transverse reinforcement in 60° and 90°, and the number of vertical legs of the internal transverse reinforcement used. Comparing the results of the beams with internal stirrups with the reference beam, it was observed that the internal stirrups provided increases of up to 14% in shear strength when compared with the closed stirrup.

**Keywords:** shear; internal transverse reinforcement; unconnected stirrups.

**Resumo:** Elementos de concreto armado com elevada taxa de armadura longitudinal e transversal podem apresentar conflitos das duas armaduras gerando redução em produtividade durante a armação do elemento e mal posicionamento da armadura transversal diminuindo a efetividade da armadura. Diante disso, essa pesquisa apresenta um tipo de armadura transversal interna como forma de mitigar esse conflito entre as barras transversais e longitudinais. Foram ensaiadas 5 vigas faixa de concreto armado, sendo uma de referência com estribos fechados e as outras 4 com estribos internos variando a inclinação das armaduras transversais internas em 60º e 90º e a quantidade de pernas verticais da armadura transversal interna utilizada. Comparando os resultados das vigas com estribos interno com a viga de referência, observou-se que os estribos internos garantiram ganhos de até 14% de capacidade de resistência ao cisalhamento em comparação com o estribo fechado.

**Palavras-chave:** cisalhamento; armadura transversal interna; estribos desconectados.

**How to cite:** D. F. Souza, J. H. C. Abrantes, L. S. Tapajós, M. P. Ferreira, and A. F. Lima Neto, "Shear in reinforced concrete beams with continuous internal transverse reinforcement," *Rev. IBRACON Estrut. Mater.*, vol. 16, no. 1, e16106, 2023, https://doi.org/10.1590/S1983-41952023000100006

**Corresponding author:** Aarão F. Lima Neto. E-mail: aaraon@ufpa.br
**Financial support:** None.
**Conflict of interest:** Nothing to declare.
**Data Availability:** The data that support the findings of this study are openly available in UFPA repository at http://repositorio.ufpa.br:8080/jspui/handle/2011/13408.

## 1 INTRODUCTION

The need to overcome larger spans with reinforced concrete elements, without interfering in the architecture design and resist greater loads, generates greater shear stresses in beams and slabs. Elements with high shear and bending stresses (Figure 1) may present conflict between the types of reinforcement used, being necessary to rearrange the distribution of the shear reinforcement to solve the conflict between the bars. However, Freitas [1] highlights that the redistribution of the transverse reinforcement might reduce the structural performance.

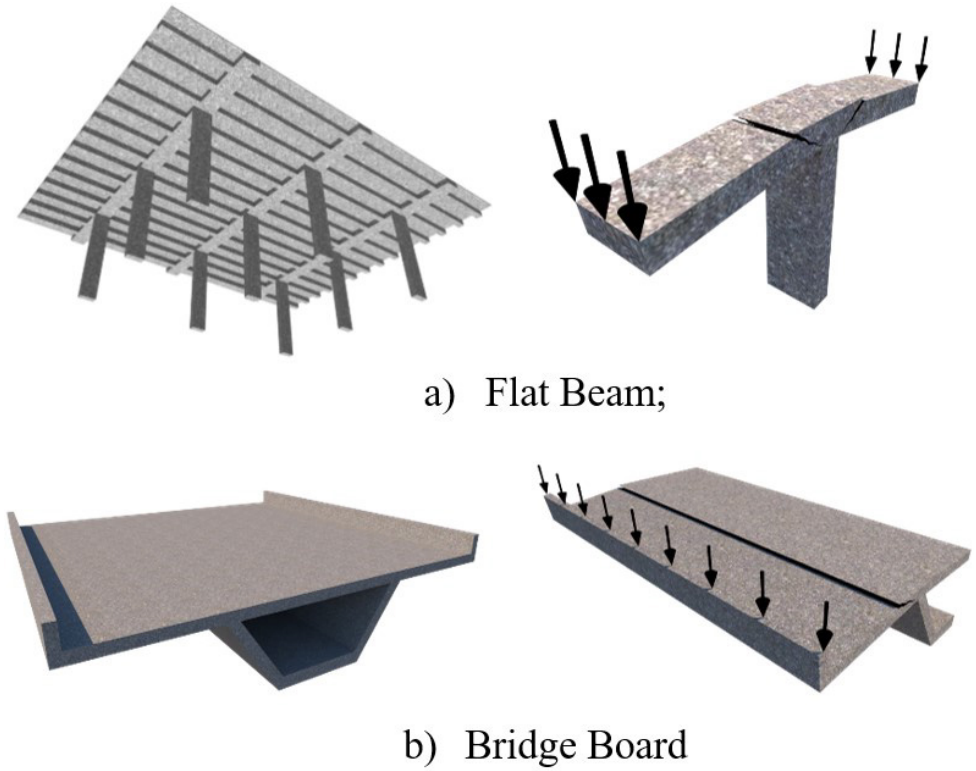


**Figure 1 -** Structures under one-way shear failure.

Today, there are many types of transverse reinforcement, such as the conventional stirrups, which can be open or closed, and the studs or dowels, which have flattened heads and are recommended for use on flat slabs to avoid punching failure, as an alternative to the conflict of reinforcement. However, there may still be a conflict between the transverse and longitudinal reinforcement, since both types of reinforcement are external, that is, the ends need to be on the longitudinal bars. One of the alternatives to avoid the conflict between reinforcement is the use of shear reinforcement with internal anchoring, positioned between the tensile and compression bars, as discussed by [2]–[4]. Figure 2 shows the types of transverse reinforcement.

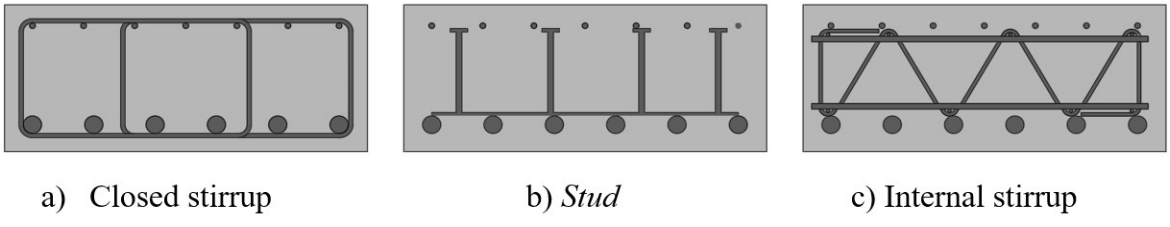


**Figure 2 –** Cross section detail with different types of transverse reinforcement.

The closed stirrup is a type of cross-sectional reinforcement widely used in Brazil, mainly in the most remote locations of large urban centers, due to the possibility of being manufactured *in loco*, not requiring specialized labor and presenting ease of manufacture, as well as meeting the recommendations of NBR 6118 [5], which recommends these stirrups to involve the flexural reinforcement to ensure better anchoring. However, the closed stirrup, in elements with a high ratio of transverse and longitudinal reinforcement, presents difficulties in assembling, which may reduce the efficiency of the service done.

In this context, the use of transverse reinforcement with internal anchoring has been highlighted, with several articles about it being published [2]–[4], [6]–[13]. As the shear reinforcement with internal anchoring are positioned between the upper and lower bars of the flexural reinforcement, their positions can be independent, avoiding the conflict of bars. This way, it is possible to industrially manufacture such reinforcement modules, speeding the construction process and generating greater savings with labor, contributing to the reduction of construction costs [14]–[16].

Despite the constructive advantages related to this type of reinforcement, [17], [18] found that the transverse bars that do not anchor to the longitudinal bars tend to show lower performance than those that have this anchoring guaranteed. In addition, some research have pointed out that premature failures and delamination cracks were related to shear reinforcement with internal anchoring [6]–[8]. However, it is worth noting that, in some cases, it was possible to control the cracking by delamination in structures with internal shear reinforcement, through a COMPLEMENTARY REINFORCEMENT, as observed in the results of Pinto [4], in which the complementary reinforcement works as well as the transverse reinforcement, allowing the flow of forces and the functioning of the Mörsh truss, resulting in strengths equal to or greater than that of elements with closed stirrups and studs [3], [4], [10].

In order to propose a new model of transverse reinforcement with internal anchoring, this work experimentally analyzes the behavior of reinforced concrete wide beams with internal stirrups with multiple legs, vertical and inclined ones, used as shear reinforcement. To evaluate the performance of these stirrups, the behavior of the beams with this type of reinforcement will be compared with that of a beam with closed stirrups, with the same transverse reinforcement ratio, as well as all the observed ultimate strengths will be compared with theoretical strengths, obtained by the recommendations of NBR 6118[5], ACI 318 [19] and Eurocode 2 [20].

## 2 CODE RECOMMENDATIONS

Several code recommendations guide that the possibility of shear failure in concrete elements be reduced through the design, due to its brittle behavior, which can occur without many warnings, making interventions impossible. According to several authors, the use of transverse reinforcement is the most viable way to guarantee the increase in strength and ductility in concrete structures [21]–[29].

Thus, it is common to find in the design codes recommendations on the use of a minimum shear reinforcement ratio, even when the tangential stress is not so high. When it is necessary to design a concrete element under shear forces, the Brazilian, American, and European codes provide recommendations regarding the calculation of the contribution portion of concrete and transverse reinforcement. These recommendations will be presented in this section. It is worth mentioning that the equations will be presented without weighting coefficients, allowing the reader to better compare the codes, thus obtaining characteristic strengths, and not design ones.

### 2.1 NBR 6118 (2014)

NBR 6118 [5] mentions two models for calculating one-way shear strength estimates in reinforced concrete elements. The models consider that the shear strength in elements with transverse reinforcement ($V_{R,cs}$) consists of concrete contribution ($V_{R,c}$) plus the contribution of steel ($V_{R,s}$), as shown in Equations 1 and 5.

Model I of the Brazilian code adopts the value of inclination of the strut equal to 45º, therefore it is recommended to use Equations 2 and 3 to calculate the contributions of concrete and steel, respectively, and it is limited by the maximum shear strength ($V_{R,max\ I}$) by Equation 4.

$$V_{R,cs\ I} = V_{R,c\ I} + V_{R,s\ I} \tag{1}$$

$$V_{R,c\ I} = 0.6 f_{ctk,inf}\ .\ b\,w.d \tag{2}$$

$$V_{R,s\ I} = \left(\frac{A_{sw}}{s}\right) \cdot 0.9 \cdot d \cdot f_{yw} \cdot (\sin\alpha + \cos\alpha) \tag{3}$$

$$V_{R,max\ I} = 0.27 \cdot \left(1 - \frac{f_{ck}}{250}\right) \cdot f_{cd} \cdot b_w \cdot d \cdot (cot\ \alpha + 1) \quad (4)$$

Where:
$V_{R,csI}$ is the shear strength of reinforced concrete elements with transverse reinforcement estimated by model I;
$V_{R,cI}$ is the shear strength of reinforced concrete elements without transverse reinforcement estimated by model I;
$V_{R,sI}$ is the contribution of transverse reinforcement to the shear strength of reinforced concrete elements estimated by model I;
$\alpha$ is the angle of inclination of the transverse reinforcement in relation to the longitudinal one.
$A_{sw}$ is the steel area of shear reinforcement per layer;
$b_w$ is the width of the beam;
$d$ is the depth;
$s$ is the spacing between the shear reinforcement layers;
$f_{ck}$ is the characteristic compressive strength of concrete;
$f_{cd}$ is the design compressive strength of the concrete, where, as the safety factors were not used, the $f_{cd} = f_{ck}$;
$f_{ctk,\ inf} = 0.7.\ f_{ct}$, m - brittle tensile strength of concrete in 5% of cases;
$f_{ct,\ m}$ is the mean tensile strength of concrete, defined for concretes with a maximum strength of 50 MPa, calculated by $f_{ct,\ m} = 0.3.\ f_{ck}^{2/3}$;
$f_{yw}$ is the yield strength of the shear reinforcement.

Model II of NBR 6118 [5] considers the effects caused by diagonal cracking, which impacts the reduction of the strut inclination and, consequently, the concrete contribution. In this model, the Brazilian code allows the variation of the inclination angle of the strut $\theta$ between 30° and 45°, only if the value of the concrete contribution ($V_{r,cII}$) is calculated by Equation 6. In this case, the concrete contribution is a function of the applied force ($V_{sd}$), calculated through an iterative process. The contribution of transverse reinforcement ($V_{R,sII}$) is calculated by Equation 7 and the maximum shear strength ($V_{R,\ max}$) by Equation 8.

$$V_{Rcs,\ II} = V_{R,c\ II} + V_{R,s\ II} \quad (5)$$

$$V_{R,c\ II} = V_{c0} \cdot \frac{V_{R,max\ II} - V_{sd}}{V_{R,max\ II} - V_{c0}} \leq V_{c0} \quad (6)$$

$$V_{R,s\ II} = \frac{A_{sw}}{s} \cdot 0.9 \cdot d \cdot f_{ywd} \cdot (cotg\ \theta + cotg\ \alpha) \cdot sin\ \alpha \quad (7)$$

$$V_{R,max\ II} = 0.54 \cdot \left(1 - \frac{f_{cd}}{250}\right) f_{cd} \cdot b_w \cdot d\ \sin^2\theta \cdot (cot\ \alpha + cot\ \theta) \quad (8)$$

Being:
θ is the angle of inclination of the strut, varying from 30° to 45°;

## 2.2 ACI 318 (2014)

The American code considers one-way shear strength of reinforced concrete elements to be like the strength of a beam, so Equation 9 is used to estimate the shear strength of beams without transverse reinforcement ($V_{R,c}$). The code adopts, among the variables that impact shear strength, only concrete strength.

$$V_{R,c} = 0.17 \cdot \sqrt{f_c} \cdot b_w \cdot d \quad (9)$$

Where:
$f_c$ is the concrete strength, obtained by tests with cylinder specimens;
$b_w$ is the width of the beam;
d is the depth of the beam.

For beams with transverse reinforcement, ACI 318 [19] considers that the shear strength ($V_{R,cs}$) is given by the contributions of concrete and transverse reinforcement ($V_{R,s}$), calculated by Equation 10, emphasizing that the code estimates that the inclination of the strut is equal to 45°. The contribution of shear reinforcement is calculated by Equation 11. In addition, the American code limits the maximum shear strength of beams given by Equation 12, which refers to failure due to crushing of the strut ($V_{R,max}$).

$$V_{R,cs} = V_{R,c} + V_{R,s} \tag{10}$$

$$V_{R,s} = \left(\frac{d}{s}\right) \cdot A_{sw} \cdot f_{yw} \cdot (sin\,\alpha + cos\,\alpha) \tag{11}$$

$$V_{R,max} = 0.66 \cdot \sqrt{f_c} \cdot b_w \cdot d \tag{12}$$

Where:
$s$ is the spacing between the transverse reinforcement layers;
$A_{sw}$ is the steel area of one layer of transverse reinforcement;
$f_{yw}$ is the yield strength of the transverse reinforcement, limited to 420 MPa;
$\alpha$ is the angle of inclination of transverse reinforcement in relation to the longitudinal one.

### 2.3 EUROCODE 2 (2004)

Eurocode 2 [20] gives Equation 13 to estimate the contribution of concrete to the shear strength of beams ($V_{R,c}$). In this equation, it is seen that the European code takes into account other factors, such as concrete strength, size effect and longitudinal reinforcement ratio, which impacts shear strength due to the dowel action.

$$V_{R,c} = max\begin{cases}(0.18 \cdot k \cdot (100 \cdot \rho_l \cdot f_c)^{1/3}) \cdot b_w \cdot d \\ 0.035 \cdot k^{\frac{3}{2}} \cdot \sqrt{f_c} \cdot b_w \cdot d\end{cases} \tag{13}$$

Where:
$k$ considers the reduction in shear strength due to size effect, calculated by Equation 14.

$$k = 1 + \sqrt{\frac{200}{d}} \leq 2 \tag{14}$$

$\rho_l$ is the portion related to the longitudinal reinforcement ratio, calculated by $\rho_l = \frac{A_s}{b_w \cdot d} \leq 2$, $A_s$ being the longitudinal steel area of the beam.

Eurocode 2 [20] suggests Equation 15 to evaluate the shear strength of beams with transverse reinforcement ($V_{R,cs}$), where it is seen that this estimate considers only the contribution of reinforcement, and its strength cannot be lower than that of a beam without shear reinforcement. In addition, the code also recommends that the angle of inclination of the strut may vary from 21.8° to 45°. The maximum shear strength ($V_{R,max}$) is estimated by Equation 16.

$$V_{R,cs} = max\begin{cases}\frac{A_{sw}}{s} \cdot 0.9 \cdot d \cdot f_{yw} \cdot (cot\,\theta + cot\,\alpha) \cdot sin\,\alpha \\ V_{R,c}\end{cases} \tag{15}$$

Being:
θ is the angle of inclination of the strut, varying from 21.8° to 45°;

$$V_{R,\max} = \frac{0.9 \cdot b_w \cdot d \cdot \nu_1 \cdot f_c \cdot \left(\cot\theta + \cot\alpha\right)}{1 + \cot^2\theta} \tag{16}$$

$\nu_1$ being determined by Equation 17;

$$\nu_1 = 0.6 \cdot \left[1 - \frac{f_c}{250}\right] \tag{17}$$

As EC2 [20] admits the variation of the inclination angle of the strut $\theta$ for the design, it suggests that Equations 15 and 16 are equalized for checking the strength, to verify the smallest angle that can be used to evaluate the strength of a beam according to its characteristics. Equalizing these two equations, Equation 18 is obtained, which provides the smallest angle that may be used.

$$\cot \quad \grave{e} = \sqrt{\frac{b_w s \cdot \nu_1 \cdot f_c}{A_{sw} \cdot f_d \cdot \operatorname{sen}\alpha}} \tag{18}$$

Where:
$f_{yd}$ – is the yielding strength of steel, recommended by EC2 as $0.8.f_{ys}$, which is the yielding strength for the characterization test of the steel.

### 2.4 Flexural strength of reinforced concrete beams

Several code recommendations, such as EC 2 [20] and ABNT NBR 6118 [5], shows simplified theories to estimate the flexural strength of reinforced concrete elements assuming that: the Bernoulli hypothesis of plane sections is valid; perfect compatibility between the strains of concrete and steel; the tensile strength of concrete is ignored for the ultimate limit state; the stress distribution in concrete can be assumed as a parabola-rectangle diagram, which can be replaced by a rectangle. To estimate the flexural strength in this study, the recommendations of ABNT NBR 6118 [5] will be used, considering that the tensile and compression flexural reinforcement reach yielding, to obtain Equations 19 to 23.

$$C_c + C_{s\prime} - T_s = 0 \tag{19}$$

$$(\eta \cdot f_c \cdot b_w \cdot c) + (A_{s\prime} \cdot f_{ys\prime}) = A_s \cdot f_{ys} \tag{20}$$

$$c = \frac{(A_s \cdot f_{ys}) - (A_{s\prime} \cdot f_{ys\prime})}{\eta \cdot f_c \cdot b_w} \tag{21}$$

$$M_{flex} = A_s \cdot f_{ys} \cdot z \tag{22}$$

$$V_{flex} = \frac{M_{flex}}{a} \tag{23}$$

Being:
$\eta$ is a constant, assumed to be 1 for constant sections and 0.9 for the other cases;
$\alpha_{cc}$ is assumed to be 0.85 for $f_c \leq 50$ MPa. In cases where the long-term effects of concrete can be neglected, such as short-time tests, 0.95 is assumed;
$c$ is the height of the concrete compression block;
a is the shear span of the element.

## 3 EXPERIMENTAL PROGRAM

This experimental program had a series of tests on five transverse reinforced concrete wide beams, with a cross section of 500 mm of width, 210 mm of height, and 2300 mm of length. In one of the beams, closed stirrups were used as shear reinforcement, being a reference for comparison with the other four beams, which had their transverse reinforcement composed by continuous stirrups with internal anchoring. The main variables analyzed were inclination of transverse reinforcement, diameter of the transverse steel bars and number of bars per layer, in such a way that these variations had the same transverse reinforcement ratio. In addition, reinforcement with internal anchoring had complementary reinforcement, to contribute to the anchoring and avoid delamination effect, with the same pieces used by [3], [4].

For the names of the beams, a system of three terms was adopted: *A*-*B*-*C*. The first term (*A*) represents the transverse reinforcement used, where, if indicated by letter *C*, it refers to the closed stirrups and, where indicated by letter *M*, it refers to the continuous internal stirrups. The second term (*B*) represents the number of vertical bars in each layer of shear reinforcement, which may be 4 or 8 legs, and the term *C* indicates the angle adopted for shear reinforcement (90º or 60º). Table 1 shows the main variables of the tested beams. Figure 3 shows the dimensions of the beams and how they were positioned in the press.

**Table 1 -** Characteristics of the tested beams

| BEAM | $Ø_w$ (mm) | α (°) | No. $Ø_w$ | $A_{sw}$ (mm²) | S (mm) | $ρ_w$ (%) | $f_{yw}$ (MPa) |
|---|---|---|---|---|---|---|---|
| C-4-90 | 6.3 | 90 | 4 | 113.10 | 100 | 0.23% | 687.12 |
| M-8-90 | 4.2 | 90 | 8 | 110.84 | | 0.22% | 612.56 |
| M-4-90 | 6.3 | 90 | 4 | 113.10 | | 0.23% | 687.12 |
| M-8-60 | 4.2 | 60 | 8 | 110.84 | | 0.26% | 612.56 |
| M-4-60 | 6.3 | 60 | 4 | 113.10 | | 0.26% | 687.12 |
| **$b_w$ (mm)** | **h (mm)** | **a (mm)** | **d (mm)** | **L (mm)** | **$Ø_f$ (mm)** | **$f_c$ (MPa)** | **$f_{ys}$ (MPa)** |
| 500 | 210 | 620 | 171.5 | 2300 | 8 | 25.01 | 531.95 |

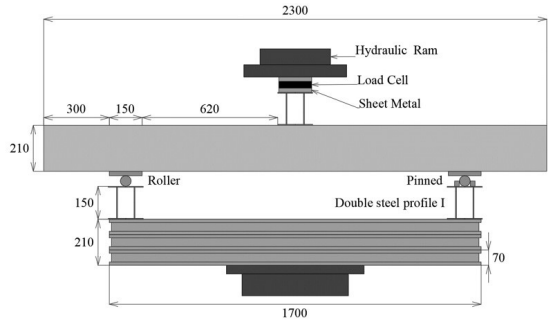


a) Characteristics and dimensions of the beams;

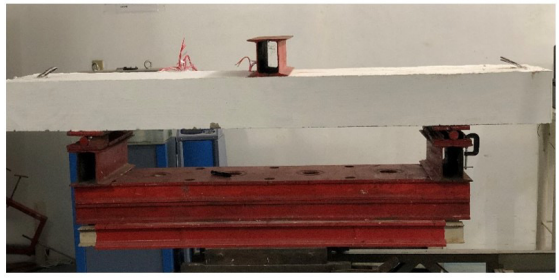

b) Beam before test.

**Figure 3 –** Characteristics and dimensions of the tested beams.

### 3.1 Flexural reinforcement

The steel bars used as flexural and transverse reinforcement were CA-50 and CA-60 types, where CA stands for Reinforced Concrete and the values 50 and 60 correspond to the characteristic strength of steel, that is, the CA-50 steel bars must have a characteristic strength of 500MPa and the CA-60 steel bars must have a characteristic strength of 600MPa.

The longitudinal reinforcement was designed so that the beams presented greater flexural strength, allowing shear failure. In the tensile region, six CA-50 steel bars with a diameter of 25.0 mm were used, and in the compression region, seven CA-50 steel bars with a diameter of 8.0 mm.

To assess the mechanical properties of the steel used, three samples of the longitudinal bars were tested under tensile force according to NBR 6892 [30]. The samples of 8.0 mm bars showed an average of $f_{ys}$= 558.56 MPa, $\varepsilon_{ys}$= 2.72‰, $E_s$= 205.65 GPa and the samples of 25.0 mm bars showed an average of $f_{ys}$= 531.95 MPa, $\varepsilon_{ys}$= 2.71‰, $E_s$= 199.66 GPa. Table 2 presents the mechanical properties of tensile and compression bars.

**Table 2 -** Mechanical properties of the flexural bars

| Ø (mm) | $E_s$ (GPa) | $f_{ys}$ (MPa) | $\varepsilon_{ys}$ (‰) |
|---|---|---|---|
| 8.0 | 205.65 | 558.56 | 2.72 |
| **STANDARD DEVIATION** | 14.05 | 19.55 | 0.09 |
| 25.0 | 196.66 | 531.95 | 2.71 |
| **STANDARD DEVIATION** | 5.68 | 8.94 | 0.06 |

### 3.2 Shear reinforcement

Beam C-4-90 was composed by 2 closed stirrups per layer, resulting in four CA-60 vertical bars with diameter of 6.0 mm in each stirrup layer. The recommendations from NBR 6118 [5] have been followed, where the stirrups involved tensile and compression reinforcement to guarantee their anchoring in the beam, as well as the bend diameter and development length were also based on the code recommendation.

Beams M-8-90 and M-8-60 were assembled with an internal transverse reinforcement, i.e., the stirrups were positioned between the flexural reinforcement of the beam. The internal stirrups, called stirrups *M*, were manufactured with CA-60 steel of 4.2 mm in diameter, with 8 vertical bars. In addition, 6.3 mm longitudinal bars with CA-50 steel were inserted inside the bending points of the internal stirrups, contributing to anchoring, as recommended by NBR 6118 [5] and Eurocode 2 [20], in addition to assist in the manufacture of shear reinforcement in modules.

Beams M-4-90 and M-4-60 were also reinforced with internal shear reinforcement, M stirrup. The stirrups were made of CA-60 steel with a diameter of 6.0 mm, composed of 4 vertical legs. To assist in anchoring, CA-50 steel longitudinal steel bars with a diameter of 10 mm were used. All beams with stirrups M were added with complementary reinforcement.

The stirrup layers of M-8-90 and M-4-90 beams were positioned at 90º in relation to the longitudinal axis of the beams, while the stirrup layers of M-8-60 and M-4-60 beams were inclined at 60º in relation to the longitudinal axis of the beams. The stirrups of all tested beams were spaced every 100.0 mm, keeping the reinforcement ratio close to that of the reference beam. Figure 4 shows the cross section, the spacing and inclination of the reinforcement of the tested beams, and Figure 5 shows the stirrups used in the beams and the assembled module.

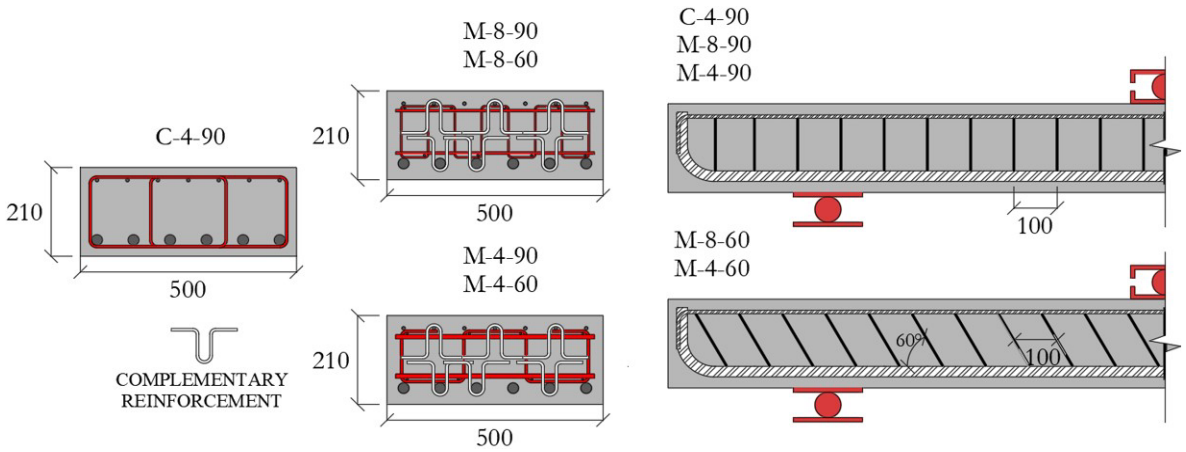


**Figure 4 -** Cross section and reinforcement layout of the tested beams.

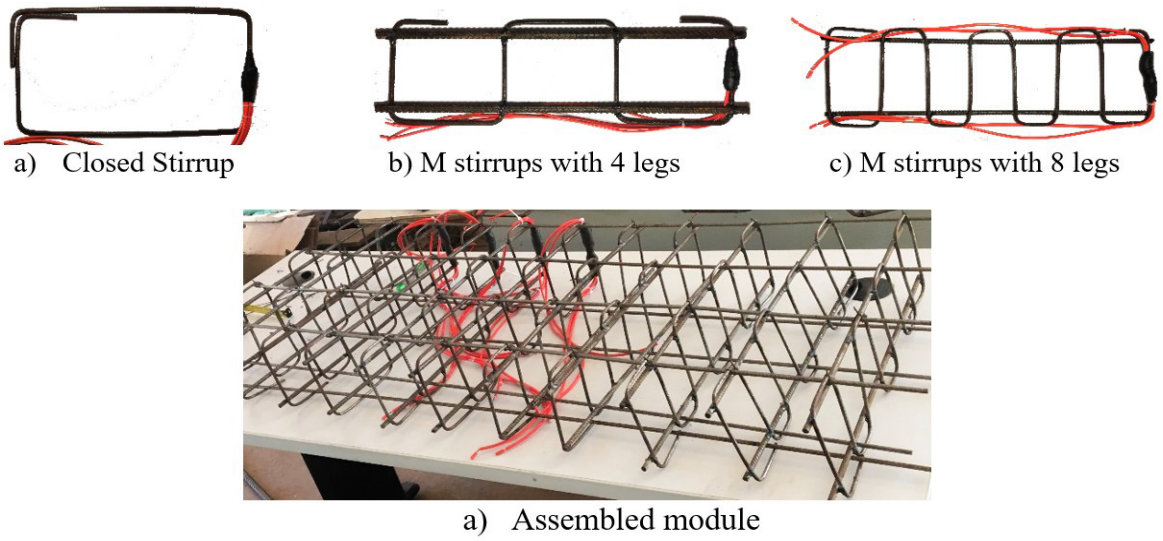


**Figure 5 –** Stirrups used in the beams.

In the studies by Ferreira et al. [2] and Tapajós [3], the beams studied with internal transverse reinforcement showed a delamination effect due to an anchoring failure of the internal stirrups. To reduce these effects, Tapajós [3] used a complementary reinforcement to mitigate delamination effect and allow the flow of internal forces. In this study, this complementary reinforcement was adopted in the four beams with internal stirrups. The complementary reinforcement was manufactured with CA-50 steel with a diameter of 6.3 mm. Six complementary reinforcements were used per stirrup layer, they were positioned in the flexural reinforcement, being 3 of them located in the compression region and the other 3 in the tensile region, totaling a complementary reinforcement ratio ρwc of 0.75% for beams with transverse reinforcement at 90º and 0.86% for beams with transverse reinforcement at 60º. Figure 6 shows the dimensions and the manufactured complementary reinforcement.


a) Dimensions of the complementary reinforcement.

b) Complementary reinforcement used.

**Figure 6 –** Complementary reinforcement.

Three samples of each diameter used were separated from the steel used in the shear reinforcement and subjected to tensile tests following the recommendations from NBR 6892 [30]. Samples of CA-60 steel of 4.2 mm presented means of $f_{ys}$ = 612.56 MPa, $\varepsilon_{ys}$ = 3.07‰, $E_s$ = 200.16 GPa, samples of CA-60 bars of 6.0 mm showed means of $f_{ys}$ = 687.12 MPa, $\varepsilon_{ys}$ = 3.60‰, $E_s$ = 192.28 GPa and samples of CA-50 bars of 6.3 mm presented means of $f_{ys}$= 585.83MPa, $\varepsilon_{ys}$= 3.08‰, $E_s$= 190.61GPa. Table 3 presents the mechanical properties of the steel bars used as transverse reinforcement of the beams.

**Table 3 -** Mechanical properties of the transverse reinforcement

| Ø (mm) | $E_s$ (GPa) | $f_{ys}$ (MPa) | $\varepsilon_{ys}$ (‰) |
|---|---|---|---|
| 4.2 | 200.16 | 612.56 | 3.07 |
| **STANDARD DEVIATION** | 10.63 | 15.07 | 0.17 |
| 6.0 | 192.28 | 687.12 | 3.60 |
| **STANDARD DEVIATION** | 17.62 | 31.28 | 0.49 |
| 6.3 | 190.61 | 585.83 | 3.08 |
| **STANDARD DEVIATION** | 11.46 | 13.81 | 0.18 |

### 3.3 Concrete

Concrete was produced with CP-II-E Portland cement (Portland cement composed with slag), medium sand as fine aggregate, gravel 01 with a maximum diameter of 19 mm as coarse aggregate and, to improve the workability of concrete, a multifunctional plasticizer and setting retarder admixture was used.

To determine the mechanical properties of concrete, 15 cylinder specimens (three for each beam) were made, with a diameter of 100 mm and height of 200 mm, following the recommendations of NBR 5738 [31]. They were used in compression tests based on NBR 5739 [32], 28 days after concreting the specimens, and tensile tests following the recommendations of NBR 7222 [33]. As the beams were tested in the same week and cast with the same batch of ready-mix concrete, their compressive strength as the mean of all tests performed, to avoid the influence of the variation of results in different tests from those samples. The concrete showed an average compressive strength of $f_c$ = 25 MPa and tensile strength of $f_{ct}$ = 3.57 MPa. Table 4 presents the mechanical properties of the concrete used in the tested beams.

**Table 4 -** Concrete compressive strength and concrete splitting strength at 28 days

| Sample | $f_{ck}$ (MPa) | $f_{ct}$ (MPa) |
|---|---|---|
| CP1 | 23.85 | 3.80 |
| CP2 | 25.78 | 3.49 |
| CP3 | 25.54 | 3.68 |
| CP4 | 25.27 | 3.59 |
| CP5 | 27.12 | 3.42 |
| CP6 | 23.79 | 3.51 |
| CP7 | 23.69 | 3.50 |
| **Mean** | **25.01** | **3.57** |
| **SD** | **1.19** | **0.12** |
| **COV** | **5%** | **3%** |

### 3.4 Instrumentation

The Mid-span Deflection of the beams was measured with the aid of a LVDT, positioned in the mid-span of the beams, then measuring the maximum deflections of the beams. The potentiometer was fixed on the Yoke (device that helps in the positioning of the equipment), to avoid that the accommodation of the beams compromises the reading of the deflections.

The monitoring of concrete strains took place from an electric strain gauge (SG), positioned on the side face of each of the beams, in the mid-span. To measure the strain of the flexural reinforcement of each beam, two SG were used in one of the central bars of the flexural reinforcement in the tensile region, adopting the mean of the two obtained readings.

The choice of the positioning of the SG in the stirrups was based on the studies by [3], who instrumented all the stirrups positioned in the shear span to, thus, evaluate different levels of transverse reinforcement strain. Thus, as the studied beams had the same spacing between the stirrups, four stirrups located in the middle of the shear span of each beam were instrumented, obtaining the reading, and observing the behavior of all layers of the transverse reinforcement in the shear span.

### 3.5 Test Set-up

The beams were tested through a three-point test, using a hydraulic ram with a capacity of up to 3000 kN, where two points represent a roller and a pinned support, and the third point represents the load application in a simply supported beam. Due to limitations in the hydraulic ram dimensions, three hollow metal plates with a length of 1700 mm, a height of 70 mm and a thickness of 15 mm were used over the center of the hydraulic ram table, so that the beams were positioned correctly. Figure 7 shows the Test Set-up used.

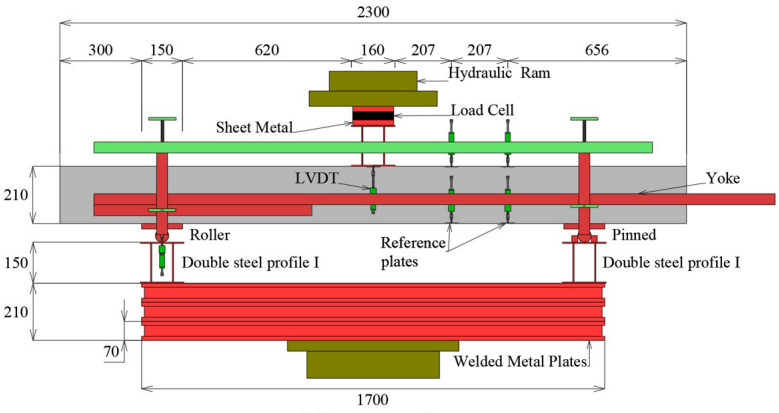


a) Test Set-up layout;

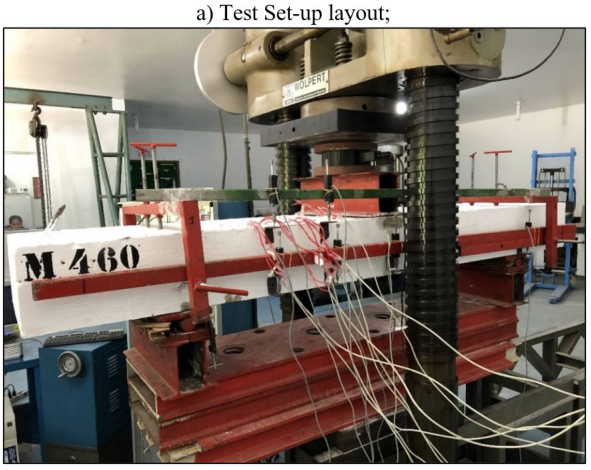


b) Beam positioned in the test set-up

**Figure 7** – Test Set-up.

For load application, a double steel I-profile with a width of 160 mm was used in the mid-span, at the top of the beam. Two double metal I-profiles, 150 mm wide, were used for the supports. Both supports had steel rollers, on top of metal plates, one being free and the other with horizontal movement restrictions that simulated conditions of roller and pinned supports, respectively. A load cell with a loading capacity of up to 3000 kN was used on the central double steel I-profile, for monitoring the loading level throughout the tests. All instruments used to monitor the tests were connected to a data acquisition module.

## 4 RESULTS AND DISCUSSIONS

### 4.1 Mid-span Deflection and Strain on the Flexural Reinforcement

Figure 8 shows the behavior of the shear force ($V$) versus deflection ($\delta$) in the mid-span of the tested beams. Due to the setting used in the test, the value of the shear force used in the graphs is half of the value obtained in the load cell.

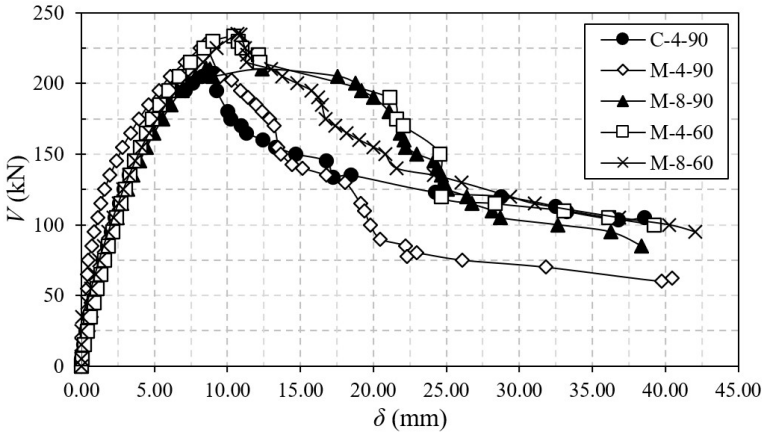


**Figure 8 –** Shear force versus Deflection of the beams.

The five tested beams, in general, presented a similar behavior for the same load until they reached the failure load and shear failure, where it was observed that the beams with internal transverse reinforcement presented greater strength and ductility than that of the beam with the closed stirrup (C-4-90), as also observed in the results of [3].

The M-4-90 beam showed a stiffer behavior for the same loading level than the other beams until the failure load, and after reaching it, presented greater strains when compared with the reference beam. This occurred due to the appearance of delamination cracks close to the failure load, reducing the post-peak performance of the beam.

Beam M-8-90 presented behavior and strength similar to that of the reference beam until the failure load, however, after failing, it presented a ductile behavior, with low load reduction for a high strain, in relation to beams C-4-90 and M-4-90, which after the failure load presented high strains for a lower loading level.

The beams with stirrups inclined to 60º, M-8-60 and M-4-60, presented greater strength capacity in comparison with the other tested beams, as observed by [4] in the tested beam with prefabricated truss stirrups inclined at 60º and with complementary reinforcement on both sides. The performance is due to the capacity of the inclined stirrups to allow a larger steel area in the cracks, ensuring greater strength to the beam. Beams M-8-60 and M-4-60, as well as beam M-8-90, presented a ductile post-peak behavior with high strain in relation to load reduction.

Figure 9 shows the behavior of the shear force versus specific strain of the flexural reinforcement ($\varepsilon_l$) of the tested beams.

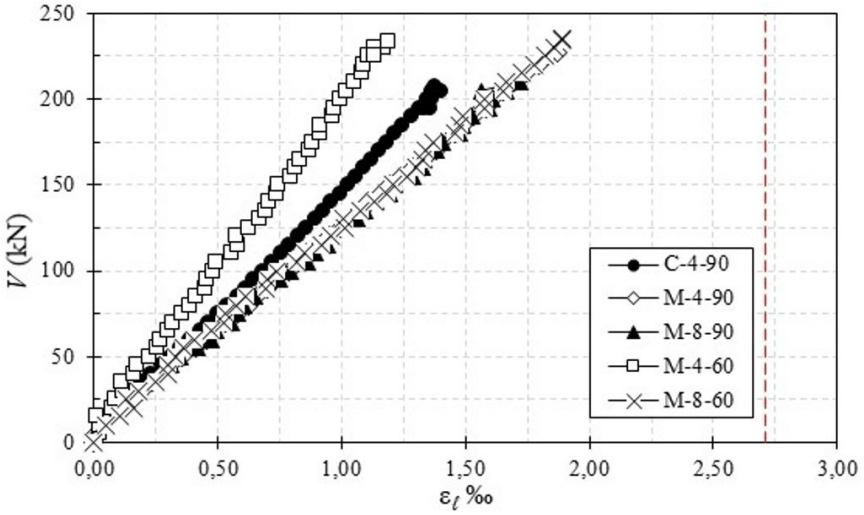


**Figure 9 –** Shear force versus Strains of the flexural reinforcement of the beams.

The beams showed similar behaviors and no flexural reinforcement reached the yielding strain, ruling out the hypothesis of a possible flexural failure. The reinforcement of beams M-4-90, M-8-60 and M-8-90 showed greater strain of the longitudinal reinforcement, for the same loading level, when compared with beams C-4-90 and M-4-60. This behavior was probably due to M stirrups presenting initial strains with a low loading level of the beams when compared with the other beams.

### 4.2 Concrete strain

Figure 10 shows the behavior with the shear force curve versus concrete strain ($\varepsilon_c$) of the tested beams.

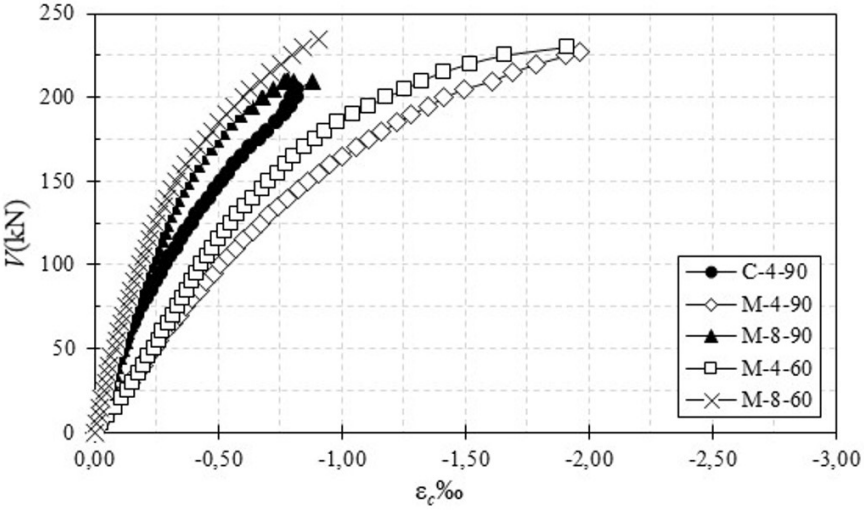


**Figure 10** – Shear force versus Concrete Strain.

The beams showed similar behavior, and in all specimens, it was observed that the maximum strain concrete was less than 2‰, discarding any hypothesis of failure due to flexural compression. Beams M-8-90 and M-8-60, with 8 vertical legs in the transverse reinforcement, presented smaller concrete strains for the same loading level in relation to the other beams. This behavior, as observed by [2]–[4], may have happened due to a larger steel area in the compression region of the beams, given that the constructive reinforcement of the modules added 78.5 mm$^2$ of steel in the transverse reinforcement ratio, and by the greater number of legs in the stirrups of beams M-8-90 and M-8-60, as observed in the

beams tested by [3], where beams with the same reinforcement ratio and less spacing presented greater stiffness in comparison with the other beams tested by the author.

Beams M-4-90 and M-4-60 showed greater concrete strain in relation to the other tested beams, probably due to the M stirrup, used in the two beams, having only 4 vertical legs per layer, thus allowing greater strains of concrete, for the same loading level, in relation to the other beams, as observed in the beams tested by [3], [4], where beams with the same reinforcement ratio, but with a greater number of stirrups, showed a stiffer behavior for the concrete strain. However, beam M-4-60 presented a difference in behavior when related to the strain of the flexural reinforcement with the concrete strain, and this difference may have occurred due to a possible failure in the instrumentation; it is necessary to carry out tests with more specimens to validate this behavior.

### 4.3 Shear reinforcement strain

Figure 11 shows the behaviors with the shear force curve versus strain of the transverse reinforcement ($\varepsilon_w$) of the tested beams.

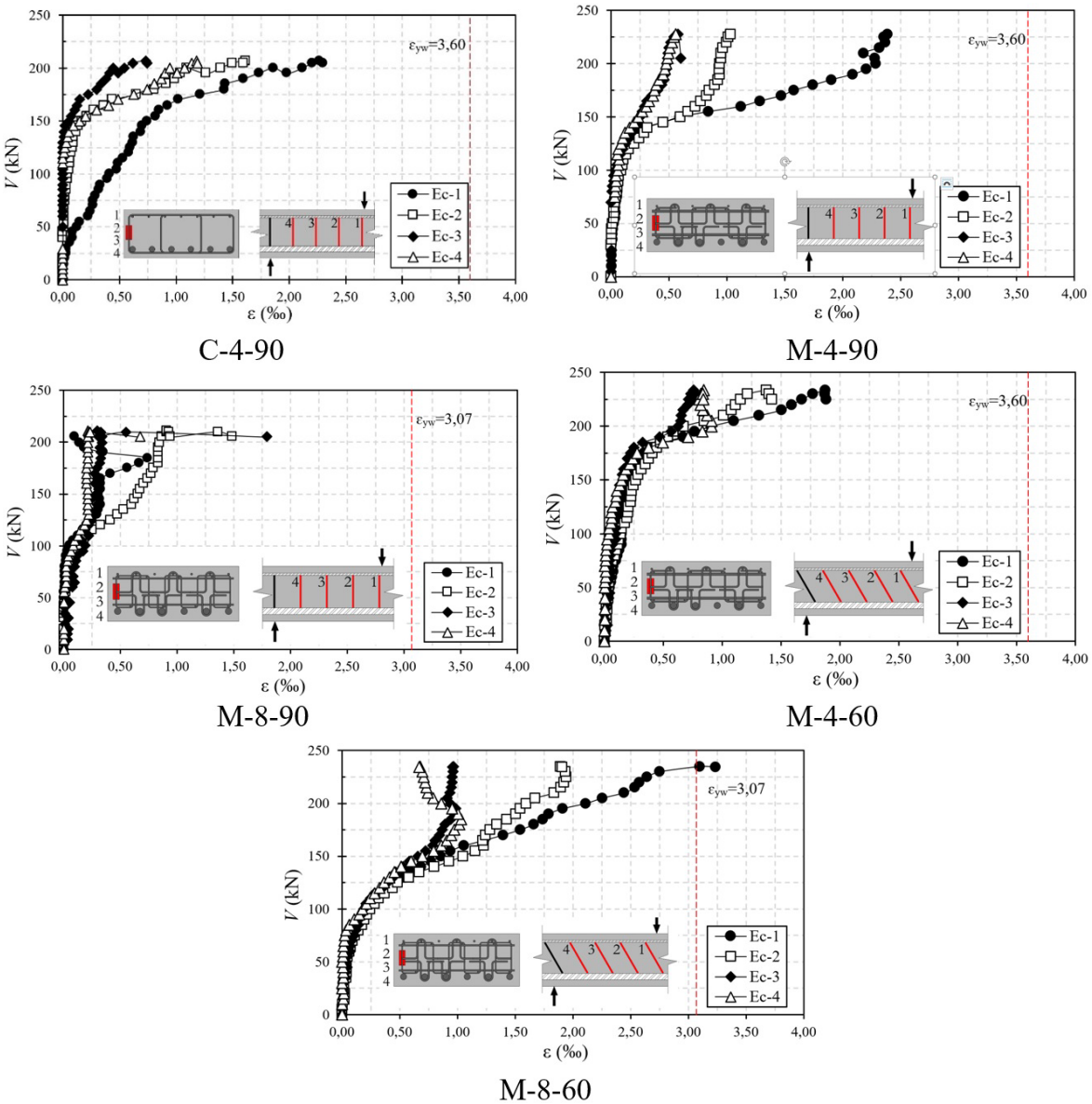


**Figure 11** – Shear force versus Strain of the transverse reinforcement of the beams.

It was observed that the transverse reinforcement bars did not reach yielding, except for M-8-60 beam, where only one layer reached the steel yielding strain value. This behavior was also observed in the second series tested by [3] and occurred due to the high transverse reinforcement ratio, which allows a greater distribution of forces between the shear reinforcement layers.

The closed stirrups, used in beam C-4-90, showed lower strains, in the initial loading stages, however for loading close to the failure load, the reinforcement presented greater strains, except for stirrup 1, which presented strains since the initial loading due to an accumulation of cracks near the stirrup.

The beams tested with M stirrup showed greater shear strength when compared with the C-4-90 reference beam, where it was seen that stirrups 1 and 2 developed more than stirrups 3 and 4 in all tested beams, due to the inclination of the cracks, where the diagonal concrete struts that rest on the longitudinal tensile bar lose anchoring. This delamination effect was seen in all beams with M stirrup, as observed by [2]–[4]. However, the efficiency of the complementary reinforcement stands out, as evidenced by [3], [4], since even with the appearance of cracks due to the delamination effect, beams with M stirrup showed greater strength when compared with C-4-90 beam.

Regarding the number of legs of the transverse reinforcement, beams M-4-90 and M-4-60 showed lower initial strains for stirrups, however they presented a ductile behavior in relation to beam M-8-90, which presented initial strain higher than the beams with 4 vertical legs, however, when approaching the failure load, stirrups presented greater stiffness, probably due to the complementary reinforcement. Again, there was an accumulation of cracks close to stirrups 1 and 2.

### 4.4 Failure Surface

Figure 12 shows the failure surfaces of the beams after the tests. All of them presented shear failure, with inclination of the main crack varying between 24º and 34º. In beams with internal shear reinforcement, even with complementary reinforcement, there was a delamination effect, however, as observed by [4], the effect was controlled by the complementary reinforcement and occurred close to the failure load, confirming the efficiency of the hooks in controlling and reducing the delamination effect.

### 4.5 Failure shear force

Regarding the failure load of the beams, they showed shear strength between 207 kN and 235 kN, in which the beams with the internal stirrups showed an increase in strength up to 10% when compared with the beam with closed stirrups (C-4-90), as observed in the results of [3], specifically in relation to the beam with prefabricated truss stirrups and complementary reinforcement. The beam with M stirrup, which presented lower performance in relation to the other beams, was M-8-90 beam, when compared with the reference beam, which showed a strength gain of only 2%. It is believed that this performance may have occurred due to the delamination cracks that appeared in the beam, thus reducing its shear strength.

The beams M-4-60 and M-8-60, with transverse reinforcement inclined at 60º, as expected, showed greater strength in comparison with the beams M-4-90 and M-8-90, with the stirrups at 90º, as observed in the study by [4], since the inclined transverse reinforcement manages to intercept a greater number of cracks, ensuring greater load capacity for the beam.

It was also observed that, when the stirrups with 4 vertical legs are compared with the stirrups with 8 legs, M-4-90 beam showed greater shear strength when compared with M-8-90 beam, however, the delamination effect may have limited the real strength of the beam.

The beams with M stirrup inclined at 60º, M-4-60 and M-8-60, presented an approximately equal strength, thus it is observed that the variation of the number of legs does not present increase in shear strength.

As for the flexural strength, it was observed that all beams had shear failure. And in relation to the reference beam, beams M-4-60 and M-8-60 showed the greatest strength increase, around 14%, followed by M-4-90 beam, which showed an increase of 10%, and finally M-8-90 beam, with a 2% strength gain, in comparison with the reference beam.

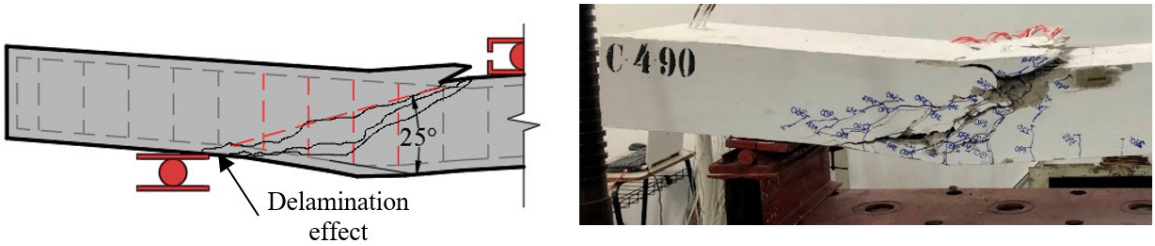


a) Cracks of beam C-4-90 and beam after the test

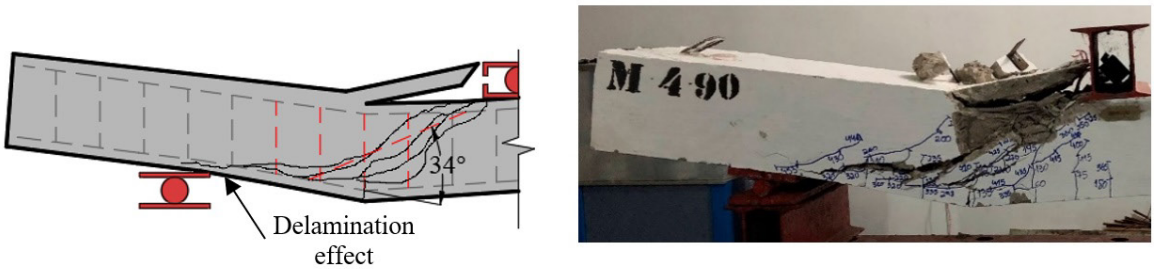


b) Cracks of beam M-4-90 and beam after the test

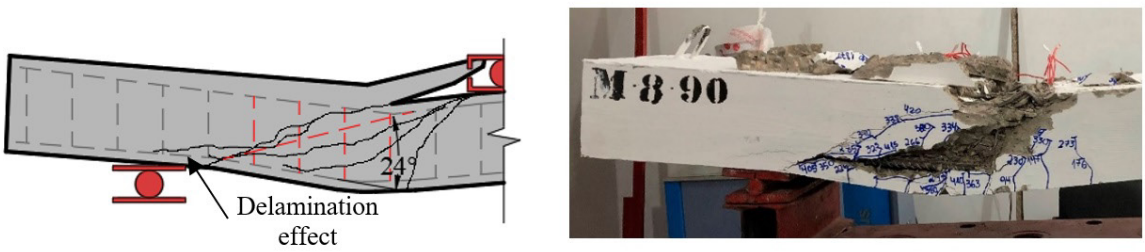


c) Cracks of beam M-8-90 and beam after the test

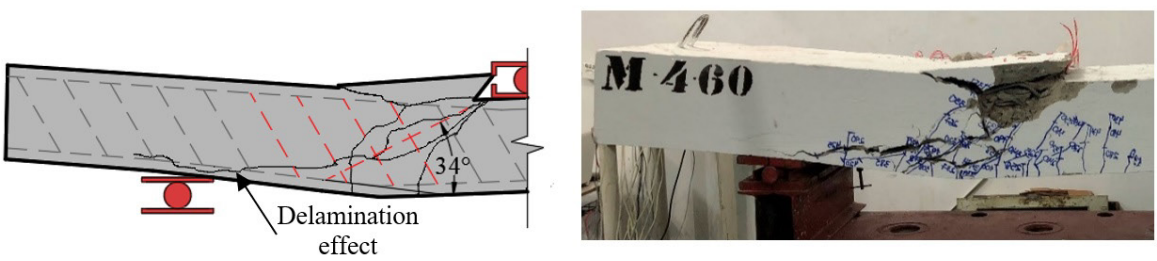


d) Cracks of beam M-4-60 and beam after the test

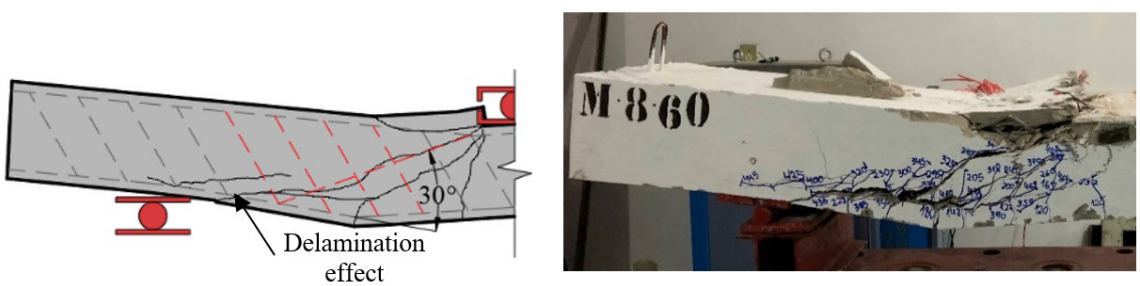


e) Cracks of beam M-8-60 and beam after the test

**Figure 12** – Failure surface of the tested beams

### 4.6 Code comparison

Table 5 shows the failure load of the beams, compared with the flexural shear and the values expected by theoretical prediction. Figure 13 shows the graph comparing the failure load with the theoretical prediction.

**Table 5 -** Failure load of the beams and comparison with theoretical estimates.

| Beams | $V_u$ (kN) | $V_u/V_{flex}$ | $V_u/V_{ref}$ | $V_u/V_{NBR-I}$ | $V_u/V_{NBR-II}$ | $V_u / V_{ACI}$ | $V_u / V_{EC2}$ |
|---|---|---|---|---|---|---|---|
| C-4-90 | 207.00 | 0.71 | 1.00 | 1.15 | 0.97 | 1.28 | 0.95 |
| M-4-90 | 227.50 | 0.78 | 1.10 | 1.27 | 1.07 | 1.41 | 1.04 |
| M-8-90 | 210.50 | 0.72 | 1.02 | 1.18 | 1.00 | 1.32 | 0.98 |
| M-4-60 | 233.50 | 0.80 | 1.13 | 1.10 | 0.97 | 1.22 | 1.00 |
| M-8-60 | 235.00 | 0.81 | 1.14 | 1.12 | 0.99 | 1.24 | 1.03 |
| **Mean** | | | | 1.17 | 1.00 | 1.30 | 1.00 |
| **Standard deviation** | | | | 0.06 | 0.04 | 0.07 | 0.04 |
| **COV (%)** | | | | 5% | 4% | 6% | 4% |

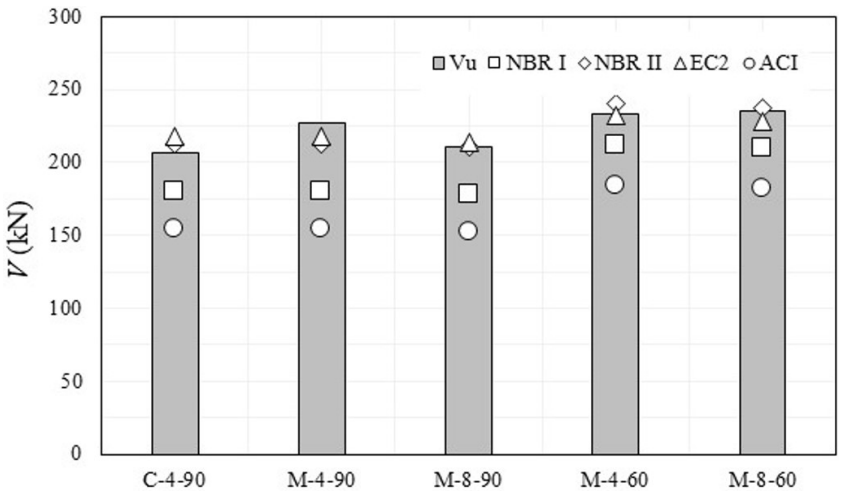


**Figure 13** - Comparative graph of failure load by theoretical estimates

In general, it is possible to observe that the level of dispersion of the results was relatively low, as well as the level of safety of the analyzed codes, for this sample universe, proves to be adequate.

Regarding the comparison with the analyzed codes, the most conservative was the American one [19], which was already expected, since it has this conservative profile in relation to safety, where all beams presented strength greater than 30% of what was estimated by it.

NBR 6118 [5] was conservative in its model I, however, model II presented all its values closer to the experimental ones, with theoretical estimates against security with the worst scenario 3% below what was predicted by the code. This approximation to the experimental values may have occurred due to model I considering only the 45º angle for the inclination of the strut in its design, while model II considers values between 30º and 45º, with this, a greater amount of transverse reinforcement layers is estimated, making the model II approach the tested values.

Eurocode 2 [20] approaches model II of NBR 6118 [5], where the mean of the comparisons of the two codes was equal to 1, and the standard deviation and variation of the code is equal to that of [5], confirming this proximity in the estimates, and this is justified since the recommendations for estimating the shear strength of the two codes are similar.

## 5 CONCLUSIONS

The main objective of this study was to evaluate the behavior of a new type of transverse reinforcement with internal anchoring, comparing it with closed stirrups, as they are a type of shear reinforcement widely used. It is worth

mentioning that the objective of the study was not to compare the consumption of steel to produce the beams, as the possible benefits of this type of reinforcement would not bring savings in material consumption, but in productivity, since this type of reinforcement allows for industrialization and prefabrication, as the position of the transverse reinforcement does not depend on the position of the longitudinal reinforcement.

The test set-up adopted to carry out this experimental study proved to be efficient, presented good behavior and all the parameters that were planned could be collected without major difficulties. In general, all beams had shear failure and the beams with M stirrups also showed delamination effects, however, the efficiency of the complementary reinforcement to control and reduce the delamination cracks stands out, due to the better anchoring of the internal transverse reinforcement, allowing the stirrups to show greater shear strength.

The beams tested with M stirrup showed mid-span strains similar to those of the reference beam and shear strength, on average, 10% higher than that of the beam with closed stirrups, the C-4-90 beam. Regarding the variation in the number of legs used in M stirrups, there was no increase in strength for stirrups with 4 vertical legs or stirrups with 8 vertical legs, but it was observed that beams with M stirrups with 4 legs showed greater ductility in relation to beams with stirrups with 8 legs.

Beams M-4-60 and M-8-60, with internal transverse reinforcement inclined at 60º, presented greater shear strength in relation to beams with M stirrups inclined at 90º. This gain in load capacity was also justified in the tests of [4] and can even be attributed to the fact that the inclined transverse reinforcement intercepts a greater number of cracks, thus allowing a better flow of internal forces.

The results of the two types of internal transverse reinforcement show the M stirrup as a promising alternative, since it can be industrially manufactured, presents ease of execution and gains in productivity, since it is only positioned between the flexural bars, thus reducing the cost with labor to manufacture the M stirrups.

Through the comparisons made with the test results of the beams with the theoretical prediction of the analyzed standards, it is possible to design efficiently and with adequate shear safety for beams with the M stirrups, as there were no large dispersions of the results of the beams strength when compared with the predicted strengths. However, it is worth mentioning that, as only one specimen of each beam was tested, more tests must be performed to observe and confirm whether this behavior is maintained in a larger sample universe, with more variables involved.

## 6 ACKNOWLEDGEMENTS

The authors would like to thank CAPES, CNPq, NUMEA, LEC CAMTUC UFPA, Eletrobras/Eletronorte and NDAE for their support in the development of this research.

## 7 REFERENCES

[1] M. V. P. Freitas, “Experimental analysis of the upper limits of puncture resistance of smooth reinforced concrete slabs with shear reinforcement,” M.S. thesis. Federal Univ. Pará, Tucuruí, 2018.

[2] M. P. Ferreira, R. N. M. Barros, M. J.M. Pereira Filho, L. S. Tapajós, and F. S. Quaresma, “One-way shear resistance of RC members with unconnected stirrups," *Lat. Am. J. Solids Struct.*, vol. 13, pp. 2670–2690, 2016.

[3] L. S. Tapajós, “Shear in reinforced concrete elements with disconnected stirrups,” M.S. thesis. Federal Univ. Pará, Belém, Brasil, 2017.

[4] R. S. Pinto, “Influence of complementary reinforcement on shear strength in reinforced concrete beams with prefabricated latticed stirrups,” M.S. thesis. Federal Univ. Pará, Tucuruí, 2019.

[5] Associação Brasileira de Normas Técnicas. *Design of concrete structures - procedure*, NBR 6118, 2014.

[6] T. Yamada, A. Nanni, and K. Endo, "Punching shear resistance of flat slabs: influence of reinforcement type and ratio," *ACI Struct. J.*, vol. 88, no. 4, pp. 555–563, 1992.

[7] R. B. Gomes and M. A. S. Andrade, “Does a punching shear reinforcement need to embrace a flexural reinforcement of a RC flat slab?, in *Proc. Int. Workshop on Punching Shear Capacity of RC Slabs, KTH Stockholm*, 2000 pp. 109-117.

[8] P. E. Regan, and, F. Samadian, Shear reinforcement against punching in reinforced concrete flat slabs," *Struct. Eng.*, vol. 79, no. 10, pp. 24–31, 2001.

[9] H. Park, K. Ahn, K. Choi, and L. Chung, "Lattice shear reinforcement for slab-column connections," *ACI Struct. J.*, vol. 104, no. 3, pp. 294–303, 2007.

[10] L. M. Trautwein, T. N. Bittencourt, R. B. Gomes, and J.C. D. Bella, “Punching strength of flat slabs with unbraced shear reinforcement," *ACI Struct. J.*, vol. 108, no. 2, pp. 197–205, 2011.

[11] A. P. Caldentey, P. P. Lavaselli, H. C. Peiretti, and F. A. Fernández, “Influence of stirrup detailing on punching shear strength of flat slabs," *Eng. Struct.*, vol. 49, pp. 855–865, 2013.

[12] M. Tapan, “Structural response of reinforced concrete wide beams reinforced with lattice girders,” *IJTS, Trans. Civ. Eng.*, vol. 38, no. 2, pp. 337-344.

[13] T. Eom, T. Song, J. Song, G. Kang, J. Yoon, and S. Kang, "Punching-shear Behavior of Slabs with Bar Truss Shear Reinforcement," *Eng. Struct.*, vol. 114, pp. 390–399, 2017.

[14] W. De Corte and V. Boel, "Effectiveness of spirally shaped stirrups in reinforced concrete beams," *Eng. Struct.*, vol. 52, pp. 667–675, 2013.

[15] C. G. Karayannis, and C. E. Chalioris,“Shear tests of reinforced concrete beams with continuous rectangular spiral reinforcement," *Constr. Build. Mater.*, vol. 46, pp. 86–97, 2013.

[16] A. S. Lubell, E. C. Bentz and M. P. Collins, “Shear reinforcement spacing in wide members," *ACI Struct. J.*, vol. 106, no. 2, pp. 205–214, 2009.

[17] P. E. Regan, "Shear reinforcement of flat slabs," in *Proc. International Workshop on Punching Shear Capacity of RC Slabs*, vol. 57, pp. 99–107, 2000. TRITA-BKN Bulletin.

[18] R. Beutel and J. Hegger, "The effect of anchorage on the effectiveness of the shear reinforcement in the punching zone," *Cement Concr. Compos.*, vol. 24, pp. 539–549, 2002.

[19] American Concrete Institute, *Building Code Requirements for Structural Concrete*, ACI 318, 2014.

[20] European Committee for Standardization, *Eurocode 2: Design of Concrete Structures — Part 1-1: General Rules and Rules for Buildings*, EN 1992-1-1, 2004.

[21] Y. Yoon, W. D. Cook, and D. Mitchell, "Minimum shear reinforcement in normal, medium, and high-strength concrete beams," *ACI Struct. J.*, vol. 93, no. 5, pp. 576–584, 1996.

[22] G. Russo and M. Pauletta, "Seismic behavior of exterior beam-column connections with plain bars and effects of upgrade," *ACI Struct. J.*, vol. 109, no. 2, pp. 225–233, 2012.

[23] B. Bresler, and A. C. Scordelis, "Shear strength of reinforced concrete beams," *ACI Struct. J.*, vol. 60, no. 1, pp. 51–74, 1963.

[24] K. N. Rahal, and K. S. Al-Shaleh, "Minimum transverse reinforcement in 65 MPa concrete beams," *ACI Struct. J.*, vol. 101, no. 6, pp. 872–878, 2004.

[25] C. Cucchiara, M. Fosseti, and M. Papia, "Minimum transverse reinforcement in 65 MPa concrete beams," *Struct. Eng. Mech.*, vol. 42, pp. 551–570, 2012.

[26] N. Spinella, P. Colajanni, and A. Recupero, "A simple plastic model for shear critical sfrc beams," *J. Struct. Eng.*, vol. 136, no. 4, pp. 390–400, 2010.

[27] P. Colajanni, A. Recupero, and N. Spinella, "Generalization of shear truss model to the case of SFRC beams with stirrups," *Comput. Concr.*, vol. 9, no. 3, pp. 227–244, 2012.

[28] N. Spinella, P. Colajanni, and L. La Mendola, "Nonlinear analysis of beams reinforced in shear with stirrups and steel," *ACI Struct. J.*, vol. 109, no. 1, pp. 53–64, 2012.

[29] G. Russo, D. Mitri, and M. Pauletta, "Shear strength design formula for RC beams with stirrups," *Eng. Struct.*, vol. 51, pp. 226–235, 2013.

[30] Associação Brasileira de Normas Técnicas, *Metallic materials - Tensile test at room temperature*, NBR 6892, 2013.

[31] Associação Brasileira de Normas Técnicas, *Concrete - Procedure for molding and curing specimens*, NBR 5738. 2008.

[32] Associação Brasileira de Normas Técnicas, *Concrete - Compression test of cylindrical specimens*, NBR 5739, 2007.

[33] Associação Brasileira de Normas Técnicas, *Mortar and concrete - Determination of the tensile strength by diametrical compression of cylindrical specimens*, NBR 7222, 2011.

**Author contributions:** DFS and LST: conceptualization, formal analysis, data curation, writing; MPF and AFLN: supervision, funding acquisition, conceptualization.

**Editors:** Ricardo Carrazedo, Guilherme Aris Parsekian.

IBRACON Structures and Materials Journal
Revista IBRACON de Estruturas e Materiais
ISSN 1983-4195 ismj.org

ORIGINAL ARTICLE

# Assessing the bearing capacity of Crestbond shear connectors to concrete pry-out

## *Resistência à ruptura do concreto por pry-out em conectores de cisalhamento Crestbond*

Ricardo Laguardia Justen de Almeida[a]
Gustavo de Souza Veríssimo[a]
José Carlos Lopes Ribeiro[a]
José Luiz Rangel Paes[a]
Rodrigo Barreto Caldas[b]
Hermano de Sousa Cardoso[c]
Ricardo Hallal Fakury[b]

[a]Universidade Federal de Viçosa – UFV, Departamento de Engenharia Civil, Viçosa, MG, Brasil
[b]Universidade Federal de Minas Gerais – UFMG, Programa de Pós-graduação em Engenharia de Estruturas, Belo Horizonte, MG, Brasil
[c]Universidade de Coimbra, Institute for Sustainability and Innovation in Structural Engineering – ISISE, Department of Civil Engineering, Coimbra, Portugal

Received 04 November, 2021
Accepted 09 May 2022

**Abstract:** In this work, a study on failure by concrete pry-out in Crestbond shear connectors is presented. The study's aim was the development of an expression that estimates the connection's bearing capacity. The analyses were carried out through numerical simulations designed to reproduce the referred failure mode. Numerical and experimental results are compared and discussed in relation to the maximum force reached and the cracking aspect typical of concrete pry-out. The proposed equation corresponded well to experimental results, with a mean ratio $P_{theo}/P_{exp}$ equal to 0,99 and a coefficient of variation of 10%. The results found in this study indicate that the concrete pry-out expression in German Technical Approval Z-26.4-56 can also be applied to Crestbond shear connectors.

**Keywords:** shear connector, Crestbond, numerical model, concrete pry-out, composite dowels.

**Resumo:** Neste trabalho é apresentado um estudo sobre a ruptura do concreto por pry-out em conectores de cisalhamento tipo Crestbond com o objetivo de obter um modelo de cálculo que estima a resistência da conexão a esse modo de falha. As análises foram realizadas por meio de simulações numéricas capazes de reproduzir o referido modo de falha. Os resultados numéricos são comparados com os experimentais e discutidos em relação à força máxima atingida e o aspecto da fissuração típica do pry-out. O modelo de cálculo proposto apresentou boa correspondência com os resultados experimentais, com uma razão média $P_{teo}/P_{exp}$ igual a 0,99 e um coeficiente de variação de 10%. Os valores encontrados nesse estudo sugerem que a expressão da Aprovação Técnica Alemã para outros conectores pode ser aplicada nos conectores Crestbond.

**Palavras-chave:** conector de cisalhamento, Crestbond, modelo numérico, pry-out do concreto, composite dowels.

**How to cite:** R. L. J. Almeida et al., "Assessing the bearing capacity of Crestbond shear connectors to concrete pry-out," *Rev. IBRACON Estrut. Mater.*, vol. 16, no. 1, e16107, 2023, https://doi.org/10.1590/S1983-41952023000100007

**Corresponding author:** Ricardo Laguardia Justen de Almeida. E-mail: ricardoljalmeida@gmail.com
**Financial support:** Coordenação de Aperfeiçoamento de Pessoal de Nível Superior (CAPES) – Finance Code 001; Universidade Federal de Viçosa.
**Conflict of interest:** Nothing to declare.
**Data Availability:** The data that support the findings of this study are available from the corresponding author, R. A., upon reasonable request.

## 1 INTRODUCTION

In recent years there has been a lot of research, especially as part of a European project called PreCo-Beam, to investigate the structural behavior of composite dowels [1]-[8], among which two shear connectors stand out due to their structural performance: the puzzle connector (PZ) - Figure 1b - and the clothoidal connector (MCL) – Figure 1c. In Brazil, a third shear connector was studied by Veríssimo [9], called Crestbond (CR) – Figure 1a.

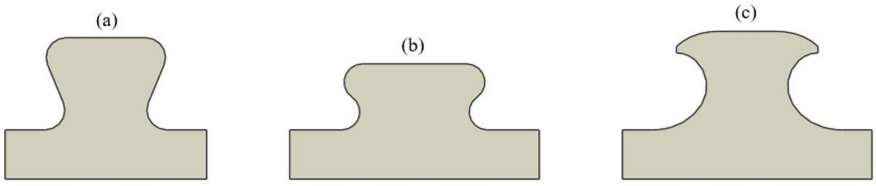


**Figure 1.** Composite dowel shear connection geometries: (a) Crestbond (CR); (b) Puzzle (PZ) and (c) Clothoidal (MCL).

Crestbond was developed due to the difficulties associated with the installation of the usual connectors in Brazil (shear-stud and C-channel) and has been the subject of research over the last few years [10]-[16]. Crestbond's geometry is similar to that of connectors studied in the PreCo-Beam project [5], particularly the puzzle shear connector. However, the Crestbond shear connector may have a different structural behavior due to its greater slenderness.

Because of the complex geometry of shear connectors, the heterogeneous behavior of concrete, and the interaction between these two elements, the strength mechanism of composite dowels cannot be sufficiently described through experimental tests alone. Therefore, a significant part of this research was carried out through numerical models capable of simulating the nonlinearities of the materials and contact interactions to better understand the behavior of composite dowels [7], [17]-[20].

The bearing capacity of composite dowels is limited to three failure modes [21]: (a) concrete shearing, (b) concrete pry-out, and (c) steel failure. Currently, German Technical Approval Z-26.4-56 [22] establishes design equations concerning these failure modes for the PZ and MCL geometries. On the other hand, the only expressions available for Crestbond failure modes are those pertaining to concrete shearing and steel failure [9], [14], [16], [23]. This work aims to suggest an expression to estimate Crestbond's bearing capacity to concrete pry-out, a third failure mode, through finite element modelling (FEM). To achieve this objective, the research was divided in two parts: (i) development and validation of a numerical model representing push-out tests with Crestbond shear connectors and (ii) a parametric study of factors that directly affect concrete pry-out resistance. Combined with the already established equations for concrete shearing and steel failure in Crestbond, a new expression that solves the matter of concrete pry-out would allow for the design and application of Crestbond shear connectors in steel-concrete composite structures.

## 2 CONCRETE PRY-OUT FAILURE MODE

Concrete pry-out occurs when the shear connector is not deeply embedded in the slab, *i.e.*, when concrete cover over the connector is small (parameters $c_t$ or $c_b$ of Figure 2). Once under load, the concrete confined in the connector's openings becomes more resistant to compression than the concrete above the connector. This results in forces aimed towards the smallest height of concrete ($h_{po}$). When the shear stresses exceed the shear strength of the concrete, a cone-shaped portion of concrete detaches from the slab (Figure 3) leading to the connection's failure [21], [24].

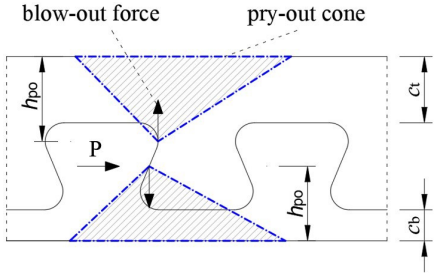


**Figure 2.** Idealization of concrete pry-out in Crestbond shear connectors.

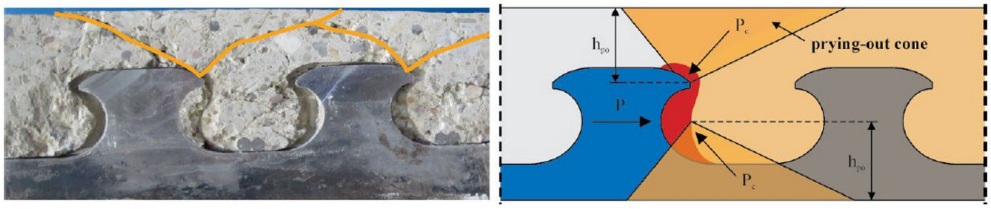


**Figure 3.** Concrete pry-out failure in MCL shear connectors – Feldmann et al. [2].

Since this failure mode was discovered, design equations have been proposed to estimate the connection's resistance to concrete pry-out [25]-[27]. These equations were established in German Technical Approval Z-26.4-56 [22], which contains all usage guidelines for MCL and PZ shear connectors. The design equation for concrete pry-out is presented in Equation 1:

$$P_{po,k} = 90\left(1+\rho_{D,i}\right)\chi_x\,\chi_y\sqrt{f_{ck}}\,h_{po}^{1,5} \tag{1}$$

where: $f_{ck}$ – compressive strength of the concrete [MPa]; $h_{po}$ – height of the pry-out cone [mm]; $P_{po,k}$ – characteristic resistance to concrete pry-out [N/dowel].
The reduction factors χx and χy consider the overlapping of the concrete cones in the longitudinal and transverse directions, respectively, and are determined according to Equation 2. In the case of a single row of connectors, factor χy is equal to 1,0.

$$\chi_x = \frac{e_x}{4{,}5\,h_{po}} \le 1 \qquad \chi_y = \frac{1}{2}\left(\frac{e_y}{9\,h_{po}}+1\right) \le 1 \tag{2}$$

The term $\rho_{D,i}$ (Equation 3) considers the influence of the effective reinforcement ratio ($A_b + A_t = A_{ef}$), *i. e.*, reinforcement passing through the opening and above the shear connector (Figure 4):

$$\rho_{D,i} = \frac{E_s\,A_{ef}}{E_{cm}\,A_{D,i}} \tag{3}$$

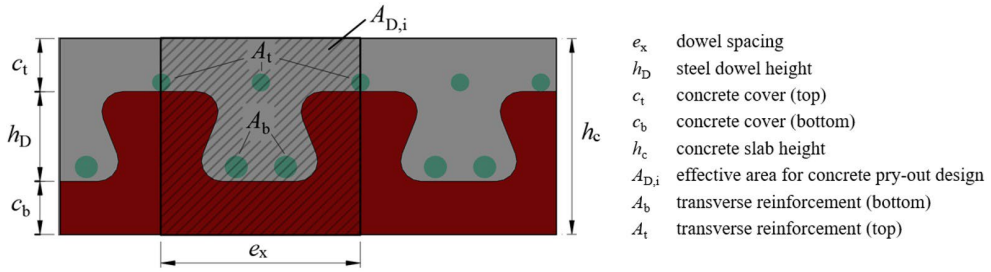


**Figure 4.** Parameters of composite dowels.

According to Z-26.4-56 [22], the height of the concrete cone ($h_{po}$) for both MCL and PZ geometries is determined as follows (Equation 4):

$$h_{po} = \min\left(c_t + 0{,}07\,e_x\,;\,c_b + 0{,}13\,e_x\right) \tag{4}$$

It should be mentioned, however, that Equation 1 estimates the characteristic resistance of composite dowels to concrete pry-out, and a large set of experimental results is required to develop expressions at characteristic-level. These expressions can be obtained through the method presented in Annex D of EN 1990:2002 [28], which converts the

engineering model (the mean value) to design load level. In this research, the expression at the mean-level was used as presented at Equation 5 [21]:

$$P_{po} = k\frac{1}{\eta}\left(1+\rho_{D,i}\right)\chi_x\,\chi_y\sqrt{f_{ck}}\,h_{po}^{1,5} \tag{5}$$

The factor $1/\eta$ was initially proposed by Heinemeyer [27] and depends significantly on the concrete strength (Equation 6). In German Technical Approval Z-26.4-56 [22], this factor was replaced by a constant value determined for the lowest concrete class (C20/25).

$$\eta = 0,4 - 0,001 f_c \tag{6}$$

The coefficient '*k*' in Equation 5 takes into consideration assumptions made for the construction of the expression, such as the admission of $\sqrt{f_{ck}}$ as the concrete's tensile strength and of parameter $h_{po}^{1,5}$, which estimates the surface area of the pry-out cone [24]. This coefficient, defined through a regression analysis, significantly affects the quality of the mechanical model, which is why an extensive database is needed for its determination. According to Kopp et al. [21], a value of 40,44 was obtained through experiments for puzzle and clothoidal shear connectors.

## 3 EXPERIMENTAL PROGRAM

The experimental program conducted in the developmental stages of the Crestbond shear connector involved 41 push-out tests, which were divided into four series (A, B, C, and D) and performed according to the specifications of EN-1994-1-1:2004 [29].

The purpose of the experimental program's series A was to evaluate the connector's behavior from a qualitative standpoint in order to define the parameters that would be employed in subsequent tests. With the results obtained in this series, Veríssimo [9] developed the CR56b shear connector used in series B and C. These series were performed in order to understand the behavior of the CR56b connector, including its shear capacity, failure modes, and ductility. Series C is identical to series B, except for the concrete's strength. The third stage of the experimental program (series D), object of study of this work, was handled by Oliveira [30] and includes tests that simulate the presence of a pre-slab, given the widespread use of composite floor systems with prefabricated concrete slabs in Brazil. In series D, specimens were assembled with a real concrete pre-slab (Figure 5a); with EPS (expanded polystyrene) plates in place of the pre-slab (Figure 5b); and without a pre-slab (Figure 5c). Fifteen tests were performed, divided into five groups, identified in Table 1. Dimensions of the shear connector used in series D (CR56b-PL) and the setup of the experiments are shown in Figure 6. The shear connectors were 12mm thick in all series.

**Table 1.** Parameters and description of specimens.

| Group | Nomenclature | Description | Specimen | $f_{cm}$ [MPa] | $A_b$ | $A_t$ | $c_b$ [mm] | $c_t$ [mm] |
|---|---|---|---|---|---|---|---|---|
| D1 | CR56b-PL30EPS-As0 | 30 mm thick EPS plate and no reinforcement | D1.a/D1.b/D1.c | 31,6/31,3/31,3 | - | - | 30 | 33,8 |
| D2 | CR56b-PL30EPS-As8 | 30 mm thick EPS plate with reinforcement | D2.a/D2.b/D2.c | 31,4/31,4/31,3 | 1 ϕ8,0 | 1 ϕ8,0 | 30 | 33,8 |
| D3 | CR56b-PL30-As0 | 30 mm thick concrete pre-slab and no reinforcement | D3.a/D3.b/D3.c | 31,6/32,4/31,1 | - | - | - | 33,8 |
| D4 | CR56b-PL45EPS-As0 | 45 mm thick EPS plate and no reinforcement | D4.a/D4.b/D4.c | 32,6/32,2/32,2 | - | - | 15 | 33,8 |
| D5 | CR56b-As0 | no pre-slab and no reinforcement | D5.a/D5.b/D5.c | 22,2/32,1/31,3 | - | - | - | 33,8 |


**Figure 5.** Specimens tested: (a) concrete pre-slab; (b) EPS plate and (c) no pre-slab.

All specimens had longitudinal reinforcement and additional transverse reinforcement arranged close to the regions of support and load application. No reinforcement was placed inside the openings of the shear connector, except for group D2.

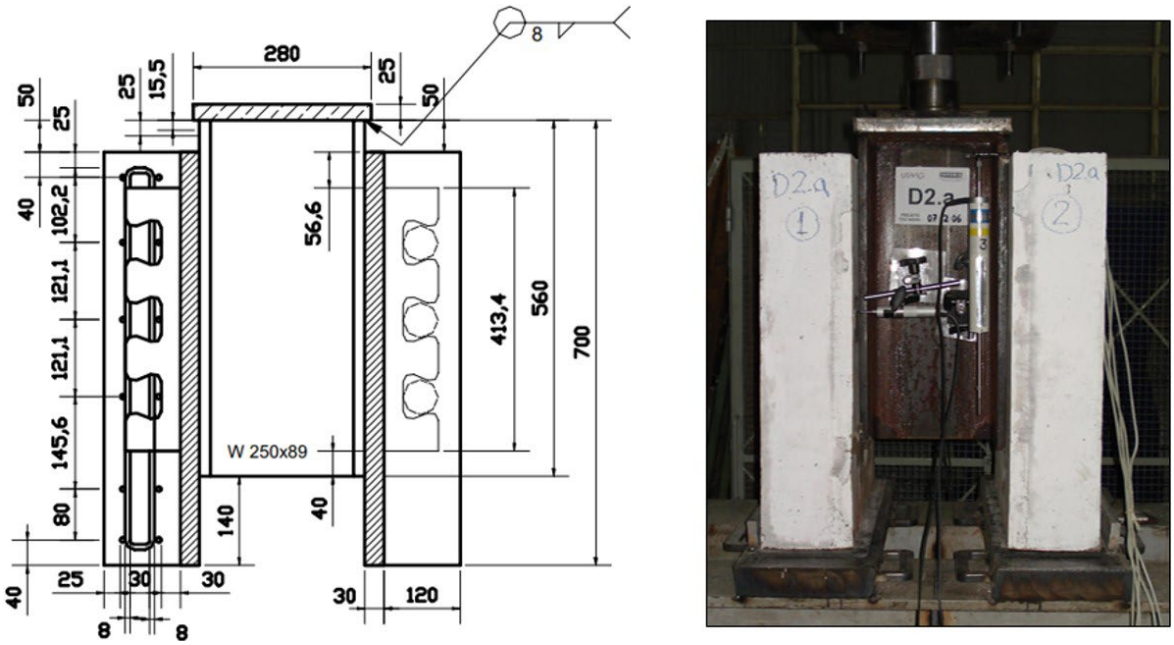


**Figure 6.** Dimensions of specimens (in mm) and experiment setup (group D2).

## 4 NUMERICAL ANALYSES

Numerical simulations were performed using finite element package ABAQUS, used by several authors to study the behavior of shear connectors [14], [17], [19], [20], [31], [32]. The description of the numerical model is presented in the subsequent sections.

### 4.1 Development and validation of the numerical model

#### 4.1.1 Geometry and boundary conditions

Due to its double symmetry, only a quarter of the specimen was modeled to reduce computational effort. The base of the slab was fixed to prevent displacement in the normal direction ($U_Z = 0$) and symmetry conditions were applied to the symmetry planes (Figure 7). The analysis was performed by means of displacement control, which was applied to the steel profile's cross section.

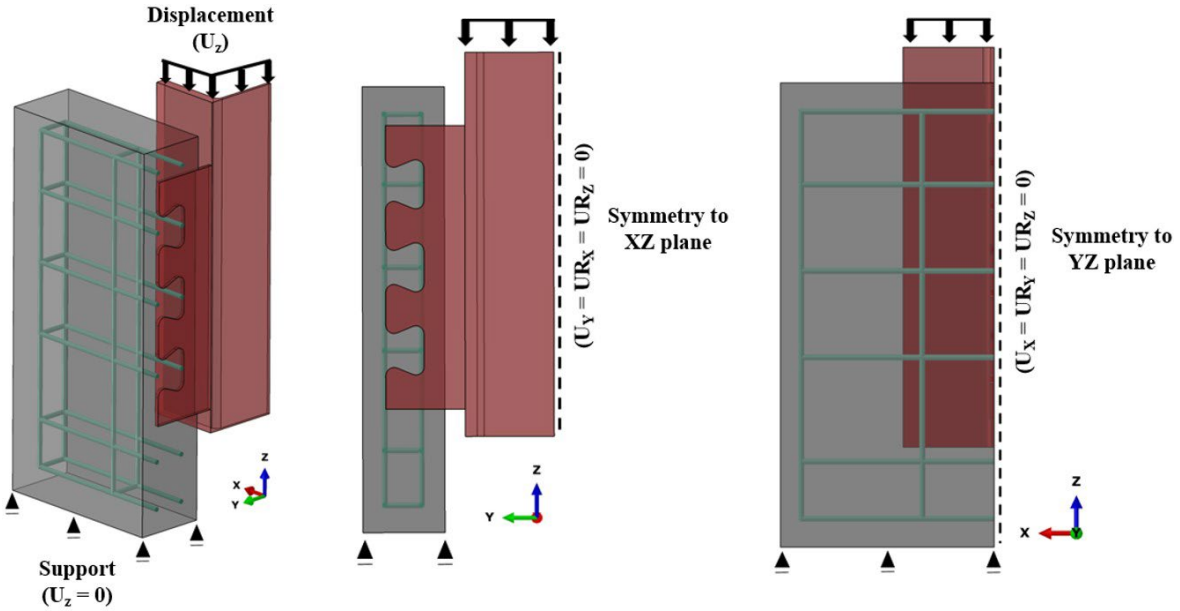


**Figure 7.** Geometry and boundary conditions of the numerical model (group D2).

Contact between the concrete slab and the steel components was simulated through the "hard contact" interaction in the normal direction. In the tangential direction, an interaction that admits friction (penalty) between the elements was adopted, with a friction coefficient of $\mu$ = 0,3 (Figure 8). Values between 0,3 and 0,5 are recommended for this type of analysis by Fink et al. [33] who investigated the value of this coefficient through an extensive parametric study. Other authors also adopt the value of 0,3 in numerical simulations of continuous shear connectors with regular openings [8], [20].

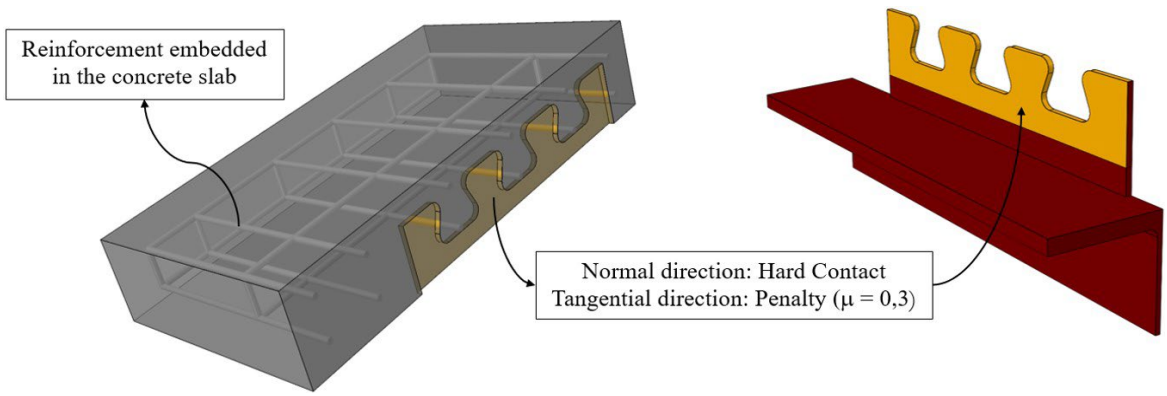


**Figure 8.** Interactions in the numerical model (Group D2).

In the specimens of groups D3 and D5, which include, respectively, a concrete pre-slab and no pre-slab, the interaction extends until the upper flange of the steel profile. The contact between the elements was simulated using the penalty contact formulation, and the perpendicular forces of contact between the shear connector and the concrete slab were determined through the finite sliding formulation, which investigates possible contact pairs between the nodes of the elements throughout the analysis [7]. The reinforcement was configured completely embedded in the concrete slab, so that the translational degrees of freedom of the reinforcement were coupled to the nodes of the surrounding concrete.

4.1.2 Finite elements mesh

A mesh convergence study was conducted to determine the finite elements' size, which also took into consideration the meshes used by Dutra [23] and Silva [34] in their numerical modeling of the Crestbond shear connector. In the transverse direction of the concrete slab, element sizes began at 5 mm around the connection and increased up to 15 mm towards the edge of the slab (Figure 9). In the longitudinal direction, the size was fixed at 5 mm. The steel profile and the shear connector were discretized into 15 and 5 mm elements, respectively. These components were modeled with solid C3D8R elements, with eight nodes and reduced integration, as the C3D8R is more appropriate for performing explicit dynamic analyses [34]. The slab reinforcement was modeled as a B31 beam element, with two nodes, and discretized into 10 mm elements.

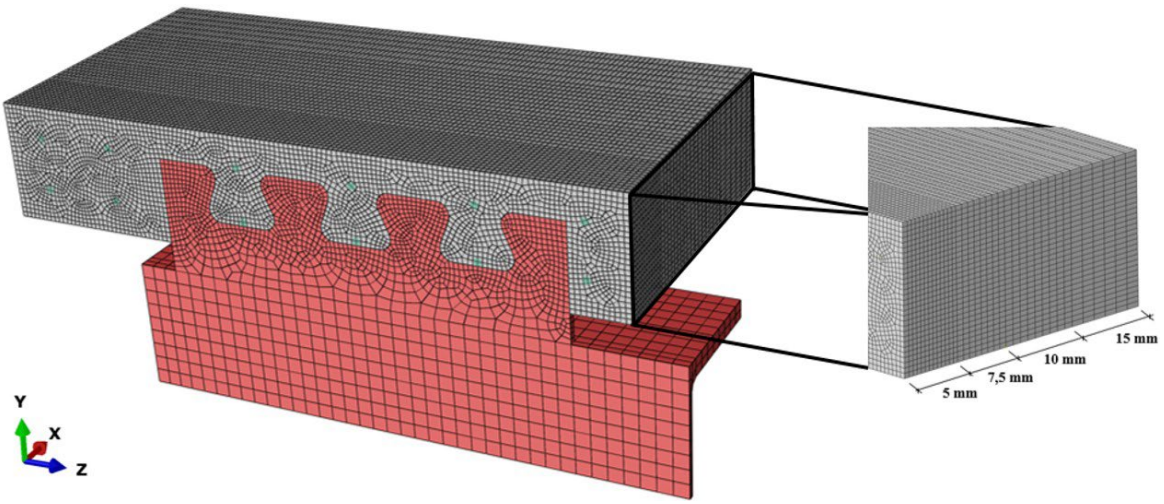


**Figure 9.** Finite element mesh.

4.1.3 Analysis method

Numerical simulations were performed through explicit dynamic analysis, recommended for very non-linear problems, where large deformations and contact interactions occur, which is the case in push-out tests [20]. Unlike implicit numerical methods (such as the usual Newton-Raphson), the explicit analysis is based on dynamic equilibrium, being frequently employed in problems involving concrete cracking and steel lamination. In the explicit dynamic analysis method, the global mass and stiffness matrices do not need to be allocated and inverted, which means that each increment results in less computational effort in comparison to the implicit analysis [23]. The most important aspect of any explicit dynamic analysis is the size of the smallest finite element in the model, since it represents an estimate of the time increment size once divided by the material's wave propagation velocity [35]. This type of analysis is generally used to model events called "quasi-static", in which the loading rate is small enough so that the inertial forces are negligible. However, a quasi-static analysis can be extremely long when modeled in real-time, requiring large computational resources. Therefore, the analysis speed is artificially increased to obtain an economically viable solution. ABAQUS offers two methods for reducing analysis processing time: time scaling and mass scaling. These methods, however, tend to increase the inertial forces in the numerical model, which can lead to unrealistic results. In this research, mass scaling was employed with a desired time increment of 0,005s, determined through preliminary analyses in order to provide the shortest possible analysis time with insignificant inertial forces [35]. This method artificially increases the mass of the elements so that the time increments are less than or equal to the time increment technically necessary for a quasi-static condition.

A quasi-static solution can also be attained through gradually applied loads or displacements. The application of an external action can induce the propagation of stress waves throughout the model, compromising the simulation's accuracy [35]. Thus, a displacement was applied based on a smooth curve in order to decrease inertial forces. ABAQUS creates a fifth-order transition polynomial between two extreme values, so that the first and the second derivatives are zero at the beginning and end of the transition. The displacement-rate adopted was 0,02 mm/s, similar to the real displacement-rate used in the experiments.

One way to verify if the numerical simulation truly reflects a quasi-static analysis is to balance the numerical model's energy. In general, the kinetic energy of the model should not exceed a small fraction (1-10%) of its internal energy throughout most of the analysis. In other words, the work exerted by external forces must be nearly equal to the internal energy of the system [35]. This balance is usually not present at the beginning of analyses, as parts of the model will be moving before any significant deformations develop.

### 4.1.4 Materials

#### *4.1.4.1 Concrete*

The non-linear behavior of concrete was simulated using the Concrete Damaged Plasticity (CDP) model implemented in the ABAQUS library. This model is widely used in numerical studies of shear connectors, and in this research its input parameters were adopted according to literature recommendations [8], [20], [32], [33], [36] as shown in Figure 10. The behavior of concrete under compression was simulated using the stress-strain relationship proposed by Pavlovic et al. [32], which adopts an extension of the curve presented in EN 1992 1 1:2010 [37], limited to an ultimate strain $\varepsilon_{cu1} = 3{,}5‰$. This strain is not a problem in conventional reinforced concrete structures since, in general, deformations in these structures remain below this value. In push-out tests, on the other hand, the concrete inside the openings undergoes large deformations and resists high compressive three-dimensional stresses, which produce a confinement effect in this region. In this situation, the behavior of the concrete becomes highly dependent on the descending branch of its stress-strain relationship. An ultimate strain of $\varepsilon_{cu1} = 3{,}5‰$ would lead to unrealistic stresses in the concrete, overestimating the connector's strength. The extension proposed by Pavlovic et al. [32] involves a series of parameters and is divided into two branches: sinusoidal and linear (Figure 10). The parameters were calibrated so that the numerical results would be as close as possible to the experimental ones.

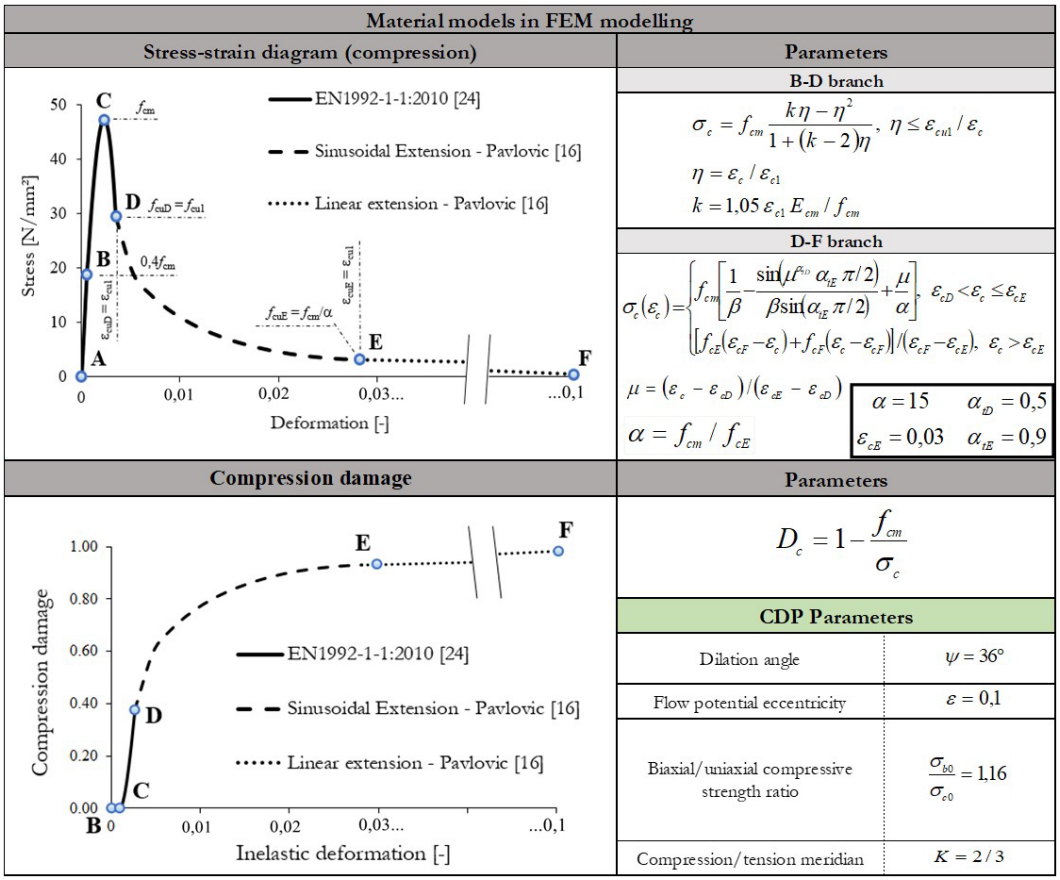


**Figure 10.** Material model for compression and CDP model parameters.

The numerical model was configured to take into consideration any damage suffered by the compressed concrete, which starts when the deformation in the concrete exceeds the deformation corresponding to the concrete strength ($\varepsilon_{c1}$).

The tensile behavior of concrete was represented by a stress-crack width model proposed by Hordijk [38]. In this model, the concrete response is governed by an exponential function (Figure 11).

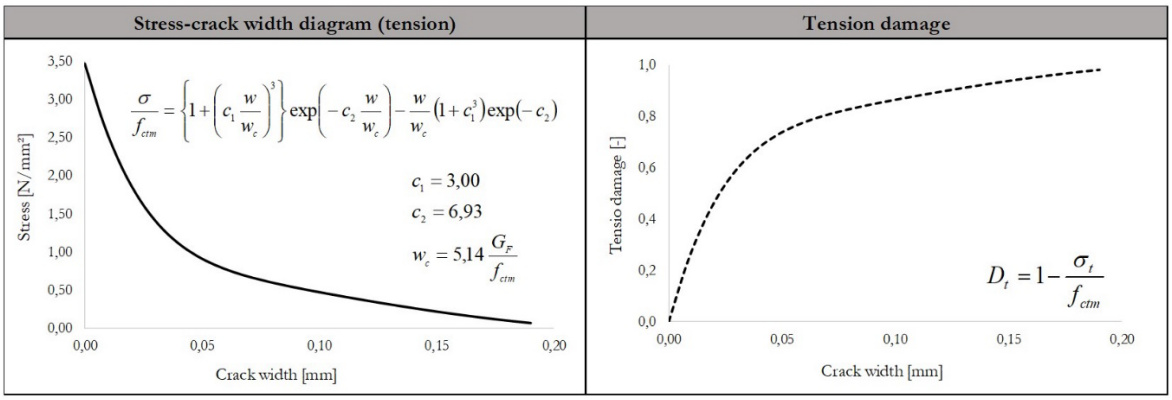


**Figure 11.** Material model for tension.

Fracture energy ($G_f$) was determined according to Model Code 2010 [39], while other properties necessary for implementing the behavior of concrete in the numerical model (such as modulus of elasticity – $E_{cm}$; mean tensile strength – $f_{ctm}$; and strain associated with the maximum compressive stress – $\varepsilon_{c1}$) were determined according to the equations presented in EN 1992 1 1:2010 [37]. The compressive strength was adopted as the mean value between models of the same group (Table 1).

### *4.1.4.2 Steel components*

The properties of the steel components (shear connector, reinforcement, and steel profile) are shown in Figure 12. Elasto-plastic diagrams were used for the reinforcement (CA-50 steel) and steel profile materials (ASTM A572 Grade 50), while a hardening modulus ($E_h$) equal to 2700 N/mm² was adopted for the shear connector. This artificial modelling was suggested by Byfield and Dhanalakshmi [40] for occasions where no material characterization tests are available.

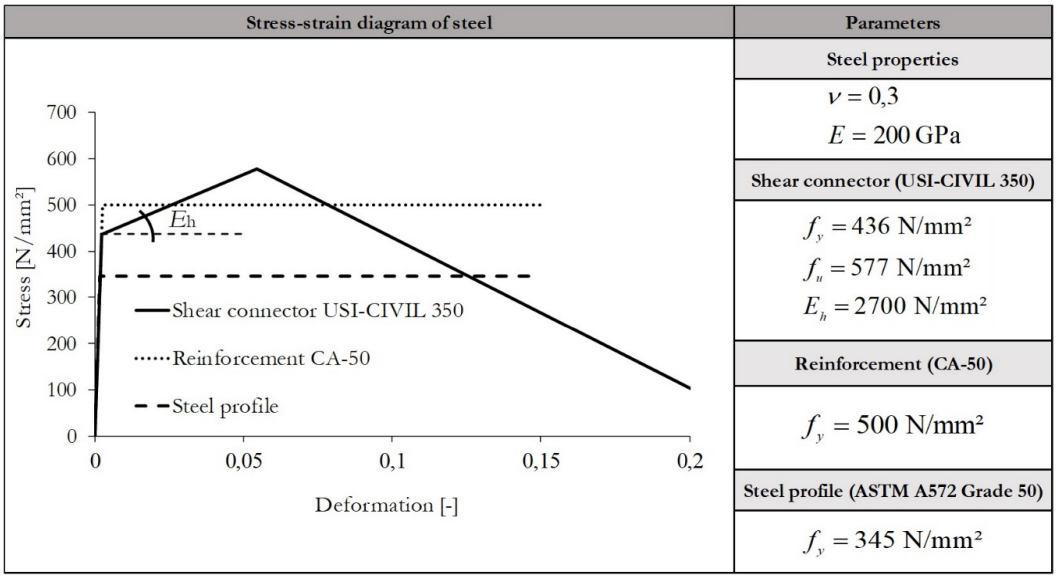


**Figure 12.** Material model for steel components.

### 4.1.5 Validation

The validation of the numerical model was based on the experimental results of Oliveira [30]. Aspects such as concrete cracking and shear connector deformations were also considered. In Figure 13, the "load-slip" curves obtained in the experiments and numerical models are compared. The maximum load obtained in the experiments and in the numerical models is presented in Table 2.

**Table 2.** Numerical and experimental results.

| Specimen | Group | Maximum force of the shear connector | | |
|---|---|---|---|---|
| | | Numerical | Test | Ratio |
| | | $F_{máx,num}$ [kN] | $F_{máx,exp}$ [kN] | $F_{máx,num}/F_{máx,exp}$ |
| CR56b PL30iso-As0 | D1 | 296,63 | 312,78 | 0,95 |
| CR56b PL30iso-As8 | D2 | 359,00 | 408,29 | 0,88 |
| CR56b PL30-As0 | D3 | 306,82 | 313,09 | 0,98 |
| CR56b PL45iso-As0 | D4 | 271,90 | 291,35 | 0,93 |
| CR56b-As0 | D5 | 331,22 | 344,37 | 0,96 |
| | | | Mean | 0,94 |
| | | | Standard deviation | 0,04 |
| | | Coefficient of variation | | 4,07% |

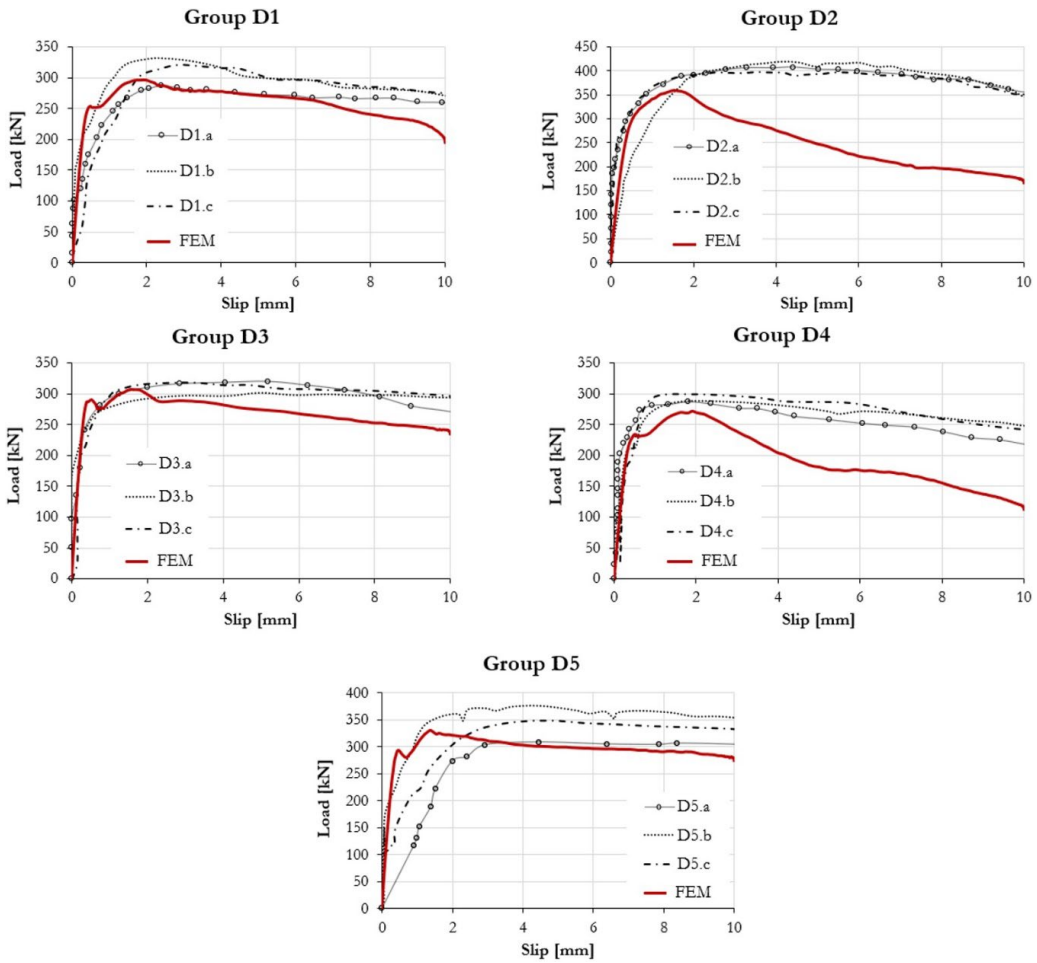


**Figure 13.** Comparison between experimental and numerical "load-slip" curves.

In all cases, the maximum numerical load reached is slightly below the respective experimental value, with a mean ratio of 0,94 and a small coefficient of variation of 4,07% (Table 2). Although the focus of this research is to analyze the behavior of the connection when it reaches its maximum strength, the numerical model was able to simulate the post-peak behavior of groups D1, D3 and D5. Modelling push-out tests in their post-peak stage is a difficult task due to all the contact interactions involved and due to the concrete cracking and plastic deformations present in this stage. The effect of the reinforcement inside the openings of the shear connector was well captured by the numerical model of group D2 in spite of the divergence in the post-peak stage. In general, the numerical model yielded reliable results in comparison to experimental ones, with the highest and lowest shear connector strength in groups D2 and D4, respectively.

In the experiments, cracks were observed on the concrete in the central region of the slab, which would later be expelled, causing the connection to fail (Figure 14a). In the numerical model, this aspect of cracking is simulated very similarly, as shown in Figure 14b.

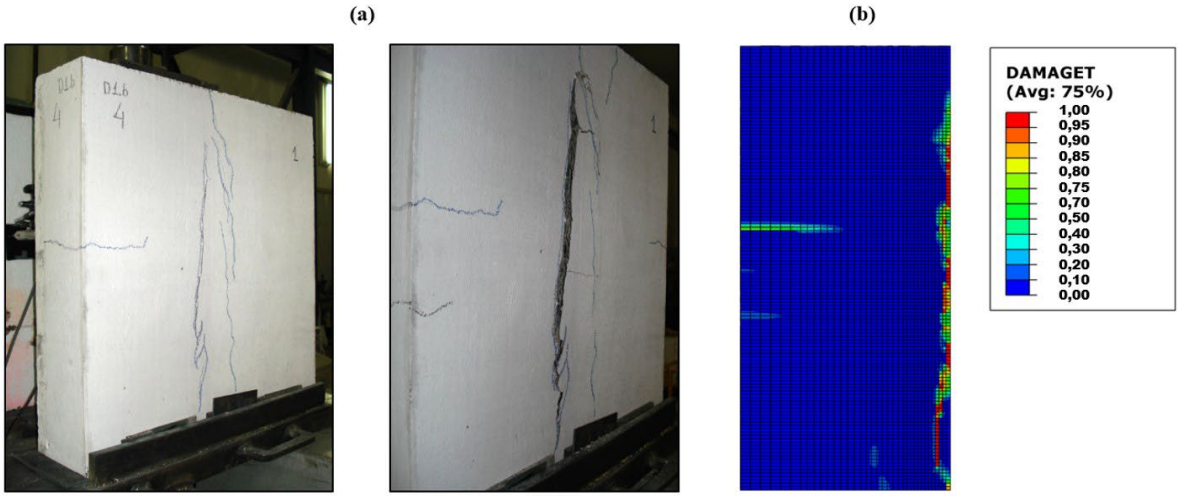


**Figure 14.** Concrete slab cracking: (a) experiment and (b) numerical model (group D1).

In the specimens with no pre-slab (group D5), a detachment of the concrete located immediately in front of the connector was observed in the internal region of the slab due to the frontal force exerted by the shear connector. In the respective numerical model, this aspect was also observed through tensile damage (Figure 15).

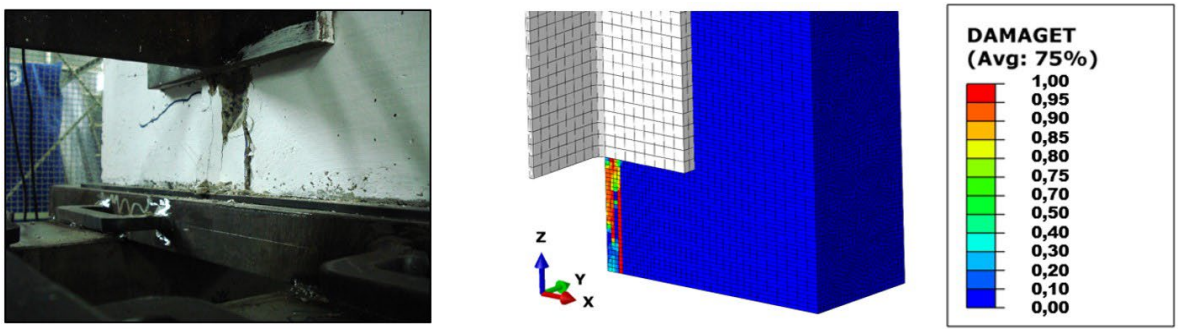


**Figure 15.** Concrete cracking in front of the shear connector.

According to Oliveira [30], in all experiments, the shear connector did not suffer significant deformations, remaining practically intact after the tests. For comparison purposes, the numerical model of group D3 is illustrated in Figure 16 in which the maximum stress reached by the shear connector (451,87 MPa) is highlighted. This value is slightly higher

than the yield stress ($f_y$ = 436 MPa) of the shear connector and was identified in a small region in the steel dowel, corroborating the observations of Oliveira [30].

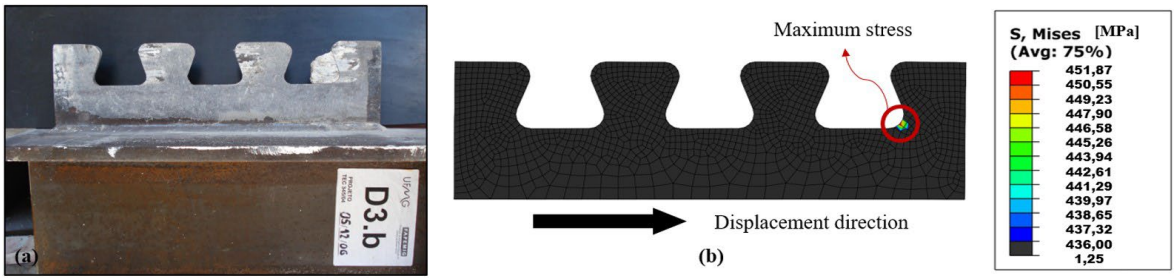


**Figure 16.** (a) Shear connector after tests; (b) stresses in numerical model (group D3).

In all experiments, the rupture was caused by a specific concrete failure mode since the connector remained practically intact in all tests. According to Kopp et al. [21], there are two possible failure modes of concrete associated with composite dowels: (a) concrete shearing and (b) concrete pry-out. In the latter case, the rupture is due to the confinement of the concrete that occurs inside the openings of the shear connector, as previously explained. The height of the pry-out cone (see Figure 2) depends on $c_t$ and $c_u$ and is one of the main factors that directly affects concrete pry-out resistance.

By associating the values of parameters $c_t$ and $c_b$ of the tested specimens (Table 1) with the experimental and numerical results (presented in Table 2), one could conclude that concrete pry-out was the failure mode that occurred during the tests. In fact, since the D4 model has the smallest cover, it was expected to have the lowest capacity among all models, with a pry-out failure in the internal region of the slab. In groups D1 and D2, due to the close values of $c_t$ and $c_b$, the failure could occur on both the inner and outer surface of the slab, while in models D3 and D5 concrete pry-out should only occur on the outer surface, since the upper flange of the steel profile prevents the expulsion of the concrete cone from the inner surface. It is important to highlight that, in specimens with EPS plates, the height of the board was not considered to calculate the concrete cover in the bottom ($c_b$) since the EPS plate would not resist the blow-out force.

The emergence of the fracture surface related to concrete pry-out was checked in numerical models by a cutting plane in the slab 30 mm away from the shear connector (Figure 17). The tensile damage present in numerical models is consistent with the concrete pry-out failure mode described: the pry-out cone was observed on internal (model D4), external (model D3), and in both (model D1) surfaces.

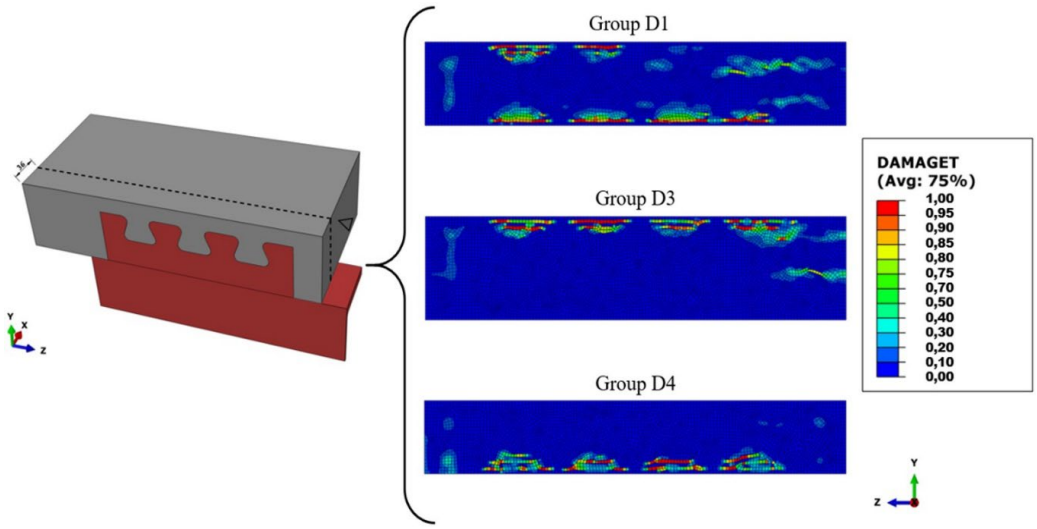


**Figure 17.** Tensile damage in the concrete slab.

### 4.2 Parametric analysis

A numerical model capable of reproducing concrete pry-out conditions was developed for a single CR50 dowel so that a parametric analysis of its pry-out resistance could be conducted (Figure 18). For this purpose, boundary conditions and reinforcement arrangement were adopted based on the research by Classen and Herbrand [20], where the authors investigated concrete pry-out in puzzle-shaped shear connectors. The reinforcement was adopted in a way that provides the necessary confinement to cause the concrete to pry-out. In addition, a 20 mm thick shear connector with a yield strength of 460 MPa (European high-strength steel S460) was used. These parameters were adopted to avoid steel failure of the shear connector, which would nullify the hypothesis of concrete pry-out. Other properties of the numerical model such as material behaviors, contact interactions, mesh, and analysis method were the same as those of the model used in the validation of the tests.

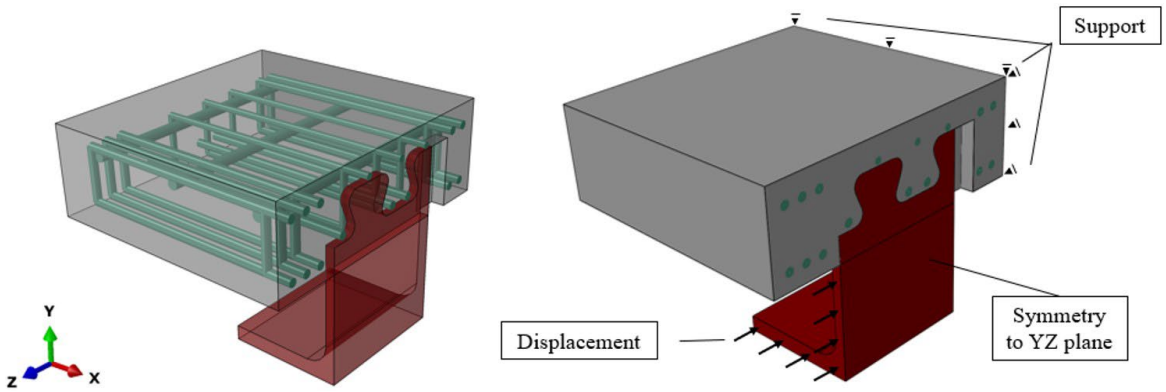


**Figure 18.** Numerical model developed for the parametric study.

The dimensions of the Crestbond shear connectors are described in terms of dowel spacing '$e_x$' and are shown in Figure 19.

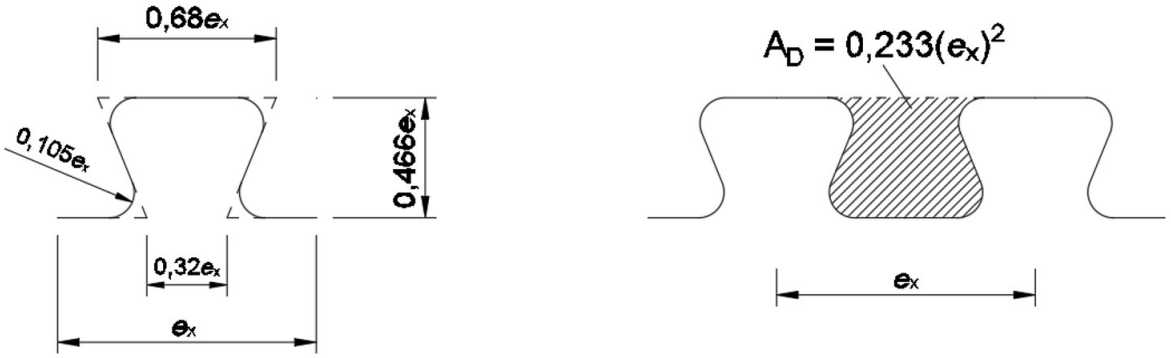


**Figure 19.** Crestbond dimensions as a function of dowel spacing $e_x$.

The main objective of this study was to create a database that would enable the adjustment of Equation 5 for the Crestbond shear connector. The range of all parameters was configured to ensure the occurrence of pry-out in all analyses. A scheme identifying the studied parameters, as well as their range, is presented in Figure 20.

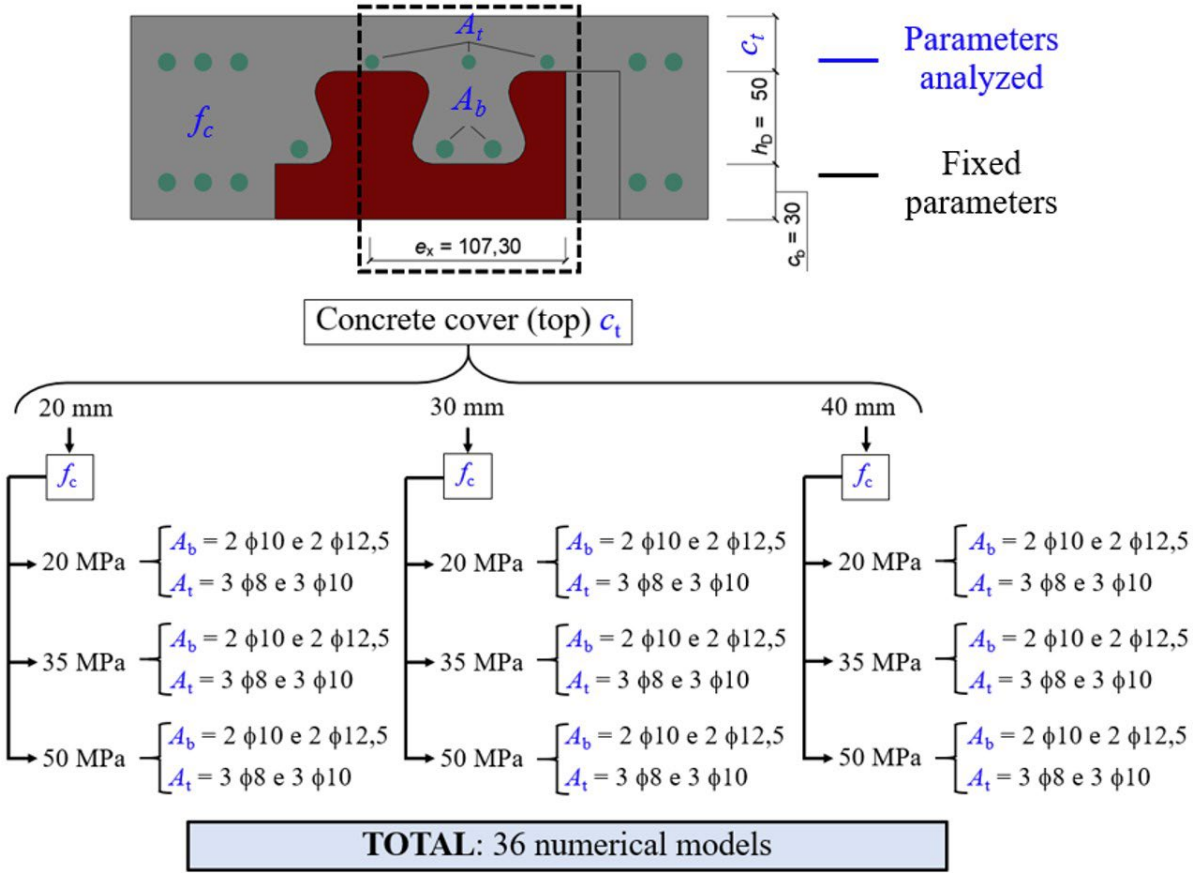


**Figure 20.** Parametric study (dimensions in mm).

The results of all 36 numerical simulations are shown in Table 3. They were divided according to the height of the concrete slab and the nomenclature of the models following the designation shown in Figure 21.


**Figure 21.** Example of nomenclature.

**Table 3.** Numerical results of the parametric study.

| | Model | Maximum force [kN] | Model | Maximum force [kN] | Model | Maximum force [kN] |
|---|---|---|---|---|---|---|
| Height of the slab (hc) = 100 mm | fc20-Ab10-At8 | 125,21 | fc20-Ab10-At8 | 132,65 | fc20-Ab10-At8 | 133,82 |
| | fc20-Ab10-At10 | 128,28 | fc20-Ab10-At10 | 135,98 | fc20-Ab10-At10 | 136,45 |
| | fc20-Ab125-At8 | 130,47 | fc20-Ab125-At8 | 138,32 | fc20-Ab125-At8 | 138,77 |
| | fc20-Ab125-At10 | 133,13 | fc20-Ab125-At10 | 141,05 | fc20-Ab125-At10 | 140,29 |
| | fc35-Ab10-At8 | 162,54 | fc35-Ab10-At8 | 171,01 | fc35-Ab10-At8 | 173,78 |
| | fc35-Ab10-At10 | 167,18 | fc35-Ab10-At10 | 176,47 | fc35-Ab10-At10 | 177,94 |
| | fc35-Ab125-At8 | 173,28 | fc35-Ab125-At8 | 181,78 | fc35-Ab125-At8 | 183,71 |
| | fc35-Ab125-At10 | 177,85 | fc35-Ab125-At10 | 185,88 | fc35-Ab125-At10 | 188,42 |
| | fc50-Ab10-At8 | 192,95 | fc50-Ab10-At8 | 199,87 | fc50-Ab10-At8 | 209,27 |
| | fc50-Ab10-At10 | 199,14 | fc50-Ab10-At10 | 208,64 | fc50-Ab10-At10 | 213,09 |
| | fc50-Ab125-At8 | 201,69 | fc50-Ab125-At8 | 206,75 | fc50-Ab125-At8 | 216,56 |
| | fc50-Ab125-At10 | 208,47 | fc50-Ab125-At10 | 215,35 | fc50-Ab125-At10 | 220,77 |

The results of all models were analyzed in order to verify the failure by concrete pry-out. Below, evidence is presented identifying this failure mode in the numerical model where its occurrence is the most unlikely, since it is the one with the highest concrete strength (50 MPa) and slab height (120 mm).

In Figure 22, tensile damage in the maximum force increment of the fc50-Ab125-At10 model indicates a cracking aspect similar to the formation of the pry-out cone, with damage appearing near the tips of the shear connector and progressing towards the slab's upper surface.

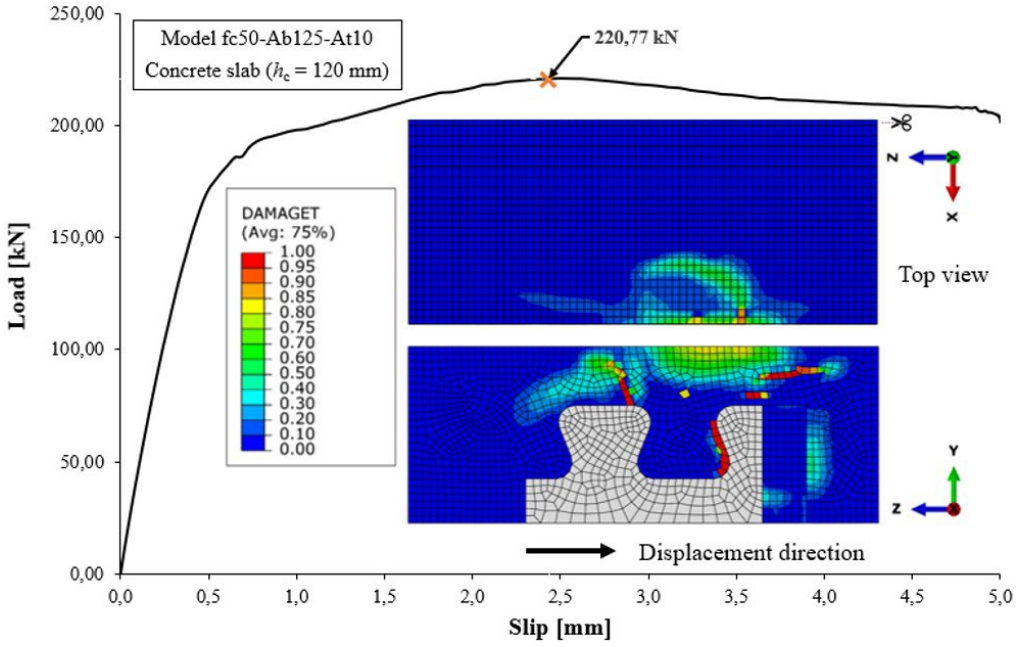


**Figure 22.** Load-slip curve of 'fc50-Ab125-At10' model ($h_c$ = 120 mm).

In Figure 23, there is a good correspondence between the tensile damage of the numerical model and the cracking pattern observed in the experiments conducted by Classen and Herbrand [20] with puzzle shear connectors. Another aspect that should be highlighted is that a vertical displacement of a concrete portion was observed in the numerical simulations, caused by the outward pry-out force (Figure 24).

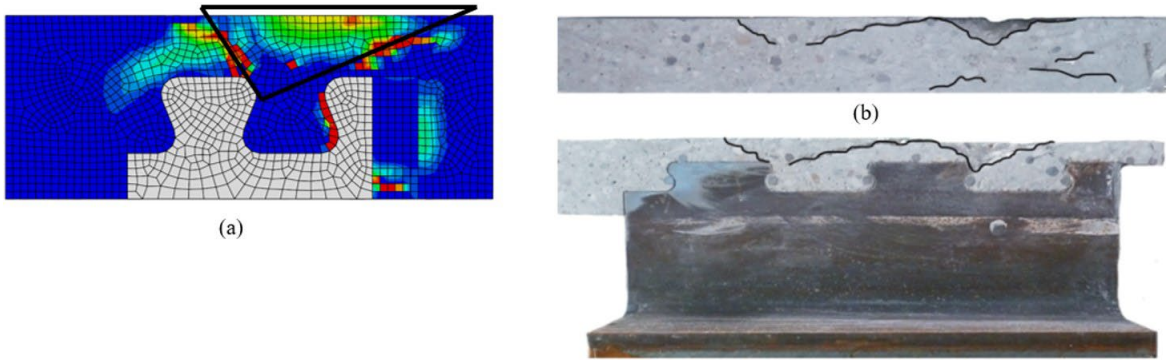


**Figure 23.** (a) Tensile damage in numerical model; (b) concrete cracking in experiments with puzzle shear connector – Classen and Herbrand [20].

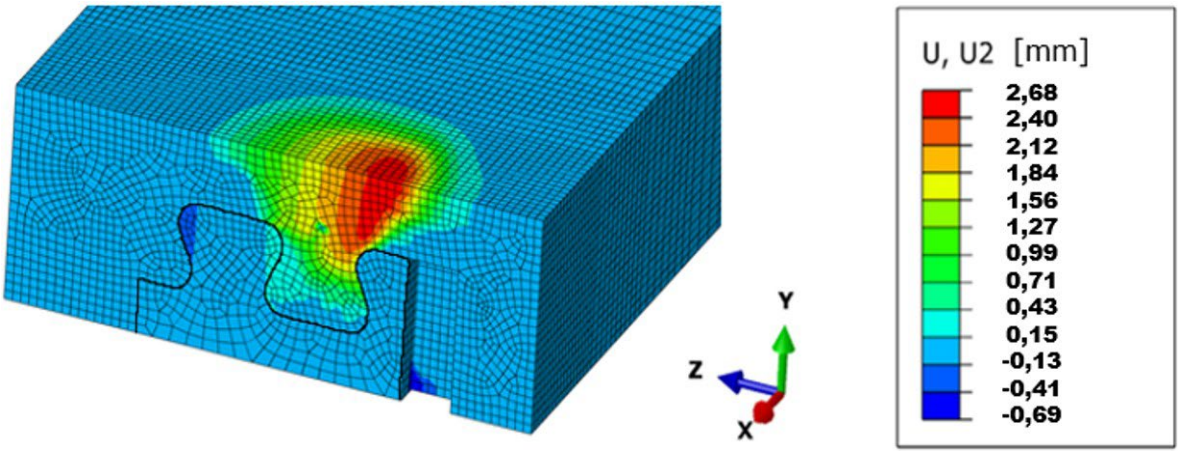


**Figure 24.** Vertical displacement of concrete due to pry-out.

Finally, tensile damage was verified in the same section of the slab (30 mm from the shear connector) as presented in Figure 17. The similarity between the cracking aspect of the model based on Veríssimo's experiments and the single dowel model is evident (Figure 25).

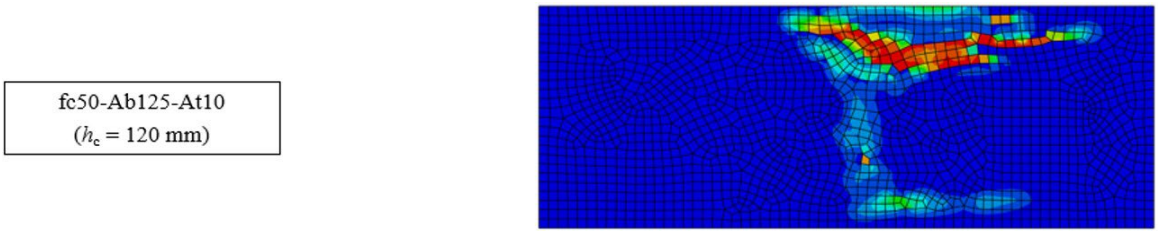


**Figure 25.** Tensile damage comparison between group D3 and fc50-Ab125-At10 ($h_c$ = 120 mm).

Considering that no steel damage was observed in the shear connector of the single dowel model, and due to the similarity of the cracking aspect of all three push-out models (physical, numerical, and single dowel), one can conclude that concrete pry-out is the failure mode occurring in all of these cases. Therefore, the results of the single dowel model's parametric analysis can be used to calibrate the analytical model.

## 5 MECHANICAL MODEL AND COMPARISON WITH EXPERIMENTAL RESULT

The mechanical model presented in Equation 5 was used to estimate Crestbond's resistance to concrete pry-out considering only one row of shear connectors ($\chi_y$ = 1,0). The height of the concrete cone was calculated according to Equation 4, valid for PZ and MCL geometries. In this work, the '*k*' coefficient was determined using the results of the parametric study through a regression analysis, and the value obtained was 37 (Equation 7), which results in a mean $P_{theo}/P_{FEM}$ value equal to 0,91 and a coefficient of variation of 24,24%.

$$P_{po,CR} = 37\frac{1}{\eta}\left(1+\rho_{D,i}\right)\chi_x\sqrt{f_{ck}}\,h_{po}^{1,5} \tag{7}$$

Finally, experimental results were compared with those obtained through Equation 7 (Figure 26), in which a mean ratio $P_{theo}/P_{exp}$ of 0,99 and a coefficient of variation of 10% were obtained. The coherence of the mechanical model is especially evident when its results are compared with those of group D4. Due to the small concrete cover ($c_b$ = 15 mm), there is a high probability of concrete pry-out in specimens of this group, and this is evident in the extremely close values between $P_{theo}$ and $P_{exp}$. This is consistent with Figure 27b, where a vertical displacement (in the direction of the smallest concrete cover - $c_b$) was observed.

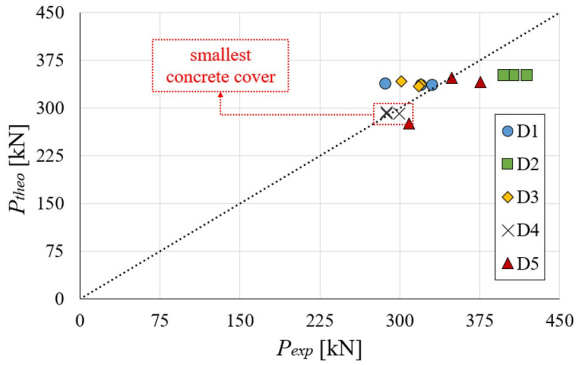


**Figure 26.** Comparison between experimental and analytical results.

The influence of the reinforcement is clearly visible when comparing the results of groups D1 and D2, which have the same concrete cover on both sides. Although the mechanical model takes the effect of the reinforcement into consideration, it is clear that its contribution to the connection's resistance is greater in the experimental values. In general, the errors between theoretical and experimental results did not exceed 15%, which demonstrates the consistency of the mechanical model.

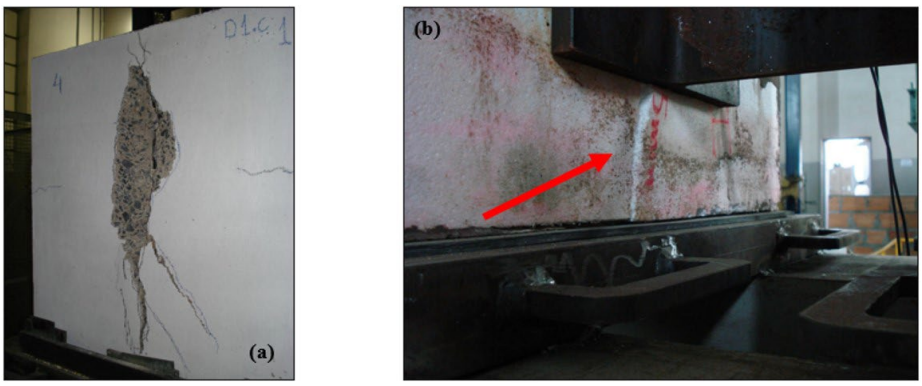


**Figure 27.** Typical cracking of concrete pry-out observed in tests: (a) D1 and (b) D4.

## 7 CONCLUSIONS

In this paper, a mechanical model was proposed to estimate the concrete pry-out resistance of Crestbond shear connectors. The model was based on already established expressions currently in use for shear connectors with puzzle and clothoidal geometries. The proposed expression was adjusted through a parametric study involving numerical simulations capable of representing the concrete pry-out failure mode. Explicit dynamic analysis was conducted and it proved to be effective in validating the numerical model, presenting a mean ratio between numerical and experimental results equal to 0,94 and a small coefficient of variation of 4,07%. The validation of the models for concrete pry-out was performed through an analysis between the concrete tensile damage observed in the numerical model and the cracking aspect in experiments. The proposed equation corresponded well to the experimental results, with a mean ratio $P_{theo}/P_{exp}$ equal to 0,99 and a coefficient of variation of 10%. The values found in this study suggest that the concrete pry-out expressions in German Technical Approval Z-26.4-56 [22] can also be applied to Crestbond shear connectors. An analysis of the structural behavior of Crestbond shear connectors in full-size beams subjected to monotonic loads is suggested as a subject for future research for the purpose of evaluating the consistency and applicability of the proposed expressions.

## 8 ACKNOWLEDGEMENTS

The authors wish to acknowledge the *Coordenação de Aperfeiçoamento de Pessoal de Nível Superior* – CAPES (Coordination for the Improvement of Persons in Higher Education) – Finance Code 001, *Universidade Federal de Viçosa,* and *Conselho Nacional de Desenvolvimento Científico e Tecnológico* – CNPq (National Council of Scientific and Technological Development) for their support in the realization and dissemination of this study.

## 9 REFERENCES

[1] W. Lorenc, "The model for a general composite section resulting from the introduction of composite dowels," *Steel Constr*, vol. 10, no. 2, pp. 154–167, May 2017, http://dx.doi.org/10.1002/stco.201710019.

[2] M. Feldmann, M. Kopp, and D. Pak, "Composite dowels as shear connectors for composite beams – background to the German technical approval," *Steel Constr.*, vol. 9, no. 2, pp. 80–88, May 2016, http://dx.doi.org/10.1002/stco.201610020.

[3] G. Seidl et al., "Composite Dowels in Bridges - Efficient solution," *Adv. Mat. Res.*, vol. 814, pp. 193–206, Sep 2013, http://dx.doi.org/10.4028/www.scientific.net/AMR.814.193.

[4] O. Hechler et al. “Continuous Shear Connectors in Bridge Construction,” in *Int. Conf. Compos. Constr. Steel and Concr*, Devil's Thumb Ranch, Tabernash, Colorado, USA, July 20-24, 2008.

[5] G. Seidl et al. *Prefabricated Enduring Composite Beams Based on Innovative Shear Transmission: Design Guide*, Brussels, 2013.

[6] W. Lorenc, M. Kożuch, and S. Rowiński, "The behaviour of puzzle-shaped composite dowels — Part I: Experimental study," *J. Construct. Steel Res.*, vol. 101, pp. 482–499, Oct 2014, http://dx.doi.org/10.1016/j.jcsr.2014.05.013.

[7] W. Lorenc, M. Kożuch, and S. Rowiński, "The behaviour of puzzle-shaped composite dowels - Part II: Theoretical investigations," *J. Construct. Steel Res.*, vol. 101, pp. 500–518, Oct 2014, http://dx.doi.org/10.1016/j.jcsr.2014.05.012.

[8] M. Classen and J. Gallwoszus, "Concrete fatigue in composite dowels," *Struct. Concr.*, vol. 17, no. 1, pp. 63–73, Apr 2016., http://dx.doi.org/10.1002/suco.201400120.

[9] G. S. Veríssimo, “Desenvolvimento de um conector de cisalhamento em chapa dentada para estruturas mistas de aço e concreto e estudo do seu comportamento,” Ph.D. dissertation, Esc. de Engenharia, Univ. Fed. de Minas Gerais, Belo Horizonte, Minas Gerais, 2007.

[10] O. P. Aguiar et al., "Estudo de conectores Crestbond em pilares mistos preenchidos com concreto," *Rev. Estr. Aco*, vol. 4, no. 3, pp. 181–199, Dec 2015.

[11] O. P. Aguiar, R. B. Caldas, F. C. Rodrigues, R. H. Fakury, and G. S. Veríssimo, "Crestbond shear connectors for load transfer in concrete filled tube columns," *Ibrac. Struct. Mater. J.*, vol. 11, no. 5, pp. 960–965, Oct 2018, http://dx.doi.org/10.1590/s1983-41952018000500004.

[12] A. R. Alves, B. V. Isabel, B. V. Washintgon, and S. V. Gustavo, "Prospective study on the behavior of composite beams with an indented shear connector," *J. Construct. Steel Res.*, vol. 148, pp. 508–524, Sep 2018, http://dx.doi.org/10.1016/j.jcsr.2018.06.015.

[13] H. S. Cardoso, R. B. Caldas, R. H. Fakury, and G. S. Veríssimo, "Estudo do Comportamento de Conectores Crestbond por meio de Simulação Numérica," *Rev. Estr. Aco*, vol. 7, no. 2, pp. 140–159, Aug 2018, http://dx.doi.org/10.17648/aco-2238-9377-7-2-4.

[14] H. S. Cardoso, R. B. Caldas, R. H. Fakury, G. S. Veríssimo, and R. L. J. Almeida, "Modelo de cálculo para o cisalhamento do concreto nos conectores Crestbond," *Rev. Estr. Aco*, vol. 7, no. 3, pp. 280–299, Dec 2018, http://dx.doi.org/10.17648/aco-2238-9377-7-3-3.

[15] H. S. Cardoso, O. P. Aguiar, R. B. Caldas, and R. H. Fakury, "Composite dowels as load introduction devices in concrete-filled steel tubular columns," *Eng. Struct.*, vol. 219, pp. 110805, Sep 2020, http://dx.doi.org/10.1016/j.engstruct.2020.110805.

[16] Almeida et al., "Capacidade resistente do conector Crestbond à falha do aço desencadeada por um mecanismo combinado de cisalhamento e flexão," *Rev. Estr. Aco*, vol. 9, no. 1, pp. 61–80, Apr 2020, http://dx.doi.org/10.17648/aco-2238-9377-9-1-3.

[17] W. Lorenc, "Concrete failure of composite dowels under cyclic loading during full-scale tests of beams for the "Wierna Rzeka" bridge," *Eng. Struct.*, vol. 209, pp. 110199, Apr 2020, http://dx.doi.org/10.1016/j.engstruct.2020.110199.

[18] M. Kozüch and W. Lorenc, "Stress concentration factors of shear connection by composite dowels with MCL shape," *Arch. Civ. Mech. Eng.*, vol. 19, no. 1, pp. 32–46, Mar 2019, http://dx.doi.org/10.1016/j.acme.2018.08.006.

[19] M. Kozüch and W. Lorenc, "The behaviour of clothoid-shaped composite dowels: Experimental and numerical investigations," *J. Construct. Steel Res.*, vol. 167, pp. 105962, Apr 2020, http://dx.doi.org/10.1016/j.jcsr.2020.105962.

[20] M. Classen and M. Herbrand, "Shear behavior of composite dowels in transversely cracked concrete," *Struct. Concr.*, vol. 16, no. 1, pp. 195–206, Dec 2014, http://dx.doi.org/10.1002/suco.201400100.

[21] M. Kopp et al., "Composite dowels as shear connectors for composite beams – background to the design concept for static loading," *J. Construct. Steel Res.*, vol. 147, pp. 488–503, Aug 2018, http://dx.doi.org/10.1016/j.jcsr.2018.04.013.

[22] Allgemeine bauaufsichtliche Zulassung der Verbunddübelleiste, *no. Z-26.4-56*, Berlin: Deutsches Institut für Bautechnik, 2018.

[23] C. M. Dutra, "Estudo do comportamento estrutural do conector Crestbond considerando variações geométricas e mecânicas," M.S. thesis, Univ. Fed. de Viçosa, Viçosa, Minas Gerais, 2014.

[24] M. Classen and J. Hegger, "Assessing the pry-out resistance of open rib shear connectors in cracked concrete – Engineering model with aggregate interlock," *Eng. Struct.*, vol. 148, pp. 254–262, Oct 2017, http://dx.doi.org/10.1016/j.engstruct.2017.06.050.

[25] C. Zapfe, "Trag- und Verformungsverhalten von Verbundträgern mit Betondübeln zur Übertragung der Längsschubkräfte," Ph.D. dissertation, Institut für Konstruktiven Ingenieurbau, Universität der Bundeswehr, München, 2001.

[26] G. Seidl, "Behavior and load bearing capacity of composite dowels in steel-concrete composite girders," Ph.D. dissertation, Wroclaw Univ. of Tech., Wrocław, 2009.

[27] S. Heinemeyer "Zum Trag- und Verformungsverhalten von Verbundträgern aus ultrahochfestem Beton mit Verbundleisten," Ph.D. dissertation, Rheinisch-Westfälischen Technischen Hochschule, Aachen, 2011.

[28] The European Union. *Basis of Structural Design*, EN 1990:2002, 2002.

[29] The European Union. *Design of Composite Steel and Concrete Structures. Part 1-1: General Rules and Rules for Buildings*, EN1994-1-1, Dec. 2004.

[30] A. F. N. Oliveira "Análise do comportamento de um conector de cisalhamento em chapa dentada para sistemas de pisos mistos com pré-laje de concreto," M.S. thesis, Esc. de Engenharia, Univ. Fed. de Minas Gerais, Belo Horizonte, 2007.

[31] S. Zheng, Y. Liu, T. Yoda, and W. Lin, "Parametric study on shear capacity of circular-hole and long-hole perfobond shear connector," *J. Construct. Steel Res.*, vol. 117, pp. 64–80, Feb 2016, http://dx.doi.org/10.1016/j.jcsr.2015.09.012.

[32] M. Pavlovic, Z. Marković, M. Veljković, and D. Buđevac, "Bolted shear connectors vs. headed studs behaviour in push-out tests," *J. Construct. Steel Res.*, vol. 88, pp. 134–149, Sep 2013, http://dx.doi.org/10.1016/j.jcsr.2013.05.003.

[33] J. Fink et al., "*Weitere neue Dübelformen für Verbundbau und numerische Simulation von PushOut-Versuchen mit ABAQUS*," Vienna, 2007. Report for TU.

[34] H. P. Silva, "Simulação numérica do comportamento de conectores de cisalhamento tipo Crestbond," M.S. thesis, Univ. Fed. de Viçosa, Viçosa, Minas Gerais, 2013.

[35] SIMULIA, *ABAQUS analysis user's manual.* Providence, USA, 2012.

[36] M. Classen, "Limitations on the use of partial shear connection in composite beams with steel T-sections and uniformly spaced rib shear connectors," *J. Construct. Steel Res.*, vol. 142, pp. 99–112, Mar 2018, http://dx.doi.org/10.1016/j.jcsr.2017.11.023.

[37] The European Union. *Design of Concrete Structures. Part 1-1: General Rules and Rules for Buildings*, EN1992-1-1, 2010.

[38] D. A. Hordijk, "Local approach to fatigue of concrete," Ph.D. dissertation, Delft Univ. of Tech., Delft, 1991.

[39] Fédération Internationale du Béton, *Model Code 2010: Final Draft*, Lausanne, Switzerland: FIB, 2011.

[40] M. P. Byfield and M. Dhanalakshmi, "Analysis of strain hardening in steel beams using mill tests," *Adv. Steel Struct*, vol. 1, pp. 139–146, 2002, http://dx.doi.org/10.1016/B978-008044017-0/50015-9.

**Author contributions:** RLJA: conceptualization, writing, data curation and formal analysis; GSV: supervision, methodology and review; JCLR and RBC: methodology and review; HSC and JLRP: review; RHF: funding acquisition and review.

**Editors:** Yury Andrés Villagrán Zaccardi, Guilherme Aris Parsekian.

IBRACON Structures and Materials Journal
Revista IBRACON de Estruturas e Materiais
ISSN 1983-4195 ismj.org

ORIGINAL ARTICLE

# Development of a numerical model to simulate the behavior of plate shear connectors applied to slender cross-section concrete-filled steel tube

## *Desenvolvimento de um modelo numérico para simular o comportamento de conectores em chapa aplicados a pilares mistos preenchidos com concreto de seção esbelta*

Ariany Cardoso Pereira[a]
Larice Gomes Justino Miranda[a]
Lucas Ribeiro dos Santos[a]
Rodrigo Barreto Caldas[a]

[a]Universidade Federal de Minas Gerais – UFMG, Departamento de Engenharia de Estruturas, Belo Horizonte, MG, Brasil

**Received** 28 October 2021
**Accepted** 10 May 2022

**Abstract:** The cross-section of concrete-filled steel tube (CFST) columns is classified according to the local slenderness of the steel tube as slender, non-compact, or compact. There are analytical models to determine the axial force of locally slender CFST columns, however studies on load transfer from beams connected to these columns are scarce. This paper presents the process of the development and validation of a numerical model to simulate the behavior of Crestbond connectors applied to CFST columns with slender steel tubes, based on the results of experiments carried out. The numerical model presented can be used for the analysis and design of the load transfer in slender columns using connectors known as composite dowels.

**Keywords:** Crestbond connector, load transfer device, CFST, composite dowels.

**Resumo:** Os pilares mistos preenchidos com concreto (PMPC) podem ter a seção transversal classificada em função da esbeltez local do perfil tubular como sendo: esbelta, semicompacta ou compacta. Embora já existam modelos de cálculo para determinação da força axial resistente dos PMPC com seção tubular esbelta, são escassos os estudos sobre a transferência de forças vindas das vigas conectadas a esses pilares. Este artigo tem como objetivo apresentar o processo de desenvolvimento e validação de um modelo numérico para simular o comportamento dos conectores Crestbond aplicados a (PMPC) de seção tubular esbelta, com base em resultados de experimentos realizados. O modelo numérico apresentado pode ser utilizado para o estudo e projeto da transferência de força em pilares de seção esbelta utilizando conectores em chapa conhecidos como *composite dowels*.

**Palavras-chave:** conector Crestbond, transferência de carga, PMPC, composite dowels.

**How to cite:** A. C. Pereira, L. G. J. Miranda, L. R. Santos, and R. B. Caldas, "Development of a numerical model to simulate the behavior of plate shear connectors applied to slender cross-section concrete-filled steel tube," *Rev. IBRACON Estrut. Mater.*, vol. 16, no. 1, e16108, 2023, https://doi.org/10.1590/S1983-41952023000100008

## 1 INTRODUCTION

The competitiveness and applicability of concrete-filled steel tubes (CFST) columns are associated with the interaction between the steel tube and the concrete core and the difficulty to connect them to the beams. In this way, when the shear stress exceeds the natural bond strength between the steel tube and the concrete core, it is necessary

**Corresponding author:** Ariany Cardoso Pereira. E-mail: eng.arianycardoso@gmail.com
**Financial support:** None.
**Conflict of interest:** Nothing to declare.
**Data Availability:** The data that support the findings of this study are available from the corresponding author, A. C. P., upon reasonable request.

to apply mechanical devices such as shear connectors. Among the devices standardized by ABNT NBR 8800:2008 [1], there are stud bolts and by ABNT NBR 16239:2013 [2], there are bolted shear connectors. Several studies on the load transfer through these connectors have already been carried out, including De Nardin and El Debs [3] and Santos et al. [4]

The behavior of the concrete-filled steel tubes (CFST) columns is also influenced by the local slenderness of the composite cross section (λ), since it is a function of the ratio between the diameter (or side, for rectangular sections) and the thickness of the tube [5]–[7]. The American standard AISC 360-16 [8] classifies CFSTs according to the local slenderness of the cross section. According to this standard, the cross section can be classified as being slender, non-compact or compact, providing the design recommendations for determining their axial strength. However, the load transfer from the beams connected to these columns still has few studies and solutions.

De Nardin and El Debs [3] verified the contribution of stud bolts, in the shear strength in the steel-concrete interface in CFST columns submitted to push-out tests. Starossek et al. [5] and Cardoso [9] experimentally evaluated the rupture mode of CFST columns subjected to an axial load while using stud bolts as shear connectors, proving the efficiency of bolted shear connectors for such application. Cardoso [9] experimental results later served as basis for studies by Santos [10] and Prates [11]. Santos [10] proposed a new analytical model to describe the behavior of bolted shear connectors when used as shear connectors in CFST. Prates [11] studied the behavior of bolted shear connectors, when used as shear connectors in columns composed of cold formed steel tubes filled with concrete, a simple and innovative solution for this type of connection, eliminating welding. The load transfer in the CFST by bolted shear connectors was also the study object of Ribeiro and Sarmanho [12] and Xavier et al. [13] Younes et al. [14] and Tao et al. [15], who evaluated the load transferred using bolted connectors in CFST columns subjected to axial and cyclical loads, respectively. Although the way in which force is applied is different, Younes et al. [14] as for Tao et al. [15] also corroborated the efficiency of this type of tool as shear connector in CFST columns.

The Crestbond connector initially studied for application in beams [16], began to be tested as a load transfer device in CSFT columns. The Crestbond dowels allow compatibility with the reinforcement rebars of the CSFT columns, and its steel plate can be designed to integrate with a beam-column connection (Figure 1).

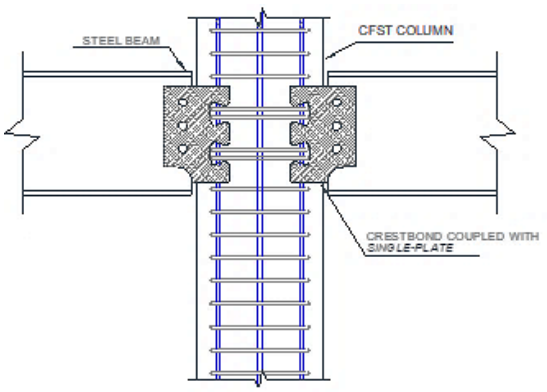


**Figure 1.** Crestbond connector with single plate extension for connection with beams [Caldas et al. [17]

Different studies carried out by researchers at the School of Engineering at Universidade Federal de Minas Gerais (UFMG) prove the efficiency of the Crestbond connector to be used as a shear load transfer device in compact section CFST columns [17]–[19]

After the efficiency of the Crestbond connector in application in CFST columns was proven, both the behavior of the Crestbond connector and the composite cross section started to be analyzed in specific ways. In this context, the present study aimed to develop and validate a numerical model to analyze the shear load transfer in locally slender composite CFST columns with the Crestbond connector.

## 2 EXPERIMENTAL PROGRAM

Two shear tests were carried out in order to experimentally evaluate the behavior of the Crestbond shear connector when used as load transfer device in slender section of the CFST columns. The execution of the tests was defined by

adapting the standard shear test procedures (push-test) prescribed in Annex B of the European Standard EN 1994-1-1:2004 [20]

As in Cardoso [18] experiments, the displacement of the CFST was restricted, while the steel tube was kept free to slide in relation to the concrete core. In addition, a release agent was applied to the internal surface of the steel tubes to minimize friction at the material interface, causing the force in the section to be transmitted, mainly, through the Crestbond CR56b-R12 shear connectors with the geometric pattern proposed by Verissimo [16] The relative displacement between the steel tube and the concrete core was measured using displacement transducers (DTs) fixed vertically in strategic positions to capture linear displacements between the tube and the concrete. From the force versus vertical relative displacement curves obtained experimentally, it was possible to develop the numerical models of the present study.

### 2.1 Compact cross section CFST

In the study by Cardoso [18], the CFST models with Crestbond shear connectors had compact tubular cross sections (local slenderness limited to $34 \leq \lambda \leq 40$) and had the force applied to the steel tube through a set of end-plates (Figure 2). The prototypes were 100 cm high with a gap of 5 cm between the top of the concrete core and the plate for applying force to the test device. The configurations of the shear test can be seen in Figure 2.

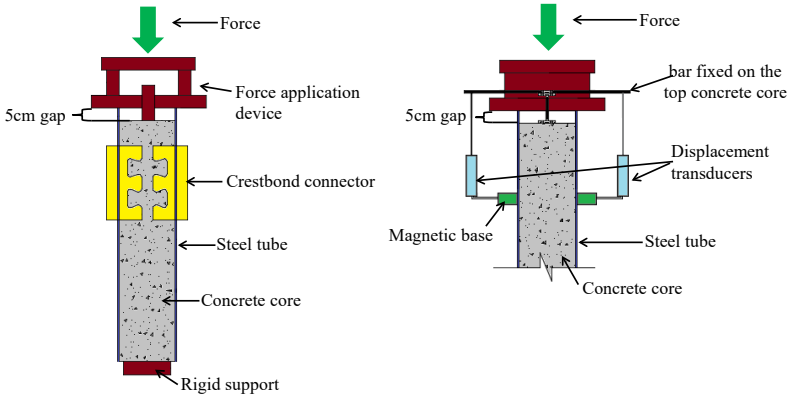


**Figure 2.** Schematic illustration of test-setup [18]

### 2.2 Slender cross section CFST

The authors experimentally evaluated the behavior of the Crestbond connector applied to slender section CFST (local slenderness equal to 153) and, due to the great local slenderness of the steel tubes, a new shear test methodology was developed [21] In this test program, the force was introduced directly into a Crestbond connector.

The CFSTs were 75 cm high and were locked by end-plates rigid enough to prevent rotation of the model that had a Crestbond with two steel dowels (CR2D). The configurations of the shear test can be seen in Figure 3.

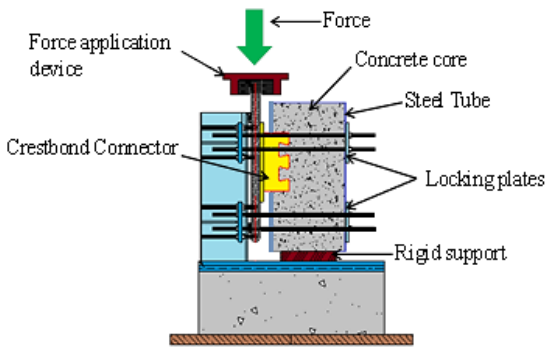


**Figure 3.** Schematic illustration of test-setup [21]

The configuration of the tested models can be seen in Figure 4 and their geometrical properties are shown in Table 1.

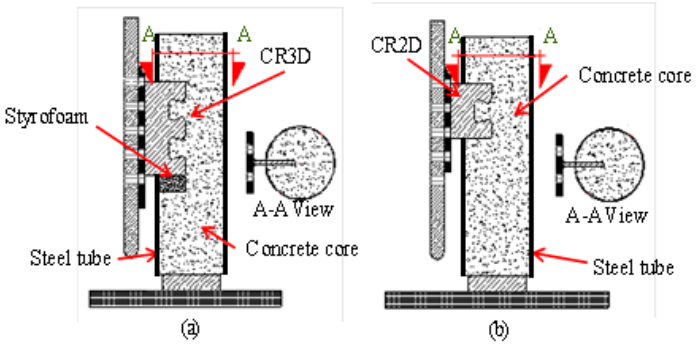


**Figure 4.** Schematic illustration: (a) C Model; (b) E Model.

The present study has the purpose to develop a finite element model able to simulate the behavior of Crestbond connectors applied in thin-walled CFST columns. Among the studies previously presented Cardoso (2018) was the principal reference by this work, because it analyzed CFST columns with compact cross-section using the same connectors.

The numerical results of Cardoso [18] were good from a numerical study calibrated based on an experimental analysis realized with more than 20 models. In this sense, the present study aims to be a continuation of the work started by Cardoso [18], but now to evaluate the slender thin-walled CFST columns tested in the same laboratory and developed by the same research group.

So, the experimental models studied by Cardoso [18] are present in Table 1 with the experimental models of the present work, because these models together formed the basis of the numerical model developed.

**Table 1.** Experimental model configuration

| Ref. | Model | Tube section | Dimensions (mm) | Steel tube | λ* | Connection description | Steel connection |
|---|---|---|---|---|---|---|---|
| Cardoso [18] | S1-04CR | Circular | 219.1 x 6.4 | VMB 350 | 34 | $4\times(3D_a+2D_c+F)$ | USI CIVIL 350 |
| | S1-02CR | Circular | 219.1 x 6.4 | VMB 350 | 34 | $2\times(3D_a+2D_c+F)$ | USI CIVIL 350 |
| | S1-02CR-ConA | Circular | 219.1 x 6.4 | VMB 350 | 34 | $2\times(3D_a+2D_c+F)$ | USI CIVIL 350 |
| | S1-02CR-E | Circular | 219.1 x 6.4 | VMB 350 | 34 | $2\times(3D_a+2D_c+F)$ | USI CIVIL 350 |
| | S1-02CR-2D | Circular | 219.1 x 6.4 | VMB 350 | 34 | $2\times(4D_a+3D_c+F)$ | USI CIVIL 350 |
| | S2-02CR | Circular | 355.6 x 9.5 | VMB 250 | 37 | $2\times(3D_a+2D_c+F)$ | USI CIVIL 350 |
| | S2-02CR-E** | Circular | 355.6 x 9.5 | VMB 250 | 37 | $2\times(3D_a+2D_c+F)$ | USI CIVIL 350 |
| | S3-02CR | Rectangular | 320 x 250 x 8.2 | VMB 250 | 39 | $2\times(3D_a+2D_c+F)$ | USI CIVIL 350 |
| | S3-02CR-E | Rectangular | 320 x 250 x 8.2 | VMB 250 | 39 | $2\times(3D_a+2D_c+F)$ | USI CIVIL 350 |
| Current work | C** | Circular | 230 x 1.50 | SAE J403 1010 | 153 | $1\times(3D_a+2D_c+SF)$ | ASTM A1018 |
| | E** | Circular | 230 x 1.50 | SAE J403 1010 | 153 | $1\times(2D_a+1D_c+F)$ | ASTM A1018 |

*λ represents the thinness index of the cross section of the composite column | ** This series features only one model | S1 - Section 219.1 x 6.4 | S2 - Section 355.6 x 9.5 | S3 - Section 320 x 250 x 8.2 | CR - Crestbond Connector | Da - number of steel dowels | Dc - number of concrete dowels | F - Concrete frontal strength | SF - Without concrete frontal strength | ConA - Self-compacting concrete | E - Stirrup | | The S1-02CR-E models; S2-02CR-E and S3-02CR-E had internal reinforcement

From the data obtained during the tests, the curves Force (kN) x Relative Displacement (mm) shown in Figure 5 and Table 2 were obtained.

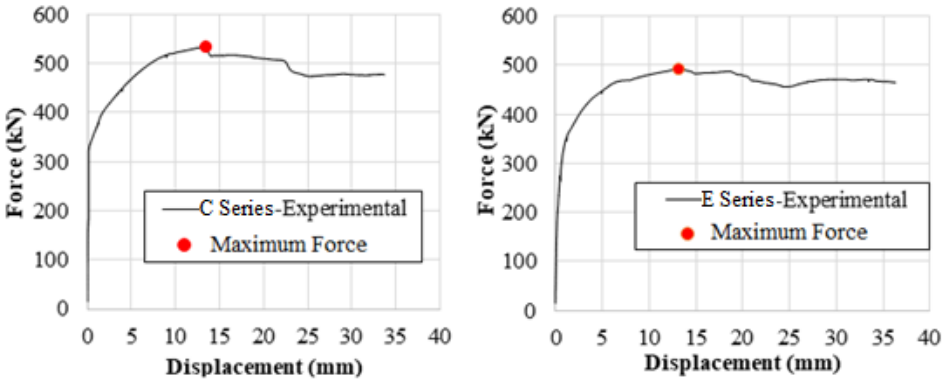


**Figure 5.** Force (kN) x Relative Displacement (mm) of the experimental models.

**Table 2.** Force and displacement numbers acquired from tests

| Model | Maximum Force (kN) | Displacement at Maximum Force (mm) |
|---|---|---|
| **C Series** | 535.24 | 13.39 |
| **E Series** | 492.99 | 13.16 |

## 3 FINITE ELEMENT MODEL

### 3.1 Generalities

The numerical analysis was developed using the finite element program ABAQUS - version 6.14. The numerical model was elaborated with the same parameters adopted in the study by Cardoso [18] The final shape of the numerical models can be seen in Figure 6.

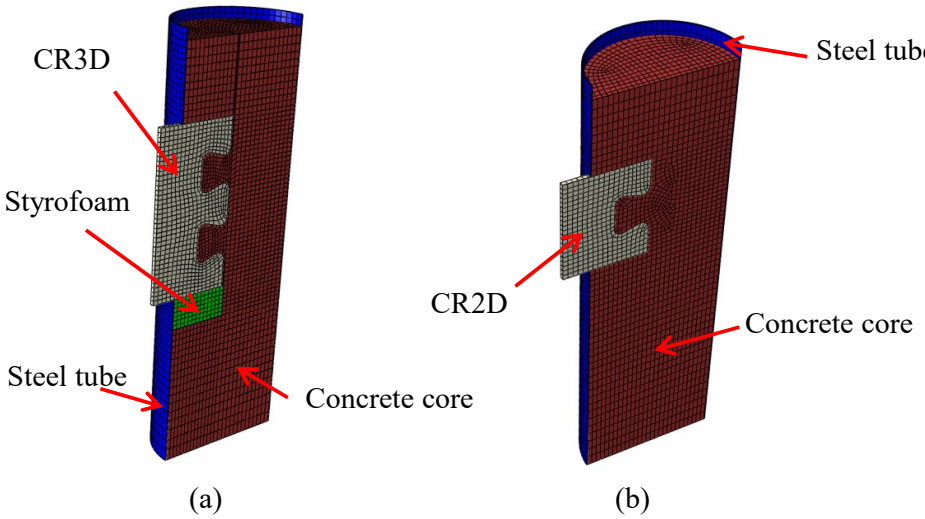


**Figure 6.** Numerical model overview: (a) SerieC Model and (b) SerieE Model.

### 3.2 Finite Element Mesh

The mesh elements adopted for the modeling of the steel tube, concrete and connector were of the C3D8 type (Continuum, hexahedral and linear), a type of solid element that has eight nodes (only at the vertices) with three degrees of freedom per node (translations in the three main directions X, Y and Z). This element is shown in Figure 7.

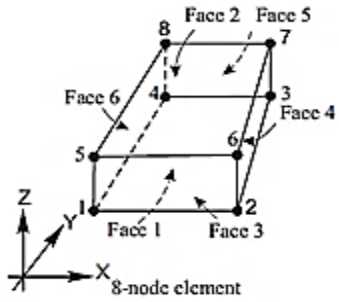


**Figure 7.** C3D8 Mesh Element [19]

The sizes of the mesh elements were defined through a study of mesh sensitivity and refinement and its discretization are illustrated in Figure 8. In Crestbond and in the region limited by around the shear connectors, mesh elements with a length of 8 mm (II) were used, which was increased as the elements moved away from the region of concentration of efforts. For the concrete and tube located in the upper region of the connector, mesh elements with a length varying between 10 mm and 15 mm (I) were applied. For the parts located in the region below the connector, the mesh was divided into elements with a length varying between 10 mm and 20 mm (III). Finally, mesh elements with a width of 10 mm were chosen for the direction corresponding to the model's transversal axis (IV).

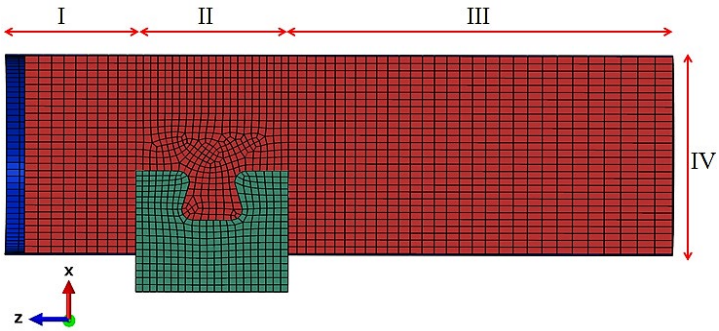


**Figure 8.** Finite element mesh distribution in numerical models.

The mesh distribution methods adopted were structured mesh and sweep mesh. Due to the complexity of the model, divisions were made to favor the allocation of the finite element mesh and are shown in Figure 9.

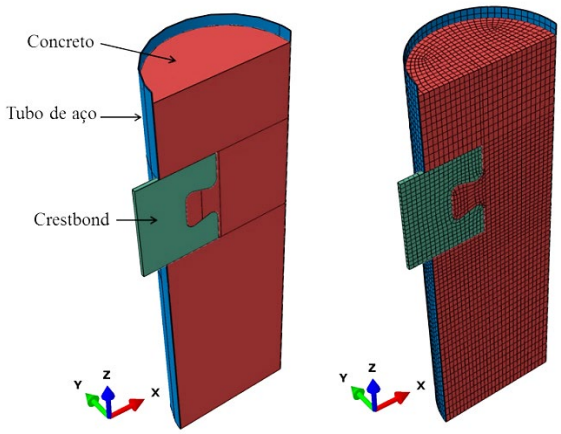


**Figure 9.** Divisions and finite element mesh adopted in numerical models

Based on the studies carried out by Santos [21] and Cardoso [18], the contact between concrete, steel profile and shear connector was simulated considering a static friction coefficient of 0.5 for the contact between the connector and the concrete, 1.0 between the connector and tube, and 0.17 between the tube and the concrete core. It was considered that in the test the friction between the steel tube and the concrete was minimized with paint and the release agent inside the tube.

The contact between concrete, steel tube and shear connectors, was simulated through face-to-face interactions and it was necessary to define separately in each contacts pairs which was the stiffer element. The rigid type of contact was defined in all the interactions which is the one that admits the minimum penetration between the surfaces of the elements. The contact pairs on the surfaces were defined as: Concrete-to-Tube (Figure 10a); Concrete-to-Connector (Figure 10b); Tube-Connector (Figure 10c).

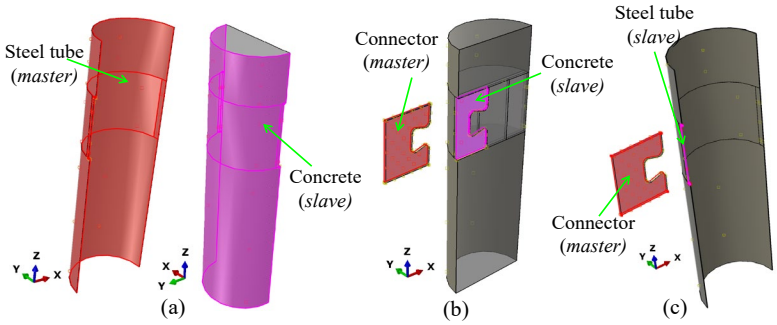


**Figure 10.** Perspective view of the contact pairs of the numerical models: (a) Concrete-to-Tube; (b) Crestbond-to-Concrete; (c) Connector-to-Tube.

### 3.2.1 Boundary Conditions

To reproduce the test conditions, the following boundary conditions were adopted: (I) restriction of the concrete core to vertical displacement to simulate the rigid support of the test; (II) rotation and horizontal displacement restrictions to represent the symmetry of the real model and (III) springs with stiffness ($k$) calculated in order to simulate the stiffness of the locking plates of the experimental model. The boundary conditions are shown in Figure 11.

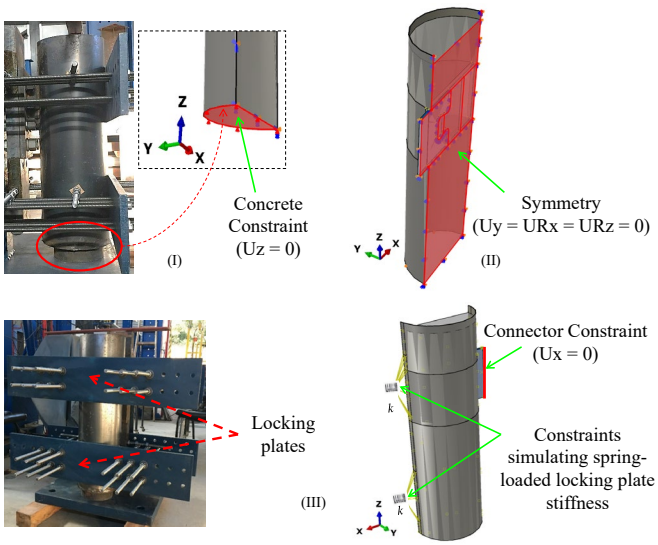


**Figure 11.** Boundaries Conditions of the Numerical Models.

### 3.2.2 Displacement Application and Data Acquisition

To simulate the monotonic loading with displacement control of the experimental test and to avoid possible convergence problems, it was decided to introduce displacement increments and obtain the corresponding reaction forces to get the force versus displacement curve of the model.

For this purpose, a reference node was created, called as Reference Point (RP) connected to the Crestbond connector plate, as shown in Figure 12. In this way, as each increment was applied, the connector moved and, because of the rigid connection with the other materials of the model, transferred the displacement in the section. In addition, it is important to note that numerical data acquisition was also carried out through the RP.

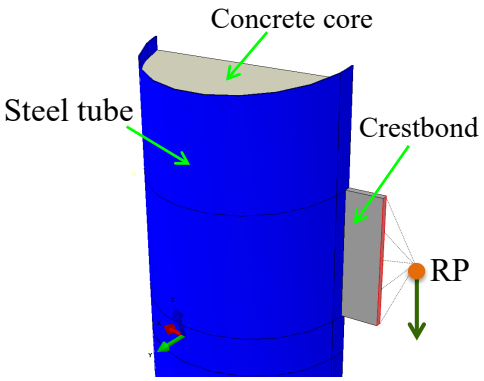


**Figure 12.** Displacement insertion point in the numerical model

For the nonlinear analysis of the models, the Dynamic Implicit analysis method was used with the quasi-static option. This method was used by Santos [10] and Cardoso [18] and it shows good convergence and satisfactory results, proving to be efficient for the analysis of shear connectors applied in CFST columns.

### 3.2.3 Concrete Constitutive Model

The Concrete Damaged Plasticity model (CDP) was used for the simulate the concrete core constitutive model and it is available in the ABAQUS library. This model is suitable for modeling fragile materials and has been widely applied for numerical modeling involving confined concrete.

The input parameters required for this model are the dilatation angle ($\psi$); the ratio between the compressive yield stress in the biaxial and uniaxial state ($\sigma_{b0}/\sigma_c$); the ratio between the second invariant stress of the tension meridian and the second invariant stress of the compression meridian ($K_c$); viscosity parameter ($\mu_{vis}$); and the eccentricity ($\epsilon$). Based on the studies by Aguiar [22] and Cardoso [18], in this work adopted: $\psi = 36$ °, $\sigma_{b0}/\sigma_c = 1.16$, $K_c = 2/3$, $\mu_{vis} = 0.00005$ and $\epsilon = 0.1$.

To represent the behavior of the confined concrete subjected to compression, it was adopted the stress versus strain relationship, proposed by Pavlović et al. [19] illustrated in Figure 13.

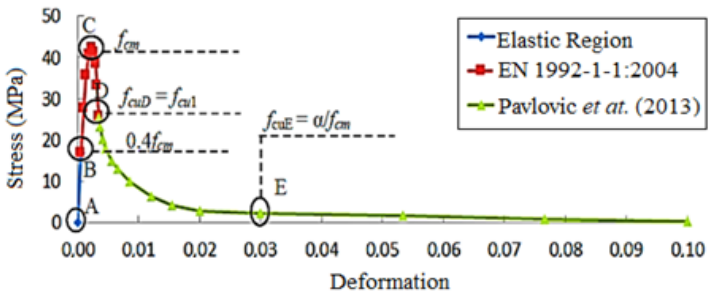


**Figure 13.** Compressive stress-strain relationship of concrete [18]

Pavlović et al. [19] proposed a continuous sinusoidal curve that starts at the point D, presented by the European standard EN 1992-1-1:2004, and continues until the strain $\varepsilon_{cu} = 0.01$, defined by the following equation:

$$\sigma_c = \begin{cases} f_{cm}\left[\frac{1}{\beta} - \frac{sen\left(\frac{\mu\alpha_{tD}\alpha_{tE}\pi}{2}\right)}{\beta sen\left(\frac{\alpha_{tE}\pi}{2}\right)} + \frac{\mu}{\alpha}\right], \ \varepsilon_{cuD} < \varepsilon_c \leq \varepsilon_{cuE} \\ \frac{f_{cuE}(\varepsilon_{cuF} - \varepsilon_c) + f_{cuF}(\varepsilon_c - \varepsilon_{cuE})}{(\varepsilon_{cuF} - \varepsilon_{cuE})}, \ \varepsilon_c > \varepsilon_{cuE} \end{cases} \quad (3.1)$$

where, $\mu = (\varepsilon_c - \varepsilon_{cuD})/(\varepsilon_{cuE} - \varepsilon_{cuD})$.

The stresses at the D and E points are defined as $f_{cuD} = f_{cu1} = \sigma_c(\varepsilon_{cu1})$; $f_{cuE} = \alpha/f_{cm}$. Strains at the D and E points are defined as $\varepsilon_{cuD} = \varepsilon_{cu1}$; $\varepsilon_{cuE} = 0.03$, respectively. The remaining parameters are defined as: $\alpha = 20$, $\alpha_{tD} = 0.5$, $\alpha_{tE} = 0.10$ e $\beta = f_{cm}/f_{cu1}$.

To reproduce the behavior of concrete under tension, the same curve used in Cardoso numerical study was adopted in this work [18] This author used the stress curve ($\sigma_t$) versus crack opening ($W_c$) proposed by Tahmasebinia et al. [23], as in Figure 14.

The damage variables $d_c$ (damage to uniaxial compression) and $d_t$ (damage to uniaxial tension), were calculated, where $d_c = 1 - \frac{\sigma_c}{f_{cm}}$ e $d_t = 1 - \frac{\sigma_t}{f_{ctm}}$ [23], and inserted in the ABAQUS program according to the plastic deformations equivalent to tension and compression, respectively.

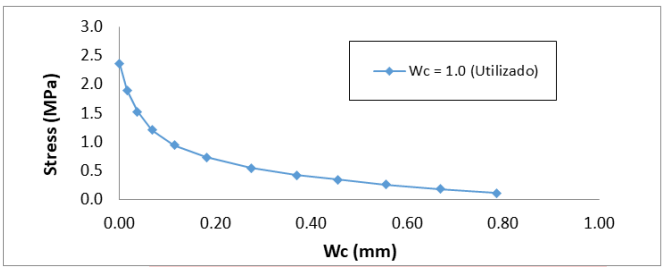


**Figure 14.** Tensile stress-crack openings relationship of concrete [23]

### 3.2.4 Tube and Connector Steel Constitutive Model

To simulate the steel behavior of the connectors and the tubes, an elastoplastic model with hardening was adopted based on the multilinear theoretical diagram in Figure 15. This model was used by Cardoso [18] The part of the graph that represents the smooth unloading (G-H in Figure 15) was adopted as a numerical solution to complete the analysis in a regime of large deformations.

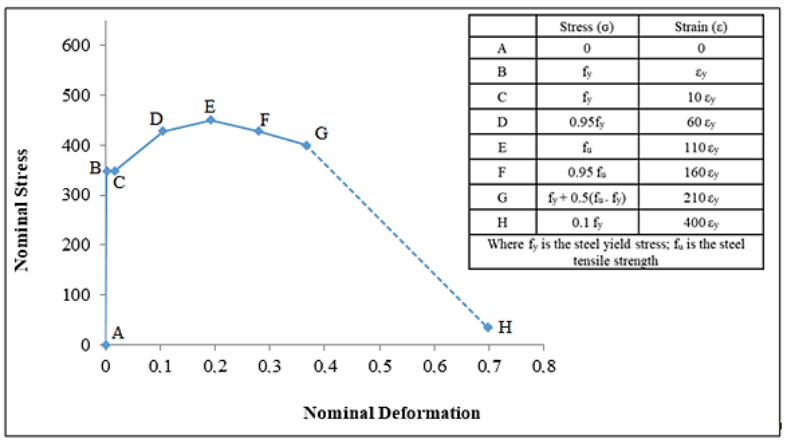


**Figure 15.** Steel stress-strain relationship for steel elements

### 3.3 Numerical Model Validation and Analysis of the Results

#### 3.3.1 Generalities

The same characteristics were adopted as in Item 2.2 with the exception for the fictitious springs that were added to the numerical model to represent the locking plate of the test device, as illustrated in Figure 16a.

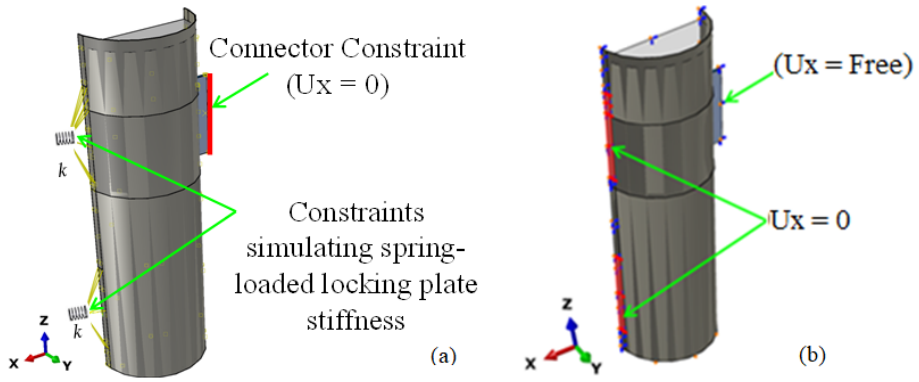


**Figure 16.** Change in boundary conditions: (a) Original model (with spring), (b) Modified model (without spring).

The numerical results were validated by comparing them to the force versus relative displacement curve obtained experimentally, evaluating the initial stiffness, the maximum force value obtained in the analyzes and the deformed configuration of the models.

Figure 17 shows the comparison between the numerical and experimental curves of the analyzed models. By comparing the curves, it is possible to observe that the numerical results were close to the experimental ones.

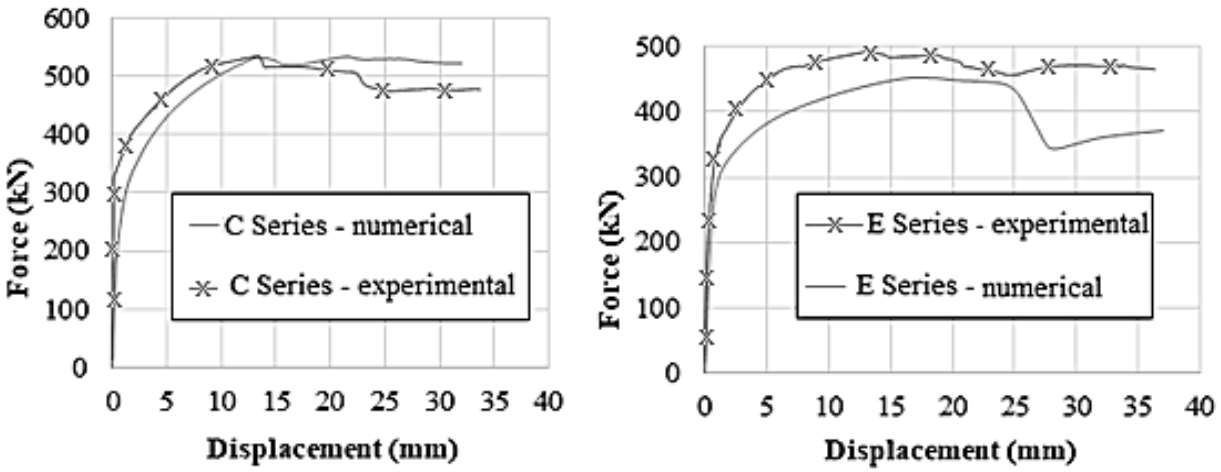


**Figure 17.** Numerical and experimental curves: C Series Model and E Series Model.

The slope of the two curves of model E practically overlapped, where the numerical model ensured the representation of a connection with an initial stiffness close to that obtained experimentally. In addition, it is observed that in C Series Model numerical curve practically coincided with the maximum force and E Series Model remained below the experimental curve, demonstrating a more conservative numerical model than the experimental one, as in Tables 3 and 4.

**Table 3.** Comparison between numerical and experimental results: C Series Model

| | Experimental | Numerical |
|---|---|---|
| Maximum force (kN) | 535.24 | 533.12 |
| Displacement at maximum force (mm) | 13.39 | 21.53 |
| Maximum displacement (mm) | 33.71 | 32.04 |
| Difference from the experimental[(1)] | | 0.40% |

[(1)] Defined at numerical model

**Table 4.** Comparison between numerical and experimental results: E Series Model

| | Experimental | Numerical |
|---|---|---|
| Maximum force (kN) | 493.00 | 452.46 |
| Displacement at maximum force (mm) | 13.16 | 17.56 |
| Maximum displacement (mm) | 36.32 | 37.00[(1)] |
| Difference from the experimental [(2)] | | 8% |

[(1)]Defined at numerical model. [(2)] Difference between the maximum force values obtained in the numerical model and in the test

For both analyzes, a good correlation was observed between the deformations of the connectors in the numerical and experimental models, as shown in Figures 18 and 19.

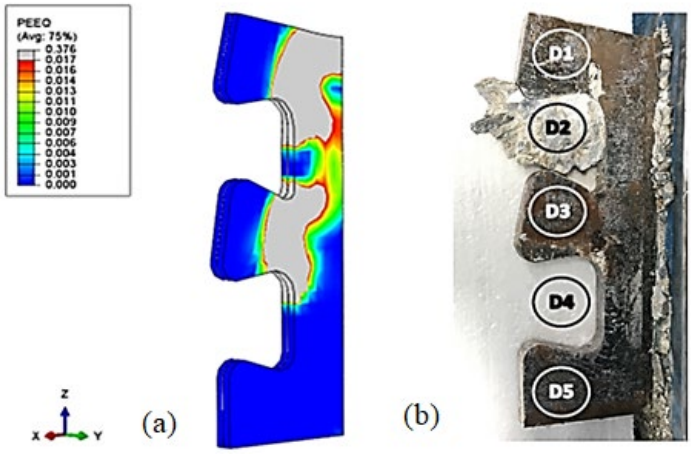


**Figure 18.** Deformed shaped for C Series Model: (a) Numerical Model; (b) Model after testing

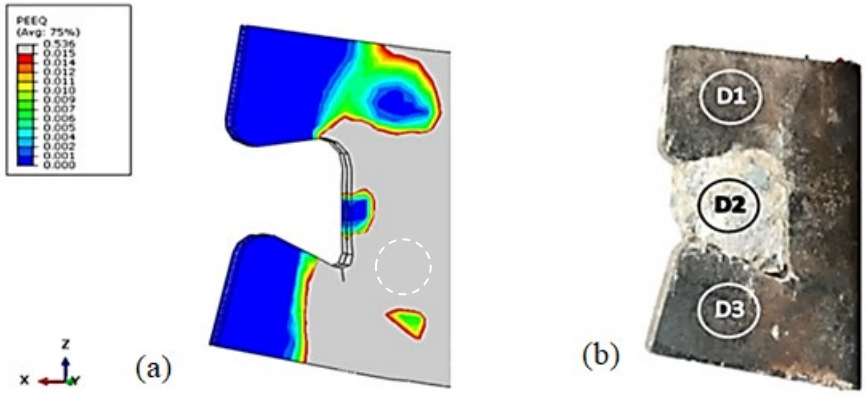


**Figure 19.** Deformed shaped for E Series Model (a) Numerical Model; (b) Model after testing

Figure 20 shows images of the numerical and experimental C series model after testing. The numerical model was able to reproduce where the concrete damage was more pronounced like the observed in the experimental analysis. For that, the results for the variable DamageT, which represents the degradation of the concrete tensile stiffness, are evaluated in the numerical model. The red region indicates a complete no stiffness, which culminated in the separation of the concrete core by tensile stresses.

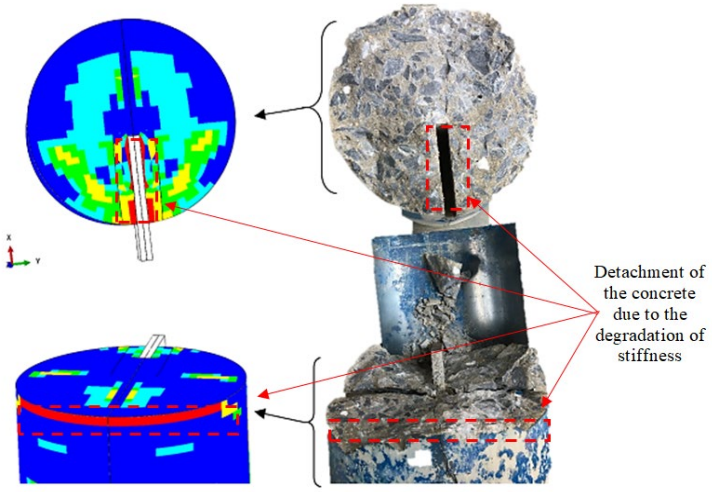


**Figure 20.** Deformed shaped for C series model: representation of the concrete cracking pattern

### 3.4 Model Geometry Transition

To simplify the numerical model so that the simulation time and the computational cost of the analyzes were lower, some sensitivity tests were necessary to validate the transition of the model geometry, including the removal of the springs and the evaluation of the model behavior with two symmetries.

#### 3.4.1 Sensitivity Test of the Locking Plate Stiffness

To enable the analysis of 1/4 of the numerical model, it was necessary to remove the springs that simulated the locking plates in the test. In addition to simplifying the model, considering zero stiffness for springs allows simulating situations more similar that occur in reality, in which there is less restriction for the connector. For that, the boundary conditions were modified, releasing the horizontal translation of the plate of the connector and restricting the regions corresponding to the location of the locking plates, as shown in Figure 16.

From the results obtained, it was possible to observe that the removal of the spring led to a more conservative model, favoring safety, shown in Figure 21 and Tables 5 and 6.

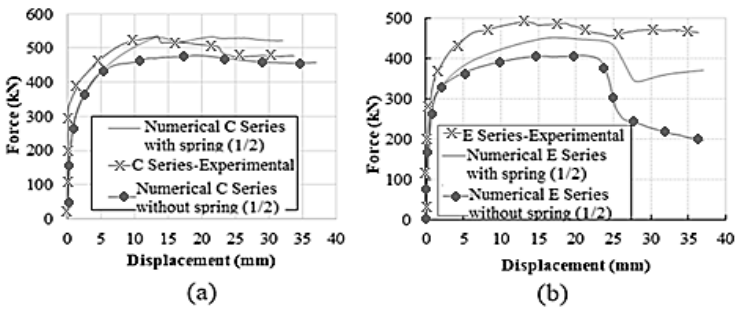


**Figure 21.** Experimental and numerical curves with and without springs: (a) C Series model and (b) E Series model

**Table 5.** Comparison between experimental and numerical results (with and without springs): C Series Model

| | Experimental | Numerical | |
|---|---|---|---|
| | | Springs | No springs |
| Maximum force (kN) | 535.24 | 533.12 | 478.8 |
| Displacement at maximum force (mm) | 13.39 | 21.53 | 19.23 |
| Maximum displacement (mm) | 33.71 | 32.07 | 37.00(1) |
| Difference from the experimental (2) | | 0.40% | 10.54% |

(1) Defined at numerical model. (2) Difference between the maximum force values obtained in the numerical model and in the test

**Table 6.** Comparison between experimental and numerical results (with and without spring): E Series Model

| | Experimental | Numerical | |
|---|---|---|---|
| | | Springs | No Springs |
| Maximum force (kN) | 493.00 | 452.46 | 408.06 |
| Displacement at maximum force (mm) | 13.16 | 17.56 | 20.86 |
| Maximum displacement (mm) | 36.32 | 37.00(1) | 37.00(1) |
| Difference from the experimental (2) | | 8% | 17% |

(1) Defined at numerical model. (2) Difference between the maximum force values obtained in the numerical model and in the test

### 3.4.2 Sensitivity Test of Transition to Double Symmetry

As concluded the evaluations that proved the possibility of removing the springs that simulated the locking plates and after observing that the curves remained more conservative (below the experimental curve), a sensitivity test was performed for the double symmetry, allowing the modeling only 1/4 of the model, illustrated in Figure 22. The model reduction to 1/4 provided more conservative results (Figure 23 and Tables 7 and 8). Furthermore, there was a reduction in processing time per model with 1/4 configuration without springs of about 10 hours, in relation to the time required for the simulation of 1/2 models with spring. Thus, it was adopted the numerical 1/4 model without springs to be used in parametric studies and analytical models of shear load transfer in slender composite sections columns through Crestbond connectors.

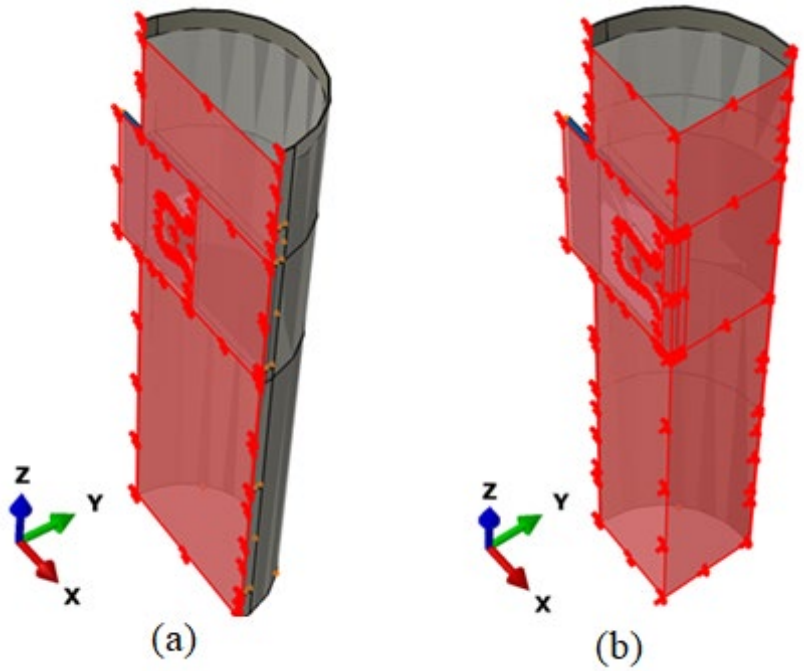


**Figure 22.** Geometry transition: (a) Original model (a plane of symmetry), (b) Modified model (double plane of symmetry)

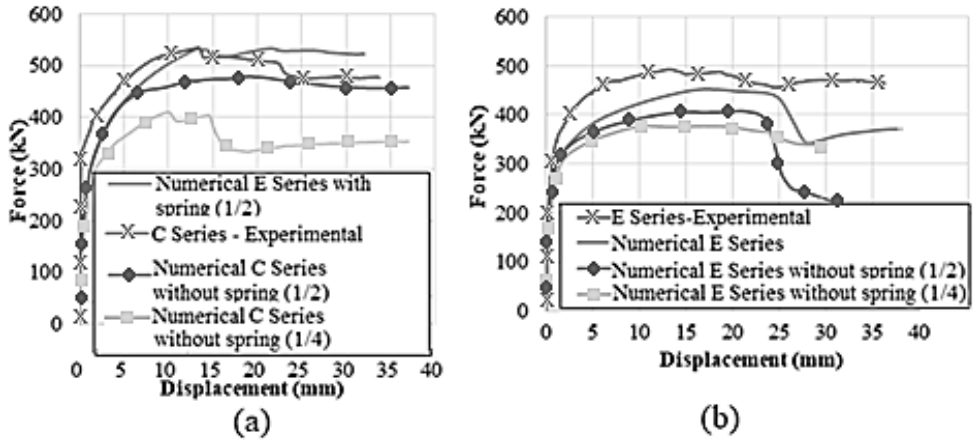


**Figure 23.** Experimental and numeric curves with springs, without springs (1/2) and without springs (1/4): C Series Model and E Series Model.

**Table 7.** Comparison between experimental and numerical results (without spring (1/2) and without spring (1/4)): C Series Model

| | Experimental | Numerical | |
|---|---|---|---|
| | | No springs (1/2) | No springs (1/4) |
| Maximum force (kN) | 535.24 | 478.80 | 410.15 |
| Displacement at maximum force (mm) | 13.39 | 20.86 | 10.98 |
| Maximum displacement (mm) | 33.71 | 37.00[(1)] | 37.00[(1)] |
| Difference from the experimental [(2)] | | 11% | 23% |

[(1)] Defined at numerical model. [(2)] Difference between the maximum force values obtained in the numerical model and in the test

**Table 8.** Comparison between experimental and numerical results (without spring (1/2) and without spring (1/4)): E Series Model

| | Experimental | Numerical | |
|---|---|---|---|
| | | No springs (1/2) | No springs (1/4) |
| Maximum force (kN) | 493.00 | 408.06 | 377.52 |
| Displacement at maximum force (mm) | 13.16 | 20.86 | 10.98 |
| Maximum displacement (mm) | 36.32 | 37.00[(1)] | 30.08 |
| Difference from the experimental [(2)] | | 17% | 23% |

[(1)] Defined at numerical model. [(2)] Difference between the maximum force values obtained in the numerical model and in the test

## 4 CONCLUSIONS

This work presents the development of a numerical model to simulate the behavior of a Crestbond shear connector applied in CFST columns with slender composite section. Although analytical models for determining the axial strength of CFST already exist, studies on the load transfer from the beams connected to these columns are scarce. Two experiments were carried out, expanding the datasets used for the development of the presented numerical model and demonstrating the applicability of this new solution.

From the calibrated numerical model, sensitivity tests were performed to reduce the processing time, which resulted in a representative and conservative numerical model. The numerical results were validated from the comparison with the relative force/displacement curves obtained experimentally, evaluating the initial stiffness, the maximum force value obtained in the analyzes and the deformed configuration of the models. The final model uses only 1/4 of the real models, due to its double symmetry, and can be used for study and design of the shear load transfer in CFST columns with slender composite section using shear connectors, which is a fundamental contribution to the development of new research and further development of a analytical model.

## ACKNOWLEDGEMENTS

The authors are grateful to FAPEMIG (Fundação de Amparo à Pesquisa do Estado de Minas Gerais), CAPES (Coordenação de Aperfeiçoamento de Pessoal de Nível Superior) and CNPq (Conselho Nacional de Desenvolvimento Científico e Tecnológico), Holcim Cimentos do Brasil and UFMG (Universidade Federal de Minas Gerais) for the financial support and willingness undertaken in the development of this research project.

## REFERENCES

[1] Associação Brasileira de Normas Técnicas, *Projeto de Estruturas de Aço e de Estruturas Mistas de Aço e Concreto de Edifícios*, NBR 8800, 2008.

[2] Associação Brasileira de Normas Técnicas, *Projeto de Estruturas de Aço e de Estruturas Mistas de Aço e Concreto de Edificações com Perfis Tubulares*, NBR 16239, 2013.

[3] S. De Nardin and A. L. H. C. El Debs, "Shear transfer mechanism in connections involving concrete filled steel columns under shear forces," *Steel Compos. Struct.*, vol. 28, pp. 449–460, 2018.

[4] L. R. Santos, R. B. Caldas, L. F. Grilo, H. Carvalho, and R. H. Fakury, "Design procedure to bearing concrete failure in concrete-filled steel tube columns with bolted shear connectors," *Eng. Struct.*, vol. 232, pp. 1–12, 2021.

[5] U. Starossek, N. Falah, and T. Löhning, "Numerical analyses of the in concrete-filled steel tube columns," in *4th Int. Conf. Adv. Struct. Eng. Mechanics (ASEM'08)*, Jeju, Korea, 2008, pp. 2651–2666, http://dx.doi.org/10.12989/sem.2010.35.2.241.

[6] W. L. A. Oliveira, "Análise teórico-experimental de pilares mistos preenchidos de seção circula," Ph.D. dissertation, Esc. Eng. Estrut., USP, São Carlos, 2008.

[7] Y. Lu, Z. Liu, S. Li, and X. Zhao, "Effect of the outer diameter on the behavior of square rc columns strengthened with self-compacting concrete filled circular steel tube," *Int. J. Steel Struct.*, vol. 19, no. 3, pp. 1042–1054, 2019, http://dx.doi.org/10.1007/s13296-018-0185-9.

[8] American Institute of Steel Construction, *Specification for Structural Steel Buildings*, ANSI/AISC 360-16, 2016.

[9] H. S. Cardoso, "Estudo teórico-experimental de parafusos utilizados como dispositivos de transferência de carga em pilares mistos tubulares preenchidos com concreto," M.S. thesis, Esc. Eng., Dept. Eng. Estrut., Univ. Federal de Minas Gerais, Belo Horizonte, 2014.

[10] L. R. Santos, "Análise numérica de conectores parafusos em pilares mistos circulares preenchidos com concreto," M.S. thesis, Esc. Eng. , Dept. Eng. Estrut., Univ. Federal de Minas Gerais, Belo Horizonte, 2017.

[11] J. A. Prates, "Estudo de conectores de cisalhamento formados por parafuso com cabeça sextavada e rebite tubular com rosca interna para pilares mistos em perfis de aço formados a frio e concreto," M.S. thesis, Esc. Eng., Dept. Eng. Estrut., Univ. Federal de Minas Gerais, Belo Horizonte, 2017.

[12] J. G. Ribeiro No. and A. M. Sarmanho, "Experimental analysis of a mechanical shear connector in concrete filled steel tube column," *Ibracon Struct. Mater. J.*, vol. 10, no. 3, pp. 592–625, 2017.

[13] E. M. Xavier, J. G. Ribeiro No., A. M. C. Sarmanho, L. Roquete, and L. G. C. Paula, "Experimental analysis of bolts employed as shear connectors in circular concrete-filled tube colums," *IBRACON Struct. Mater. J.*, vol. 12, no. 2, pp. 337–370, Apr 2019.

[14] M. Y. Younes, H. M. Ramadan, and S. A. Mourad, "Stiffening of short small-size circular composite steel-concrete columns with shear connectors," *J. Adv. Res.*, vol. 7, no. 3, pp. 525–538, 2016, http://dx.doi.org/10.1016/j.jare.2015.08.001.

[15] Z. Tao, W. Li, B. L. Shi, and L. H. Han, "Behaviour of bolted end-plate connections to concrete-filled steel 2 columns," *J. Construct. Steel Res.*, vol. 134, pp. 194–208, 2017, http://dx.doi.org/10.1016/j.jcsr.2017.04.002.

[16] G. S. Veríssimo, "Desenvolvimento de um conector de cisalhamento em chapa dentada para estruturas mistas de aço e concreto e estudo do seu comportamento," Ph.D. dissertation, Dept. Eng. Estrut., Univ. Federal de Minas Gerais, Belo Horizonte, 2007.

[17] R. B. Caldas, R. H. Fakury, G. S. Veríssimo, F. C. Rodrigues, J. L. R. Paes, and A. L. R. Castro e Silva, *Análise Teórico-Experimental de Dispositivos de Transferência de Cargas em Pilares Mistos Formados por Tubos de Aço Preenchidos com Concreto, Projeto de Pesquisa*. Belo Horizonte, 2010.

[18] H. S. Cardoso, "Avaliação do comportamento de conectores constituídos por chapas de aço com recortes regulares — ênfase em conectores de geometria crestbond aplicados em pilares," Ph.D. dissertation, Esc. Eng., Dept. Eng. Estrut., Univ. Federal de Minas Gerais, Belo Horizonte, 2018.

[19] M. Pavlović, Z. Marković, M. Veljković, and D. Buđevac, "Bolted shear connectors vs. headed studs behaviour in push-out tests," *J. Construct. Steel Res.*, vol. 88, pp. 134–149, 2013, http://dx.doi.org/10.1016/j.jcsr.2013.05.003.

[20] European Standard, EN 1994-1-1:2004, 2004.

[21] L. R. Santos, "Conectores Crestbond aplicados a pilares mistos de seção esbelta," Ph.D. dissertation, Dept. Eng. Estrut., Univ. Federal de Minas Gerais, Belo Horizont, 2018.

[22] O. P. Aguiar, “Estudo do comportamento de conectores Crestbond em pilares mistos tubulares preenchidos com concreto,” Ph.D. dissertation, Esc. Eng., Dept. Eng. Estrut., Univ. Federal de Minas Gerais, Belo Horizonte, 2015.

[23] F. Tahmasebinia, G. Ranzi, and A. Zona, "Probabilistic three-dimensional finite element study on composite beam with steel trapezoidal decking," *J. Construct. Steel Res.*, vol. 80, pp. 394–411, 2013, http://dx.doi.org/10.1016/j.jcsr.2012.10.003.

**Author contributions:** ACP: conceptualization, data curation, formal analysis, methodology, writing; LGJM: conceptualization, supervision, writing; LRS: conceptualization, supervision, writing; RBC: conceptualization, funding acquisition, supervision.

**Editors:** Osvaldo Manzoli, Guilherme Aris Parsekian.

IBRACON Structures and Materials Journal
Revista IBRACON de Estruturas e Materiais
ISSN 1983-4195 ismj.org

ORIGINAL ARTICLE

# Considerations on the design of indirect supports in reinforced concrete beams

## *Considerações sobre o projeto de apoios indiretos em vigas de concreto armado*

Mateus Araújo de Souza Celestino[a]
Bernardo Horowitz[a]

[a]Universidade Federal de Pernambuco – UFPE, Departamento de Engenharia Civil, Recife, PE, Brasil

Received March 15, 2022
Accepted June 17, 2022

**Abstract:** Indirect supports consist of beams being supported by others beams, demanding the presence of a hanger reinforcement, required by ABNT NBR 6118, that will act as a tie hanging the applied load from the supported beam to the upper chord of the supporting beam. Therefore, the present work, through the study of experimental results in the literature, aims to present recommendations for the design of indirect supports and hanger reinforcements in reinforced concrete beams. Through a parametric analysis, was obtained an equation that calculates the load to be suspended as a function of the dimensions of the beams. It was observed that in some cases the reinforcement can be dispensed. The hanger reinforcement must be added to the shear reinforcement and in the case of regions where there is a torsional moment acting on the support beam, it was noticed that only the inner legs of the support beam stirrups collaborate to hang the load.

**Keywords:** indirect support; hanger reinforcement; design recommendations.

**Resumo:** Os apoios indiretos consistem no apoio de vigas sobre vigas sendo necessária a presença de uma armadura de suspensão, exigida pela ABNT NBR 6118, que irá atuar como um tirante suspendendo a carga aplicada da viga apoiada até o banzo superior da viga de suporte. Diante disso o presente trabalho, através do estudo de resultados experimentais na literatura, tem como objetivo apresentar recomendações para o projeto dos apoios indiretos e das armaduras de suspensão em vigas de concreto armado. Obteve-se, através de uma análise paramétrica, uma equação que calcula a carga a ser suspensa em função das dimensões das vigas. Observou-se que em alguns casos a armadura pode ser dispensada. A armadura de suspensão deve ser adicionada à armadura de cisalhamento e no caso de regiões em que existe momento torsor atuando na viga de suporte percebeu-se que apenas as pernas internas dos estribos da viga de suporte colaboram para suspensão da carga.

**Palavras-chave:** apoio indireto; armadura de suspensão; recomendações de projeto.

**How to cite:** M. A. S. Celestino, and B. Horowitz, "Considerations on the design of indirect supports in reinforced concrete beams," *Rev. IBRACON Estrut. Mater.*, vol. 16, no. 1, e16109, 2023, https://doi.org/10.1590/S1983-41952023000100009

## 1 INTRODUCTION

In structural design, beams are usually supported by columns or other beams, with a predominance of columns. The case in which the column is the support is called direct support and indirect support is characterized by the support of one beam over another. Indirect supports are provided in the structural planning stage of the project and normally occur to meet architectural demands, for example in cases where longer spans are desired without the presence of columns.

In situations of indirect support, a beam ends up transferring its load to another beam, requiring the presence of a hanger reinforcement to ensure that this load acts on the upper face of the supporting beam, allowing it to adequately resist this force. The presence of this reinforcement allows the balance of internal forces in the structure, thus ensuring

**Corresponding author:** Mateus Araújo de Souza Celestino. E-mail: mateus.celestino@ufpe.br
**Financial support:** This study was financed in part by the Coordenação de Aperfeiçoamento de Pessoal de Nível Superior – Brasil (CAPES) – Finance Code 001.
**Conflict of interest:** Nothing to declare.
**Data Availability:** Data-sharing is not applicable to this article as no new data were created or analyzed in this study.

its safety, and if not considered, it can cause premature failure due to shear or premature yielding of the longitudinal reinforcement of the supporting beam. Yet, its design and specification are often neglected by designers [1].

Although hanger reinforcement is necessary and recommended by the standards, sufficient criteria are not presented for the design and detailing for this type of reinforcement in most standards. The Brazilian standard ABNT NBR 6118 [2], for example, deals very briefly with the subject, recommending only the need for reinforcement without further indications. Limitations on requirements are also observed in the American standard ACI 318-19 [3], in the European standard EN 1992-1-1:2004 [4] among others. The Canadian standard CSA A23.3-04 [5] among all the standards is the most complete and brings a broader approach to the design of hanger reinforcement.

Therefore, the main references on the subject consist of studies carried out by researchers that have been published in articles or academic works. Initially, Leonhardt and Mönnig [6] should be highlighted, being a theoretical basis used by other studies as a reference. In this work, considerations about the load to be hung, details of the longitudinal reinforcement present in the joint and the region of distribution of the hanger reinforcement are presented.

The experiments carried out by Mattock and Shen [7] and Mattock and Kumar [8] proved the influence of the hanger reinforcement on the behavior of beams in situations of indirect support. In the case of Mattock and Shen [7] it is worth highlighting the verification that for cases in which the supported beam has a lower height than the supporting beam, the load to be hung by the reinforcement can be reduced.

In addition, there are situations in which the supported beams transfer moment to the supporting beam that are neglected by the standards. In the study carried out by Collins and Lampert [9] it is observed that in the beam failure, despite the presence of the hanger reinforcement. The supporting beam presented inadequate behavior with the detachment of the lower zone of the connection region. In this context, the study by Mattock and Shen [7] considered the action of the torsional moment, and a cracking behavior similar to that seen in the study by Collins and Lampert [9] was observed.

The need for an adequate design of the hanger reinforcement for the proper behavior of the connection between beams, especially in situations with torsional moment acting on the supporting beam, still ignored by the standards, justify the present work that, through the analysis of experimental results present in the literature aims to provide recommendations that help in the design of these elements and serve as a basis for future studies.

## 2 BEHAVIOR OF INDIRECT SUPPORT

Concrete beams transmit their loads to the support preferentially through compression struts so that in the case of indirect supports, this load that arrives at the bottom is introduced into the supporting beam [6], as can be seen in Figure 1.

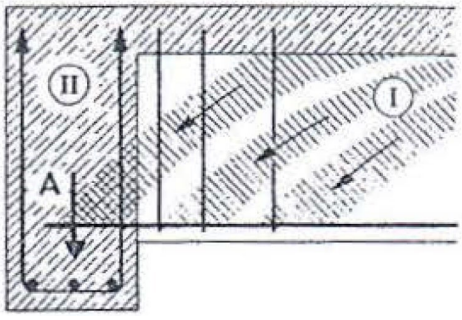


**Figure 1.** Loads transmission on beams in case of indirect support [6]

In order to obtain the balance of internal forces (Figure 2), is necessary at the intersection of the two beams, a reinforcement that acts as a tie to hang the load applied by the supported beam to the upper flange of the supporting beam, and this reinforcement it is called hanger reinforcement ([6], [10]). To calculate this reinforcement, two strut ant tie models are connected, one for the supported beam and the other for the supporting beam.

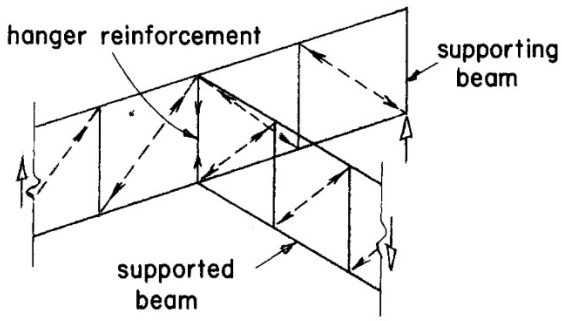


**Figure 2.** Strut and tie model in indirect supports [7]

Thoma [11] used a nonlinear finite element analysis (NFLE) to model numerically the static behavior of different experimentally tested beams, with one being a case of a prestressed beam with an indirect support. The beam studied is shown in Figure 3.

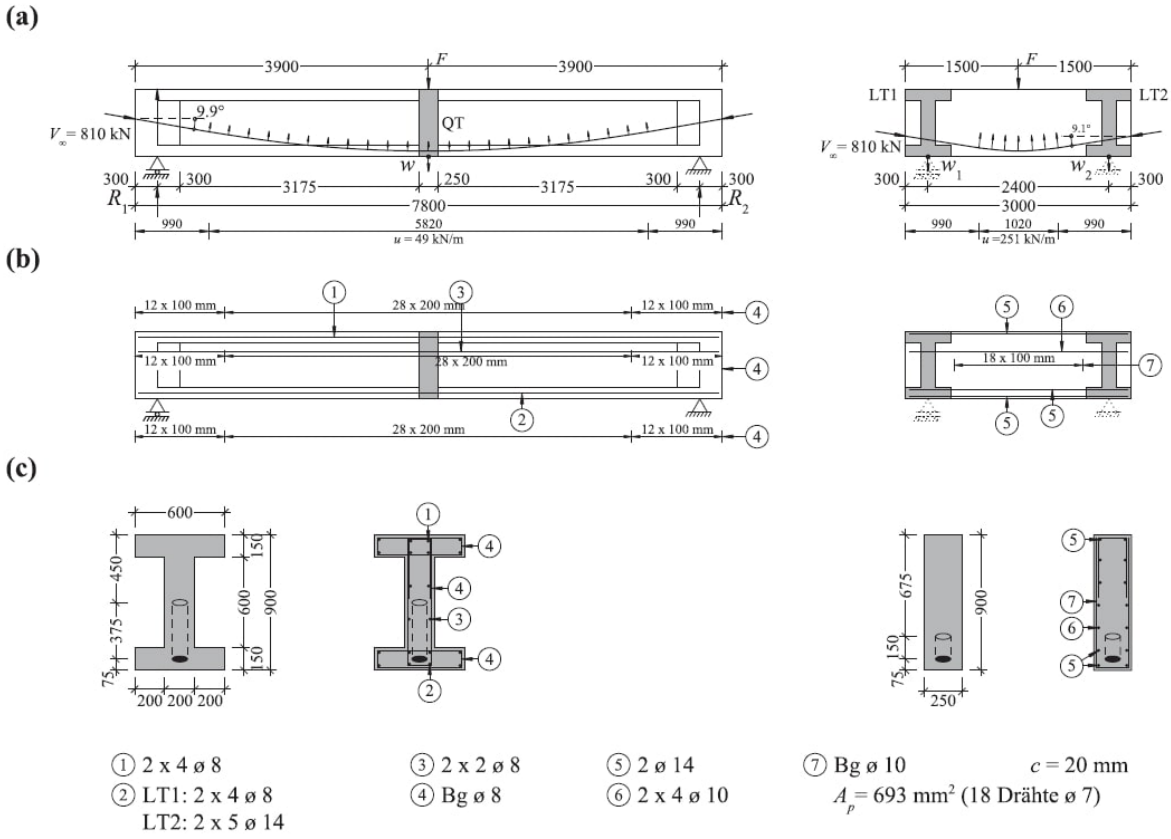


**Figure 3.** PC beam test carried out by Büeler and Thoma apud Thoma [11]

It was observed that both the crack orientation and the decompressed area in the longitudinal girder are determined sufficiently well by the NLFE analysis. The similar behavior can be seen in Figure 4 where the red lines represent the NFLE analysis.

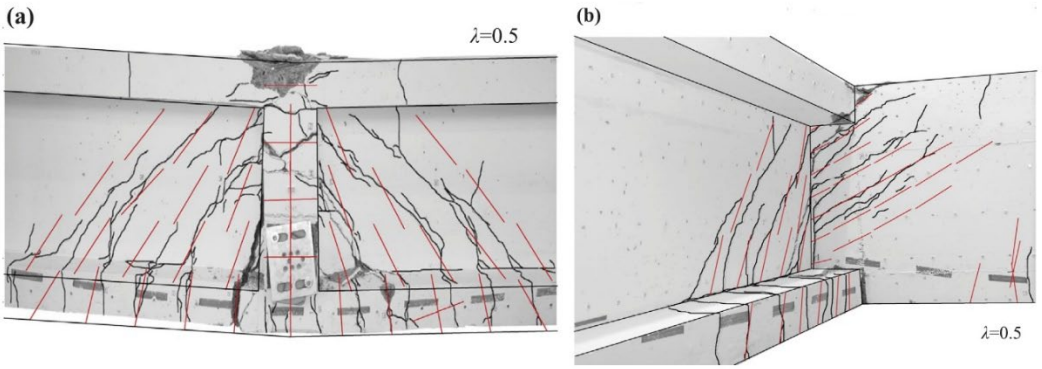


**Figure 4.** Crack pattern at failure: (a) view of longitudinal girder; (b) view of transverse girder–longitudinal girder. [11]

In the test, the flexural compression zone failed locally, as expected, at the intersection of the transverse and longitudinal girders. This phenomenon has not been implemented in the NFLE analysis. Despite that, the NFLE analysis showed that it could be a good method to model the indirect support with the development of new studies.

There are several types of indirect supports due to the arrangement between the supported beam and the supporting beam. In this case, the distribution of the load applied by the supported beam is different, so three cases of indirect supports will be shown in which attention must be paid when determining the load to be hung by the reinforcement.

It is initially considered the simplest case where both beams have the same height (Figure 5) and thus 100% of the load must be hung.

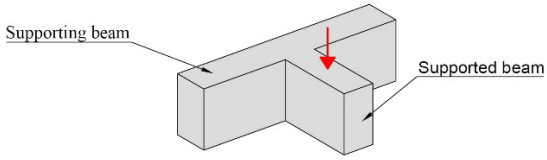


**Figure 5.** Indirect support where $h_1 = h_2$

The second case corresponds to the case of the supported beam ($h_1$) having a lower height than the supporting beam ($h_2$). Within this case, there are two situations in which the height of the supported beam is much smaller compared to the height of the supporting beam ($h_1 << h_2$) in which attention must be paid.

The first situation (called support from the top) is characterized by being a situation of indirect support where the upper surface of the supported and supporting beams coincide (Figure 6), in this condition the load to be hung can be reduced because in elements of reinforced concrete that are subject to shear forces, in addition to the truss model, there are other alternative resistant mechanisms (such as the arch effect and the aggregate interlock) that transfer the internal stresses from one cross-section to another [12].

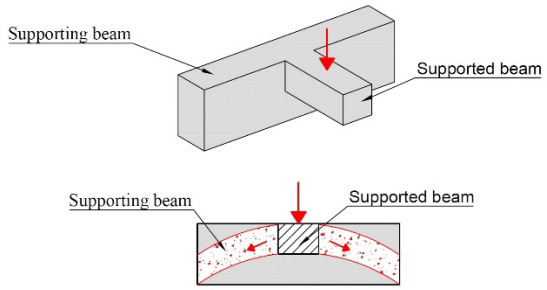


**Figure 6.** Indirect support with support from the top (where $h_1 << h_2$)

The second situation (called support from below) it is characterized by being an indirect support in which the lower surface of the supported and supporting beams coincide (Figure 7), in this condition is necessary to hang the entire load.

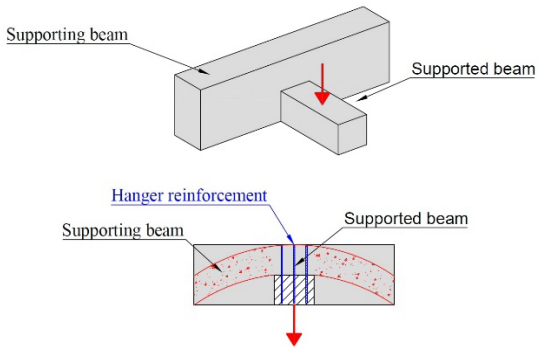


**Figure 7.** Indirect support with support from below (where $h_1 << h_2$)

Finally, the third case corresponds to the case where the supported beam is higher than the support beam (Figure 8). In this situation, 100% of the load must be hung.

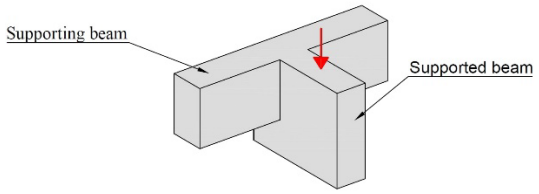


**Figure 8.** Indirect support where $h_1 > h_2$

With this, it is observed that attention is needed to the load to be hung in the design of indirect supports so that you can optimize your project by reducing this load and maintaining structural safety, in situations where it is possible.

In addition, an important situation that modifies the behavior of this region is the case where there is an action of a torsional moment in the supporting beam. The superposition of the forces resulting from the shear force and the torsional moment ends up altering the distribution of forces in the support beam and results in a weakening of this beam, where the stirrup legs adjacent to the back face of the support beam do not effectively contribute to the hanging of the beam load.

To understand this alteration, it is initially considered a beam subjected to torsional moment (T), in which shear stresses are developed at the top and on the side surfaces, as can be seen in Figure 9a. The principal stresses are shown in Figure 9b. These principal stresses eventually cause cracking around the body as seen by the line A-B-C-D-E in Figure 9c.

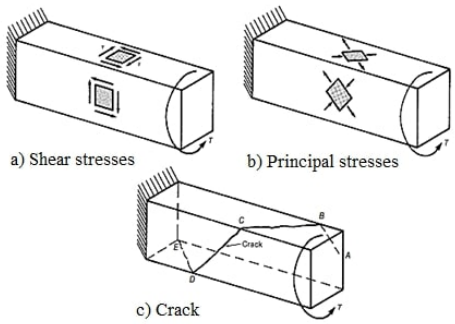


**Figure 9.** Principal stresses and crack pattern due to pure torsion [13]

However, if the beam is subjected to combined torsion and shear, the two shear components are added on one face (front face of Figure 10) and act in the opposite direction to each other on the other face. As a result, the inclined crack (Figure 10c) starts at the face where the stresses add up (crack AB) and extends along the top face of the beam (crack BC). If the bending moment acting on the part is large enough, the (bending) cracks extend almost vertically along the back face (crack CD). The compression zone due to bending near the bottom of the beam prevents cracks from extending over the entire height of the faces.

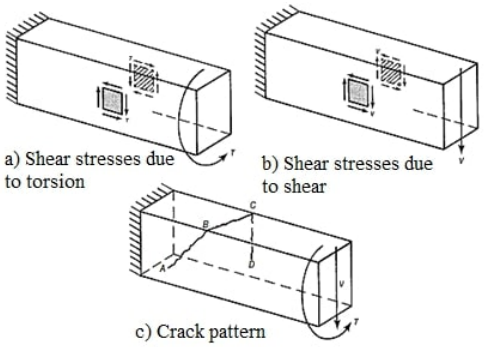


**Figure 10.** Shear stresses and crack pattern due to the combination of torsion and shear[13]

From the behavior of the structure when subjected to both shearing force and torsional moment, it is observed that since the posterior face presents only flexural cracking, the stirrup leg in this region does not act as a hanger reinforcement, only the inner leg of the stirrup does. Based on this consideration, in the case of a torsional moment, a different analysis is required regarding the hanger reinforcement.

## 3 INDIRECT SUPPORT DESIGN

With this, experimental results and design recommendations will be presented regarding four important topics in the design of indirect supports: load to be hung by the reinforcement, addition of the hanger reinforcement to the shear reinforcement, limit stress for which the reinforcement is not necessary and cases with rotation restraint.

### 3.1 Load to be hung

To determine the load for the design of hanger reinforcement, it is preferable to opt for the adoption of an analysis by a strut and tie model, but to simplify the design, Leonhardt and Mönnig [6] and Wight [13] propose equations that allow the calculation of the load to be hung, these expressions being indicated in Equations 1 and 2 respectively.

$$A_{sus} = \frac{h_1}{h_2} \cdot \frac{V_{u1}}{f_{yd}} \tag{1}$$

where $A_{sus}$ = cross-sectional area of hanger reinforcement ($m^2$); $V_{u1}$ = factored shear at the end of the supported beam (kN); $f_{yd}$ = design yield strength of transverse reinforcement ($kN/m^2$); $h_1$= supported beam height (m); $h_2$ = supporting beam height (m).

$$A_{sus} = \left(1 - \frac{h_b}{h_2}\right) \cdot \frac{V_{u1}}{f_{yd}} \tag{2}$$

where $h_b$ = vertical distance between the bottom of the two beams (m).

Equation 1 suggested by Leonhardt and Mönnig [6] has limitations, underestimating the loads for the case of support from below and overestimating for supported beams with a height greater than the supporting beam. The underestimation behavior for the case of support from below can be observed in Figure 11, where the green line corresponds to the expected behavior and the blue line corresponds to the expression of Equation 1. In this case, the

values obtained by the equation are equal to the value expected until the $h_1/h_2$ ratio is equal to 1, where after that point it starts to present higher values.

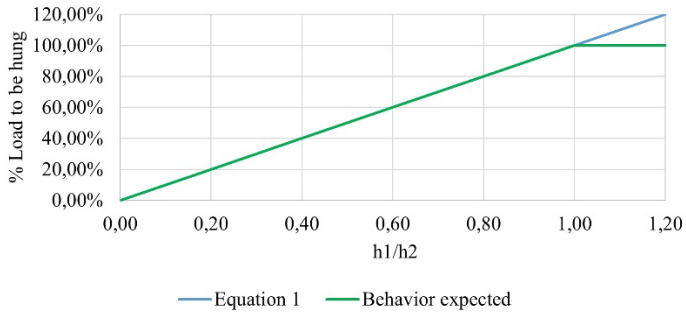


**Figure 11.** Relation between h1/h2 and load to be hung – Support from below

Regarding the support from the top, it can be noted that the values obtained from Equation 1 are below the expected result until the h1/h2 ratio is equal to 1. For a ratio higher than 1, Equation 1 overestimates the load to be hung (Figure 12), which despite being a more difficult situation to occur in the practice of projects, causes oversizing of the reinforcement.

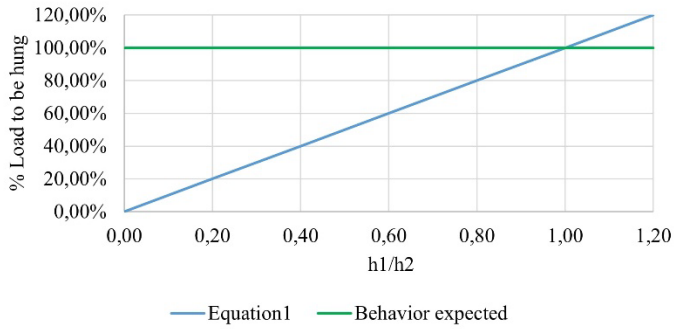


**Figure 12.** Relation between h1/h2 and load to be hung – Support from the top

Equation 2 suggested by Wight [13], which is the same as indicated by the Canadian standard CSA A23.3-04 [5], presents a more adequate behavior for situations with support from below, with the values obtained by the equation equal to the ones that are expected, despite having the same limitations as Equation 1 for cases with support from the top.

In view of the observed, it is necessary to adopt the following restriction (Equation 4) to use the expression indicated by Wight [13], and the load is calculated using the Equations 3 and 4:

$$A_{sus} = \left(1 - \frac{h_b}{h_2}\right) \cdot \frac{V_{u1}}{f_{yd}} \text{ to } h_1 \leq h_2 \tag{3}$$

$$A_{sus} = \frac{V_{u1}}{f_{yd}} \text{ to } h_1 > h_2 \tag{4}$$

The study carried out by Baek [1] aimed to study the influence of the depth of lateral load application on the behavior of the connection region between the beams. The experiment was carried out on two specimens, where the dimensioning and detailing of the reinforcements followed the determinations of the Canadian standard CSA A23.3-04 [5].

Two specimens were made where the beams were intentionally designed so that shear failure occurs in the supporting beam, with all other failure mechanisms avoided. The first specimen (B1) has two crucifix forms, where the supported beams are H4 and H5, and the supporting beam is called B1. Beams H4 and H5 correspond to 4/6 and 5/6 of the 600mm height of the supporting beam. The beam layout as well as the dimensions (in mm) of the beams are shown in Figure 13.

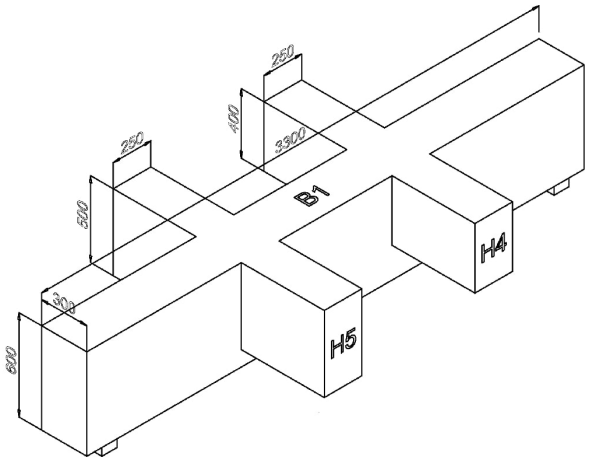


**Figure 13.** Description of specimen B1 (dimensions in mm) [1]

The specimen (B2) has only a crucifix shape, consisting of a supporting beam (B2) with the same height as the beam B1 of the first specimen and the beam H6 supported at the same height as the beam B2. In addition, beam B2 is loaded by direct loading at the top indicated by H0. The beam layout as well as the dimensions (in mm) of the beams are shown in Figure 14.

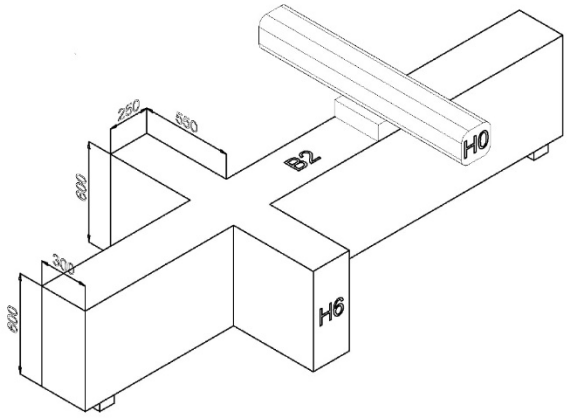


**Figure 14.** Description of specimen B2 (dimensions in mm) [1]

The hanger reinforcements were designed according to the simplified equation of CSA A23.3-04 [5] presented in Equation 2. If the load to be carried by the hanger reinforcement is taken by F then the reinforcements need to hang 0.67·F, 0.83·F, 1.0·F and 0 for the supported beams H4, H5, H6 and H0, respectively.

The test consisted of two phases for each specimen. Initially, the load was applied to the beams until one of the shear spans of the supporting beam failed. In the second phase, the span that failed was stiffened and loading was resumed until the failure of the other span (Figure 15). In this way the four spans could be tested.

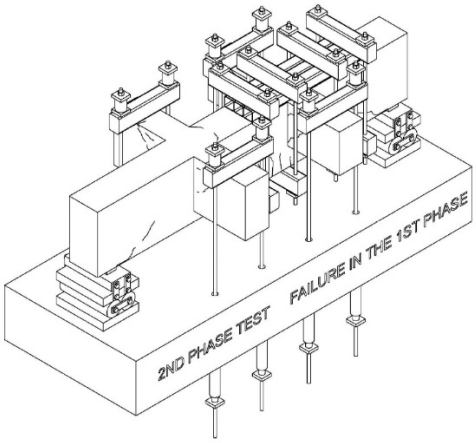


**Figure 15.** Test scheme [1]

With the results for the two specimens, the effect of the beam depth on the forces acting on the hanger reinforcements can be evaluated, comparing the design force calculated according to CSA A23.3-04 [5] with the forces corresponding to the deformations measured in the hanger reinforcement. Figure 16 shows the comparison between the estimated force and the force observed in the tests for beams H6, H5 and H4.

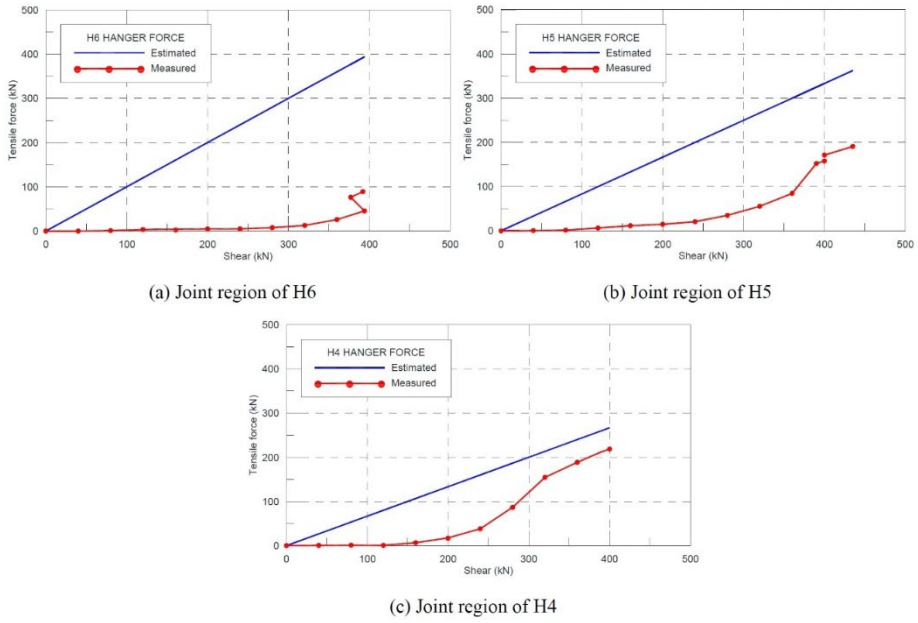


(a) Joint region of H6

(b) Joint region of H5

(c) Joint region of H4

**Figure 16.** Tensile force on hanger reinforcement [1]

Thus, it is observed that the load on beam H6 in the test was only 20% of the design value estimated by CSA A23.3-04 [5]. For beam H5, the load on the hanger reinforcement was 46% lower than expected in the design and finally, for beam H4 the load was only 12% lower than the design force. The reference values are the highest observed in the tests and were observed for the maximum loads supported by the beams.

In order to better visualize this comparison, the author makes the relationship between the ratio hb⁄h2 used in the design equation and the values obtained in the tests. This analysis for the maximum load is shown in Figure 17.

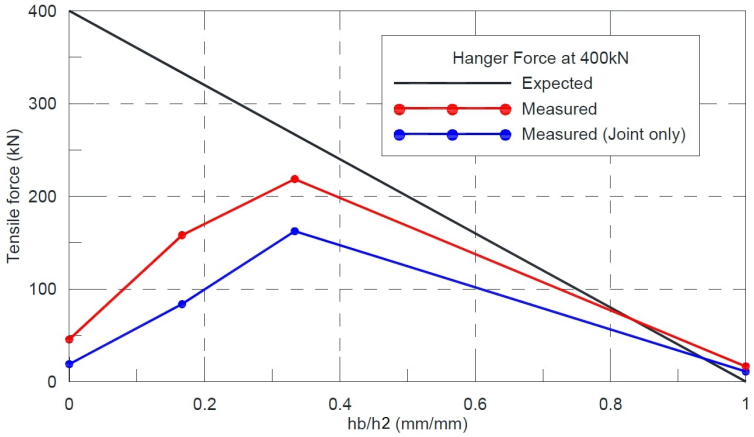


**Figure 17.** Development of tensile force as a function of the ratio hb/h2 [1]

It was expected that the maximum load on the hanger reinforcements would occur for the case of the deepest supported beam (H6), but this was not achieved, observing that the maximum load to be hung was obtained in the beam H4, which has a height of 4/6 of the height of the supporting beam and compared to beams H5 and H6 should be, by the design equation, the smallest load.

According to the author, the presence of diagonal tensile cracks in the concrete was observed, indicating that compressive stresses were flowing from the supported beam to the supporting beam throughout the height of the supporting beam. This means that there was force transfer over the height of the supported beam and not just at the bottom, as assumed by the Canadian code. This flow of compressive stresses was likely present for H6, H5 and H4, as evidenced by diagonal cracks formed in the supported beam and flowing into the supporting beam, as shown in the Figure 18.

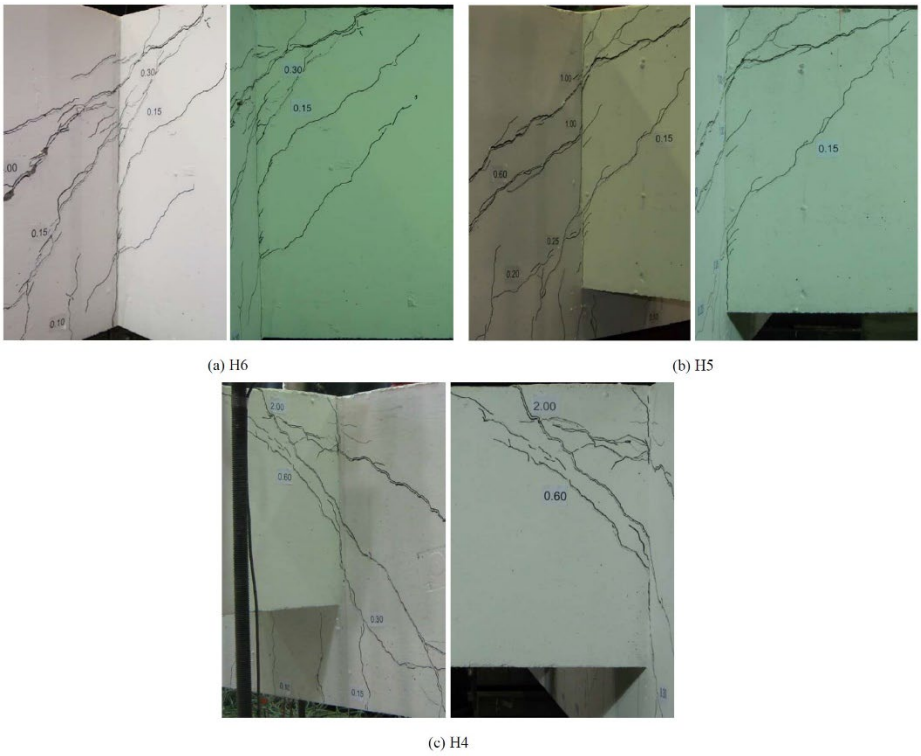


**Figure 18.** Cracking at the joint interface between the beams [1]

Given the data of the hanging loads, the remainder of the load was transferred directly by diagonal compression stresses from the supported beam to the supporting beam. The value of this portion referring to direct transmission was determined by subtracting the hanging force from the total load applied to the interface. The comparison between the hanging load and direct transmission values is shown in Figure 19.

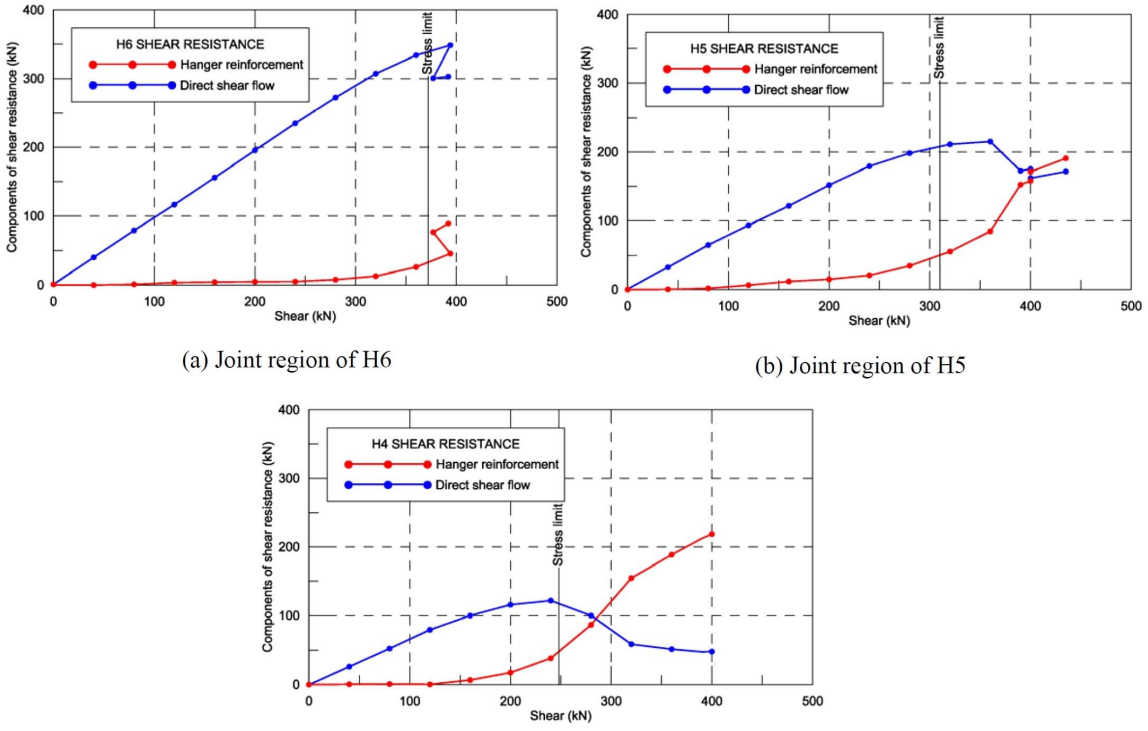


(a) Joint region of H6




(b) Joint region of H5




(c) Joint region of H4

**Figure 19.** Comparison between the forces transmitted by the hanger reinforcement and the direct shear flow [1]

It is observed that the direct transmission by diagonal compression was much higher than that transferred by the hanger reinforcement in beam H6 (Figure 19a). For beam H4 the two mechanisms contributed similarly (Figure 19b), while the shear transferred by the hanger reinforcement is predominant in beam H4 (Figure 19c). Thus, as the depth of the supported beam is greater than 2/3 of the height of the supporting beam, there is a reduction in the demand for hanger reinforcement due to direct transfer so for these cases the equation for the design of the CSA A23.3-04 [5] proved to be conservative.

Due to the low sampling in which this behavior was observed, more studies are needed to be focused on this consideration for an adequate use of this greater reduction and future application in design standards for concrete structures. At the current moment of knowledge on the subject, it is not understood properly which portion is transferred directly by compression through the height, so due to the safety of the structure, it is recommended to use Equation 3, which is based on the Canadian standard.

### 3.2 Addition of the hanger reinforcement to shear reinforcement

This is one of the main points of attention because, in the case of superposition case of superposition of reinforcements, congestion can occur in the intersection region, and if this superposition is necessary and not considered, the section weakens. Leonhardt and Monnig [6] defend that the highest of the values between the hanger reinforcement and the necessary shear reinforcement should be adopted, but the CSA A23.3-04 [5], ACI 318-19 [3] and EN 1992- 1-1:2004 [4] consider that the reinforcement overlap is necessary.

Using the strut and tie model formulated by Mattock and Shen [7] it is observed that as the load is applied to the lower part, the presence of a tie is necessary to hang the load transferred by the supported beam. In order to observe this behavior, a truss can be taken with a load applied to the center of its span in two situations: the first is considered the load applied to the upper face and the second to the load applied to the lower face.

It was observed that for the first situation (direct loading) the vertical tie in the region of application of the load did not present axial force and could therefore be disregarded for the balance of the region, having the schematic of its structure shown in Figure 20.

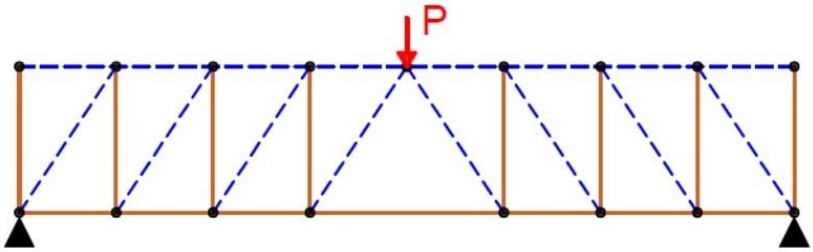


**Figure 20.** Strut and tie model for a bi-supported beam with centered force applied to the upper face

When taking the second situation (indirect loading) it was noticed that the vertical tie is loaded exactly with the value of the applied load, which indicates that it acts by hanging 100% of the applied load and consequently its presence is necessary to balance the region, being observed the schematic of the structure in Figure 21.

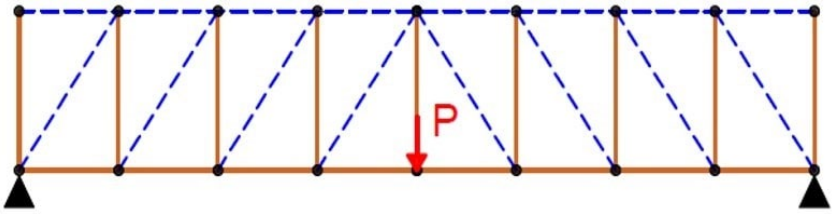


**Figure 21.** Strut and tie model for a bi-supported beam with centered force applied to the lower face

Given this and associated with the current knowledge regarding the behavior of the intersection zones, the superposition of hanger and shear reinforcements is recommended, and attention should be doubled on the congestion of reinforcements, observing the limitations imposed by the codes for shear reinforcement rate as well as limitations of spacing so that an adequate vibration of the concrete of the structure can be ensured.

### 3.3 Limit stress for which the hanger reinforcement is not required

In reinforced concrete elements that are subject to shear forces, in addition to the truss model, there are other alternative resistant mechanisms that transfer the internal stresses from one cross section to another [12]. The arc effect and the aggregate interlock are two examples of these mechanisms, where they are considered in ABNT NBR 6118 [2] by an additional portion defined in the standard as $V_c$. Thus, the hanger reinforcement in certain circumstances can be dispensed because for low stresses other mechanisms may be sufficient to adequately transmit the load.

Fusco [10] comments that only in cases of very thin web beams ($b_w/b_f = 1/6$, represented in Figure 22) the truss scheme is mobilized at the beginning of cracking, so that on the other beams, the alternative resistant schemes act preliminarily, whose contribution progressively decreases as the part cracks.

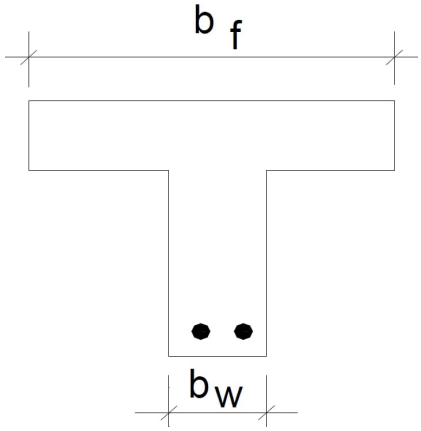


**Figure 22.** T-beam cross section [10]

One of the studies that evaluated the limiting stress was carried out by Mattock and Shen [7]. In this study, the authors aimed to evaluate the efficiency of the hanger reinforcement in the case where the supported beam rests on one side of the supporting beam of same height. The specimens were E-shaped grids (Figure 23), where the supporting beam presents a restriction to rotate in order to create a negative moment in the supported beam in the intersection region.

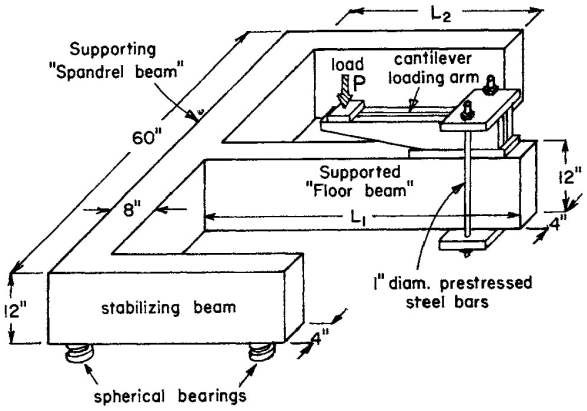


**Figure 23.** Typical structure of the tested specimens [7]

The specimens were dimensioned by varying the arrangement of the hanger reinforcement, the shear forces and the maximum resistant moment of the section. Specimens 1 and 4 were designed so that the shear force on the supported beam was close to $0.21b_w \cdot d \cdot \sqrt{f_c'}$ (in MPa). The same flexural strength was designed for specimen 2, but due to a lower a/d ratio, the shear for this case was close to the maximum allowed by the American standard in its 1989 version $0.83 \cdot b_w \cdot d \cdot \sqrt{f_c'}$ (in MPa). To maintain the shear value at the failure of specimen 2, specimen 3 was dimensioned so that its flexural strength was twice that of specimen 2. Specimen 5 was designed so that the shear was $0.66 \cdot b_w \cdot d \cdot \sqrt{f_c'}$ (in MPa) and the flexural strength corresponding to this shear value.

With regard to the hanger reinforcement, in all cases, sufficient reinforcement was provided to satisfy the requirements of the American standard, wherein specimens 1 and 4 the minimum reinforcement requirement ruled. In specimens 1, 2 and 3, the hanger reinforcement was arranged adjacent to the interface between the two beams, being designed with a yield strength equal to the shear at failure by bending of the supported beam.

In the case of specimens 4 and 5, their design was carried out considering that the stirrups to support all the shear transferred from the supported beam to the supporting beam must be positioned in a region of 0.5 times the height of

the beam for each side of the beams, which may be waived if the stress is less than $0.25 \cdot \sqrt{f_c'}$ (in MPa), if $h_b > h_l/2$, or in case the supported beam rests on the supporting beam by its lower face. Therefore, for specimen 4, hanger reinforcement was not available since the maximum stress in the supported beam was less than $0.25 \cdot \sqrt{f_c'}$ (in Mpa). In specimen 5, all stirrups on the supporting beam within a distance of d/2 from the axis to each side were considered as hanger reinforcement. The data from the tests are presented in Table 1.

**Table 1.** Test results [7]

| Specimen | 1 | 2 | 3 | 4 | 5 |
|---|---|---|---|---|---|
| $P_{max}$ (kips) | 8.18 | 35.00 | 35.00 | 8.90 | 25.80 |
| $V_{test}$ (kips) | 8.64 | 35.37 | 35.41 | 9.36 | 26.20 |
| $\frac{V_{test}}{b_w \cdot d/\sqrt{f_c'}}$ | 2.86 | 12.14 | 12.93 | 3.09 | 8.73 |
| $M_{test}$ (kips·in) | 181.1 | 180.0 | 317.8 | 168.3 | 84.6 |
| $M_{calc}$ (kips·in) | 165.0 | 165.7 | 296.4 | 166.4 | 128.4 |
| $\frac{M_{test}}{M_{calc}}$ | 1.10 | 1.09 | 1.07 | 1.01 | 0.66 |

After the tests, it was observed that specimens 1 and 4, with the ratio $V_{test}/(b_w \cdot d/\sqrt{f_c'})$, presented in Table 1, close to 3) behaved similarly, even though the hanger reinforcement was only arranged in specimen 1. Thus, this similar behavior shows that the criterion for waiving the use of hanger reinforcement is suitable for loads less than $0.25 b_w \cdot d \cdot \sqrt{f_c'}$ (in MPa). In the case of specimen 1, the hanger reinforcement did not yield and only carried 35% of the shear at failure. Diagonal tensile cracking did not develop in these specimens and, therefore, the truss behavior was not significant.

In specimens 2 and 3, the desired behavior was achieved, being observed the appearance of a pattern of diagonal cracks by tension (Figure 24) that define the diagonal compression struts in the truss behavior of the supported beam. In addition, the hanger reinforcement yielded before failure and carried a maximum load close to shear in yielding the longitudinal flexural reinforcement. In these specimens, the stress was above the limit stress so the presence of hanger reinforcement is necessary for the structure to behave properly.

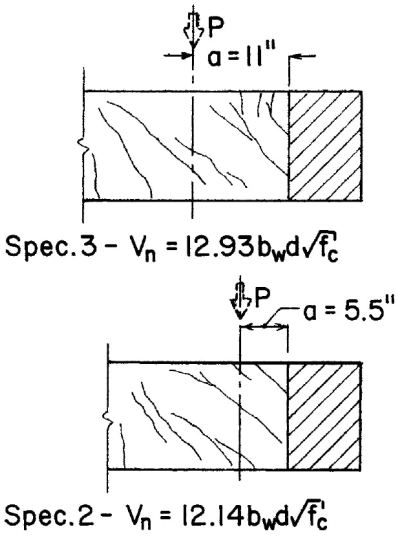


**Figure 24.** Cracking pattern of specimens 2 and 3 [7]

Therefore, the Canadian standard CSA A23.3-04 [5] in Equation 5 as well as Mattock and Shen [7] and Wight [13] in Equation 6 indicate the possibility of waiving the hanger reinforcement by assigning a limit stress ($\tau_{lim}$) at the interface between the beams.

$$\tau_{lim} = 0.23 \cdot \lambda \cdot \phi_c \cdot \sqrt{f'_c} \quad (5)$$

$$\tau_{lim} = 0.25 \cdot \sqrt{f'_c} \quad (6)$$

where $\hat{o}_{lim}$ = limit stress for reinforcement waiver (MPa); $\lambda$ = factor to consider low density concrete; $f'_c$ = specified compressive strenght of concrete (MPa); $\phi_c$ = resistance factor for concrete [5].

Pereira et al. [14] present cases of indirect support to evaluate the limiting stresses indicated by Mattock and Shen [7] and the Canadian standard [5]. The case diagrams are presented in Figure 25, where the hatched beam corresponds to the supported beam, and the results of the cases are presented in Table 2.

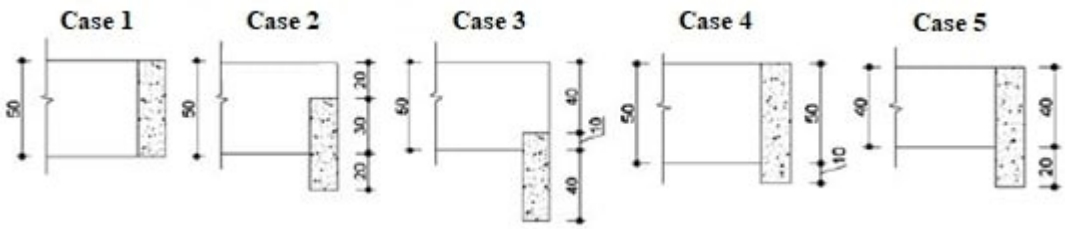


**Figure 25.** Support situations analyzed by Pereira et al. [14]

**Table 2.** Shear stress values at the supported beam interface and limits [14]

| Case | b (cm) | h (cm) | $\tau_d$ (MPa) | CSA A.23.3-04 [5] (MPa) | Mattock e Shen [7] (MPa) |
|---|---|---|---|---|---|
| 1 | 15.00 | 50.00 | 1.15 | 0.85 | 1.43 |
| 2 | 15.00 | 50.00 | 1.15 | 0.85 | 1.43 |
| 3 | 15.00 | 50.00 | 1.15 | 0.85 | 1.43 |
| 4 | 15.00 | 50.00 | 1.16 | 0.85 | 1.43 |
| 5 | 15.00 | 40.00 | 1.38 | 0.85 | 1.43 |

It is important to highlight that the analysis of this criterion by the Canadian standard is only allowed for situations in which the upper surfaces of the beams coincide, so that, by this consideration, only cases 1 and 5 would allow this analysis. Even so, it can be observed that the limit of the Canadian standard was exceeded in all cases, but for the limit of Mattock and Shen [7] none of the cases would require hanger reinforcement.

It appears that the expression indicated by Mattock and Shen [7] allows higher stresses at the interface in which it is possible to dispense the hanger reinforcement, but it has been observed in only a specimen, so for the structure safety, the adoption of a more conservative criterion as presented by the Canadian standard is the most recommended.

To use Equation 5 according to the Brazilian standard ABNT NBR 6118 [2] it is necessary to convert the resistance $f'_c$, present in the Canadian standard, to the resistance $f_{ck}$ present in the Brazilian standard. Considering a standard deviation of the compressive strength of 3 MPa, Souza and Bittencourt [15] present an expression that relates the two factors and is expressed in Equation 7.

$$f'_c = f_{ck} - 2.04 \quad (7)$$

where $f_{ck}$= characteristic compressive resistance of concrete (MPa).

Substituting Equation 7 in Equation 5, the limit stress for application of the Brazilian standard is presented in Equation 8:

$$\tau_{lim} = 0.23 \cdot \lambda \cdot \phi_c \cdot \sqrt{f_{ck} - 2.04} \quad (8)$$

The $\lambda$ factor considers the possibility of using low-density concrete, having 1 as the value for normal-density concrete and the $\phi_c$ factor assuming the value indicated by the Canadian standard of 0.65 since it does not have a corresponding value in the Brazilian standard. Substituting these two values in Equation 8, Equation 9 is obtained, which represents the stress limit for waiver of reinforcement to be applied in projects carried out with concrete of normal density according to the Brazilian standard.

$$\tau_{lim} = 0.15 \cdot \sqrt{f_{ck} - 2.04} \quad (9)$$

According to the Canadian standard CSA A23.3-04 [5] normal density concretes have a density greater than 2150kg/m$^3$ and this restriction should be added since for ABNT NBR 8953 [16] normal density structural concretes have a density greater than 2000kg/m$^3$.

### 3.4 Cases with rotation restraint

A special situation in the design of indirect supports consists of cases where a torsional moment acts on the supporting beam, where a real example is shown in Figure 26. In this example, the balcony beams (VP3 and VP4) are displaced from the columns and are supported in beam VP1, which presents an increase in section in the region close to the columns and corresponds to a fixed section in which the transfer of torsional moment to the supporting beam occurs.

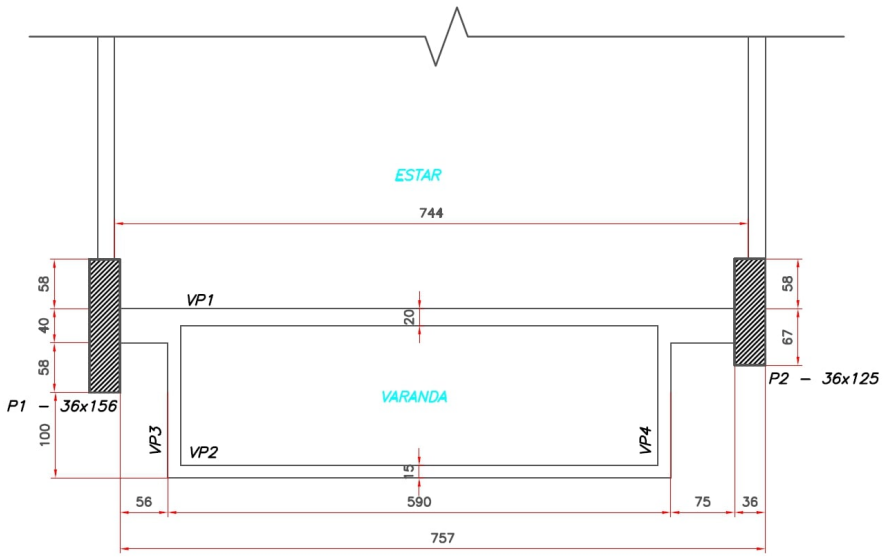


**Figure 26.** Example of indirect support situation with application of torsion in the supporting beam (dimensions in cm)

The study of indirect supports in situations with restraint to the rotation of the supporting beam is still very limited, and it is worth mentioning initially the test carried out by Collins and Lampert [9]. The main objective of this experimental program was to evaluate design methods for parts subjected to compatibility torsion, choosing a two-beam structure (called floor beam-spandrel beam by the author) shown in Figure 27. Although the focus of this study is the analysis of the distribution of moments in the cracking, here will be brought, mainly, the observed results referring to the behavior of the structures in the connection joints between the beams.

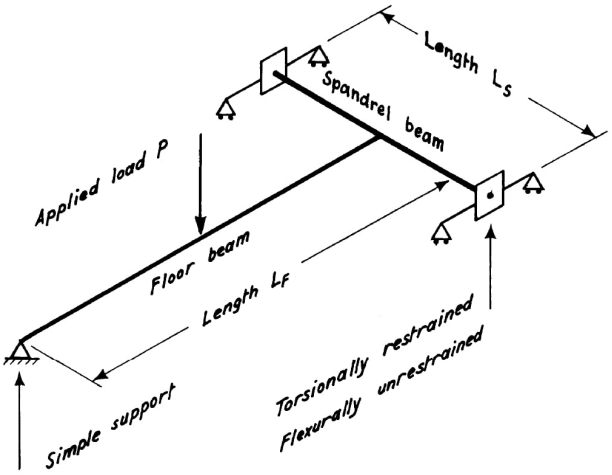


**Figure 27.** Structural scheme used by Collins and Lampert [9]

This structure was designed by two methods: method A (conventional design in which the supporting beam was subjected to compatibility torsion) and method B (design considering that the supporting beam does not present torsion resistance).

Thus, six specimens were tested, with specimens S1 and S3 dimensioned by method A and specimens S2, S4, S5 and S6 by method B. For the interests of this article, attention is focused on specimens S3 and S4. Specimen S3 was dimensioned by method A while specimen S4 was dimensioned by method B to establish a comparison between them.

After the tests, specimen S4 failed by crushing of the concrete compression zone. The joint in specimen S3 was the cause of the failure despite the care taken in detailing these joints. The design of this region was in accordance with the recommendations for indirect support by Leonhardt (1965) apud Collins and Lumpert [9], with the hanger reinforcement in the joint being made designed to hang 100% of the load on the supporting beam, in addition, it was arranged the longitudinal bars of the supported beam (floor beam) above the longitudinal bars of the supporting beam (spandrel beam). Despite these precautions, the failure occurred in this region, as can be seen in the case of specimen S3 shown in Figure 28.

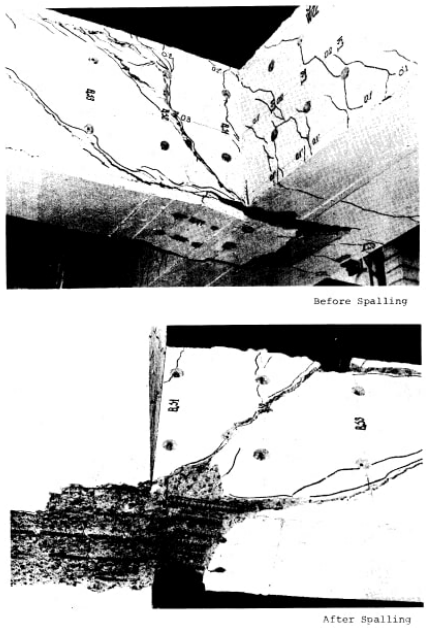


**Figure 28.** Joint failure in specimen S3 [9]

For the case of method A (specimen S3), the supporting beam is subjected to torsion and, as previously presented, structures in this situation present a weakening because only the inner legs are expected to act as a hanger reinforcement. While the specimen S4 does not present a torsional moment acting on the supporting beam behaved as expected. It follows that the design provisions that were made did not consider the negative effect of the presence of torsional moment in the supporting beam.

Because of this, the authors suggested that it would be practical to provide a reinforcement capable of hanging 100% of the load in the supported beam, in addition to keep the reinforcement on the supporting beam hanging also 100% of the load, with that it would be provided the double of hanger reinforcement compared to the suggestion of Leonhardt. However, it is observed that the author did not consider that the fact that there is a transmission of bending moment between the beams interferes with the behavior of the joint.

A later study carried out by Mattock and Shen [7] evaluated the behavior of indirect supports in which there is a torsional moment acting on the supporting beam. Since the experiment was previously presented from the perspective of the evaluation of the limiting stress for waiver of the hanger reinforcement, attention will now be given to specimens 2 and 5 to evaluate the interference of the torsional moment acting on the supporting beam.

For specimen 5, an unsatisfactory behavior was observed since the longitudinal reinforcement yielded with only 55% of the projected dead load and 66% of the calculated flexural strength. In this case, only 57% of the load was resisted by the hanger reinforcement. Despite the cracking scheme of the supporting beam of the specimen (Figure 29a) being very similar to that presented in specimen 2 (Figure 29b), the hanger reinforcement did not provide sufficient support from the lower part of the supporting beam at the intersection of the beams.

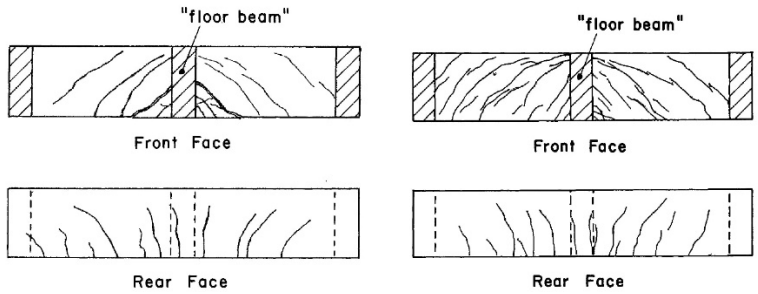


**Figure 29.** Cracking pattern of the supporting beam in specimens 5 and 2 [7]

As previously described, the combination of shear and torque on the supporting beam on the rear face act in the opposite direction to each other. The cracking scheme observed in Figure 29a indicates the presence of flexural cracks, so that the stirrup leg was not cut by the crack and thus did not act as a hanger reinforcement. It can be noted that the cracking scheme observed in Figure 29a is similar to the one suggested in Figure 10 for the case of the torsional moment combined with the shear.

Thus, only the inner leg is expected to act as a hanger reinforcement, which may explain the failure of this region with the detachment of the lower region of the intersection region, because the hanger reinforcement is not sufficient to hang the entire applied load. As for specimen 2 in the same study, which considered only the adjacently disposed reinforcement as hanger reinforcement, an adequate behavior was observed despite being dimensioned for a higher shear when compared to specimen 5.

Thus, in these cases, only the inner leg (adjacent to the interface between the beams) of the stirrups should be considered as hanger reinforcement, highlighting the importance of further experimental studies to better understand the behavior of the intersection zone and what is the portion of the contribution of the external legs of the stirrups in the hanging of the load.

## 4 CONCLUSIONS

Based on the results presented in the present work, the following conclusions can be drawn:

- The value of the load to be hang is calculated according to Equations 3 and 4;
- Hanger reinforcement must be added to the shear reinforcement;

- There is a shear stress limit transferred by the supported beam at which, for stress values lower than this limit, hanger reinforcement can be dispensed with this stress calculated by Equation 9;
- In situations where the supported beam transfers torsional moment to the supporting beam, only the stirrup legs adjacent to the interface of the connection between the beams must be considered as hanger reinforcement.

## REFERENCES


[1] K. R. Baek, *Response of Reinforced Concrete Beams with Indirect Loading.* Montreal, Canada: McGill University; 2016.

[2] Associação Brasileira de Normas Técnicas, *Projeto de Estruturas de Concreto – Procedimento*, ABNT NBR 6118, 2014.

[3] American Concrete Institute, *Building Code Requirements for Structural Concrete and Commentary*, ACI 318-19, 2019.

[4] British Standard. *Eurocode 2: Design of Concrete Structures—. Part 1-1: General Rules and Rules for Building,* EN 1992-1-1:2004, 2004.

[5] Canadian Standards Association, *Design of Concrete Structures*, CSA A23.3-04, 2004.

[6] F. Leonhardt, and E. Mönning. *Construções de Concreto, vol. 3: Princípios Básicos sobre a Armação de Estruturas de Concreto Armado*. Rio de Janeiro: Interciência, 1978.

[7] A. H. Mattock and J. F. Shen, "Joints between reinforced concrete members of similar depth," *Struct. J.*, vol. 89, no. 3, pp. 290–295, 1992.

[8] A. H. Mattock and A. Kumar, "Flexural reinforcement stress in an indirectly supported reinforced," *Struct. J.*, vol. 89, no. 4, pp. 398–404, 1992.

[9] M. P. Collins, and P. Lampert. "Redistribution of moments at cracking-the key to simpler torsion design?," *ACI Spec. Publ.*, vol. 35, pp. 343–384, 1973.

[10] Fusco Péricles Brasiliense. *Técnicas de Armar as Estruturas de Concreto*. 2. ed. Pini, 2013.

[11] K. Thoma, "Finite element analysis of experimentally tested RC and PC beams using the cracked membrane model," *Eng. Struct.*, vol. 167, pp. 592–607, 2018.

[12] J.S. Giongo, *Concreto Armado: Dimensionamento de Elementos Estruturais Fletidos Solicitados por Força Cortante*. EESC, 2011.

[13] J.K. Wight. *Reinforced Concrete: Mechanics and Design*. Prentice Hall, 2015.

[14] E. M. V. Pereira, Í.S.S. Araújo, and P. G. B. Nóbrega, "ARMSUSP: um aplicativo computacional para cálculo da armadura de suspensão em apoios indiretos," *Rev. Eng. Civ. IMED*, vol. 7, no. 1, pp. 179–201, 2020.

[15] R. A. Souza, and T. N. Bittencourt, "Definição de expressões visando relacionar f˙c e fck," in *IV Enc. Tecnol. Eng. Civ. e Arquit*. 2003.

[16] Associação Brasileira de Normas Técnicas. *Concreto para fins estruturais - Classificação pela massa Específica, por Grupos de Resistência e Consistência*, ABNT NBR 8953, 2015.


**Author contributions:** MASC: data curation, formal analysis, methodology, writing. BH: supervision, manuscript writing and review.

**Editors:** Mauro de Vasconcellos Real, Guilherme Aris Parsekian.

IBRACON Structures and Materials Journal
Revista IBRACON de Estruturas e Materiais
ISSN 1983-4195 ismj.org

ORIGINAL ARTICLE

# Assessment of stiffness and structural behavior of reinforced concrete beams rehabilitated with CFRP and crack injection

## *Avaliação da rigidez e do comportamento estrutural de vigas de concreto armado reabilitadas com CFRP e injeção de fissuras*

Luis Felipe Fernandes Guim[a]
Gustavo Emilio Soares de Lima[a]
Gustavo de Souza Veríssimo[a]
José Luiz Rangel Paes[a]

[a]Universidade Federal de Viçosa – UFV, Departamento de Engenharia Civil, Viçosa, MG, Brasil

**Received** 09 December 2021
**Accepted** 23 June 2022

**Abstract:** In this paper, an experimental program was developed in order to evaluate the structural behavior of RC beams rehabilitated with CFRP sheets and crack injections. The specimens' stiffness before and after structural rehabilitation was assessed through vibration tests. Bending tests were employed to obtain load-deflection curves and evaluate failure modes. Results indicate that all beams displayed higher stiffness values after structural rehabilitation. The CFRP sheet fostered an increase of the specimens' ultimate load. Crack injections influenced stiffness but did not affect the ultimate load.

**Keywords:** structural rehabilitation; NDT; RC beam; reinforcements with CFRP; crack injection.

**Resumo:** Neste trabalho, foi desenvolvido um programa experimental com o objetivo de avaliar o comportamento estrutural de vigas de concreto armado reabilitadas com manta de CFRP e injeções de fissuras. A rigidez dos modelos antes e depois da reabilitação estrutural foi avaliada por meio de ensaios de vibração. Foram realizados ensaios de flexão para obter curvas de carga-flecha e avaliar modos de falha. Os resultados indicam que todas as vigas apresentaram valores de rigidez mais elevados após a reabilitação estrutural. A manta de CFRP promoveu um aumento da carga final dos modelos. As injeções de fissura influenciaram a rigidez, mas não afetaram a carga final.

**Palavras-chave:** reabilitação estrutural; END; viga de concreto armado; reforço com CFRP; injeção de fissuras.

**How to cite:** L. F. F. Guim, G. E. S. de Lima, G. S. Veríssimo, and J. L. R. Paes, "Assessment of stiffness and structural behavior of reinforced concrete beams rehabilitated with CFRP and crack injection," *Rev. IBRACON Estrut. Mater.*, vol. 16, no. 1, e16110, 2023, https://doi.org/10.1590/S1983-41952023000100010

## 1 INTRODUCTION

According to the fib Model Code for Concrete Structures [1], a structure is considered durable when it meets performance requirements throughout the lifespan specified in its project. In cases where these requirements are not met, structural rehabilitation procedures must be conducted if the structure is to remain operational. According to Souza and Ripper [2], these procedures can be used to meet service and durability conditions (repair) or to increase or reestablish the structure's bearing capacity (reinforcement), which requires additional materials.

In the case of reinforced concrete members subject to bending, the cracking process, albeit inevitable, may influence the structure's performance. von Fay [3] states that excessive cracking can expose the reinforcement bars to the action of external agents and reduce the element's stiffness. According to this author, cracks with openings between 0.05mm

**Corresponding author:** Luis Felipe Fernandes Guim. E-mail: luisf.guim@gmail.com
**Financial support:** None.
**Conflict of interest:** Nothing to declare.
**Data Availability:** The data that support the findings of this study are available from the corresponding author, L. F. F. G., upon reasonable request.

and 6.3mm should be injected with epoxy resins for structural repair purposes. These resins react with the concrete, producing very resistant solids with a relatively high modulus of elasticity. Al-Nu'man and Al-Sahlani [4] present studies from several authors who affirm that a structure restored with crack injection can show an ultimate resistance and stiffness equivalent to that of the earlier undamaged monolithic structure.

In order to increase or reestablish the ultimate resistance of a structure subject to bending, Beber [5] cites that reinforcing with CFRP is a good option, especially due to their mechanical properties. CFRP presents a large resistance/self-weight ratio, performing well at high temperatures. Juvandes and Figueiras [6] highlight that the fibers possess linear elastic behavior and brittle failure, with ultimate strength at 3500 MPa, modulus of elasticity varying between 150 GPa and 600 GPa, and maximum elongation at approximately 1.5%. CFRP reinforcement work like tensioned steel for reinforced concrete elements. The analysis and design of elements reinforced with CFRP subject to bending can be done using the same regular hypotheses applied to reinforced concrete elements, with an additional verification limiting the fiber's strain to avoid debonding [7], [8]. According to Salgado et al. [9] although CFRP reinforcements improve an element's ultimate resistance, they exert little influence over its stiffness.

In order to know the residual characteristics of structural elements, which are necessary for decision-making in the structural rehabilitation process, non-destructive testing (NDT) is often conducted, as pointed by Helal et al. [10]. Salawu [11] presents studies demonstrating that vibration analysis has been widely employed to obtain information about the mechanical characteristics of structures. The modal parameters of a given structure (natural frequencies, mode shapes, and modal damping) are sensitive to alterations in the structure's physical parameters (mass and stiffness). Any alteration in a structural element's stiffness is directly related to a change in its natural vibration frequencies, depending also on boundary conditions and support stiffness. With the aid of vibration analyses and conventional bending tests, the increase in stiffness and ultimate resistance of reinforced concrete beams rehabilitated with CFRP and crack injection can be assessed.

The purpose of this paper is to evaluate the stiffness of beams rehabilitated with CFRP, with and without crack injection, in order to provide a more realistic evaluation of their structural behavior. Currently there are no recommendations regarding which stiffness percentage is acceptable in the evaluation of the behavior of rehabilitated structural elements. Moreover, most of the research on beams reinforced with CFRP employed test specimens that were perfectly whole. The rehabilitation of damaged elements adopted in this work resembles real situations of structural rehabilitation more closely. This can contribute to a better understanding of the behavior of reinforced structures.

## 2 MATERIALS AND EXPERIMENTAL PROGRAM

### 2.1 Specimens

This study employed nine specimens that were initially produced in the context of Lima's [12] research. The dimensions of all beams were 9 x 18 x 180 cm. The beams' concrete had a water/cement ratio of 0.60 and three different steel reinforcement ratios, resulting in three different groups of three specimens with the same reinforcement ratio in each group. Figure 1 displays general schematics of the beams.

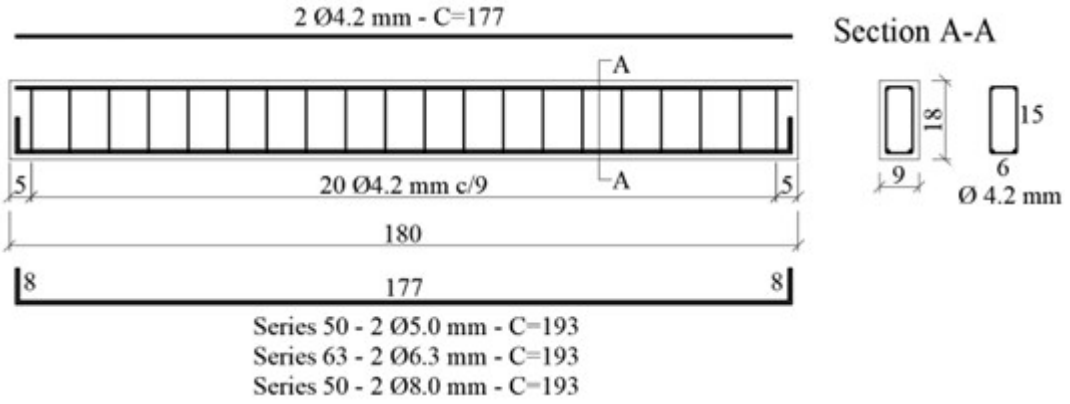


**Figure 1.** Schematics of original undamaged specimens. Dimensions in centimeters unless otherwise specified.

The original models were subjected to bending tests, with a vertically induced load from top to bottom, causing tensile stress on the element's lower surface. In these tests all models failed due to steel yielding. The tests also caused permanent deflection in all models. The models were displayed with the surface that suffered tension turned upwards to facilitate the observation of deflections and cracks as shown in Figure 2. The beams' state of degradation after the bending test performed by Lima [12] – before rehabilitation procedures – can also be seen in this figure.

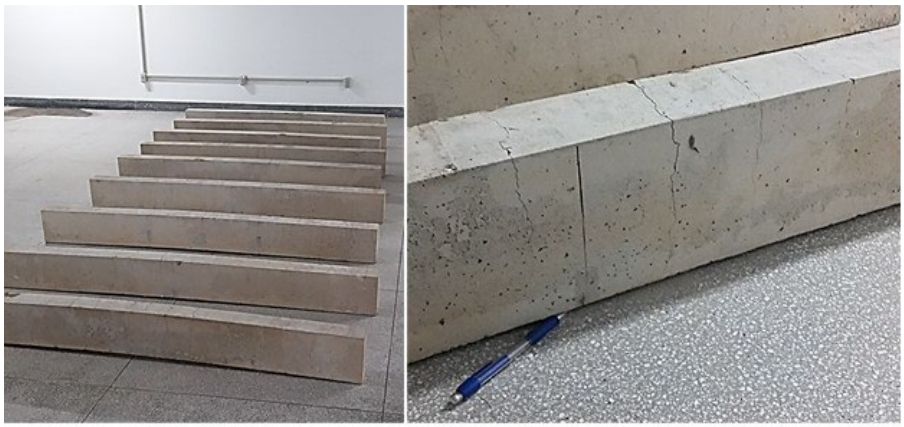


**Figure 2.** Original specimens after mechanical d'+amage (a); detail of cracking and permanent deflection (b).

A preliminary inspection of the damaged beams was conducted in order to select which materials and procedures should be adopted for the rehabilitation. Table 1 contains a summary of the general characteristics of the beams used in this work. Codes 50, 63, and 80 represent beams with positive reinforcements of 2ϕ5.0, 2ϕ6.3, and 2ϕ8.0, respectively. Codes R1, R2, and R3 represent specimen numbers.

**Table 1.** Specimen characteristics.

| | **Series** | **50** | | | **63** | | | **80** | | |
|---|---|---|---|---|---|---|---|---|---|---|
| | **Specimen** | **R1** | **R2** | **R3** | **R1** | **R2** | **R3** | **R1** | **R2** | **R3** |
| Technical features | $E_s$ (MPa) | | 210000 | | | 210000 | | | 210000 | |
| | $f_c$ (MPa) | | 50.2 | | | 50.2 | | | 50.2 | |
| | $f_{ct,m}$ (MPa) | | 3.6 | | | 3.6 | | | 3.6 | |
| | $E_c$ (MPa) | | 26880 | | | 26880 | | | 26880 | |
| | Ultimate load (kN) | 19.61 | 19.43 | 19.82 | 26.64 | 26.40 | 25.66 | 43.96 | 47.75 | 48.06 |
| | $EI$ x $10^5$ ($Nm^2$) - Initial | 9.71 | 10.52 | 10.87 | 9.84 | 9.61 | 9.89 | 9.80 | 9.91 | 10.34 |
| | $EI$ x $10^5$ ($Nm^2$) - Final | 4.12 | 3.80 | 4.37 | 5.62 | 5.43 | 5.60 | 5.66 | 4.95 | 5.20 |
| | Biggest crack (mm) | 0.70 | 0.83 | 0.77 | 0.90 | 0.60 | 0.70 | 0.63 | 0.70 | 0.53 |
| | Smallest crack (mm) | 0.23 | 0.20 | 0.20 | 0.20 | 0.40 | 0.30 | 0.30 | 0.40 | 0.13 |
| | Permanent deflection (mm) | 4.81 | 4.62 | 4.62 | 4.35 | 4.61 | 4.67 | 7.11 | 11.17 | 8.10 |

The three beam specimens of each group, which had the same reinforcement ratio, underwent different structural rehabilitation procedures. The first specimen did not undergo crack injection. The cracks on the second specimen were injected with resin type 1, recommended for cracks larger than 0.3 mm. The cracks on the third specimen were injected with resin type 2, recommended for cracks larger than 0.1 mm. After the injection procedure, all specimens were reinforced with a CFRP sheet. Table 2 shows the nomenclature used to identify each specimen in relation to its characteristics. The prefix CR represents the reinforcement with the carbon fiber sheet (CFRP sheet). The number next to the prefix represents the diameter of the rebars. The suffix indicates which injection process was adopted: NI (no injection), I1 (injection with resin type 1), and I2 (injection with resin type 2).

**Table 2.** Specimen IDs according to structural rehabilitation process.

| Reinforcement | Rehabilitation Process | | | ID |
|---|---|---|---|---|
| | Carbon Reinforcement | Injection | | |
| Ц (mm) | | Resin type 1 (> 0.3 mm) | Resin type 2 (> 0.1 mm) | |
| 5.0 | x | | | CR50-NI |
| 5.0 | x | x | | CR50-I1 |
| 5.0 | x | | x | CR50-I2 |
| 6.3 | x | | | CR63-NI |
| 6.3 | x | x | | CR63-I1 |
| 6.3 | x | | x | CR63-I2 |
| 8.0 | x | | | CR80-NI |
| 8.0 | x | x | | CR80-I1 |
| 8.0 | x | | x | CR80-I2 |

CR-## – CR50 - 2ϕ5.0, CR63 - 2ϕ6.3; CR80 - 2ϕ8.0.
NI – No injection; I1 – Injection with resin type 1; I2 – Injection with resin type 2.

## 2.2 Crack injections

Table 3 displays the physical and mechanical characteristics of the two different resins used in the crack injections.

**Table 3.** Characteristics of resins

| Epoxy resin | Penetration | *c* | Visc. | $\gamma_{comp.}$ | $\gamma_{trac.}$ | $e_{max}$ | E |
|---|---|---|---|---|---|---|---|
| | | (g/cm³) | (mPa·s) | (MPa) | (MPa) | | (MPa) |
| Type 1 | ≥ 0.3 mm | 1.08 | 300 | 70 | 30 | 6.0% | 2600 |
| Type 2 | ≥ 0.1 mm | 1.07 | 145 | 75 | 65 | 4.5% | 3000 |

Due to the models' small size, surface packers were utilized in the injection process (Figure 3), same procedure utilized by Ekenel and Myers [13], Nikopour and Nehdi [14] and Griffin et al. [15]. The alternative would be to employ borehole packers, which is an invasive procedure that could cause damage to the models and undermine the final rehabilitation process.

**Figure 3.** Surface packers.

For one single crack, epoxy resin manufacturers usually recommend a distance between surface packers smaller than the structural element's thickness. In the models employed in this study, the cracks spanned the entire width of the transversal section, which was small. For this reason, only one surface packer was placed over each crack, contributing to the resin's penetration. The packers were secured with a nail after being glued to the specimen. The placement of the surface packers is displayed in Figure 4.

**Figure 4.** Surface packers secured with nails.

After the beams were cleaned, the cracks were sealed and the surface packers were glued with an epoxy adhesive and secured with nails. In Figure 5 one can observe the gluing of the surface packers and the superficial sealing of each crack, which extended through the entire lateral section. All cracks visible to the naked eye on the surface of the model that underwent tension were injected.

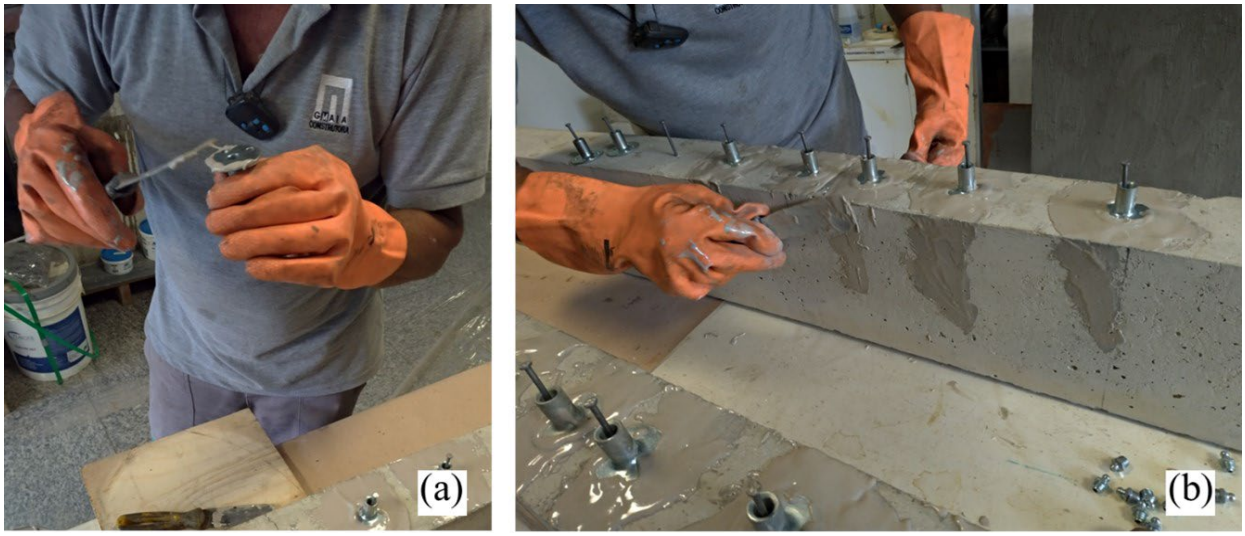


**Figure 5.** Gluing of surface packers (a); sealing the cracks (b).

The cracks received epoxy resin injections after the sealing adhesive finished curing. The bicomponent resin was mixed and all cracks were injected as shown in Figure 6.

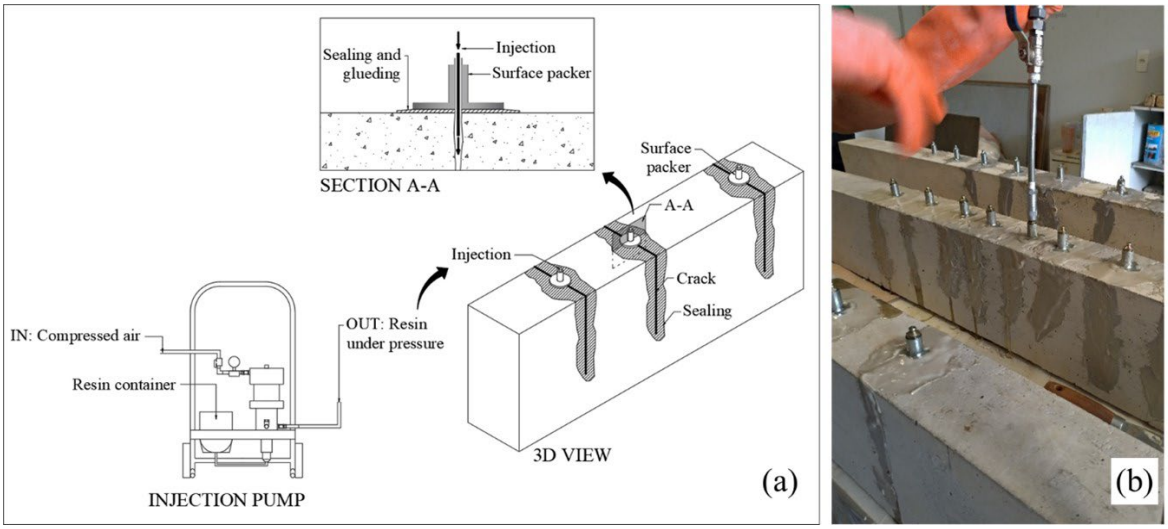


**Figure 6.** General schematics of crack injection in the models (a); crack injection procedure (b)

The entire injection process was performed with pressures varying between 35 bar and 100 bar, values below the 200 bar recommended by the manufacturer as the maximum pressure for crack injection. The injection procedure of each crack was finished when the injected material overflowed.

### 2.3 Reinforcement with CFRP sheet

The structural reinforcement with the CFRP sheet was done after the beams' cracks were injected. All surface packers were removed before the structural reinforcement with CFRP was carried out. The adhesive employed in the sealing of cracks and gluing of surface packers was also removed with a grinding machine.

The flexural reinforcement was designed according to the ACI 440.2R [8]. The ultimate load reached in each specimen of Lima's [12] work was adopted as design criteria. All elements were reinforced with a single layer of CFRP. For specimens CR63 and CR80, where ultimate loads surpassed that of specimen CR50, a transverse anchorage was necessary in order to meet criteria established in the ACI 440.2R [8]. Figure 7 displays the schematics of beams reinforced with CFRP. Table 4 indicates the physical and mechanical characteristics of materials employed in the reinforcement.

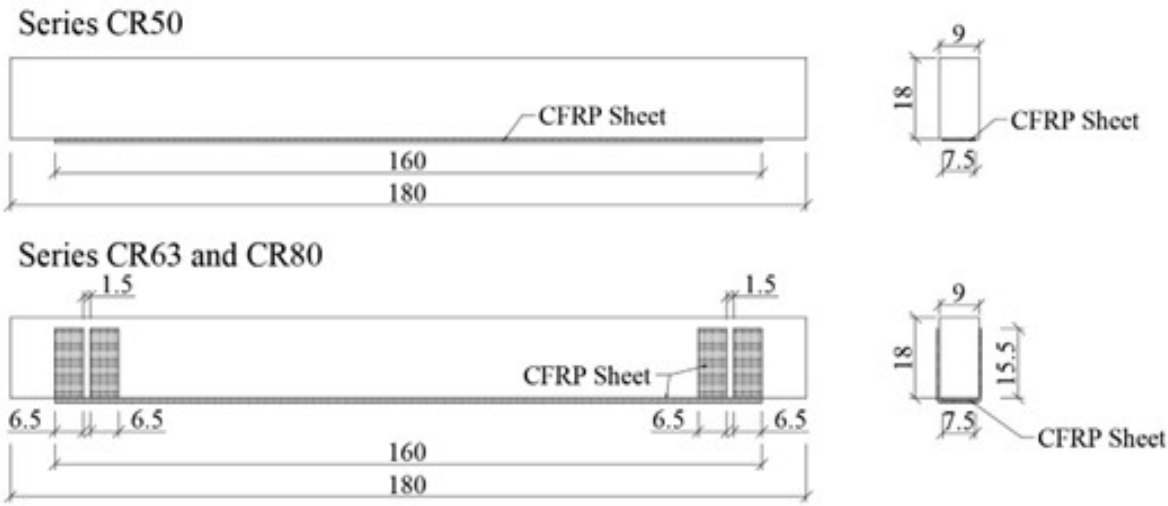


**Figure 7.** Schematics of beams reinforced with CFRP sheet. Dimensions in centimeters.

**Table 4.** Characteristics of materials employed in reinforcements with CFRP

| | $c$ | $y_{trac.}$ | $y_{ader.}$ | $E$ | $e_{max}$ | $t$ |
|---|---|---|---|---|---|---|
| | (g/m²) | (MPa) | (MPa) | (MPa) | (%) | (mm) |
| CFRP sheet | 300 | 3600 | - | 230000 | 2.1 | 0.166 |
| Thixotropic adhesive | 1.33 | - | 14 | 4700 | - | - |
| Laminating resin | 1.12 | - | 14 | 3000 | - | - |

The regions where CFRP sheets were attached (lower part and the sides that received anchorage) were sanded with a grinder in order to expand the concrete's pores and contribute to its bonding to the thixotropic adhesive. Subsequently, the concrete's surface was cleaned in order to remove dust particles, grease, or any other contaminant that might hinder adherence.

The lamination resin was applied after the thixotropic adhesive finished curing, with the sheet already attached. A foam paint roller was used to drench the CFRP sheet in the lamination resin, ensuring that the carbon fiber sheet was completely soaked with resin. Figure 8 shows part of the beam specimens after the rehabilitation process, highlighting the lower faces where the CFRP sheet was applied.


**Figure 8.** Beams reinforced with CFRP without anchorage (a), and with anchorage (b).

## 2.4 Bending test

The bending test followed the same procedure employed in the reference experiments conducted by Lima [12]. The Stuttgart Test configuration was adopted, with four load application points. Loads were applied 55 cm away from supports and were 60 cm apart, as shown in Figure 9.

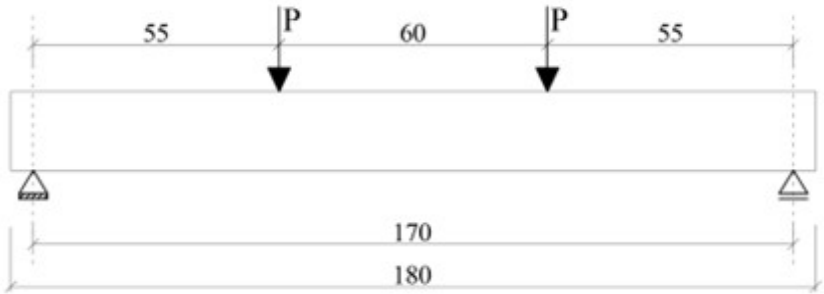


**Figure 9.** Bending test structural model. Dimensions in centimeters

The load was applied continuously with displacement control at a rate of 0.01 mm/s. The steel reaction beam was strategically placed over the universal testing machine in order to provide a 170 cm span for the specimens.

Two displacement transducers (DT) were installed in the center of the span in order to measure displacements. Additionally, two strain gauges were employed, both placed on the piece's central axis. One of the strain gauges was placed on the top of the element (SG_TOP) and the other at the bottom (SG_BOT) to measure deformations in the concrete and in the carbon fiber, respectively. A 200kN load cell was placed between the load transmission device and the actuator's spherical seating in the universal testing machine. Figure 10 displays the bending test's assembly schematics.

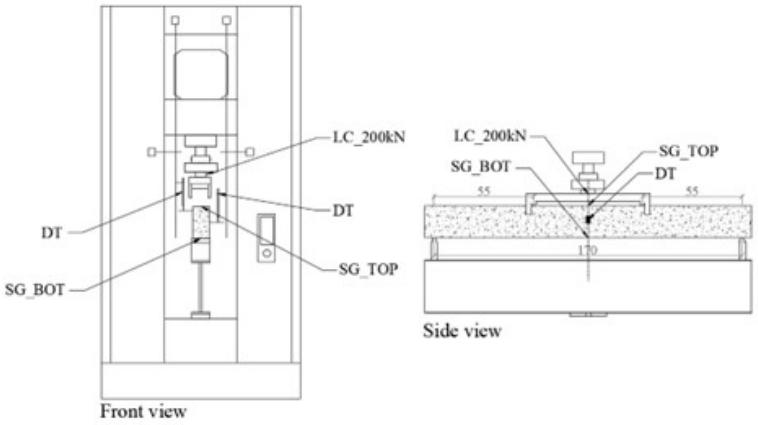


**Figure 10.** Bending test assembly schematics. Dimensions in centimeters.

The beam specimens were subjected to progressive load stages where displacement and deformations were measured. At the end of each stage the load was completely removed, the actuator having been suspended, reestablishing the beam's original simply supported condition. This procedure restores the element's elastic deformation while maintaining the inelastic deformation resulting from each stage.

## 2.5 Vibration test

The beams were instrumented as shown in Figure 11, with an accelerometer in position 1. The beam was struck with a rubber hammer in position 2 so that its fundamental frequency could be obtained.

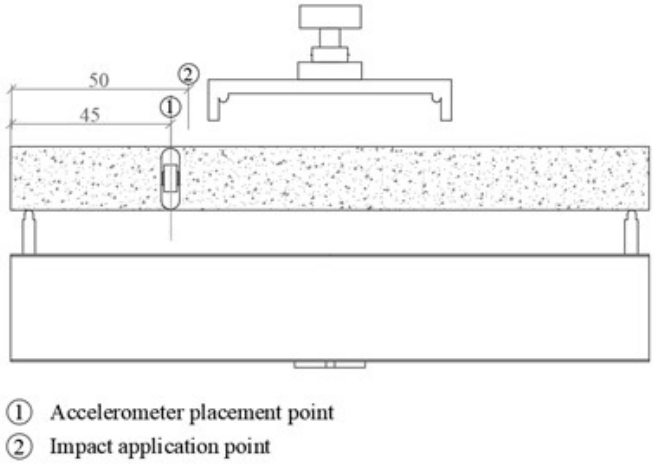


**Figure 11.** Accelerometer placement and impact application point in the vibration test.

The vibration test of specimens was performed before and after rehabilitation procedures. In both cases, the beam was simply supported. The fundamental frequency of each specimen was determined through the Fast Fourier Transform (FFT) applied to acceleration and time data.

After the fundamental vibration frequency was obtained, with the simply supported boundary condition maintained, the stiffness was calculated according to Equation 1 [16].

$$EI = \frac{f^2(2\pi L^2)^2(\rho A)}{(\beta^2)^2} \quad (1)$$

where: $f$ = fundamental vibration frequency (Hz); $L$ = span (m); $\rho$ = beam's specific mass (kg/m$^3$); $A$ = cross-section area (m$^2$); $\beta^2$ = constant dependent on boundary conditions (9.869).

## 3 RESULTS AND DISCUSSION

### 3.1 Stiffness after the rehabilitation process

Based on acceleration and frequency values obtained in the vibration tests, the stiffness before and after structural rehabilitation was estimated through Equation 1. Figure 12 displays the stiffness of each beam specimen before and after rehabilitation, as well as the stiffness values of the original undamaged beams obtained by Lima [12].

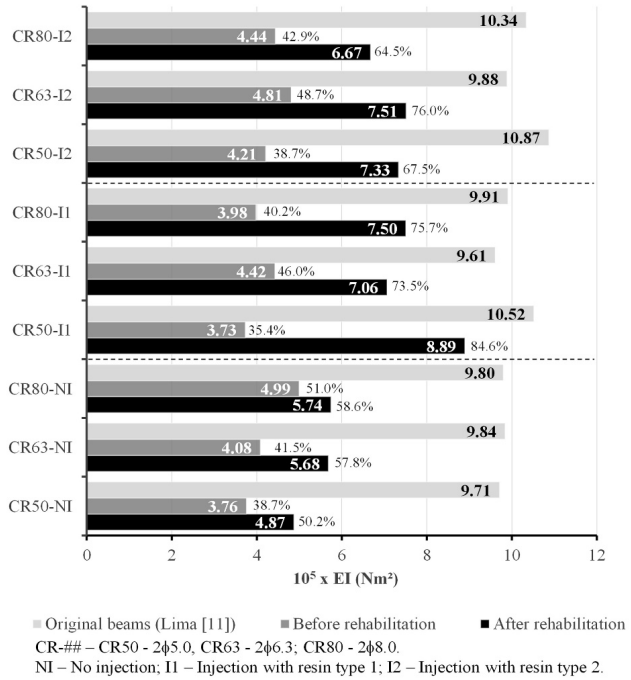


**Figure 12.** Estimated stiffness of the beams.

After structural rehabilitation, elements that went through the injection process and were reinforced with CFRP (CR##-I1 and CR##-I2) displayed an average stiffness of 74% of the original beams' stiffness, as observed in the results shown in Figure 12. In contrast, elements that were only reinforced with CFRP and were not injected (CR##-NI) displayed an average 55% of the original specimens' stiffness. Therefore, in both cases (with and without crack injection) stiffness was higher than the estimated stiffness of damaged specimens before rehabilitation. It is also evident that specimens with crack injection (CR##-I1 and CR##-I2) displayed a stiffness superior to those only reinforced with

CFRP (CR##-NI). These results confirm what was observed by Salgado et al. [9] and by Al Nu'man and Al-Sahlani [4] regarding the influence of the rehabilitation process in the element's stiffness.

Resin type 2 (less viscous) was expected to re-establish a higher degree of the element's original monolithic configuration since, unlike resin type 1, it would also fill cracks with openings between 0.1 mm and 0.3 mm. However, stiffness results did not corroborate this expectation as seen in Figure 12. Based on the estimated stiffness after injection, beam stiffness results for both resins fell in the same range.

Figure 13 displays load-deflection curves obtained in the bending tests. In addition to test curves, one extra curve has been plotted based on the analytical model proposed by Branson [17], which considers the CFRP sheet in the same way as the reinforcement bars for purposes of cross-section homogenization.

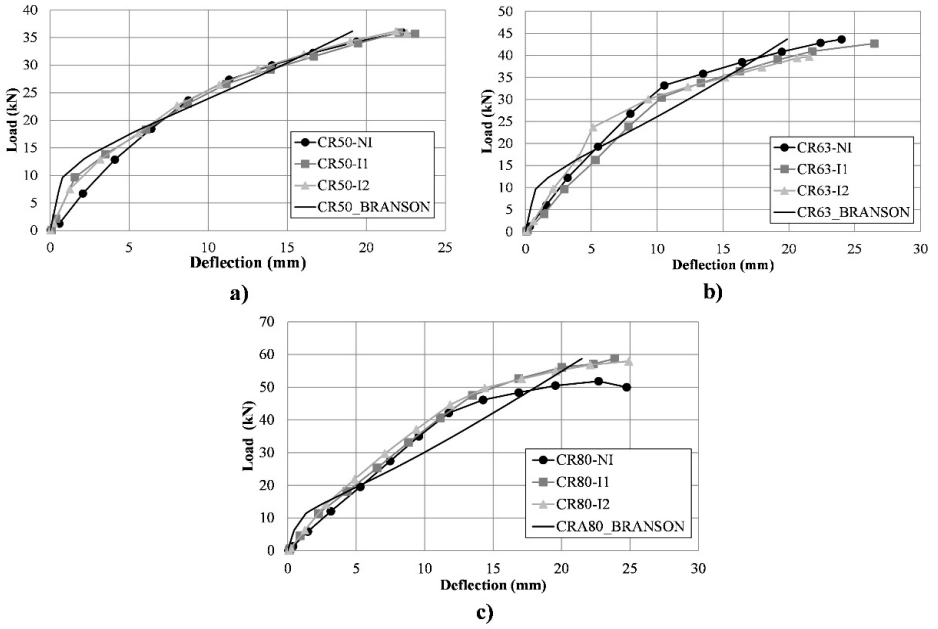


**Figure 13.** Load-deflection curves obtained in the bending test for beams: a) CR50; b) CR63; c) CR80. Load (kN) represents the sum of the loads (2*P*) applied to the beam.

By observing curve slopes in Figure 13, one can note a difference in element stiffness during initial load stages. This difference is related to the adoption of the structural rehabilitation process. Non-injected beams (CR##-NI) had a lower initial stiffness than injected beams, except for beam CR63-NI. This lower initial stiffness in non-injected specimens is consistent with the results obtained with vibration tests, displayed in Figure 12. Moreover, the difference in stiffness becomes less pronounced during load application and the stiffness decay level tends to be the same in all beams in stages with more elevated loads.

When experimental results and analytically estimated results are compared, it is evident that Branson's analytic model [17] predicts a higher initial stiffness. This model considers that the parts are uncracked at the beginning of the test. However, according to what has been observed in the vibration tests, in the case of rehabilitated elements, not even parts that underwent crack injections with epoxy resins displayed a stiffness level equal to that of uncracked parts. Therefore, the difference in stiffness during initial load stages that can be seen in the load-displacement curves is due to a degradation already present in all elements.

### 3.2 The structural behavior of rehabilitated beams

Figure 14 displays load-displacement curves obtained through the bending test. The deflection relative to each load stage corresponds to the deflection obtained in the test added to the residual deflection measured prior to testing, according to figures presented in Table 1. The average curve of the original undamaged specimen tests obtained by Lima [12] is also displayed with each group of beams with the same reinforcement ratio. This allows for the comparison of the original specimens' behavior as tested by Lima [12] and after structural rehabilitation.

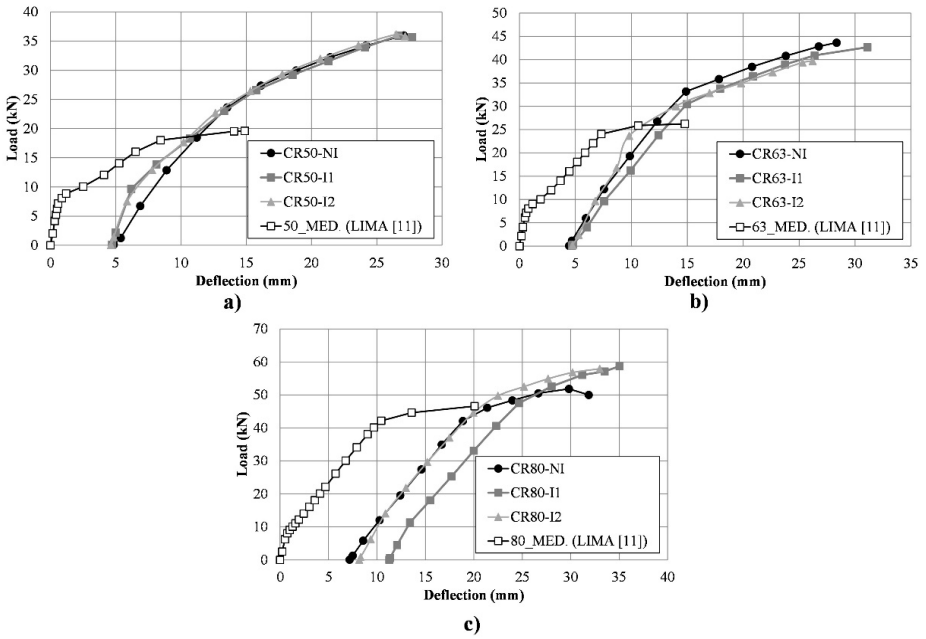


**Figure 14.** Load-deflection curves comparing rehabilitated beams with the original undamaged beams tested by Lima [12]: a) CR50; b) CR63; c) CR80. Load (kN) represents the sum of the loads (2P) applied to the beam.

Based on Figure 14, one can note that non-injected elements (CR##-NI) presented a stiffness like that of the original beam in State II (##_MED). In contrast, the stiffness of beams that underwent the crack injection procedure (CR##-I1 and CR##-I2) was lower in comparison to the original beam in State I (##_MED), but higher in State II. After the injected beams' (CR##-I1 and CR##-I2) cracking load was reached, which is evident in the inclination change seen in the load-displacement curve, their stiffness remained close to that of the original beams in State II (##_MED) and to that of the non-injected reinforced beams (CR##-NI).

Figure 15 displays ultimate load values reached in the testing of the original undamaged beams and of the reinforced beams, as well as the ultimate load estimated according to design specifications in the ACI 440.2R [8]. The three specimens in each group, which had the same rebars and received reinforcements, displayed similar ultimate loads, indicating that the injection procedure did not influence the ultimate load level. CFRP sheet reinforcements significantly increased ultimate load, especially in the CR50 beams, which displayed an increase in resistance of 84% in comparison to the original undamaged specimens. Moreover, all ultimate loads in the tests surpassed those predicted by design specifications in the ACI 440.2R [8].

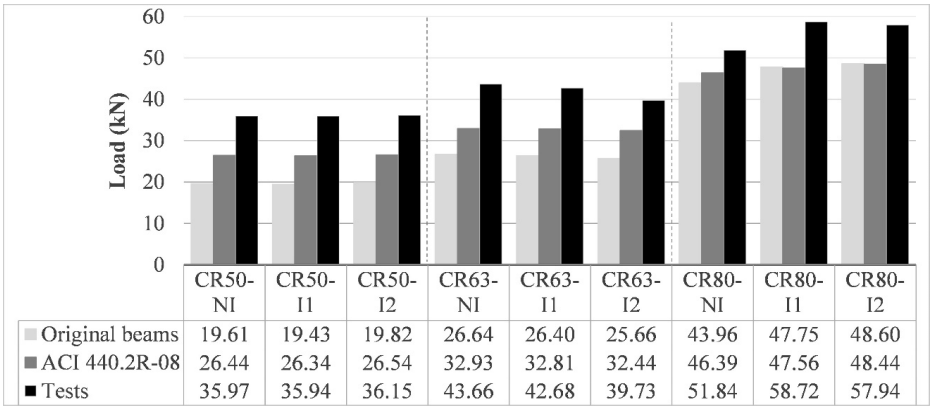


**Figure 15.** Ultimate loads obtained for the original beams based on design specifications in the ACI 440.2R [8] and through tests. Load (kN) represents the sum of the loads (2*P*) applied to the beam.

Beams with the same reinforcement ratio displayed similar failure modes. The maximum values reached for load, deflection and deformation can be seen in Figure 16, along with a sketch exemplifying the failure mode of each beam. Note that concrete deflection and deformation results include residual values already present before the test.

**Failure Mode - CR50-NI**

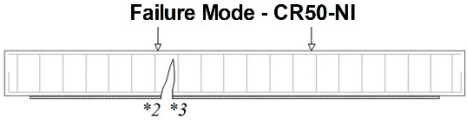


| Load (kN) | Deflection (mm) | CFRP Strain (‰) | Conc. Strain (‰) |
|---|---|---|---|
| 35.97 | 22.26 | 7.78 | -2.65 |

**Failure Mode - CR63-NI**

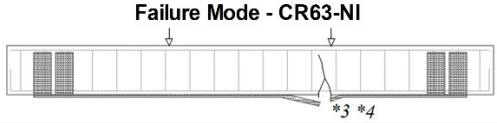


| Load (kN) | Deflection (mm) | CFRP Strain (‰) | Conc. Strain (‰) |
|---|---|---|---|
| 43.66 | 24.00 | 8.63 | -3.07 |

**Failure Mode - CR50-I1**

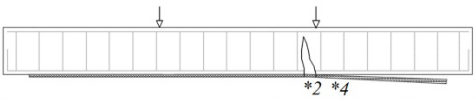


| Load (kN) | Deflection (mm) | CFRP Strain (‰) | Conc. Strain (‰) |
|---|---|---|---|
| 35.94 | 23.09 | 8.61 | -2.98 |

**Failure Mode - CR63-I1**

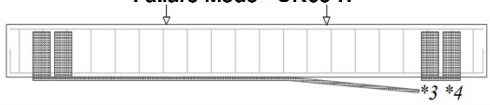


| Load (kN) | Deflection (mm) | CFRP Strain (‰) | Conc. Strain (‰) |
|---|---|---|---|
| 42.68 | 26.49 | 9.03 | -3.09 |

**Failure Mode - CR50-I2**

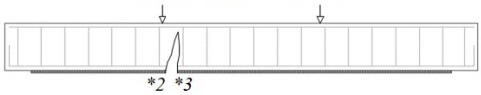


| Load (kN) | Deflection (mm) | CFRP Strain (‰) | Conc. Strain (‰) |
|---|---|---|---|
| 36.15 | 22.55 | 8.41 | -2.82 |

**Failure Mode - CR63-I2**

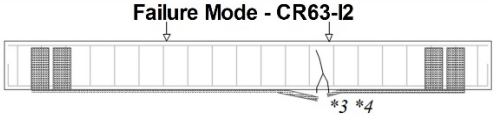


| Load (kN) | Deflection (mm) | CFRP Strain (‰) | Conc. Strain (‰) |
|---|---|---|---|
| 39.73 | 21.55 | 7.93 | -2.86 |

**Failure Mode - CR80-NI**

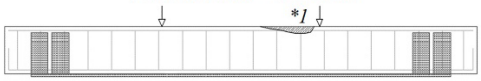


| Load (kN) | Deflection (mm) | CFRP Strain (‰) | Conc. Strain (‰) |
|---|---|---|---|
| 51.84 | 24.76 | 7.06 | -3.62 |

**Failure Mode - CR80-I1**

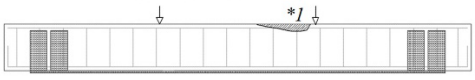


| Load (kN) | Deflection (mm) | CFRP Strain (‰) | Conc. Strain (‰) |
|---|---|---|---|
| 58.72 | 23.88 | 7.97 | -4.27 |

**Failure Mode - CR80-I2**

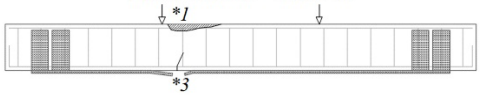


| Load (kN) | Deflection (mm) | CFRP Strain (‰) | Conc. Strain (‰) |
|---|---|---|---|
| 57.94 | 24.91 | 8.10 | -4.44 |

Note:
*1 – Concrete crushing
*2 – Rupture of reinforcement bars
*3 – Rupture of CFRP sheet
*4 – Debonding of CFRP sheet.

**Figure 16.** Failure modes displayed by the specimens. Load (kN) represents the sum of the loads (2*P*) applied to the beams.

All CR50 beams displayed reinforcement bar failure associated to the rupture or debonding of the CFRP reinforcement. This indicates that the reinforcement bars ruptured first, causing the entire traction load to fall upon the CFRP reinforcement, causing its failure (Figure 17).

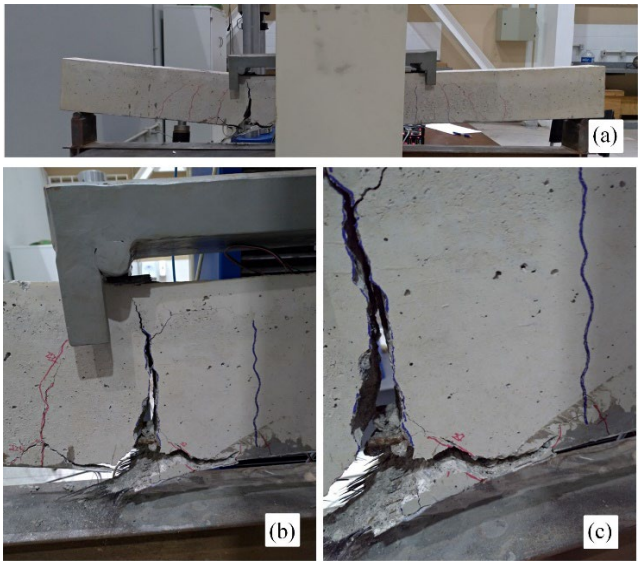


**Figure 17.** Failure of specimen CR50-NI (a); Detail of the specimen's failure location (b); Detail of the rupture of the CFRP sheet and positive reinforcement (c).

CR63 beams displayed failure due to the rupture of the CFRP sheet combined with its debonding from the concrete surface. A horizontal failure surface and a high cracking level were evident, characterizing failure due to the reinforcement's sudden peel off caused by shear cracks. The detachment of concrete parts previously joined to the reinforcement was also observed (Figure 18).


**Figure 18.** Failure of beam CR63-NI (a); Detail of the rupture and debonding of the CFRP sheet (b); Detail of the non-rupture of the positive reinforcement (c).

All beams in the CR80 series displayed the same failure mode, which was the crushing of the compressed concrete. Figure 19 displays the failure mode seen in specimen CR80-I2. In all cases, the concrete's deformation was greater than 3.5‰, corroborating its behavior. Moreover, CR80 beams showed a 20% difference in ultimate load in comparison to the ultimate load predicted by the ACI 440.2R [8], while for the other beams this difference was approximately 30%. This may be related to the failure mode, which occurred in the tensioned region in CR50 and CR63 elements and in the compressed region of CR80 elements.

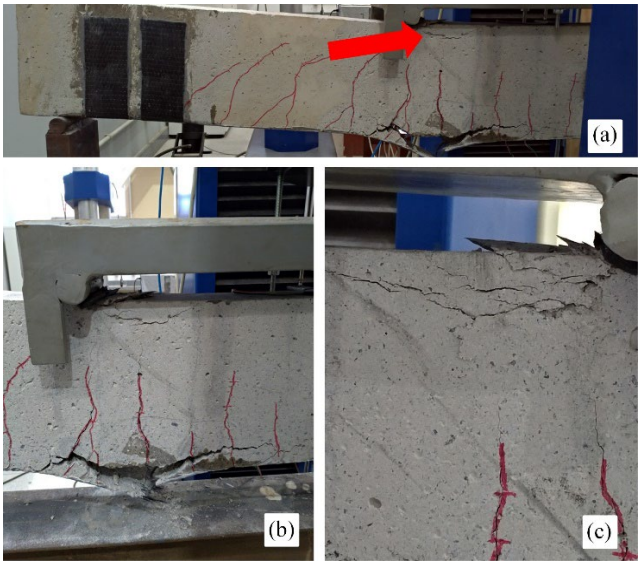


**Figure 19.** Failure of beam CR80-I2 (a); Detail of the crushed concrete and of the CFRP sheet rupture (b); Magnified detail of the crushed concrete (c).

Non-injected beams suffered an increase in already-present cracks and the emergence of new cracks throughout the element. Specimens that received epoxy resin injections reached failure with a cracking pattern similar to that of non-injected specimens, but only displayed cracks that spawned during testing. Injected cracks did not reopen and new cracks appeared in the surroundings of those that had been injected, as shown in Figure 20. In some cases, the new cracks crossed previously injected cracks, confirming the efficacy of the injection process and the successful recovery of monolithism in the previously cracked region.

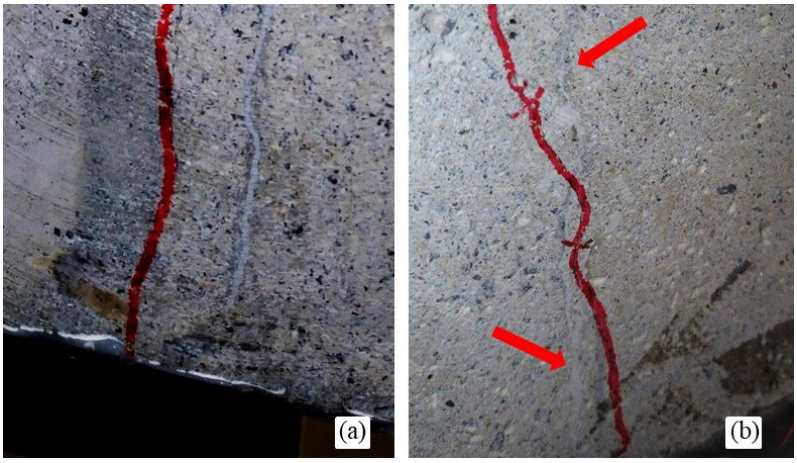


**Figure 20.** Detail of a new crack next to an injected crack (a); Detail of a new crack crossing an injected crack (b).

## 5 CONCLUSIONS

This work employed vibration tests, a non-destructive test (NDT), in order to evaluate the structural behavior of reinforced concrete beams rehabilitated with CFRP and crack injection. The main conclusions reached in this study are presented below:

(1) All specimens displayed an increase in their fundamental vibration frequency and, consequently, in their stiffness after the structural rehabilitation process. The crack injections with epoxy resins were responsible for this increase in stiffness. Beams that received crack injections (CR##-I1 and CR##-I2) displayed an average stiffness of 74% of the original undamaged beams' (##_MED) stiffness, while non-injected beams (CR##-NI) displayed around 55% of the original beams' stiffness. Additionally, there were no significant changes regarding the stiffness increase in beams injected with the resin indicated for cracks larger than 0.3 mm (type I1) and in those injected with the resin indicated for cracks larger than 0.1 mm (type I2).

(2) The curve based on the analytical model proposed by Branson [17] displays an initial segment with more inclination than the one obtained experimentally, since this model considers that parts are perfectly monolithic at the beginning of the test. It was evident, however, that even parts subjected to crack injections do not display the same stiffness of the original parts.

(3) Rehabilitated beams displayed an increase in their ultimate load when compared to the original specimens. It is noted that the crack injection process did not influence the ultimate load reached by beams in the bending test. However, non-injected beams (CR##-NI) display a stiffness very similar to the original beams' State II (##_MED). In contrast, the initial stiffness of injected beams (CR##-I1 and CR##-I2), remained between that of the original beams' (##_MED) State I and State II. After reaching cracking load, the injected beams' (CR##-I1 and CR##-I2) stiffness was very close to that of the original beams' State II (##_MED) and to that of the non-injected beam (CR##-NI).

(4) The failure modes of beams with the same reinforcement ratio were similar. All CR50 beams displayed reinforcement bar failure along with the rupture or debonding of the CFRP sheet. CR63 beams displayed failure due to the CFRP's rupture combined with its debonding from the concrete surface. In these cases, a detachment of concrete parts that were previously joined to the rebars also occurred. All CR80 beams displayed failure due to the compressed concrete's crushing. It is noted that in all cases the ultimate load value was superior to the value predicted by the ACI 440.2R [8].

## ACKNOWLEDGEMENTS

The authors wish to acknowledge the *Coordenação de Aperfeiçoamento de Pessoal de Nível Superior* – CAPES (Coordination for the Improvement of Persons in Higher Education); *Conselho Nacional de Desenvolvimento Científico e Tecnológico* – CNPq (National Council of Scientific and Technological Development); *Fundação de Amparo à Pesquisa do Estado de Minas Gerais* – FAPEMIG (Research Support Foundation of the State of Minas Gerais); and the Federal University of Viçosa – UFV for their support in the realization and dissemination of this study. The authors also acknowledge Pórtico Engenharia and engineer Fábio Poltronieri, G-Maia Construtora and Architect Gustavo Maia, and MC Bauchemie for the materials supplied and technical support.

## REFERENCES

[1] Federation Internacional du Betón. *fib Model Code for Concrete Structures 2010*, Wiley-VCH Verlag GmbH & Co. KGaA, Weinheim, Germany, 2013. https://doi.org/10.1002/9783433604090.

[2] V. C. Souza and T. Ripper, *Pathology, recovery and structural reinforcement of concrete*, 1st ed. São Paulo, Brazil: Pini, 1998.

[3] K. F. von Fay, *Guide to Concrete Repair*, 2th ed., US Department of the Interior Building – Bureau of Reclamation, Washington, DC, 2015.

[4] B. S. Al-Nu'man and M. H. Al-Sahlani, "Behavior of repaired reinforced concrete beams failed in shear," *J Eng Dev*, vol. 10, no. 3, pp. 115–134, Sep 2006.

[5] A. J. Beber, "Structural behavior of reinforced concrete beams reinforced with carbon fiber composites", Ph.D. dissertation, Univ. Fed. do Rio Grande do Sul, Porto Alegre, Brasil, 2003.

[6] L.P. Juvandes and J.A. Figueiras, "Design and security concepts for reinforcement projects with composite FRP systems", *Concr. Estrut*., pp. 1–10, 2000.

[7] L. C. Bank, *Composites for Construction: Structural Design with FRP Materials*, John Wiley & Sons, Inc., Hoboken, NJ, USA, 2006. https://doi.org/10.1002/9780470121429.

[8] American Concrete Institute, *Guide for the Design and Construction of Externally Bonded FRP Systems for Strengthening Concrete Structures*, ACI PRC-440.2-17, 2017.

[9] R. Salgado et al., "Structural assessment of concrete beams strengthened with CFRP laminate strips by their dynamic response," *Port. J. Struct. Eng.*, vol. 3, pp. 37–46, 2017.

[10] J. Helal et al., "Non-destructive testing of concrete: a review of methods," *EJSE Int.*, vol. 1, pp. 97–105, 2015.

[11] O. S. Salawu, "Detection of structural damage through changes in frequency: a review," *Eng. Struct.*, vol. 19, pp. 718–723, 1997, http://dx.doi.org/10.1016/S0141-0296(96)00149-6.

[12] G. E. S. de Lima, "Avaliação dinâmica do comportamento estrutural de vigas de concreto armado submetidos à degradação da rigidez", M.S. thesis, Univ. Fed. de Viçosa, Viçosa, Brazil, 2017.

[13] M. Ekenel and J. J. Myers, "Durability performance of RC beams strengthened with epoxy injection and CFRP fabrics," *Constr. Build. Mater.*, vol. 21, pp. 1182–1190, 2007, http://dx.doi.org/10.1016/j.conbuildmat.2006.06.020.

[14] H. Nikopour and M. Nehdi, "Shear repair of RC beams using epoxy injection and hybrid external FRP," *Mater. Struct.*, vol. 44, pp. 1865–1877, 2011, http://dx.doi.org/10.1617/s11527-011-9743-8.

[15] S. Griffin, H. Askarinejad, and B. Ferrant, "Evaluation of epoxy injection method for concrete crack repair," *Int. J. Struct. Civ. Eng. Res.*, vol. 6, pp. 177–181, 2017, http://dx.doi.org/10.18178/ijscer.6.3.177-181.

[16] A. W. Leissa and M. S. Qatu, *Vibration of Continuous Systems*, Mc Graw Hill, New York, 2011.

[17] D. E. Branson, "Deflections of reinforced concrete flexural members," *J. Am. Concr. Inst.*, vol. 63, no. 6, pp. 637–667, 1966.

**Author contributions:** LFFG: conceptualization, experimental analysis, data curation, formal analysis and writing; GESL: experimental analysis and methodology; JLRP and GSV: funding acquisition, conceptualization, methodology, data curation, formal analysis, writing and supervision.

**Editors:** Mauro de Vasconcellos Real, Guilherme Aris Parsekian.